

Multimodal Image Analysis of the Human Brain

Multimodale beeldanalyse van het menselijk brein

Ivana Despotovic

Promotor: prof. dr. ir. W. Philips
Proefschrift ingediend tot het behalen van de graad van
Doctor in de Ingenieurswetenschappen

Vakgroep Telecommunicatie en Informatieverwerking
Voorzitter: prof. dr. ir. H. Bruneel
Faculteit Ingenieurswetenschappen en Architectuur
Academiejaar 2013 - 2014



ISBN 978-90-8578-658-0
NUR 954
Wettelijk depot: D/2014/10.500/4

*The scientific man does not aim at an immediate result.
He does not expect that his advanced ideas will be readily taken up...
His duty is to lay the foundation for those who are to come, and point the way.*
– Nikola Tesla

Members of the jury

prof. dr. ir. Rik Van de Walle (Ghent University, chairman)
prof. dr. ir. Sabine Wittevrongel (Ghent University, secretary)
prof. dr. ir. Wilfried Philips (Ghent University, supervisor)
prof. dr. ir. Sabine Van Huffel (KU Leuven)
prof. dr. ir. Maarten De Vos (Carl von Ossietzky University of Oldenburg)
prof. dr. ir. Bart Goossens (Ghent University)
dr. med. Paul Govaert (Erasmus MC-Sophia Children's Hospital)
dr. lic. Ewout Vansteenkiste (Ghent University)
dr. ir. Hans Hallez (KU Leuven)
dr. ir. Ljubomir Jovanov (Ghent University)

Affiliations

Research Group for Image Processing and Interpretation (IPI)
Department of Telecommunications and Information Processing (TELIN)
Faculty of Engineering and Architecture
Ghent University
iMinds

Sint-Pietersnieuwstraat 41
B-9000 Ghent
Belgium



Acknowledgements

If I have seen further, it is because I stood on the shoulders of giants.
Sir Isaac Newton

The acknowledgement is the part of the thesis that attracts the most of the attention - for good reasons! Writing a dissertation is a long and lonely process, but research in general and a thesis in particular is never done in isolation. In my Ph.D. journey I found a lot of help, luck, and encouragement along the way and I wish to acknowledge the goodwill, advice and support that I have received from many others in completing this thesis.

In particular, I would like to thank my promoter Prof. Wilfried Philips for providing me with the opportunity to undertake this exciting research and to present my work at numerous international conferences. I am very grateful for his trust, support, patience and enthusiasm through this project. Next, I would like to thank Dr. Ewout Vansteenkiste for following my work during all these years, for constructive discussions about my research topic and for giving me great encouragement and motivation. A special thanks goes to Prof. Aleksandra Pižurica for inviting me to come to Belgium and do my Ph.D. at Ghent University.

This thesis would not be possible without a relatively large international team, which reflects the diversity of the medical imaging and the EEG signal processing community. I want to thank Dr. Paul Govaert, Dr. Maarten Lequin, Dr. Renate Swarte, Dr. Jeroen Dudink, Dr. Joseph Perumpillichira and Dr. Gerhard Visser (medical doctors from Erasmus MC-Sophia Children's Hospital, Rotterdam) for providing MR images and EEG data of the neonatal brain, for sharing with me their vast knowledge about the human brain and for giving me courage and support in my research. I want to thank Prof. Sabine Van Huffel, Prof. Maarten De Vos and Dr. Wouter Deburchgraeve for their advice, cooperation and innovative ideas in the field of neonatal EEG signal processing. Without their knowledge and inputs, the realization of neonatal EEG source localization would not be possible. More specifically, I want to acknowledge Dr. Hans Hallez for providing me his codes and fruitful cooperation in the area of EEG dipole source analysis. It has been a great privilege and pleasure for me to interact with all of you!

I want to thank the members of the radiology department of the Ghent University Hospital and especially Prof. Karel Deblaere for providing brain MR images of FCD patients. Thank you for the support and constructive feedback.

Furthermore, I would like to thank my dear colleague Prof. Bart Goossens for his interest in my research and for giving me valuable feedback and support. His profound way of working has been stimulating for me. I would also like to thank to all my TELIN colleagues with whom I collaborated on a daily basis. Thank you for the pleasant working atmosphere. Spacial thanks to my colleagues Jonas De Vylder and Jan Aelterman for their help in translating my English summary to Dutch. Also, many thanks to Philippe Serbruyns and Davy Moreels for their excellent IT support and Annette Nevejans, Patrick Schaillee and Sylvia Moeneclaeys for their precious administrative assistance.

I am very grateful to my Ph.D. committee for critically reading this thesis and making constructive remarks. I believe that their suggestions have increased the clearness and the quality of my work.

Everyone who contributed to my education is also kindly acknowledged for their part in my personal discovery of the world we live in.

I am infinitely grateful to my parents Vaso and Radojka for their invaluable love, trust and encouragement through all my life. Thank you so much for everything and without you nothing would be possible! Finally, I would like to thank my husband Vedran for his endless love, patience, encouragement, immense understanding and unconditional support in all my doings. Thank you for loving me and being my strength and inspiration!

*Ivana Despotović
November, 2013.*

Samenvatting

Gedurende de laatste decennia heeft de snelle ontwikkeling van niet-invasieve hersenbeeldvorming technologieën een revolutie teweeg gebracht in de mogelijkheid om de structuur en functionaliteit van hersens te bestuderen. Er is grote vooruitgang geboekt in het beoordelen van hersenschade en het verkennen van de anatomie van de hersens door gebruik te maken van MRI, terwijl EEG beschouwd wordt als de gouden standaard voor diagnose van neurologische afwijkingen. Beide beeldvormingstechnieken hebben hun voor- en nadelen, en geen enkele individuele methode is perfect geschikt voor alle klinische toepassingen. Daarom is er stijgende interesse in het bestuderen van multimodale hersenbeeldvorming, dit is het benutten van de intrinsieke krachten van verschillende beeldvormingstechnieken, of verschillende modaliteiten van dezelfde techniek, door die technieken te combineren. Bijvoorbeeld, de integratie van EEG en MRI data laat toe om bronnen van neurale hersenactiviteit te lokaliseren in 3D ruimte via EEG en die onmiddellijk te vergelijken met zichtbare hersenletsels uit het MRI beeld. Een ander voorbeeld is het combineren van verschillende MRI sequenties van de hersenen, zoals T1-gewogen of T2-gewogen MRI, diffusie gewogen MRI of functionele MRI, waardoor we meer herseninformatie kunnen vergaren en betere hersenletseldetectie kunnen doen.

De vooruitgang in hersenbeeldvorming technologie resulteert in een grote hoeveelheid data met steeds hogere kwaliteit. De analyse van deze grote en complexe multimodale datasets is een langdradig en complexe taak voor klinici, die de relevante informatie manueel moeten visualiseren en extraheren. Deze manuele analyse is niet alleen tijdrovend, maar ook gevoelig voor fouten, zoals vastgesteld bij verschillende inter- en intra-operator variabiliteitsstudies. Deze uitdagingen in hersendata-analyse resulteerde in de nood voor geautomatiseerde methoden om ziektediagnoses te verbeteren en te testen. De dag van vandaag wordt computer geholpen diagnose (CAD) vaak gebruikt om artsen bij te staan bij het maken van kwalitatieve diagnoses, onder de vorm van computeralgoritmen voor beeldsegmentatie, registratie en visualisatie.

In deze thesis focussen we op de ontwikkeling van nieuwe en verbeterde computertechnieken voor multimodale analyse van het menselijke brein, waaronder MRI segmentatie en EEG bronlokalisatie. We besteden veel aandacht aan de verbetering en ontwikkeling van nieuwe methoden voor accurate en ruisrobuuste beeldsegmentatie, dewelke daarna succesvol gebruikt worden voor de segmentatie van hersens in MRI van zowel volwassen als pasgeborenen, alsook voor de ontwikkeling van realistische hoofdmodellen van pasgeborenen. Daarenboven ontwikkelden we een geïntegreerde, multimodale EEG-MRI methode voor de lokalisatie van abnormale neuronale

activiteit in de hersenen van een pasgeborene. Deze lokalisatie wordt gebruikt voor de vergelijkende studie tussen een beroertes, gedetecteerd via EEG en acute perinatale hersenletsels, zichtbaar in MRI. Hiervoor voegen we theorie en praktijk samen waarbij we focussen op twee medische applicaties: (1) automatische 3D MRI segmentatie van de volwassen hersenen in de aanwezigheid van een subtiel epileptisch hersenletsel, veroorzaakt door focal cortical dysplasia (FCD) en (2) multi-modale data analyse van de hersens van een pasgeborene met perinatale hersenschade, veroorzaakt door asphyxia en hypoxische-ischemische encefalopathie, een aandoening van ernstig tekort aan zuurstof of bloed in de hersens.

Beeldsegmentatie niet triviaal omdat MRI beelden imperfecties vertonen. Daarenboven zijn beelden dikwijls gedegradeerd door ruis en andere artefacten. De diversiteit van beeldverwerkingstoepassingen hebben tot de ontwikkeling van verschillende segmentatietechnieken geleid, die zowel verschillen in precisie als in complexiteit. Dit komt omdat er geen methode bestaat die bruikbaar is voor alle afbeeldingen, noch zijn alle methoden even goed voor een bepaald type van afbeelding. Bijvoorbeeld, sommige methoden gebruiken enkel het intensiteitshistogram, terwijl sommige spatiale beeldinformatie integreren om zo robuuster te zijn tegen ruis. Sommige methoden gebruiken theorieën uit het kansrekenen of uit de theorie van vaagverzamelingen, terwijl sommige andere methoden voorkennis integreren (specifieke beeldvormingmodellen, bv. MRI hersenatlassen) om de segmentatieresultaten verder te verbeteren. Daarenboven zijn sommige methoden enkel bruikbaar voor 2D afbeeldingen, terwijl andere methoden toelaten om 3D volumes te segmenteren.

In deze thesis stellen we nieuwe ruisrobuuste en accurate beeldsegmentatie methoden voor. In de context van automatische hersensegmentatie in MRI stellen we een drie-labels graph cut methode voor. Dit resulteert in automatische, meer accuraat 3D MRI segmentatie van het hersenweefsel, bestaande uit witte stof (WM), grijze stof (GM) en liquor cerebrospinalis (CSF). In de context van ruisrobuuste en multimodale beeldsegmentatie stellen we een fuzzy c-mean segmentatiemethode voor, waarbij we de nadruk leggen op het gebruik van spatiale contextmodellering, door zowel spatiale als intensiteitsinformatie van naburige pixels te incorporeren om zo beeldruis te verwijderen. De kracht van de voorgestelde methode wordt aangetoond aan de hand van MRI hersenscans, waar we succesvol theorie en praktijk combineren; tegelijkertijd maken we gebruik van een aantal heuristieken om de complexiteit van de algoritmen te beperken en om hogere performantie en flexibiliteit te behalen. De automatische 3D graph cuts methode wordt gebruikt voor de segmentatie van de hersenschors in de aanwezigheid van subtiele FCD laesies. De ruisrobuuste fuzzy c-means clustering wordt gebruikt voor mult-modale segmentatie van het hersenweefsel bij pasgeborenen en voor het realistisch modelleren van het hoofd van een pasgeboren baby.

Een realistisch hoofdmodel voor elektrische volumegeleiding ontwikkelen, is een belangrijke stap naar het niet-invasief onderzoeken van neuro-elektrische activiteit in de hersenen. Voor volwassenen zijn reeds verschillende hoofdmodellen ontwikkeld en succesvol gebruikt voor EEG bronlokalisatie. Daarentegen is het ontwikkelen van een geschikt hoofdmodel voor pasgeborenen een uitdagende taak. Dit komt hoofdzak-

kelijk door de complexe anatomie van de ontwikkelende hersenen van de pasgeborene, en door de ontoereikende kennis van de geleidbaarheid van de weefsels in het hoofd. Binnen deze thesis stellen we een raamwerk voor voor het modelleren van een realistisch volumegeleidingsmodellen voor het hoofd van pasgeboren baby's, waarbij we de uitdagingen hiervoor bespreken en onze oplossingen voorstellen. De uitdagingen voor het opstellen van het model zijn ondermeer het segmenteren van het hoofd van de pasgeborene, het schatten van de geleidbaarheid van de verschillende structuren in het hoofd en de positionering van de EEG elektroden op het hoofd. Daarenboven gebruiken we ons realistisch hoofdmodel voor volumegeleiding voor EEG bronlokalisatie bij pasgeborenen.

Tenslotte presenteren we een geïntegreerde methode voor ictale EEG dipool bronlokalisatie, gebaseerd op een realistisch hoofdmodel. We onderzoeken de bruikbaarheid van EEG bronlokalisatie bij pasgeborenen met postasphyxiale aanvallen. Dit is de eerste objectieve studie die het verband tussen EEG aanvallen en acute perinatale hersenschade, zichtbaar op MRI, vergelijkt. In het verleden werd EEG bronlokalisatie succesvol gebruikt voor deze doeleinden bij volwassenen, maar werd niet uitvoerig bestudeerd bij pasgeborenen. We gebruiken onze methode om de dipool aanval lokalisatie te vergelijken met acute perinatale hersenschade zichtbaar op MRI in 10 voldragen zuigelingen met neonatale encephalopathie. We bestudeerden ook experimenteel de gevoeligheid voor fouten op het plaatsen van de elektrodes en het effect van variaties in de geometrie en geleidbaarheid van het hoofd van pasgeborenen op onze methode. De lokalisatieresultaten van 45 focale beroertes van 10 pasgeborenen zijn vergeleken met de visuele analyse van EEG en MRI data, geannoteerd door specialisten. De resultaten van onze gefuseerde methode geven aan dat ictale EEG bronlokalisatie bruikbaar is bij pasgeborenen en mits verdere bestudering, kan deze techniek een nuttig diagnostisch middel worden.

Dit werk resulteerde in 2 tijdschriftpublicaties opgenomen in de Science Citation Index. In totaal zijn daarnaast 19 artikels verschenen in internationale en nationale conferenties, waarvan 15 als eerste auteur.

Summary

In the last decades, the rapid development of non-invasive brain imaging technologies has revolutionized our ability to investigate brain structure and function. Enormous progress in accessing brain injury and exploring brain anatomy has been made using magnetic resonance imaging (MRI), while electroencephalography (EEG) has been considered as the gold standard in the diagnosis of neurological dysfunction. Each of these brain imaging techniques has its strengths and weaknesses, and no single method is best suited for all experimental or clinical conditions. Therefore, there is an increased interest in studying multimodal brain imaging, by combining different techniques or different modalities of the same technique, to synthesize the strengths inherent in each. For instance, by integrating EEG and MRI data and performing EEG source imaging, we can localize neural activity of the brain in 3D space and do direct comparison with brain lesions visible on MRI. On the other hand, by combining different MRI sequences of the brain, such as T_1 -weighted and T_2 -weighted MRI, diffusion weighted MRI or functional MRI, we can capture more brain information and do better lesion detection.

The advances in brain imaging technologies have also provided large amount of data with an increasingly high level of quality. The analysis of these large and complex multimodal datasets has become a tedious and complex task for clinicians, who have to visualize and manually extract important information. This manual analysis is not only time-consuming, but also prone to errors, as assessed by various inter- or intra-operator variability studies. These difficulties in brain data analysis required inventions in computerized methods to improve disease diagnosis and testing. Nowadays, computer-aided diagnosis (CAD) has been extensively used to assist doctors in qualitative diagnosis by providing computerized algorithms for image segmentation, registration and visualization.

In this dissertation, we focus on developing new and improved computerized techniques for multimodal analysis of the human brain, including brain MRI segmentation and EEG source localization. We pay a great attention to improve and develop new methods for more accurate and noise-robust image segmentation, which are then successfully used for brain MRI segmentation in both adults and neonates, as well as for a realistic head modeling in neonates. Additionally, we develop an integrated multimodal EEG-MRI method for localizing abnormal neuronal activity in the neonatal brain. This method is used for the comparative study between EEG seizures and acute perinatal brain lesions visible on MRI. In doing so, we merge theory with practice and focus on two medical applications: (1) automatic 3D MRI segmentation of

the adult brain in the presence of subtle epileptic lesions caused by focal cortical dysplasia (FCD), and (2) multimodal data analysis of the neonatal brain with perinatal brain injuries caused by asphyxia and hypoxic-ischemic encephalopathy, a condition of severely deficient supply of oxygen or blood to the brain.

In both medical applications, the segmentation of brain MRI is essential because it influences the outcome of the entire analysis. This is because different processing steps such as the cortical thickness measurement, brain volume estimation or dipole source localization, rely on accurate segmentation of anatomical regions. In the context of EEG dipole source localization, it is necessary to reconstruct a patient-specific head model to accurately locate the sources of abnormal brain activity. For that purpose, it is necessary to segment the patient's MRI of the head into the scalp, skull and brain tissue. Also, in the case of FCD lesion detection, accurate segmentation of the brain cortex is important in measuring the cortical thickness, which is an important feature for the lesion detection.

In general, MRI segmentation is not a trivial task, because acquired MR images are imperfect and often corrupted by noise and other image artifacts. Also, the diversity of image processing applications has led to development of various segmentation techniques of different accuracy and degree of complexity. This is because there is no single method that can be suitable for all images, nor are all methods equally good for a particular type of image. For example, some of the methods use only the gray level histogram, while some integrate spatial image information to be robust for noisy environments. Some methods use probabilistic or fuzzy set theoretic approaches, while some additionally integrate prior knowledge (a specific image formation model, e.g. MRI brain atlas) to further improve segmentation performance. Also, some of the methods are suitable only for 2D images, while others are capable to segment 3D volumes.

In this dissertation, we propose new methods for more accurate and noise-robust image segmentation. In the context of automatic MRI segmentation of the adult brain, we propose a three-label graph cuts method for more accurate 3D MRI segmentation of three brain tissues: white matter (WM), gray matter (GM) and cerebrospinal fluid (CSF). In the context of noise-robust and multimodal image segmentation, we propose a modified fuzzy C-means segmentation method. In this method, we emphasize the use of spatial context modeling by integrating spatial and intensity information of the neighboring pixels to eliminate image noise. The performance of the proposed segmentation methods is demonstrated on brain MRI, where we successfully merged theory with practice, but at the same time we employ heuristics to reduce the complexity of the algorithms and to achieve higher performance and flexibility. The automatic 3D graph cuts method is used for brain cortex segmentation in the presence of subtle FCD lesions, while the noise-robust fuzzy C-means clustering is used for multimodal segmentation of the neonatal brain tissue and for a realistic head modeling of the neonatal head.

Developing a realistic volume conductor head model is an important step towards a non-invasive investigation of neuro-electrical activity in the brain. For adults, different volume conductor head models have been designed and successfully used for EEG source analysis. However, creating appropriate neonatal volume conductor head model is a challenging task mainly due to the complex anatomy of the developing newborn brain and insufficient knowledge of head tissue conductivities. In this dissertation, we present a pipeline for modeling a realistic volume conductor model of the neonatal head, where we address the modeling challenges and propose our solutions. The modeling challenges include the neonatal head segmentation, the conductivity estimation of different head structures and the EEG electrode positioning on the scalp. Further on, we use our realistic head model for neonatal EEG source localization.

Finally, we propose an integrated method for ictal EEG dipole source localization based on a realistic head model to investigate the utility of EEG source imaging in neonates with postasphyxial seizures. This is the first objective study to compare the relationship of EEG seizures to acute perinatal brain lesions visible on MRI. In the past EEG source localization was successfully used for this purpose in adults, but it has not been sufficiently explored in neonates. In this thesis, we use our method to compare the dipole seizure localization results with acute perinatal lesions seen on brain MRI in 10 full-term infants with neonatal encephalopathy. Through experimental studies, we also explore the sensitivity of our method to the electrode positioning errors and to variations in neonatal skull geometry and conductivity. The localization results of 45 focal seizures from 10 neonates are compared with the visual analysis of EEG and MRI data, scored by expert physicians. The performance of our fused method indicated that ictal EEG source imaging is feasible in neonates and with further validation studies, this technique can become a useful diagnostic tool.

This work resulted in 2 journal papers cited in the Science Citation Index. In total, 19 other papers appeared in the proceedings of international and national conferences, of which 15 as the first author.

Contents

1	Introduction	1
1.1	Motivation	1
1.1.1	Multimodal brain analysis	2
1.2	Thesis and contributions	5
1.2.1	Novelties	5
1.2.2	Publications	7
1.3	Organization of the thesis	9
2	Brain data analysis	13
2.1	Brain anatomy and development	13
2.1.1	Human brain anatomy	14
2.1.2	Brain development	18
2.1.3	Brain injuries: clinical challenges of the thesis	20
2.1.3.1	Asphyxia and hypoxic-ischemic encephalopathy	20
2.1.3.2	Focal cortical dysplasia - FCD	21
2.2	Magnetic Resonance Imaging - MRI	22
2.2.1	History of MRI	22
2.2.2	The physics of MRI	23
2.2.2.1	Basic principles	24
2.2.2.2	Creating an MR signal	27
2.2.2.3	MR imaging principles	31
2.2.2.4	Basic MRI pulse sequences	35
2.2.2.5	The MRI scanner system	38
2.2.3	MRI of the brain	40
2.2.3.1	Challenges in brain MRI analysis - imaging artifacts	42
2.2.3.2	Neonatal brain imaging	44
2.3	Electroencephalography - EEG	47
2.3.1	Electrical activity of the brain	47

2.3.2	EEG recording	48
2.3.2.1	EEG's wave patterns	51
2.3.3	Advantages and limitations of EEG	52
2.3.4	Applications of EEG analysis	53
2.4	Conclusion	54
3	Brain MRI segmentation	57
3.1	Basic concepts	57
3.1.1	2D and 3D images	58
3.1.2	Image segmentation	60
3.1.3	Image Features	61
3.1.4	Intensity distribution in brain MRI	63
3.1.4.1	T_1 -W and T_2 -W intensity distribution	66
3.2	Preprocessing	68
3.2.1	Bias field correction	68
3.2.2	Image registration	70
3.2.2.1	Similarity measures	72
3.2.2.2	Templates and probabilistic atlases	73
3.2.3	Removal of non-brain tissue	74
3.3	Image segmentation methods	75
3.3.1	Manual segmentation	76
3.3.2	Intensity-based methods	77
3.3.2.1	Thresholding	77
3.3.2.2	Region growing	78
3.3.2.3	Classification methods	79
3.3.2.4	Clustering methods	82
3.3.3	Atlas-based methods	82
3.3.4	Surface-based methods	83
3.4	Modeling the spatial context	85
3.4.1	Neighborhood system	85
3.4.1.1	Cliques	86
3.4.2	Markov Random Field models	88
3.4.3	Energy functions and optimization criteria	89
3.5	Validation of brain MRI segmentation	90
3.6	Conclusions	91

4	Three-label graph cut for 3D brain MRI segmentation	93
4.1	Graph cut approach - background	94
4.1.1	The min-cut and max-flow problems	94
4.1.2	Energy function for binary optimization	97
4.1.3	Multi-label optimization	99
4.1.3.1	Approximate optimization	99
4.1.3.2	α -expansion algorithm	100
4.2	Three-label graph for brain segmentation	102
4.2.1	Data term	102
4.2.2	Smoothness term	103
4.2.3	Graph construction and energy minimization	104
4.3	Experimental results	106
4.3.1	Simulated brain MRI data - BrainWeb	107
4.3.1.1	Quantitative results	107
4.3.1.2	Qualitative results	111
4.3.2	Real MRI data - IBSR	112
4.3.2.1	Quantitative results	112
4.4	3D brain cortex segmentation in patients with FCD	114
4.4.1	Qualitative validation	115
4.5	Computational efficiency	118
4.6	Discussion	119
4.7	Future directions	121
4.8	Conclusion	122
5	Noise-robust FCM clustering	125
5.1	Introduction	126
5.2	FCM algorithm	127
5.3	Phase congruency, local phase and energy	129
5.4	Accurate and noise-robust image segmentation	134
5.4.1	Neighborhood configuration	134
5.4.2	Integrating neighborhood information	134
5.4.2.1	Parameters α and β	137
5.4.3	Algorithm steps	138
5.5	Experimental results	139
5.5.1	Synthetic images	139
5.5.2	Simulated brain MRI data - BrainWeb	143

5.5.3	Real images	145
5.6	Multimodal spatially constrained FCM clustering	147
5.6.1	SCFCM algorithm	147
5.6.2	Experimental results - simulated brain MRI data	149
5.7	Computational efficiency	154
5.8	Future directions	155
5.9	Conclusion	155
6	Developing a realistic head model in neonates	157
6.1	Introduction	157
6.2	MRI segmentation of the neonatal head	159
6.2.1	Preprocessing steps	161
6.2.2	Brain volume segmentation	162
6.2.2.1	Image smoothing	164
6.2.2.2	Brain mask generation	164
6.2.2.3	Brain extraction results	167
6.2.3	Brain tissue segmentation	170
6.2.4	Scalp and skull segmentation	171
6.3	Realistic head modeling	171
6.4	Conclusion	173
7	Neonatal EEG source imaging	175
7.1	Introduction	176
7.1.1	Neonatal seizures and their diagnosis	176
7.1.2	Challenges in neonatal EEG source imaging	177
7.1.3	Goals and implementation overview	179
7.2	Materials	179
7.2.1	Studied patients	179
7.2.2	Data acquisition	180
7.3	Multimodal data fusion for EEG source imaging	182
7.3.1	Head modeling	182
7.3.1.1	Head MRI segmentation	182
7.3.1.2	Head conductivity selection	183
7.3.1.3	Electrode placement	184
7.3.2	EEG event detection	185
7.3.2.1	Automatic seizure detection and localization	186

7.3.3	EEG dipole source localization	188
7.3.3.1	The current dipole	188
7.3.3.2	Solving the forward and inverse problem	189
7.4	Experimental setup	191
7.4.1	Conductivity and geometry of the skull	191
7.4.2	Influence of electrode mislocalization	192
7.5	Results	193
7.5.1	Relationship of seizure foci to brain lesions detected by MRI .	193
7.5.2	Dipole position errors due to volume conductor model errors .	200
7.6	Discussion	202
7.6.1	Comparisons with previous studies	202
7.6.2	Estimation of the skull conductivity	203
7.6.3	Strengths and limitations	204
7.7	Future directions	205
7.8	Conclusion	205
8	Conclusions	207
8.1	Future work	210
8.2	Brief summary of the main contributions	211

List of Acronyms

1D	One-Dimensional
2D	Two-Dimensional
3D	Three-Dimensional
3DGC	Three-Dimensional Graph Cuts
BET	Brain Extraction Tool
BEM	Boundary Element Method
CAD	Computer-Aided Diagnosis
CSF	Cerebrospinal Fluid
CNS	Central Nervous System
CT	Computed Tomography
DWI	Diffusion Weighted Imaging
ECG	Electrocardiography
EEG	Electroencephalography
cEEG	continuous EEG
EM	Expectation-Maximization
EMG	Electromyography
EOG	Electrooculography
FCD	Focal Cortical Dysplasia
FCM	Fuzzy C-Means
FDM	Finite Difference Method
FID	Free Inductive Decay
FLAIR	Fluid Attenuated Inversion Recovery
GE	Gradient Echo
GM	Gray Matter
GMM	Gaussian Mixture Model
GOF	Goodness Of Fit
GUI	Graphical User Interface
HIE	Hypoxic-Ischemic Encephalopathy
MAP	Maximum A posteriori Probability
MNI	Montreal Neurological Institute
MR	Magnetic Resonance
MRF	Markov Random Field
MRI	Magnetic Resonance Imaging
fMRI	functional Magnetic Resonance Imaging
NICU	Neonatal Intensive Care Unit
NLEO	Non-Linear Energy Operator

NMR	Nuclear Magnetic Resonance
kNN	k -Nearest Neighbor
PARAFAC	Parallel Factor Analysis
PDF	Probability Density Function
PET	Positron Emission Tomography
PC	Phase Congruency
PP	Post Partum
PVE	Partial Volume Effect
RF	Radio-Frequency
ROI	Region Of Interest
RRE	Relative Residual Energy
SE	Spin Echo
SPGR	Spoiled Gradient Echo
SNR	Signal to Noise Ratio
SOR	Successive Over-Relaxation
SPECT	Spectral Positron Emission Computer Tomography
SCFCM	Spatially Constrained Fuzzy C-Means
T ₁ -W	T ₁ -weighted MRI sequence
T ₂ -W	T ₂ -weighted MRI sequence
TE	Echo Time
TR	Repetition Time
WM	White Matter

1

Introduction

I have no special talents. I am only passionately curious.
– Albert Einstein

1.1 Motivation

In the last decades, the rapid development of non-invasive brain imaging technologies has opened new horizons in the study of brain structure and function. Different techniques, such as magnetic resonance imaging (MRI) and electroencephalography (EEG), are now available to capture features of brain anatomy and function, and map neuronal dynamics as well as growth and degenerative processes. In addition to MRI, cranial ultrasound is used for diagnosing brain injury in neonates.

Among all brain imaging techniques, MRI is the most frequently used technique in clinical neuroscience for non-invasive diagnosis, quantitative evaluation and image guiding therapy in both adults and neonates [Blakemore, 2012, Rutherford, 2012]. This is because MRI does not involve ionising radiation, in contrast to X-ray computer tomography (CT) or positron emission tomography (PET), and provides high resolution 3D volumetric images of soft tissues and organs inside the body. Since MRI signals can penetrate through bone, MRI is very well suited for analyzing the anatomy of the human brain as well as for analyzing the vasculature and microstructure of brain tissues. In the last 20 years, MRI has been extensively used as a research and clinical imaging tool in neonatology and neonatal intensive care, together with cranial ultrasound imaging [Prastawa, 2007, Dudink, 2010, Rutherford, 2012].

Cranial ultrasound imaging is usually the first and the most suitable brain imaging tool in neonates, allowing real-time bed-side scanning [Barr, 1999, Vansteenkiste, 2007]. In adults, cranial ultrasound is not possible because ultrasound waves can not penetrate through the bone and once the fontanelles (gaps between the bones of the cranium) have been closed (usually between ages 3 months and one year), cranial ultrasound imaging cannot be performed. The advantage of ultrasound imaging compared to MRI is its superior resolution and ultrasound machines are far less expensive than

MRI scanners. Also, cranial ultrasound is more sensitive to measure changes in brain microstructure than MRI [Plaisier et al., 2013]. However, ultrasound imaging has limited field of view and difficulty in assessing deeper structures. Also, the contrast between soft tissues provided by cranial ultrasound is not sufficient for detecting subtle lesions in brain anatomy. Thus, although ultrasound is an independent diagnostic tool, it is often combined with MRI in diagnosis of more severe patients with subtle brain lesions.

The location and magnitude of brain activity is often studied using tools such as EEG, which indirectly measures the electrical signals generated in the brain between neurons as a function of time. Non-invasive EEG is acquired using electrodes to monitor the electrical activity at different points of the scalp, and is suitable for both adults and neonates [De Vos, 2009]. In recent years, the study of the brain function and behavior has led to an increasing interest in the location of the source of the electrical signals generated by neurons. Also, in certain brain diseases (such as epilepsy), it is important to know with more accuracy what is the nature of the disease and the exact location of the problem in the brain. This is usually done by performing EEG dipole source localization [Vanrumste, 2001, Hallez, 2008].

1.1.1 Multimodal brain analysis

Each of the existing non-invasive brain imaging techniques has its strengths and weaknesses, and no single method is best suited for all experimental or clinical conditions. Therefore, there is an increased interest in studying multimodal brain imaging, by combining different techniques or different modalities of the same technique, to synthesize the strengths inherent in each, [Biagioni et al., 2001, Roche-Labarbe et al., 2008, Despotovic et al., 2013a, Prastawa et al., 2005, Weisenfeld and Warfield, 2009, Murgasova, 2008, Maalouf et al., 2001].

For instance, localizing neuronal activity in the brain, both in time and in space, is a central challenge in understanding brain function. EEG data provide high temporal resolution (measured in milliseconds), but limited spatial resolution. In contrast, MRI provides better spatial, but relatively poor temporal resolution. By performing EEG source localization and integrating both EEG and MRI data, we can localize neural activity of the brain in 3D space and the location of an EEG source can be compared to lesions visible on MRI, see Fig. 1.1 [Despotovic et al., 2013a, Biagioni et al., 2001, Roche-Labarbe et al., 2008]. On the other hand, by combining different MRI modalities of the brain, such as T_1 -weighted (T_1 -W), T_2 -weighted (T_2 -W), Fluid Attenuated Inversion Recovery (FLAIR) or Diffusion Weighted Imaging (DWI), we can capture more brain information and do better lesion detection (see Fig. 1.2).

Brain imaging has achieved remarkable advances over the past few decades, providing more and more data with an increasingly high level of quality. The analysis of these large datasets has become a tedious and complex task for clinicians, who have to visualize and manually extract important information. This manual analysis is not only time-consuming, but also prone to errors, as assessed by various inter- or intra-

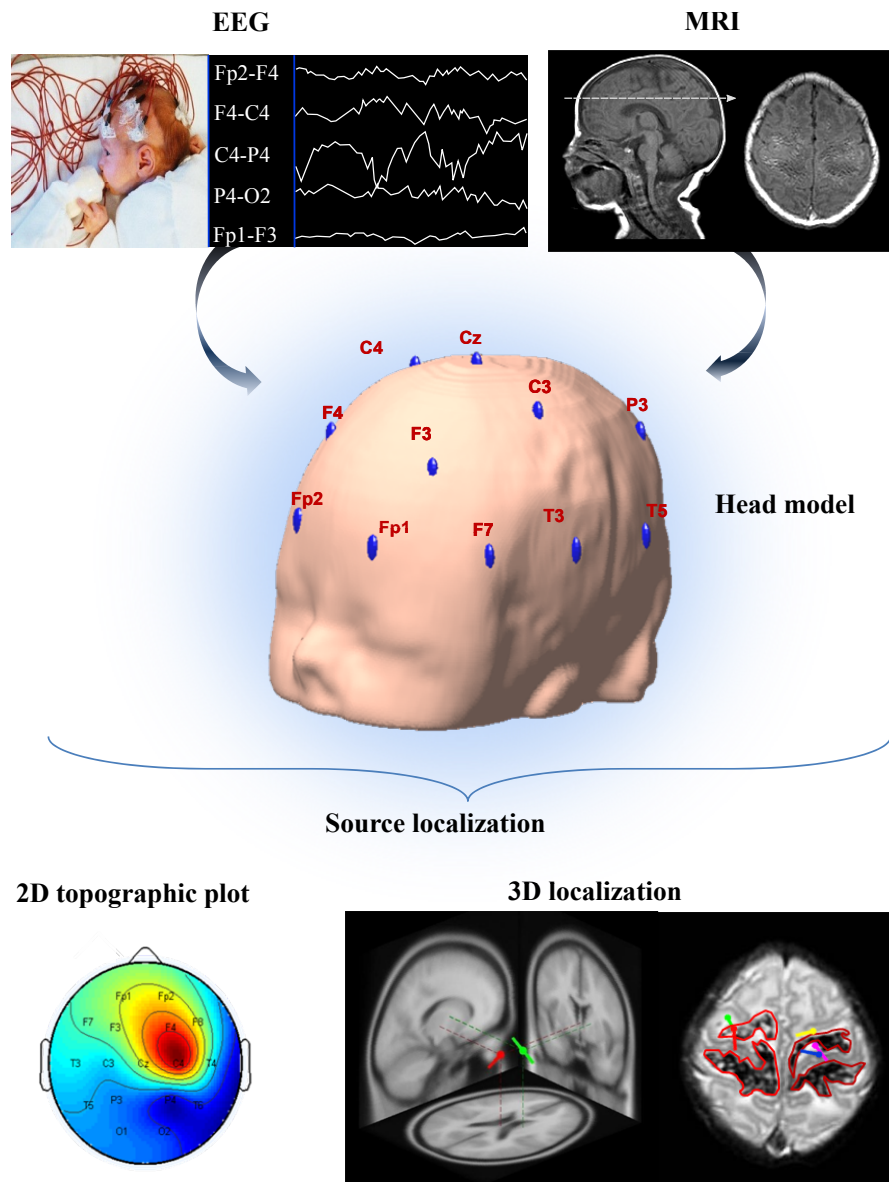


Figure 1.1: Overview of a multimodal brain analysis integrating EEG and MRI data for 3D dipole source localization in neonates.

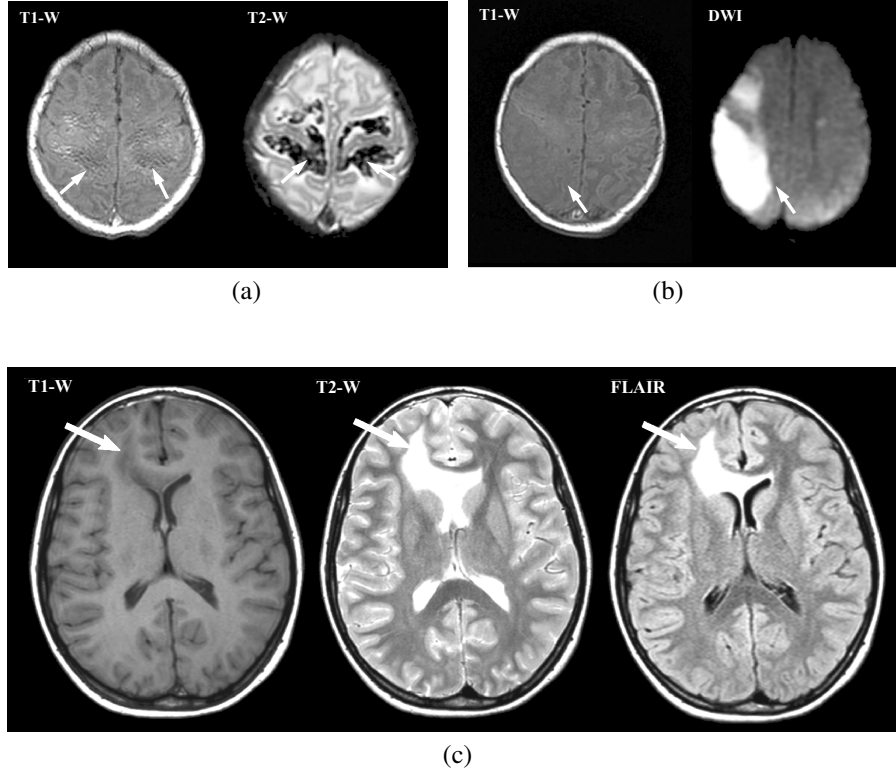


Figure 1.2: Examples of a brain lesion visibility using different MRI modalities. The lesions are indicated with arrows. (a) An example of a haemorrhage lesion hardly visible on the T_1 -W image (left), but clearly noticeable on the T_2 -W image (right). (b) An example of a big focal brain lesion only visible on the DWI image (right). (c) An example of a tumor lesion on T_1 -W, T_2 -W and FLAIR MR images. The tumor can be identified in all three cases, but the easiest on the FLAIR image. The first two examples (a) and (b) show a neonatal brain and the last example (c) shows an adult brain.

operator variability studies [Collier et al., 2003, Vansteenkiste, 2007]. These difficulties in brain data analysis required inventions in computational methods to improve disease diagnosis and testing. Nowadays, computer-aided diagnosis (CAD) has been extensively used to assist doctors in qualitative diagnosis by providing computer algorithms and tools that extract important clinical information from images. For example, multiple imaging modalities used for automated recognition and diagnosis, require computerized algorithms for pattern matching, image registration, segmentation, enhancement and visualization.

Due to all these advances, the multimodal image analysis is now a fast-moving, demanding and exciting multidisciplinary activity with a continuous need in developing newer and better methods to help doctors to find the source of the problem.

1.2 Thesis and contributions

This thesis is about multimodal image analysis of the human brain, with the focus on a development of supervised and unsupervised brain MRI segmentation algorithms and neonatal EEG source localization. Throughout the work we concentrate on two practical applications:

1. Improving brain cortex segmentation for the detection of subtle brain lesions in patients with focal cortical dysplasia (FCD).
2. Developing and testing neonatal EEG dipole source localization, using a realistic head model and multimodal data fusion in babies with perinatal brain injuries caused by asphyxia.

In both applications, the segmentation of brain MR images is essential because it influences the outcome of the entire analysis. This is because different processing steps in the analysis (like cortical thickness measurement, brain volume estimation, dipole source localization, etc.) rely on accurate segmentation of anatomical regions. For instance, in the context of EEG dipole source localization, it is necessary to reconstruct a patient-specific head model (using MRI segmentation) to accurately locate the sources of abnormal brain activity, where the brain signals are generated using the information acquired with the electrodes located over the patient's head, Fig. 1.1. For that purpose, we have to segment the patient's MRI of the head into the scalp, skull and brain tissue. Also, in the case of FCD lesion detection, accurate segmentation of the brain cortex is important in measuring the cortical thickness, which is an important feature for the lesion detection.

However, image segmentation is not a trivial task because images are often corrupted by noise and other image artifacts. Therefore, we pay a great attention to study and develop new methods for accurate and noise-robust image segmentation. To eliminate noise and other image artifacts, we emphasize the use of spatial context modeling by integrating neighborhood information of the image elements (pixels for a 2D image or voxels for a 3D image) in the proposed segmentation methods. The performance of the proposed segmentation methods is demonstrated on brain MRI (in both adults and neonates) where we successfully merged theory with practice, but at the same time we employ heuristics to reduce the complexity of the algorithms or to achieve higher flexibility.

1.2.1 Novelties

The novelties and contributions of this thesis can be divided in two groups: (1) those related to image segmentation with application to brain MRI and (2) those integrating our MRI segmentation research and EEG monitoring of the neonatal brain, and resulting in the application for neonatal EEG source localization [Deburchgraeve et al., 2010, Deburchgraeve et al., 2009, De Vos, 2009, Hallez, 2008].

In the first group we have contributed the following algorithms and methods:

1. An improved 3D graph cut algorithm for brain tissue segmentation with application to more accurate brain cortex segmentation and epileptic lesion detection in FCD patients. Our method uses three-label graph cut and preforms automatic 3D MRI brain segmentation by integrating intensity and boundary information into the Markov random field-based energy function. This method outperforms existing graph cut algorithms and also competes favourably with other state-of-the-art algorithms for MRI segmentation, [Despotovic et al., 2011b, Despotovic et al., 2011c].
2. A new fuzzy clustering method for accurate and noise-robust image segmentation. Our method uses the joint spatial and intensity feature space, and integrates an anisotropic neighborhood model. This method allows multi-feature segmentation and can be used in many different applications. In this thesis the performance of the algorithm is evaluated on brain MRI datasets, but its segmentation potential is shown in other applications as well [Despotovic et al., 2010b, Despotovic et al., 2010c, Despotovic et al., 2010a, Despotovic et al., 2010d, Despotovic et al., 2013c].
3. An integrated algorithm for the neonatal brain volume segmentation (brain extraction) using T_1 -W and T_2 -W MRI of the neonatal brain. This method combines thresholding, active contours and mathematical morphology [Despotovic et al., 2010e].
4. An algorithm for 3D realistic head modeling in newborn infants. This algorithm integrates the MRI method for the neonatal brain extraction, mathematical morphology, and noise-robust fuzzy segmentation [Despotovic et al., 2009a, Despotovic et al., 2009b, Despotovic et al., 2010f, Despotovic et al., 2013b].

In the second group we have created the following contributions:

1. The first integrated method for ictal EEG dipole source localization in newborn infants based on a realistic head model, [Despotovic et al., 2013a, Despotovic et al., 2011a].
2. The experimental studies for investigating the utility of EEG source imaging in neonates with postasphyxial seizures. We explored the sensitivity of our method to the electrode positioning errors and to variations in neonatal skull geometry and conductivity, [Despotovic et al., 2013a, Despotovic et al., 2012].
3. The first objective study of the relationship between the localization of neonatal seizures and associated MRI patterns of brain injury, [Despotovic et al., 2013a].

1.2.2 Publications

In terms of publications, so far this work resulted in 17 publications as the first author:

- 2 accepted A1 journal publications in the field of image segmentation [Despotovic et al., 2013c] and multimodal EEG and MRI data analysis of the neonatal brain [Despotovic et al., 2013a].
- 10 publications published in the proceedings of international peer-reviewed conferences in the field of image segmentation (with application to MRI brain segmentation) [Despotovic et al., 2010d], [Despotovic et al., 2010a], [Despotovic et al., 2010c], [Despotovic et al., 2011c], [Despotovic et al., 2011b], 3D realistic head modeling and EEG source localization in newborn infants [Despotovic et al., 2009a], [Despotovic et al., 2010e], [Despotovic et al., 2012], [Despotovic et al., 2013b] and ultrasound signal and image analysis [Despotovic et al., 2008];
- 5 publications in national conferences [Despotovic et al., 2009b], [Despotovic et al., 2010f], [Despotovic et al., 2010b], [Despotovic et al., 2011d], [Despotovic et al., 2011a].

Also, this research contributed to 4 publications by other first authors in the field of MRI analysis of the brain in patients with epileptic lesions (FCD lesion detection) [Kumcu et al., 2012, Platisa et al., 2011, Platisa et al., 2012, Qu et al., 2013].

The following listed articles are a selection of the most important publications that were published during the course of this research:

A1 journals

1. Despotovic, I., Vansteenkiste, E., and Philips, W. (2013). Spatially coherent fuzzy clustering for accurate and noise-robust image segmentation. In *Journal IEEE Signal Processing Letters*, Volume 20, Issue 4, pages 295-298.
2. Despotovic, I., Cherian, P.J., De Vos, M., Hallez, H., Deburchgraeve, W., Goovaert, P., Lequin, M., Visser, G.H., Swarte, R.M., Vansteenkiste, E., Van Huffel, S. and Philips, W. (2013). Relationship of EEG sources of neonatal seizures to acute perinatal brain lesions seen on MRI: A pilot study. In *Journal Human Brain Mapping*, Volume 34, Issue 10, pages 2402-2417.

International conference proceedings

1. Despotovic, I., Vansteenkiste, E. and, Philips, W. (2013). A realistic volume conductor model of the neonatal head: methods, challenges and applications. In *Proc. IEEE International Conference on Engineering in Medicine and Biology Society Conference (EMBC)*, pages 3303-3306, Osaka, Japan.

2. Despotovic, I., Cherian, P.J., De Vos, M., Hallez, H., Govaert, P., Lequin, M., Visser, G.V., Swarte, R., Vansteenkiste, E., Van Huffel, S. and Philips, W. (2012). Influence of Volume Conductor Model Errors on Dipole Source Localization in Neonates. In *Proc. International Society for Magnetic Resonance in Medicine (ISMRM)*, page 3647, Melbourne, Australia.
3. Despotovic, I., Segers, I., Platasa, Lj., Vansteenkiste, E., Pizurica, A., Deblaere, K. and Philips, W. (2011). Automatic 3D graph cuts for brain cortex segmentation in patients with focal cortical dysplasia. In *Proc. IEEE International Conference on Engineering in Medicine and Biology Society Conference (EMBC)*, pages 7981-7984, Boston, Massachusetts, USA.
4. Despotovic, I., Segers, I., Platasa, Lj., Vansteenkiste, E., Pizurica, A., Deblaere, K. and Philips, W. (2011). Brain MRI Segmentation for Focal Cortical Dysplasia Lesion Detection. In *Proc. International Society for Magnetic Resonance in Medicine (ISMRM)*, page 4277, Montreal, Canada.
5. Despotovic, I., Goossens, B., Vansteenkiste, E. and Philips, W. (2010). An improved fuzzy clustering approach for image segmentation. In *Proc. IEEE International Conference on Image Processing (ICIP)*, pages 249-252, Hong Kong, China.
6. Despotovic, I., Goossens, B., Vansteenkiste, E. and Philips, W. (2010). T1- and T2-weighted Spatially Constrained Fuzzy C-Means Clustering for Brain MRI Segmentation. In *Proc. SPIE Medical Imaging*, 76231V, 9 pages, San Diego, California, USA.
7. Despotovic, I., Jelaca, V., Vansteenkiste, E. and Philips, W. (2010). Noise-robust method for image segmentation. In *Proc. Advanced Concepts for Intelligent Vision Systems (ACIVS)*, pages 153-162, Sydney, Australia.
8. Despotovic, I., Vansteenkiste, E., Philips, W. (2010). Brain volume segmentation in newborn infants using brain MRI with a low inter-slice resolution. In *Proc. IEEE International Conference on Engineering in Medicine and Biology Society Conference (EMBC)*, pages 5038-5041, Buenos Aires, Argentina.
9. Despotovic, I., Deburchgraeve, W., Hallez, H., Vansteenkiste, E. and Philips, W. (2009). Development of a Realistic Head Model for EEG Event-Detection and Source Localization in Newborn Infants. In *Proc. IEEE International Conference on Engineering in Medicine and Biology Society (EMBC)*, pages 2296-2299, Minneapolis, Minnesota, USA.

1.3 Organization of the thesis

This section presents an overview of the content of the following Chapters of the thesis.

Chapter 2: Brain data analysis.

In this chapter we present background information on the human brain anatomy and review the development of non-invasive brain imaging techniques, such as MRI and EEG. We start with a brief introduction to the human brain anatomy and neurophysiology and discuss the phases of the brain development, from neonate till adulthood. Next, we describe two brain injuries, birth asphyxia and epilepsy with FCD lesions that are the clinical challenges of the thesis. Furthermore, we explain the physics and acquisition of MRI, as well as the challenges in MRI analysis and the differences between imaging adult and neonatal brains. Finally, we explain the main concepts of EEG brain data analysis, necessary for understanding neonatal EEG source imaging in Chapter 7.

Chapter 3: Brain MRI segmentation.

In this chapter we review the image segmentation methods commonly used for MRI brain tissue segmentation. Firstly, we introduce the basic concepts of image segmentation, which are necessary for a good understanding of this and the following Chapters. Then, we explain different preprocessing steps such as the bias field correction, image registration and brain extraction. Next, we review the most popular brain MRI segmentation techniques and highlight differences between them. Finally, we discuss the validation problem in brain MRI segmentation.

Chapter 4: Three-label graph cut for 3D brain MRI segmentation.

In this chapter we propose the modification of the standard graph cut method for more accurate and automatic 3D brain MRI segmentation. The proposed method uses three-label graph cut (labels: white matter (WM), gray matter (GM) and cerebrospinal fluid (CSF)) and performs automatic 3D MRI brain segmentation integrating intensity and boundary information. The performance of the method is tested on both simulated and real MR brain images with different noise levels and real patients with FCD lesions. The experimental qualitative and quantitative segmentation results are presented, where we also compare the performance of the proposed method with other brain MRI segmentation methods. The qualitative validation for FCD patients is scored by the expert physician.

This work is done in collaboration with my master thesis student Ief Segers [Segers et al., 2010] who implemented the proposed segmentation algorithm in C++, created the graphical user interface (GUI) and did an initial testing of the method on patients with FCD lesions.

Chapter 5: Noise-robust FCM clustering.

This chapter is about segmenting medical images using fuzzy models where we present our novel solution for noise-robust fuzzy C-means clustering. Firstly, we review the recent research efforts involving supervised and unsupervised fuzzy segmentation of MRI for brain tissue analysis. Following this, we present our solution for

spatially coherent and noise-robust fuzzy clustering. Here, instead of modeling the spatial context using the Markov Random Field (MRF), we model it by much simpler techniques, using low complexity locally adaptive methods. For more accurate segmentation we propose an anisotropic neighborhood model based on phase congruency features. Then, we present the new spatially coherent solution for the FCM clustering that uses both T_1 -W and T_2 -W MRI for brain tissue segmentation. The performance of our methods is tested on several datasets: on synthetic images with different noise levels, on variety of real images, on simulated adult MR brain images with different noise levels and on neonatal MR brain images with the gestational age of 40 weeks. Both qualitative and quantitative segmentation results are compared with the related FCM-based techniques as well as with the state-of-the-art MRI segmentation methods.

Chapter 6: Development of a realistic head model in neonates.

In this chapter we present a new interactive hybrid segmentation method for realistic head modeling in newborn infants, which we use later for neonatal EEG source analysis in Chapter 7. Our method combines our new FCM clustering (Chapter 5), active contours and mathematical morphology. To build a realistic head model, we also developed a method for brain volume segmentation in neonates (brain extraction) using T_1 -W and T_2 -W MRI. This is because the existing brain volume segmentation techniques are mainly developed for adults and are not applicable to neonates or require additional corrections. Both brain extraction and 3D realistic head reconstruction methods are explained. The brain extraction algorithm is tested on real neonatal brain MRI with a gestational age between 39-41 weeks. The segmentation results are compared to manual segmentation and results show that our method is effective and more accurate than existing brain volume segmentation methods originally developed for adults.

Chapter 7: Neonatal EEG source imaging.

In this chapter we present an integrated method for ictal EEG dipole source localization in neonates, based on a realistic head model. The focus here is to investigate the utility of EEG source imaging in neonates with postasphyxial seizures and explore the relationship between dipole locations and brain lesions visible on MRI. Firstly, we explain the cause and diagnosis of neonatal seizures and discuss the challenges in neonatal EEG source localization. Then, we describe the test population (10 full-term infants with neonatal encephalopathy) and the procedure for acquisition of MRI and EEG data. Following this, we explain our method and compare the dipole seizure localization results with acute perinatal lesions seen on brain MRI. Through experimental studies, we explore the sensitivity of our method to the electrode positioning errors and to variations in neonatal skull geometry and conductivity. Finally, we compare the localization results of 45 focal seizures from 10 neonates with the visual analysis of EEG and MRI data, scored by expert physicians.

This work is done in cooperation with Erasmus MC-Sophia Hospital in Rotterdam, MEDISIP group from Ghent University and ESAT-STADIUS division from KU Leuven. Erasmus MC-Sophia Hospital provided us with the necessary MRI and EEG data, clinical diagnosis of the patients and validations of the experimental results. The MEDISIP group provided us with the source localization method (initially developed

for adults), which has been modified in this research for the purpose of neonatal EEG source imaging. Finally, the EEG data analysis and automatic EEG seizure detection is done by the ESAT-STADIUS division, whose results we used as an input for EEG source localization.

Chapter 8: Conclusions.

This final chapter includes the overall conclusions of the thesis and points out in which direction further related research might proceed.

2

Brain data analysis

*Surely, the brain must hold the key to human nature:
understanding it will allow us to make sense of so much that puzzles us about ourselves.*
– Adam Zeman

This chapter provides the necessary background on the human brain anatomy and on MRI and EEG brain data analysis. Section 2.1 explains the anatomy and development of the human brain, including an explanation of the two brain injuries (birth asphyxia and epilepsy with FCD) that are the clinical challenges of the thesis. Since MRI analysis of the neonatal and adult brain is the central subject of the thesis, it is necessary to understand how MR images are formed, what they show, how they differ, how we can analyze them and what are the challenges. This is the subject of the Section 2.2. Subsequently, in Section 2.3 we explain the most important concepts of EEG brain data analysis that is necessary for understanding neonatal EEG source imaging in the Chapter 7.

2.1 Brain anatomy and development

The brain is the most complex vital organ of the human body. It controls our physical senses and stores our memories and processes our thoughts and emotions. Our brain consists of millions and millions of nerve cells (neurones), which are connected and communicate with each other. When communication between neurons is broken or interrupted for a long time, brain degeneration occurs, causing brain injury, which can vary greatly in severity. Many of the questions about how the brain develops, works and dies are still unanswered, but doctors and scientists continuously stepped up their efforts to learn more about the brain every day.

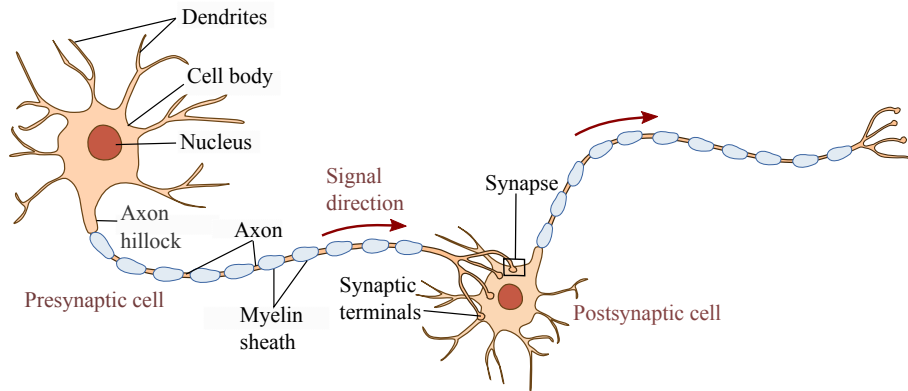


Figure 2.1: The basic parts of a neuron are the cell body, dendrites, the axon and synaptic terminals.

2.1.1 Human brain anatomy

The brain is the central part of the central nervous system (CNS) and is largely composed of nerve cells or neurons and glial cells. There are over 100 billion neurons in the brain and an even greater number of glial cells.

Neurons are information messengers. They use electrical impulses and chemical signals to transmit information between different areas of the brain, and between the brain and the rest of the nervous system. The size and shape of neurons can vary, but all neurons have three basic parts: a cell body or soma and two extensions called an axon and a dendrite (see Fig. 2.1). The cell body contains the cell nucleus, in which all vital proteins are synthesized. Neurons communicate with each other via synaptic terminals by releasing chemicals (neurotransmitters). Dendrites extend from the cell body and have a function of receiving information to the cell body from synaptic connections, while axons take information away from the cell body. A single cell can connect with as many as 15000 other cells, building an incredibly complex network of connections. The majority of neurons are unable to undergo regeneration or further divide, and this results in irreversible damage to the nervous system after trauma, intoxication, oxygen deficiency (like in asphyxia) or stroke.

Glial cells are major constituents of the central nervous system and play a pivotal role during development and adulthood. Although they do not have a direct role in neurotransmission, glial cells have a supporting role that helps define synaptic contacts and maintain the signaling abilities of neurons. Glial cells lack axons and dendrites and are smaller than neurons. Some evidence also suggests that glial cells aid (or, in some cases, prevent) recovery from neuronal injury and that they are involved in a number of diseases, such as Alzheimer's disease or multiple sclerosis [Nagele et al., 2004].

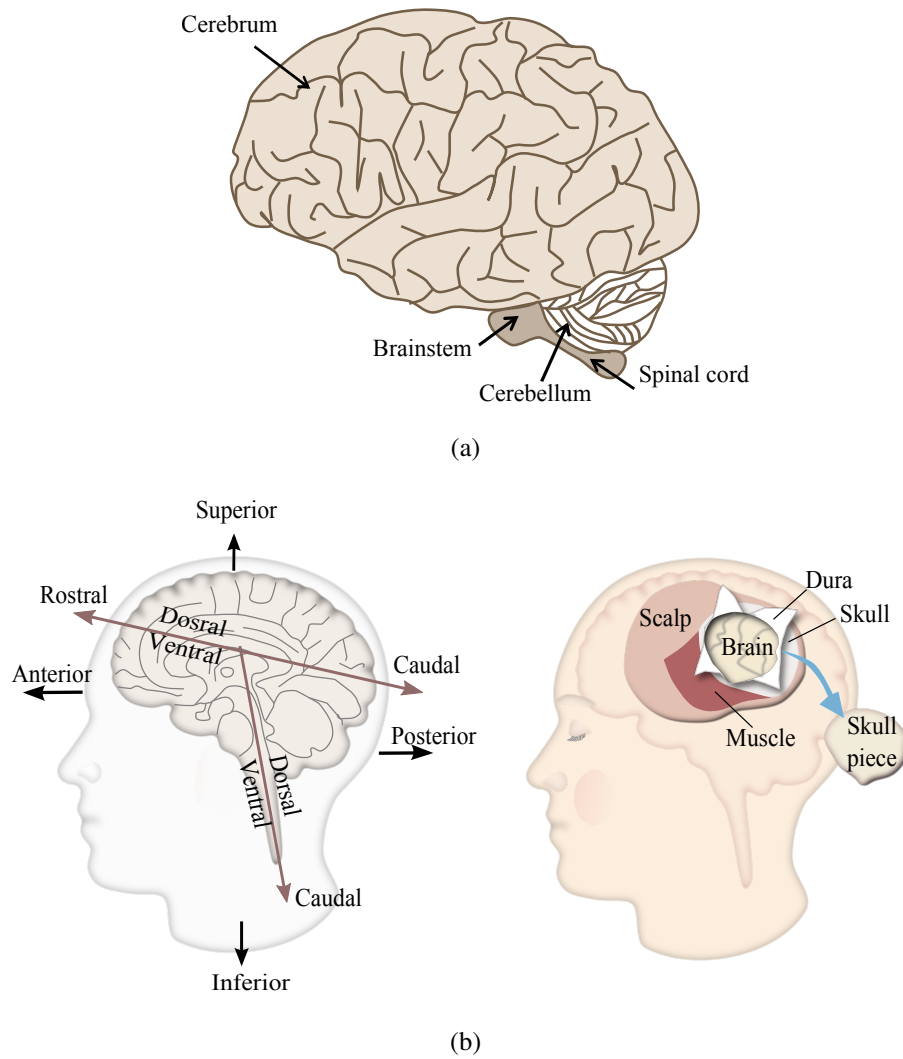


Figure 2.2: The brain anatomy. (a) The main brain parts such as cerebrum, cerebellum and brain stem are indicated. (b) On the left side: the terminology to describe position and orientation of brain structures. On the right side: the human head structures (scalp, skull and brain).

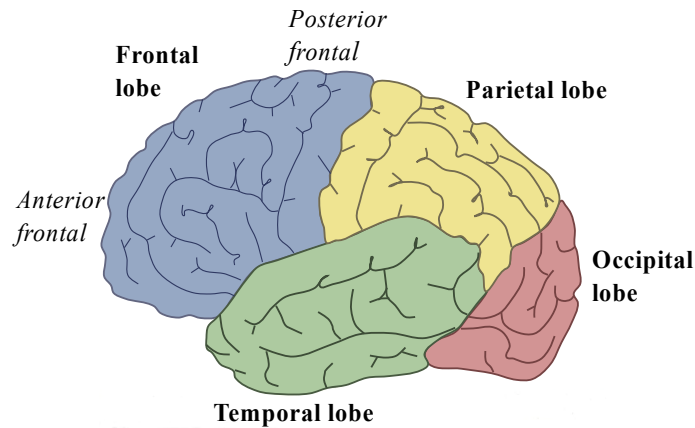


Figure 2.3: The four brain lobes: frontal, temporal, occipital and parietal.

The main parts of the brain are cerebrum, cerebellum and brain stem. Their location is illustrated in Fig. 2.2(a). The cerebrum is the largest part of the brain (accounts for two-thirds of the total weight of the brain) and controls voluntary actions, speech, senses, thoughts, and memory. The outer layer of the brain is known as the cerebral cortex (or cortical gray matter). Its surface has grooves or fissures (called sulci) and ridges (called gyri). The brain is immersed in cerebrospinal fluid (CSF), which provides essential substances for the metabolism of the brain and is encapsulated within the skull and scalp, which act as protective layers against trauma, Fig. 2.2(b). Within the brain there are a number of cavities called ventricles. They are filled with CSF, which is produced within the ventricle wall.

The cerebrum is divided into two hemispheres (left and right), which are further subdivided into four lobes: frontal, temporal, parietal and occipital. This is illustrated in Fig. 2.3. The left hemisphere is functionally dominant, controlling language and speech, while the right hemisphere interprets visual and spatial information. All lobes are interconnected and each lobe has a specific function. The frontal lobes are located in the front of the brain and are responsible for problem solving, judgment and motor function. The parietal lobes are located at the top back of the brain and they manage sensation, handwriting, and body position. The temporal lobes are located on each side of the brain, above ears, and they process memory, auditory (hearing) information, speech and language functions. The occipital lobes are located at the back of the brain and they receive and process visual information.

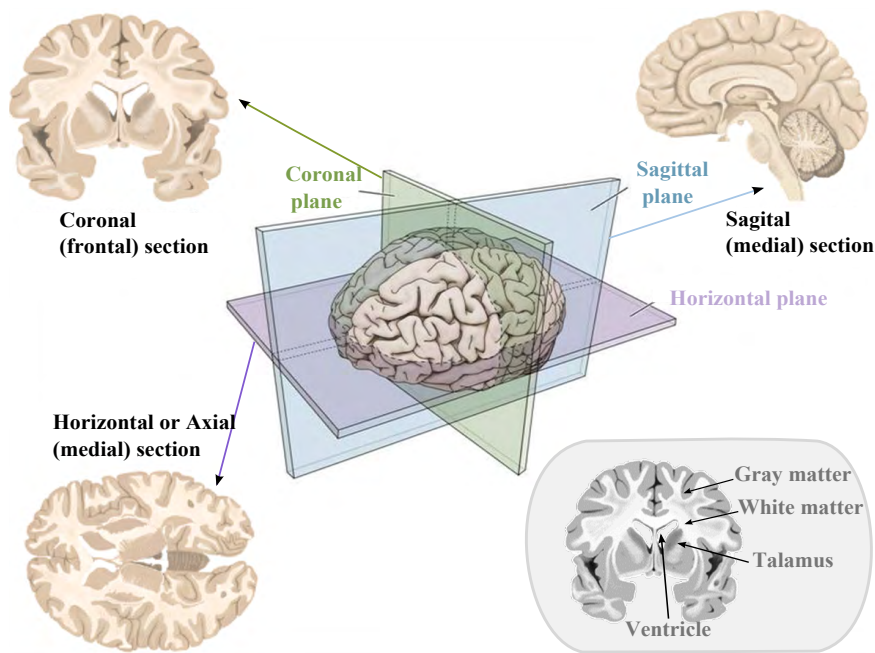


Figure 2.4: Illustration of the typical three cross-sections through the brain: axial, corona and sagittal. The right-bottom image shows the coronal section of the brain where the gray matter, white matter, talamus and ventricles are indicated with arrows. Note that axial plane is also called horizontal or transverse plane. Parts of the figure are from [Uzwiak, 2013].

The brain tissues can be divided into gray matter (GM) and white matter (WM), see Fig. 2.4. The gray matter is found at the brain cortex and in some deep brain structures, such as the thalamus, caudate nuclei, putamen and globus palidus. The cortical gray matter predominantly contains closely packed neuron cell bodies and actively participates in the storage and processing of information. It is estimated that there are more than 10 billion cells in the cerebral cortex alone. The white matter consists mainly of glial cells and long myelinated axons, which connect different parts of the gray matter and transmit signals from one part of the brain to another. The term white matter is due to a glistening whitish appearance of myelin which is mainly composed of lipid tissue.

The brain and the different areas of the brain can be analyzed and illustrated using images of the brain in different orientations or planes. The three most commonly used planes are: sagittal, coronal and axial, as illustrated in Fig. 2.4. Further readings on the anatomy of the neuron and the brain can be found in [Nolte, 2002].

2.1.2 Brain development

Human brain maturation is a complex, lifelong process that involves a complex sequence of morphological, functional and organizational changes. Although these changes are complex they occur in an organized sequence. Pathological studies have been important in documenting the process of brain maturation, but brain imaging offers the added value of being able to study the live fetus and infant in the earliest and most important phases of maturation, see Fig. 2.5.

The development of the human brain and CNS consists of several synchronized processes, some of which are completed before birth, while others continue into adulthood. At about three weeks gestation (three weeks of pregnancy) the neural tube forms, creating the basis for all further CNS development. From the first to the fourth month of gestation, major regions of the human brain can be recognized in primitive form. The spinal cord develops at one end of the neural tube, and forebrain and facial structures at the other. During this period, the ventricles are formed in the central region of the tube that will become the brain, see Fig. 2.6.

Beginning at the fifth month of gestation the surface of the growing brain begins to fold into sulci and gyri [Levine and Barnes, 1999]. Between the sixth and seventh month of gestation, the major sulci are visible and myelination occurs regionally beginning with the brain stem [Inder and Huppi, 2000] and generally proceeds from inferior to superior and posterior to anterior. Myelin is an insulating layer made up of fatty substances and protein that allows rapid and efficient transmission of impulses along the nerve cells. Proximal pathways tend to myelinate before distal and sensory before motor [Volpe, 2000]. The process of myelination is the most rapid during the first 2-3 years of life and by the age of 3 years, most major tracts are significantly myelinated [Parazzini et al., 2002]. However, due to the refined structure of the adult brain and subtle changes in appearance, axons within the cortex and in some regions such as a white matter bundle near the temporal lobe, continue to myelinate into the second and third decades of life [Yakovlev and Lecours, 1967]. By birth, nearly all sulcal and gyral patterns are present and after birth they continue to increase in complexity.

At birth, almost all of the neurons (30 billion or more) have been formed. During the first year of life, synaptic density increases rapidly, reaching by 2-years of age a level approximately 50% greater than that typically seen in adults [Huttenlocher, 1979]. This is because the brain develops a functional architecture through the rapid formation of these synapses or new connection, myelination of the axonal fibres and growth of glial cells. In the first 2 years of live the brain growth is rapid and the brain weight reaches 80% of its adult weight. Throughout the first decade of life a child's brain is superdense and at about age 11, a brain gets rid of extra connections in a process calling "pruning". By age 5 years brain size is approximately 90% of adult brain size [Dekaban and Sadowsky, 1978, Lenroot and Giedd, 2006] and reaches its maximum weight at age 20. However, significant remodeling of gray and white matter continues into the third decade of life, something that could not be fully appreciated until MRI became available.

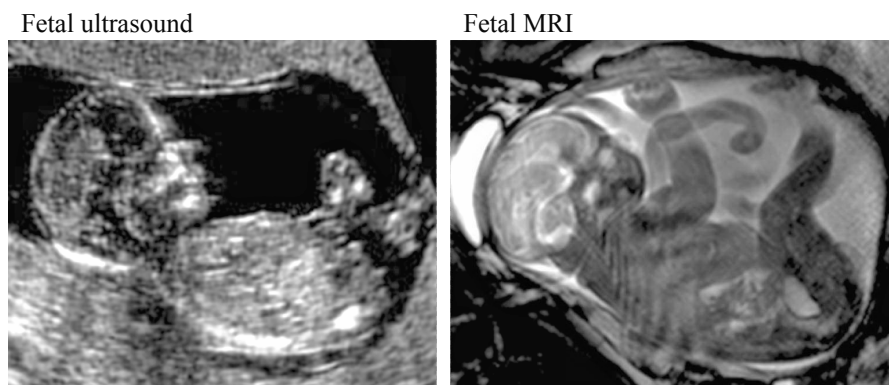


Figure 2.5: Imaging of the brain maturation before birth using ultrasound and fetal MRI.

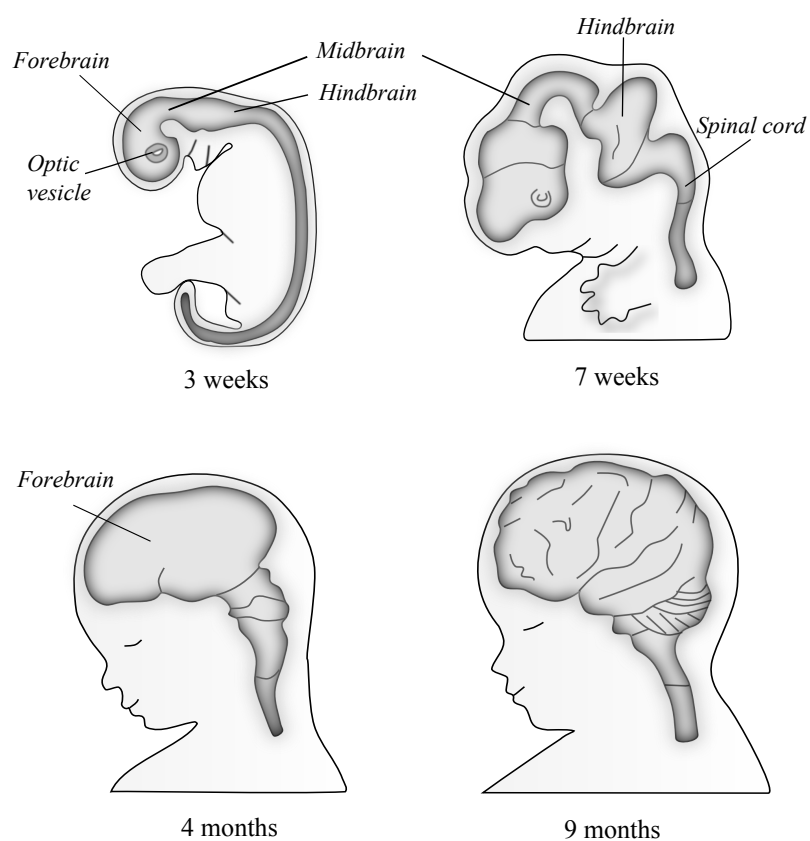


Figure 2.6: Phases of the brain development.

2.1.3 Brain injuries: clinical challenges of the thesis

2.1.3.1 Asphyxia and hypoxic-ischemic encephalopathy

Asphyxia is a condition of severely deficient supply of oxygen to the brain and occurs due to breathing difficulties or other problems that prevent the baby from receiving sufficient amounts of oxygenated blood. An acute reduction in oxygen delivery to the brain results in break down of the neuronal energy metabolism within minutes. This causes seizures as a common manifestation of neurological dysfunction [Volpe, 2008] and requires early detection to enable prompt treatment with the aim to prevent further brain injury. Asphyxia is a major cause of permanent disability in very preterm infants who survive after neonatal intensive care. Despite improvements in perinatal care in the developed world, asphyxia remains a major cause of mortality, resulting in up to 25% of perinatal mortality and morbidity.

Infants who have been asphyxiated during delivery may develop signs of hypoxic-ischemic encephalopathy (HIE), where hypoxia is inadequate supply of oxygen in the blood, ischemia is decrease in blood flow and encephalopathy is brain disease. Although both preterm and term infants are at high risk of asphyxia, the HIE staging is reserved for term infants (gestation > 37 weeks). The most typical abnormal neurological sign in HIE are convulsions (called “generalized tonic-clonic” seizures), which are the most dramatic type of seizure involving the whole body. Convulsions are causing sudden, rapid, violent movements and occasionally loss of consciousness. These convulsions can start with focal movements (involving one specific part of the body) and progress to generalized movements (i.e., both sides of the body).

Infants with signs of HIE may be scanned with two different techniques during the neonatal period: cranial ultrasound and MRI. Cranial ultrasound has the advantage of being mobile equipment and therefore is easily used bedside in the neonatal unit. It is ideal for daily or half daily scans to follow the evolution of changes within the brain. Cranial ultrasound allows screening and monitoring the evolution of lesions but is not as good as MRI at determining the exact site, and extent of lesions. The combination of cranial ultrasound and MRI is ideal for assessing the newborn brain.

MRI has been widely used to investigate the asphyxiated infant [Rutherford, 2001]. The pattern of injury seen on MRI is related to the type and severity of the insult. During the first week after delivery, six main areas of abnormality may be identified on MRI in infants with HIE [Cowan and Denis, 2007]. Whilst one particular pattern may dominate, in most infants a combination of abnormalities is present. The early MRI findings are: brain swelling, loss of the normal signal in the posterior limb of the internal capsule (see Fig. 2.7), abnormal signal intensities in the basal ganglia and thalami, brain stem lesions, loss of GM/WM differentiation and cortical highlighting [Rutherford, 2012, Cowan and Denis, 2007].

Monitoring of brain function using the EEG, continuously or by serial EEGs is well-suited to give insight into brain function and its dynamic changes in neonatal HIE and helps to guide treatment as well as prognostication [Perumpillichira, 2010]. A good

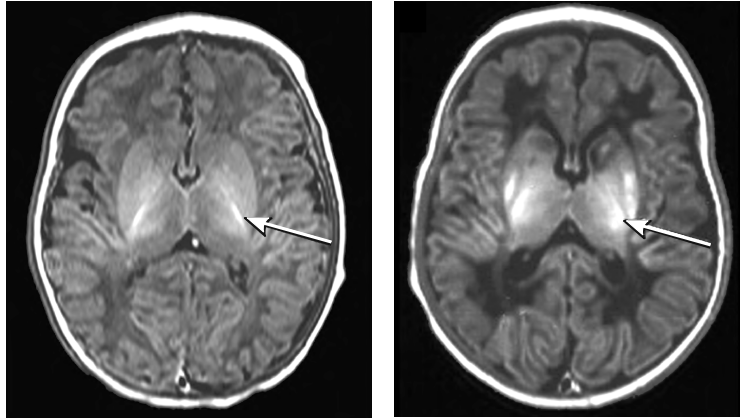


Figure 2.7: Illustration of the asphyxiated brain. Normal (on the left) and abnormal (on the right) signal intensities within the posterior limb of the internal capsule are indicated with arrows. From [Cowan and Denis, 2007].

understanding of the pathophysiology of HIE is needed not only in the selection of suitable diagnostic tests and treatment methods, but also to develop new therapeutic strategies. Confirmation by video electroencephalography (EEG) is considered the gold standard in the diagnosis of neonatal seizures.

2.1.3.2 Focal cortical dysplasia - FCD

The prevalence of epilepsy is estimated to be around 1% of the population and up to 40% of these patients continue to have seizures despite optimal drug treatment. These patients represent a high socio-economical burden due to direct and indirect medical costs. Most of these refractory patients might benefit from epilepsy surgery, requiring a precise localisation of the epileptogenic zone. Epilepsy surgery in an optimally selected population yields a high chance of seizure freedom. In patients in whom the abnormal electrical brain activity can be correlated to an identifiable anatomical lesion, up to 80% seizure freedom can be achieved by surgery. The success depends on the type of lesion.

Focal cortical dysplasias (FCDs) are localized malformations of cortical development increasingly associated with drug refractory epilepsy and more frequently being operated on in epilepsy centers. Magnetic resonance imaging plays a pivoting role in the presurgical evaluation of patients with refractory epilepsy and although MRI quality has significantly improved through the advent of high field clinical MRI systems (3 Tesla), FCD still remains a diagnostic challenge. This is mainly due to the subtle lesions, the complex convolution of the human cerebral cortex and the dependence on the expertise and attention of the radiologist viewing the MR images. It is estimated that about 25% of these lesions are being overlooked on the optimized epilepsy MR imaging protocols [Deblaere and Achten, 2008].

2.2 Magnetic Resonance Imaging - MRI

2.2.1 History of MRI

MRI is a relatively new technology with its early foundations in the late 1930's, when Isidor Isaac Rabi designed a process by which the magnetic strengths of atomic nuclei could be recorded [Rabi et al., 1938]. He received the Nobel prize in physics in 1944.

In 1946, Felix Bloch and Edward Purcell, working independently, devised improvements upon Rabi's process and were the first to demonstrate magnetic resonance phenomena in condensed matter. For the experiments Bloch used liquid water [Bloch et al., 1946, Bloch, 1946], while Purcell used solid paraffin [Purcell et al., 1946]. In 1952, they received the Nobel Prize in physics for nuclear magnetic resonance (NMR) spectroscopy. Up until the 1970's NMR was being used for chemical and physical analysis.

Then, in 1971 Raymond V. Damadian was the first to experiment with NMR on living tissue. He tested NMR on rat tissues and discovered that nuclear magnetic relaxation times of healthy tissue and malignant tumors were different [Damadian, 1971]. This motivated doctors and scientists to use NMR to detect areas of disease inside the body, which previously required exploratory surgery. With the inventions in computer technologies it was possible to develop images from NMR information in 1973, and echo-planar imaging (a rapid imaging technique) in 1977. The same year, Damadian acquired the first human body image, showing an axial slice through the thorax [Damadian et al., 1977].

The next step towards the modern MRI was made by the inventions of Paul C. Lauterbur and Sir Peter Mansfield in 1973 [Lauterbur, 1973, Mansfield, 1977]. They showed that much higher resolution could be obtained by manipulating the local magnetic field using gradient fields, and this idea is still successfully used in modern MRI. For their work, Lauterbur and Mansfield received the Nobel prize in medicine and physiology in 2003. In the late 1980's the name NMR had been changed to a more "friendly" term MRI that does not evoke a sense of danger to patients who need the exam.

The first MRI had low spatial resolution and the equipment used resistive magnets with weak magnetic fields. Even then, it was obvious that MRI capability in discriminating the soft tissue was superior to that of X-ray-based computer tomography (CT) and allows better and earlier diagnosis. Following this, many scientists over the next 20 years developed MRI into the technology that we know today.

Perhaps one of the most exciting MRI developments was the invention of superconductors over the 1980s and 1990s. These superconductors make the strong magnetic fields used in MRI possible and enable high image resolution with excellent soft-tissue contrast. Also, images can be acquired in any imaging plane. Since then, advances in computing has made the MRI process much faster. Today MR imaging is widespread and helps human accomplish something that cannot be done any other way.

2.2.2 The physics of MRI

The principle of MRI is based on a non-invasive interaction between radio waves and nuclei of atoms in the body in the presence of a strong magnetic field. This principle uses a physical phenomenon of nuclear magnetic resonance, and is related to the natural spinning of nuclei of atoms (charged particles in motion).

Every nucleus is composed of protons (positively charged particles) and neutrons (particles without electric charge), which have an intrinsic angular momentum, called spin. The combination of these particles in a nucleus, possesses a total angular momentum J , called nuclear spin. Nuclear spin can have values of 0, half-integers or whole integers. Nuclei with even atomic number (even number of protons) have nuclear spin zero ($J = 0$) and they are unaffected by a magnetic field and can not be detected by magnetic resonance. Nuclei with odd atomic number (odd number of protons) have integer or half-integer nuclear spin number (odd spin) and are affected by magnetic fields and can be observed by MR spectroscopy. However, only nuclei with half-integer spin number are of interest for the purpose of MRI. Table 2.1 shows a list of some nuclei useful in MRI and spectroscopy, from [Bushberg and Seibert, 1994, Haake et al., 1999].

Table 2.1: Spin values of several nuclei of interest in MR imaging and spectroscopy.

Nucleus	Spin number	Magnetic moment μ
^1H	1/2	2.79
^{17}O	5/2	1.89
^{19}F	1/2	2.63
^{23}Na	3/2	2.22
^{31}P	1/2	1.13

Clinical MRI (e.g. MRI of the brain) focuses on the hydrogen atom ^1H (contains nuclei with one proton). This is because of the nature of ^1H , which in comparison with other nucleus (see Table 2.1), has the strongest magnetic moment $\mu = 2.79$, very high isotropic abundance of 99.98% and the highest concentration in the human body. On an average, the human body is composed of 60% water (H_2O - consists of two hydrogen atoms and one oxygen). The water content highly depends on body size, age and gender, and also different body parts (e.g. tissues and organs) contain different amount of water [Ulijaszek et al., 1998], see Table 2.2. For instance, the average human brain is composed of 75% water, while the lungs are nearly 85% water. Hydrogen is also present in fat and most other tissues in the body.

The varying molecular structures and the amount of hydrogen in various tissues effect how the protons behave in the external field. For example, because of the total amount of hydrogen in water, it has one of the strongest net magnetization vectors relative to other tissues. Other tissues within the body have less hydrogen concentration and become magnetized to a lesser extent (their net magnetization is less intense).

Table 2.2: Body water content (percentages) for different period of life and different tissue types in adults.

Period of life	Water %	Tissue in adults	Water %
Fetus	94%	Skin	64%
Infant	75%	Skeleton (bones)	31%
Adult - man	60%	Muscle	80%
Adult - woman	55%	Lungs	85%
Elderly	50%	Brain	75%

2.2.2.1 Basic principles

A nucleus with odd spin (such as the hydrogen atom ^1H) can be represented as a magnetic moment vector that causes the nucleus to behave just like a magnet, with one north pole and one south pole, see Fig. 2.8(a). This is because a nucleus has a positive charge and, if it is spinning around an axis, then we have rotating charges which produce a small magnetic field. We can calculate the magnetic moment μ with the following expression:

$$\mu = \gamma \mathbf{J}. \quad (2.1)$$

where γ is the gyromagnetic ratio and \mathbf{J} is the nuclear spin. Vectors μ and \mathbf{J} are parallel and their direction defines atomic axis. For hydrogen nucleus, $\gamma = 42.58 \text{ MHz/T}$, which is in the radio-frequency (RF) range.

In an ensemble of nuclei, the sum of all of the magnetic moment vectors of the individual nuclei yields the net magnetization vector \mathbf{M} :

$$\mathbf{M} = \sum_i \mu_i. \quad (2.2)$$

Since \mathbf{M} is a vector quantity, it represent changes in the average orientation and distribution of magnetic moments.

Under normal circumstances and at room temperature, magnetic moments have no fixed orientation and there is no overall magnetic field. The proton spins are randomly distributed due to thermal agitation and the Brownian motion, which results in no net magnetization vector for the protons in the tissue, $\mathbf{M} = 0$, see Fig. 2.8(c). However, when nuclei are placed in an external magnetic field \mathbf{B} (e.g. when a patient is placed in the MRI scanner), they tend to align with the applied magnetic field, see Fig. 2.8(d). The interaction between \mathbf{B} and μ results in a periodic motion (a precessional movement of the nucleus around the applied magnetic field) and a potential energy E , see Fig. 2.8(b). This periodic motion is known as Larmor precession and is described by the Larmor (angular) frequency ω_L as follows:

$$\omega_L = \gamma B_0. \quad (2.3)$$

The frequency of precession is directly related to the strength of the applied magnetic field B_0 .

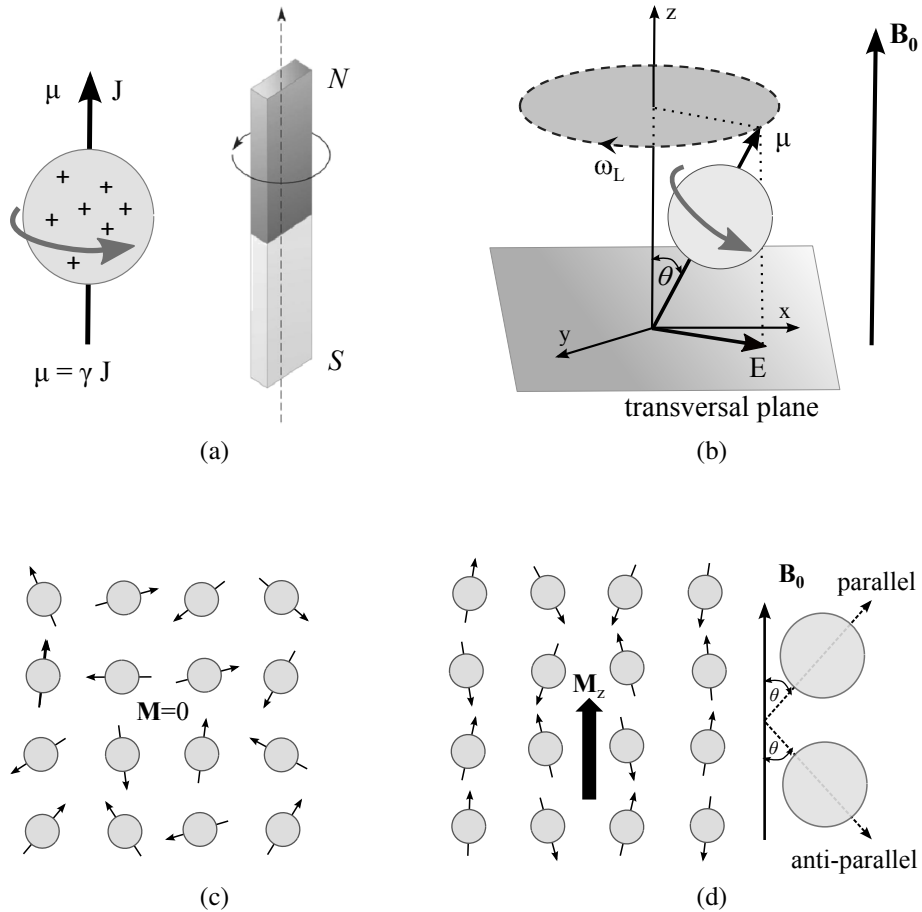


Figure 2.8: (a) A nucleus has a property called spin. The spinning positive charge causes a magnetic moment μ , which causes the nucleus to behave as a magnet where N is a north pole and S is a south pole. (b) Inside a magnetic field with intensity B_0 , the magnetic moment aligns with the magnetic field, resulting in a potential energy E and a precessional movement of the nucleus around the applied magnetic field with the Larmor angular frequency ω_L . (c) At room temperature, no net magnetization exists due to Brownian motion. (d) Inside a magnetic field, B_0 , the magnetic moments align with the magnetic field. There is a slight preference for the parallel alignment resulting in longitudinal net magnetization M_z .

Conventionally, the orientation of the static magnetic field B_0 is taken to be along the z -axis of a three-dimensional (3D) Cartesian coordinate system. The z -axis represents the longitudinal direction and the x - and y -axis (lying in the plane perpendicular to the z -axis), form a transverse x , y -plane, see Fig. 2.8(b).

The potential energy E of the single particle in an external magnetic field is defined as:

$$E = -\boldsymbol{\mu} \cdot \mathbf{B} = -\gamma JB_0 \cos \theta, \quad (2.4)$$

where B_0 is the external magnetic field strength, θ is the angle between the external magnetic field and the magnetic moment $\boldsymbol{\mu}$, see Fig. 2.8(b). In classical mechanics, any value of E is possible because there is no limitation on the energy of the particle. However, in quantum mechanics, which deals with physical phenomena at microscopic scales, the particle can only have a limited number of energy values (only a finite number of directions). This phenomenon is called space quantization (or Zeeman effect) and discrete energy levels can be described as follows:

$$E = -m\gamma\hbar B_0, \quad m = -j, -j+1, \dots, j-1, j \quad (2.5)$$

where $\gamma\hbar B_0$ is the quantum, j is the spin quantum number and \hbar is the reduced Planck constant or Dirac constant (1.0546×10^{-34} Js). The spin quantum number depends on the number of protons and neutrons in the nucleus, see Table 2.1.

In the case of the hydrogen nucleus (a single proton with a spin quantum number, $j = 1/2$), the quantization of the magnetic moments results in two discrete energy levels:

$$\begin{aligned} E_p &= -\frac{1}{2}\gamma\hbar B_0 \\ E_{ap} &= +\frac{1}{2}\gamma\hbar B_0, \end{aligned} \quad (2.6)$$

where “p” stands for parallel and “ap” for anti-parallel alignment of the magnetic moments with the magnetic field, see Fig. 2.8(d). The anti-parallel alignment corresponds to a high energy state where the magnetic moments are opposing the external magnetic field, while the parallel alignment corresponds to a low energy state in which the nuclei are in the direction of the magnetic field. There is a slight preference for the parallel alignment, creating a net magnetisation in the direction of the main magnetic field, where a larger B_0 will produce a larger net magnetization. The population difference $N_p - N_{ap}$ (for parallel and anti-parallel alignment) causes a longitudinal magnetization M_z , see Fig. 2.8(d).

A transition of proton from the parallel (low energy) to the anti-parallel (high energy) state can be only made by absorbing a photon with energy equal to:

$$E_{ap} - E_p = \gamma\hbar B_0. \quad (2.7)$$

For a photon with energy $E = \hbar\omega_L$, the resonance condition is described by the Larmor (angular) frequency:

$$\omega_L = \gamma B_0. \quad (2.8)$$

Note that the angular frequency of precessing magnetic moment derived from the classical mechanical relations in Eq. (2.3) is the same Larmor angular frequency derived from the quantum mechanical relations in Eq. (2.8).

Once the tissue has become magnetized (the spins are in either the high or low energy state), a condition known as thermal equilibrium is reached. In this configuration, the equilibrium magnetization M_0 equals M_z and is parallel to B_0 . The population ratio at equilibrium is given by the Boltzmann factor for the energy difference $\Delta E = \gamma \hbar B_0$:

$$\frac{N_{ap}}{N_p} = \exp \frac{-\gamma \hbar B_0}{k_B T}, \quad (2.9)$$

where k_B is Boltzmann's constant (1.3807×10^{-23} J/K) and T is the absolute temperature. This indicates that the energy difference and the sensitivity of the MRI technique, can be altered by reducing the temperature or increasing the magnetic field. Therefore, MRI needs a strong magnetic field B_0 , which for modern clinical scanners is between 0.5 and 3.0 T (Tesla). To put the magnitude of this field into context, 1 Tesla is equal to 10,000 Gauss and the Earth's magnetic field varies from between 0.3 – 0.7 Gauss.

2.2.2.2 Creating an MR signal

At thermal equilibrium, there is no net magnetization in the transverse plane, see Fig. 2.8(b). To create an MR signal and perform MR imaging, it is necessary to perturb the magnetic moments precessing about the external magnetic field B_0 . This can be accomplished by applying a radio frequency (RF) energy pulse (an oscillating electromagnetic field B_1) with a frequency equal to the Larmor frequency and perpendicular to the z -axis and B_0 , see Fig. 2.9(a). The nuclei resonate, gain energy, change their alignment by transiting from the lower to the higher energy state. The anti-parallel state becomes occupied, and the parallel state becomes less occupied. The result of this perturbation is that the net magnetization vector \mathbf{M} is rotating away from the z -axis and towards the x, y -plane, and has both longitudinal M_z and transverse M_{xy} component, see Fig. 2.9(b). The angle of rotation α is called “flip angle” and depends on the amplitude B_1 and on the duration of the pulse t_p :

$$\alpha = \int_0^{t_p} \gamma B_1 d\tau = \gamma B_1 t_p. \quad (2.10)$$

By an appropriate selection of the amplitude B_1 and the pulse duration t_p , any flip angle α can be obtained. In MR imaging the most important RF pulses are the $\alpha = 90^\circ$ and $\alpha = 180^\circ$ pulse. The 90° pulse results in the net magnetization vector oriented in the x, y -plane, where there is no longitudinal magnetization $M_z = 0$. The 180° pulse results in the net magnetization vector oriented in the opposite direction of the z -axis, see Fig. 2.9(c). Additionally to the effect of bringing more spins in the anti-parallel state, the RF field also forces all individual spins to rotate in phase. This phenomena is called phase coherence, and makes it possible that the net magnetization vector has a transverse component in non-equilibrium conditions.

When the transmission of RF pulse is turned off the nuclei gradually lose energy and return to its equilibrium state. This process is called relaxation. Relaxation is governed by two physical phenomena: spin-lattice relaxation and spin-spin relaxation. Both phenomena are illustrated in Fig. 2.10.

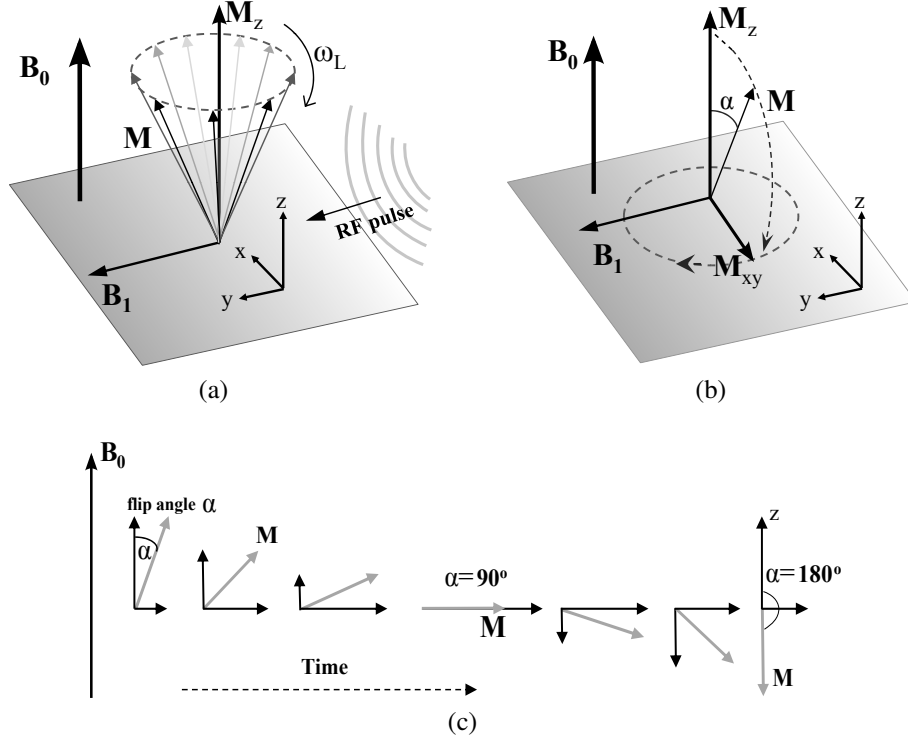


Figure 2.9: (a) The generation of an oscillating electromagnetic field B_1 perpendicular to the magnetic field B_0 using an RF pulse. (b) The decrease of the longitudinal magnetization M_z and generation of the transverse magnetization M_{xy} . (c) Illustration of the “flip angle” α .

The spin-lattice relaxation is an energy phenomenon that describes the return of the spins to the energy equilibrium (the favored parallel alignment state). The energy difference between the favored parallel alignment state and the anti-parallel state, $\hbar\omega_L = \gamma\hbar B_0$, is dissipated as heat to the ensemble. This return to thermal equilibrium leads to an increase of the longitudinal magnetization M_z with time t as follows:

$$M_z = M_0[1 - e^{-t/T_1}], \quad (2.11)$$

where M_0 is the net magnetization at equilibrium in the z -direction. The spin-lattice relaxation follows an exponential course of growth characterized by the time constant T_1 (longitudinal relaxation time), which is a measure for the restoration of the longitudinal magnetization M_z . After time T_1 , the longitudinal magnetization M_z is recovered to approximately 63% of its final value. After $5 T_1$ times, $M_z = M_0[1 - e^{-5}]$, the recovery of M_z is complete, see Fig. 2.10(a).

The spin-spin relaxation phenomenon leads to dephasing of the spins (loss of the phase coherence), which causes the disappearance of the transverse magnetization M_{xy} . This phenomenon is caused by the small differences in local magnetic fields

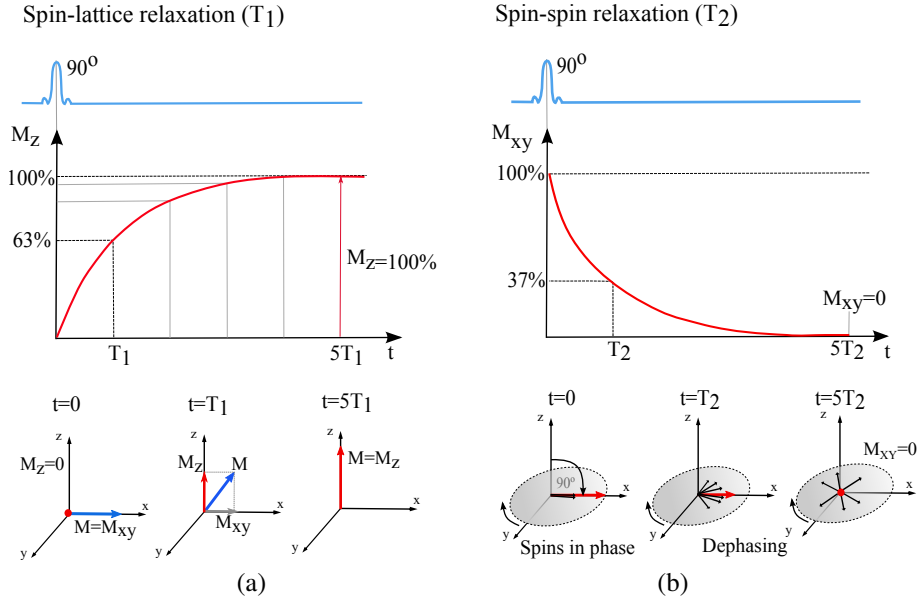


Figure 2.10: (a) The spin-lattice relaxation process. After $t = T_1$ the longitudinal magnetization M_z has reached 63% of its equilibrium value. (b) The spin-spin relaxation process. After $t = T_2$ the transverse magnetization M_{xy} has decreased to 37% of its value at $t = 0$.

that are experienced by the spins. These small differences are caused by the chemical environment of the spins, which depends on material composition. Dephasing, however, does not influence the state of the individual magnetic moments which determine the longitudinal magnetization. The decrease of the transverse component of the net magnetization during spin-spin relaxation can be described with the equation:

$$M_{xy} = M_0 e^{-t/T_2}, \quad (2.12)$$

where M_0 is the initial transverse magnetization at $t = 0$, when the RF pulse has been turned off. The spin-spin relaxation follows an exponential decay curve characterized by the time constant T_2 (transverse relaxation time), which is a measure of the nuclear spin dephasing. After time T_2 , the phase coherence of the spins has dropped to approximately 37%. After $5 T_2$ time, phase coherence has just about disappeared and $M_{xy} = 0$, see Fig. 2.10(b).

The T_1 and T_2 relaxation constants considerably depend on the tissue type. Additionally, T_1 time depends on the strength of the external magnetic field: the higher the field, the higher T_1 , see Table 2.3. For all tissues T_2 time is shorter than T_1 time. This results in transverse magnetization M_{xy} to decay faster than the time required by longitudinal magnetization M_z to recover, see Fig. 2.11.

Dephasing of the spins in non-homogeneous media (e.g. the human body) can be additionally affected by magnetic field inhomogeneities of the static magnetic field. These inhomogeneities can be related to the field itself (e.g. the magnet does not

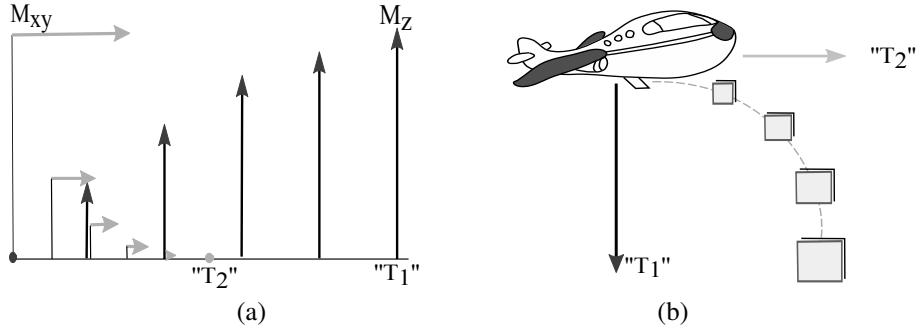


Figure 2.11: (a) The transverse magnetization M_{xy} decays more rapidly than the time required by longitudinal magnetization M_z to recover. (b) Example of the “falling box”. If the box is thrown from an airplane, two simultaneous “forces” are included: the Earth’s gravity and the kinematic energy in the direction of flight. The actual movement of the box is the superposition of two motions performed independent of each other. While the box is traveling toward the earth, coming closer and closer, it barely continues in the direction of flight.

Table 2.3: T_1 and T_2 relaxation times for various tissues. From [Bushberg and Seibert, 1994].

Period of life	T_1 (0.5T)(ms)	T_1 (1.5T)(ms)	T_2 (ms)
CSF	1800	2400	1400
White Matter	500	780	90
Gray Matter	650	900	100
Muscle	550	870	45
Liver	350	500	40
Fat	210	260	80

provide a homogeneous field), or by different magnetic susceptibilities of the materials present in the field. This is called the T_2^* effect, where $T_2^* < T_2$, see Fig. 2.12(b).

During relaxation, the longitudinal magnetization M_z is becoming greater than the transverse magnetization M_{xy} , resulting in the net magnetization M to spiral up around the z -axis. The nuclei precess about the z -axis at the Larmor frequency. The energy emitted during relaxation is an RF signal at the Larmor frequency. This signal is called the free induction decay (FID) response signal and MR is based on the recording of this signal in the x, y -plane, see Fig. 2.12(a),(b). The FID response signal is measured by a conductive field coil (receiver coil) placed around the object being imaged.

Note that only the transverse magnetization M_{xy} produces signal and a receiver can be set to detect this magnetization. Also, note that the B_1 field is much smaller than the static field B_0 . The effects of the B_1 field are cumulative, so that a B_1 field of few gauss can cause realignment of the net magnetic vector even though the static B_0 field is measured in thousands of gauss.

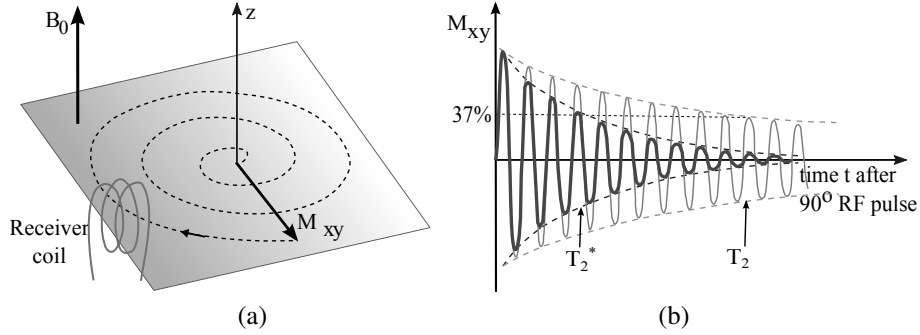


Figure 2.12: (a) The spiral behavior of the magnetic moment \mathbf{M} due to the influence of the RF pulse is illustrated on the transverse plane with the transverse magnetization M_{xy} . (b) The diagram is showing the process of transverse relaxation after a 90° RF pulse is applied at equilibrium. The resultant decaying signal shown in red color is known as the free induction decay (FID) - actual decay due to T_2^* relaxation including the effects of field inhomogeneities. This signal represents the loss of phase coherence and reduction of $M_{xy} = 0$.

2.2.2.3 MR imaging principles

The MR signal described above is obtained from the complete volume in the static field, and does not contain any position-dependent information. However, the basis of MR imaging is the spatial allocation of individual MR signals that reflect the respective anatomical structure. Thus, to produce 2D or 3D MR images, the MR signal must be encoded for each spatial dimension. The common method is to spatially vary the magnetic field at each location in an image or volume that we want to obtain, which will then influences the nuclear spins to rotate with uniquely different precessional frequencies at different locations.

The spatial differentiation of the magnetic field can be achieved by superimposing a series of linear magnetic field gradients in the three orthogonal directions x , y and z onto the existing z component of the main field. This produces a linear variation in precessional frequencies along applied direction and provides information about the spatial location of the nuclei in the body. This can be described with the modified Larmor equation:

$$\omega_L(\mathbf{r}) = \gamma(B_0 + \mathbf{G} \cdot \mathbf{r}) \quad (2.13)$$

where $\mathbf{r} = (x, y, z)$ is the position vector, $\omega_L(\mathbf{r})$ is the Larmor frequency of nucleus at location \mathbf{r} , $\mathbf{G} = (G_x, G_y, G_z)$ is a linear magnetic field gradient with the three components in the orthogonal directions x , y and z , and $\mathbf{G} \cdot \mathbf{r} = (G_x x + G_y y + G_z z)$ is the inner product between the two vectors. This equation is fundamental to MR imaging process because it indicates that the frequency of precession is a function of the static field and the gradient field at each location \mathbf{r} . This indicates that the precession frequency for each nucleus is uniquely defined by its position.

The advantage of the magnetic field gradients is to allow us to position slice planes at random in MR imaging. To illustrate the principle of a transverse slice selection,

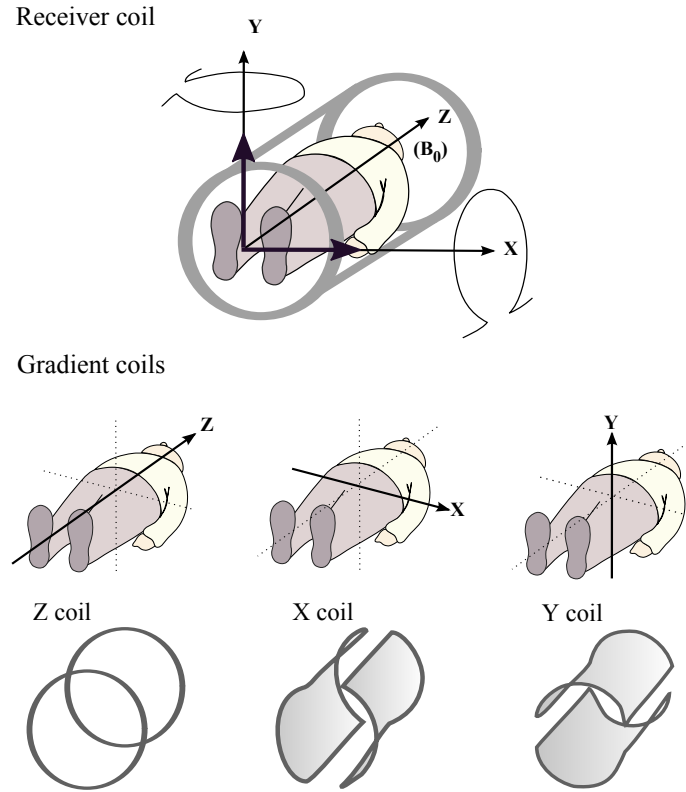


Figure 2.13: Illustration of the RF receiver coils (top) and 3 gradient coils (bottom). The static magnetic field B_0 is oriented in the z direction.

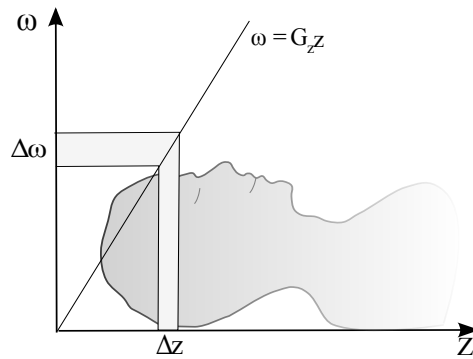


Figure 2.14: The principle of slice (2D imaging) or slab (for 3D imaging) selection. Only the spins in a slice with thickness Δz are excited by applying an RF pulse with a bandwidth $\Delta\omega$ in the presence of the slice selection gradient G_z in the z -direction.

where a slice is oriented perpendicular to the z -axis, consider that only a linear gradient G_z is switched on and $\mathbf{G} = (0, 0, G_z)$. Then, the Larmor frequency of the spins in the imaging volume depends on the z -position:

$$\omega_L(z) = \gamma(B_0 + G_z z). \quad (2.14)$$

At the moment when an RF pulse with a finite bandwidth is transmitted, only the spins in a slice perpendicular to the z -direction will be excited. The location of the center of the slice depends on the gradient. This is illustrated in Fig. 2.14. The slice thickness Δz depends on the steepness of the gradient and the bandwidth of the RF pulse:

$$\Delta z = \frac{\Delta \omega}{\gamma G_z}, \quad (2.15)$$

where $\Delta \omega$ is the bandwidth of the RF pulse. In 2D imaging, a narrow-bandwidth pulse is used to excite only a limited slice. In 3D imaging, a broad-bandwidth pulse is used to excite a larger volume and the excited volume is called a slab rather than a slice.

Slice or volume selection is not sufficient for imaging because it only allows position encoding in a single direction. The question is how do we get an image from the slice? It is important to understand that the image is computed from the raw data generated from the MR signal, where the MR signal is produced with the transverse magnetization M_{xy} , see 2.2.2.2. To encode position within the slice, additional magnetic field gradients G_x and G_y are used. Then, MR image information such as voxel intensity is obtained in the spatial frequency domain, which is often referred to as k -space. The k -space concept is independently introduced by Ljunggren and Twieg in 1983 [Ljunggren, 1983, Twieg, 1983]. The MR imaging procedure is explained in more detail as follows.

First, note that after RF excitation the transverse component of the net magnetization vector describes a rotation around the z -axis:

$$M_{xy}(t) = M_{xy} e^{-i\omega t}. \quad (2.16)$$

When a 3D magnetic field gradient \mathbf{G} is applied (where in general the gradient \mathbf{G} is time-dependent), the angular frequency ω can be written as:

$$\omega(\mathbf{r}, t) = \gamma \int_0^t \mathbf{G}(\tau) \cdot \mathbf{r} d\tau. \quad (2.17)$$

When the transverse component of the net magnetization is recorded while the gradient is switched on, the signal from all the spins in the imaging volume is recorded. This can be seen as an integration in the space domain over the entire imaging volume:

$$s(t) = \int \int \int \rho(x, y, z) e^{-i\gamma \int_0^t \mathbf{G}(\tau) \cdot \mathbf{r} d\tau} dx dy dz, \quad (2.18)$$

where $s(t)$ is the measured signal, $\rho(x, y, z)$ is the position-dependent spin density.

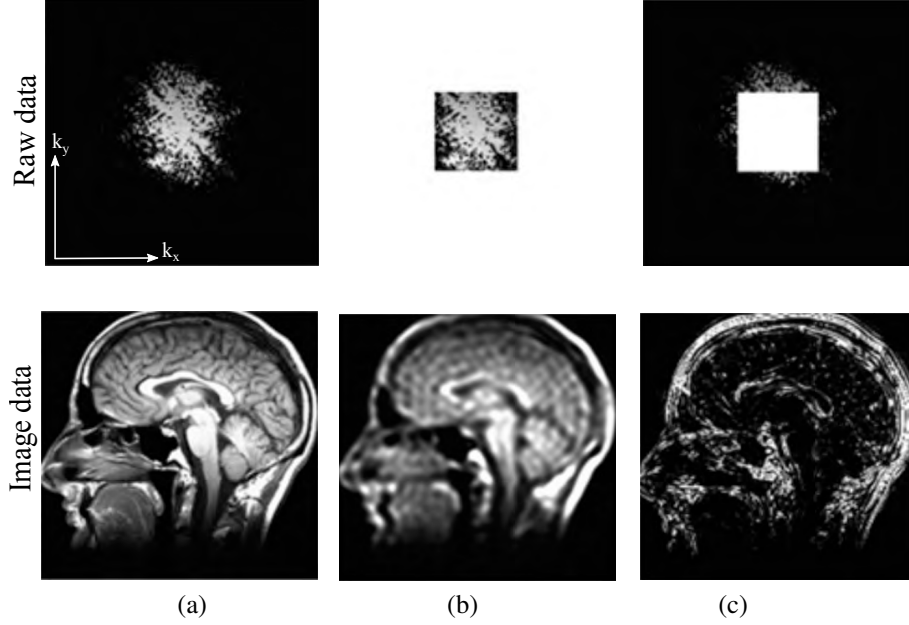


Figure 2.15: Illustration of an MR image reconstruction from raw data. (a) The first row shows the 2D k-space raw data matrix. The second row shows the MR image reconstructed via an inverse 2D Fourier transform. (b) The center of the 2D k-space raw data contains a low spatial frequency and determines the rough structure and the image contrast in the reconstructed MR image. (c) The k-space raw data along the margin contain a high spatial frequency and provide information of the finer structures (such as edges) in the image and determine the resolution.

Relaxation effects T_1 and T_2 can be included by multiplying the spin density with two relaxation functions $g(t, T_1)$ and $h(t, T_2)$:

$$s(t) = \int \int \int \rho(x, y, z) g(t, T_1) h(t, T_2) e^{-i\gamma \int_0^t \mathbf{G}(\tau) \cdot \mathbf{r} d\tau} dx dy dz. \quad (2.19)$$

It is well known that the Fourier transform of a 3D function $f(x, y, z)$ is:

$$F(\mathbf{k}) = \int \int \int f(x, y, z) e^{-2\pi i \mathbf{k} \cdot \mathbf{r}} dx dy dz, \quad (2.20)$$

where $\mathbf{k} = (k_x, k_y, k_z)$ is the spatial frequency vector.

Comparing Eqs. 2.19 and 2.20, we see that measured signal $s(t)$ is equal to the Fourier transform $F(\mathbf{k})$ of the image to be reconstructed $f(x, y, z)$ if the following conditions are satisfied:

1. The relaxation functions $g(t, T_1)$ and $h(t, T_2)$ in Eq. (2.19) are time independent. This is assumed to be true in practice, which implies that the relaxation times T_1 and T_2 do not change over the imaging volume during the short readout time (during the period the receiver coil measures the signal).

2. The spatial frequency vector \mathbf{k} is defined as:

$$\mathbf{k}(t) = \frac{\gamma}{2\pi} \int_0^t \mathbf{G}(\tau) d(\tau). \quad (2.21)$$

This is known as the \mathbf{k} -theorem [Mansfield, 1977].

From Eq. (2.21), it is clear that a longer measurement time or stronger gradient strength leads to a larger \mathbf{k} -space. This produces images with a better spatial resolution. The sampling in \mathbf{k} -space is determined by the time evolution of the magnetic gradient \mathbf{G} . By manipulating the gradients, any point in \mathbf{k} -space can be sampled, see 2.2.2.4. Once all of \mathbf{k} -space has been assembled, the inverse Fourier transform is performed to obtain the image. MR images represent a weighted proton density that depends on the relaxation time constants T_1 and T_2 and the moment of the measurement. An example of the reconstruction of an MRI image from raw data (\mathbf{k} -space) is shown in Fig. 2.15.

2.2.2.4 Basic MRI pulse sequences

To sum up, the signal acquired during MRI depends on:

1. The magnetic fields generated by the MRI system:
 - the static field \mathbf{B}_0 (which aligns the spins),
 - the RF field \mathbf{B}_1 (used for excitation of the protons - flip angle),
 - the gradient fields \mathbf{G} (used for position-encoding).
2. The properties of the protons in the volume:
 - proton density,
 - relaxation properties (T_1 and T_2 time constants),
 - the local field inhomogeneities (T_2^* effects).

The static field can not be manipulated, but the RF field and the gradient fields can be changed in time. Acquisition of MR images with different kinds of contrast can be obtained by using different sequences of RF and gradient fields. These sequences are called MRI pulse sequences. This is a big advantage of MRI over e.g. CT where only contrast based on the electron density of tissue can be obtained.

Since the free inductive decay (FID) signal (transmitted by the spins returning to the equilibrium) quickly vanishes, it does not allow the gradient switching that is needed to encode the \mathbf{k} -space trajectory. Therefore, MRI sequences use methods for rephasing the spins after the gradients have been applied. The coherent RF signal that is emitted after rephasing is called an echo. There are different ways to generate an echo and two basic schemes used in MRI are the spin echo (SE) pulse sequence and the gradient echo (GE) pulse sequence.

The Spin Echo pulse sequence

The spin echo (SE) sequence consists of the 90° RF excitation pulse, followed by a 180° RF pulse for rephasing the spins. The effect of the 180° pulse can be explained on a single spin in the rotating reference frame. After excitation with a 90° pulse, the spin is oriented along the x -axis. Suppose that the rotational frequency of the spin is slightly higher than the expected Larmor frequency and the spin is dephasing in the clockwise direction. In the rotating reference frame, the spin will move away from the x -axis. By applying a 180° pulse, the spin is rotated 180° about the y -axis. If it continues to rotate in the clockwise direction, it is now moving towards the x -axis rather than away from it. The time it takes for the spin to align with the x -axis, and be in coherence, is exactly the time between the 90° and the 180° pulses. This is half of the echo time TE. The spin echo sequence is repeated with repetition time TR as often as the k -space is filled with echoes. The number of raw data lines corresponds to the number of repetitions of the sequence.

A diagram of a 2D SE pulse sequence and the trajectory that is sampled in k -space is shown in Fig. 2.16. A slice selection gradient G_z is applied together with the 90° RF excitation pulse and later with the 180° RF pulse to flip the spins and make them rotate back towards coherence. A phase-encoding gradient G_y is applied along the y -axis. Then, the spin-echo signal is acquired in echo time TE, while a frequency-encoding gradient G_x along the x -axis is switched on. Thus, the frequency-encoding gradient is also known as the readout gradient. The amplitude of the phase-encoding gradient G_y determines the k_y coordinate of the line that will be sampled in k -space, while the frequency-encoding gradient G_x scans a line in k -space in the k_x direction. The next line in k -space is acquired in the same manner after the repetition time TR. For a matrix of size 256×256 , gradient switching of the spin echo sequence is repeated 256 times with repetition time TR and with the phase-encoding gradient G_y increasing step-by-step. The gradient step amplitudes are frequently represented in the pulse diagrams by a multitude of horizontal lines in the bar - positive or negative.

The Gradient Echo sequence

The acquisition time of the SE sequences can be relatively long. This is the case in T_2 -W MR images, as the acquisition of the next line in k -space can only be acquired when T_1 relaxation of all spins is finished. Because the SE sequence uses a 90° RF excitation pulse, T_1 relaxation can take a long time. This can be avoided by using a gradient echo (GE) sequence, which uses gradients with opposite signs to dephase and rephase the spins, see Fig. 2.17. In this case there is no 180° pulse to flip spin angles for RF excitation. Therefore, a shorter TR can be achieved, leading to shorter acquisition times. The flip angle is smaller than 90° , usually between 20° and 60° .

The downside of the GE sequences is that the local field inhomogeneities due to susceptibility effects are not compensated by the echo. Then, the signal is governed by T_2^* rather than T_2 . This leads to T_2^* -W images instead of T_2 -W images. GE sequences are therefore mainly used for very fast imaging techniques in 2D or 3D.

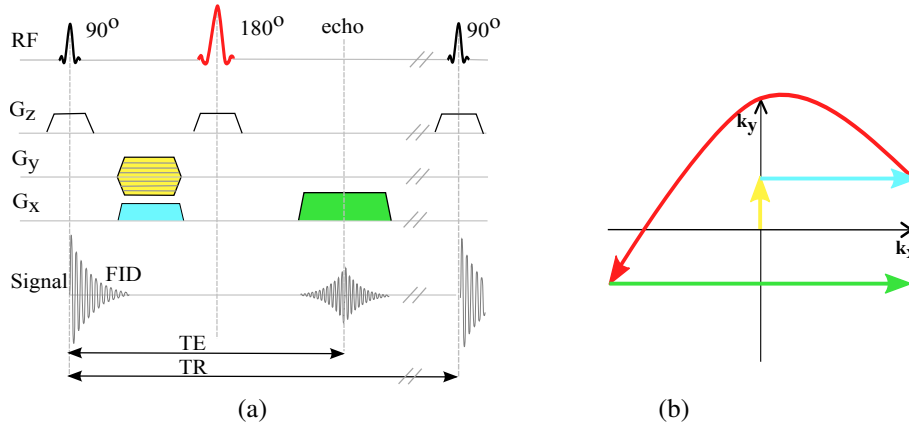


Figure 2.16: (a) Schematic illustration of a 2D spin echo pulse sequence; (b) The associated k-space trajectory in the k_x, k_y plane for one positive phase-encoding gradient value G_y . By modifying G_y , a different trajectory in k-space is traversed. The data is acquired while scanning the green line in k-space.

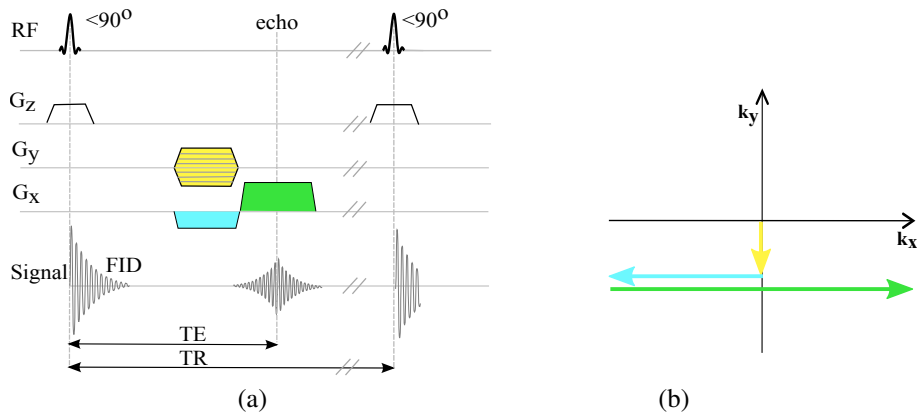


Figure 2.17: (a) Schematic illustration of a 2D gradient echo sequence; (b) The associated k-space trajectory in the k_x, k_y plane. The data is acquired while scanning the green line in k-space. Note the opposite polarities of the gradients along the x -axis and the RF pulse which can have a flip angle smaller than 90° .

The image contrast is determined by manipulating TE and TR. In MRI, three main contrast types can be discriminated: T_1 -W, T_2 -W and proton density (PD) weighted. To obtain a T_1 -W image, a short TR is used. To obtain a T_2 -W image, a long TE is used. To obtain a PD-weighted image, a long TR is combined with a short TE. For the brain MRI, these contrasts are explained and illustrated in Section 2.2.3, Fig. 2.19.

2.2.2.5 The MRI scanner system

The essential components of an MRI system include: (1) a large magnet which generates a uniform magnetic field B_0 , (2) smaller electromagnetic coils to generate magnetic field gradients G_x, G_y, G_z for imaging, and (3) a radio transmitter and receiver and its associated transmitting and receiving antennae or coils. In addition to these fundamental components, a computer is necessary to coordinate signal generation and acquisition and image formation and display. The schematic diagram of the functional configuration of an MRI unit is shown in Fig. 2.18.

In MRI the patient is placed inside the scanner which is made up of a moveable bed-like structure and a large hollow tube. The outer part of the tube contains the main magnet that generates the very strong magnetic field. The static magnetic field B_0 is commonly generated by a superconducting magnet, using a superconductor current loop. Usually niobium-titanium (NbTi) or niobium-tin (Nb₃Sn) superconductors are used, cooled with liquid helium. The lines of force for the main magnet are configured to pass parallel to the chamber axis (and thus follow the length of the patient's body). Between the patient and the outer part of the tube is the outer casing of the scanner, the RF body coil (send and receive), 3 pairs of gradient coils (for the x, y and z direction), and the temperature shields. Two different RF coils are used for transmission and reception of signals. This is because the signal reception quality is strongly dependent on the distance between the spins and the coil. Therefore, one large integrated RF coil is present for excitation of the spins and one smaller RF coil is used very close to the body for better signal quality. Specific RF coils exist for different body parts such as the brain, chest, knee, spine, etc. Some of these coils can also transmit RF waves. The received MR signal is collected and processed by computer to form MR images.

The room in which the scanner is located needs to shield the surroundings from stray magnetic fields, but also shield the scanner from sources that might affect the field homogeneity. Stray magnetic fields outside the scanner room can unintentionally affect magnetic materials, like machines, credit cards, pacemakers, etc. MRI requires shielding to block specific radio waves that may distort images created by the MRI and to keep stray magnetic field strengths within accepted risk levels. All scanner room walls, ceiling, and flooring must be covered with shield plates, comprising a Faraday cage. The shield plates are commonly made of metals such as copper, galvanized steel or aluminium. Further readings on the MRI physics can be found in [Blink, 2004, Beutel et al., 2000].

In summary, MRI works as follows. The tissue inside a magnet becomes temporarily magnetized when the hydrogen nuclei in the body align with the static magnetic field B_0 . Then, the tissue responds to exposure to RF waves (the RF field B_1) at a particular frequency by sending back an RF wave signal. This phenomenon only occurs at the Larmor frequency ω_L corresponding to the specific strength of the magnetic field. The detected signal is composed of multiple frequencies, reflecting different positions along the magnetic field gradient. When the signal is broken into its component frequencies, the magnitude of the signal at each frequency is proportional to the hydrogen density at that location, thus allowing an MR image to be constructed.

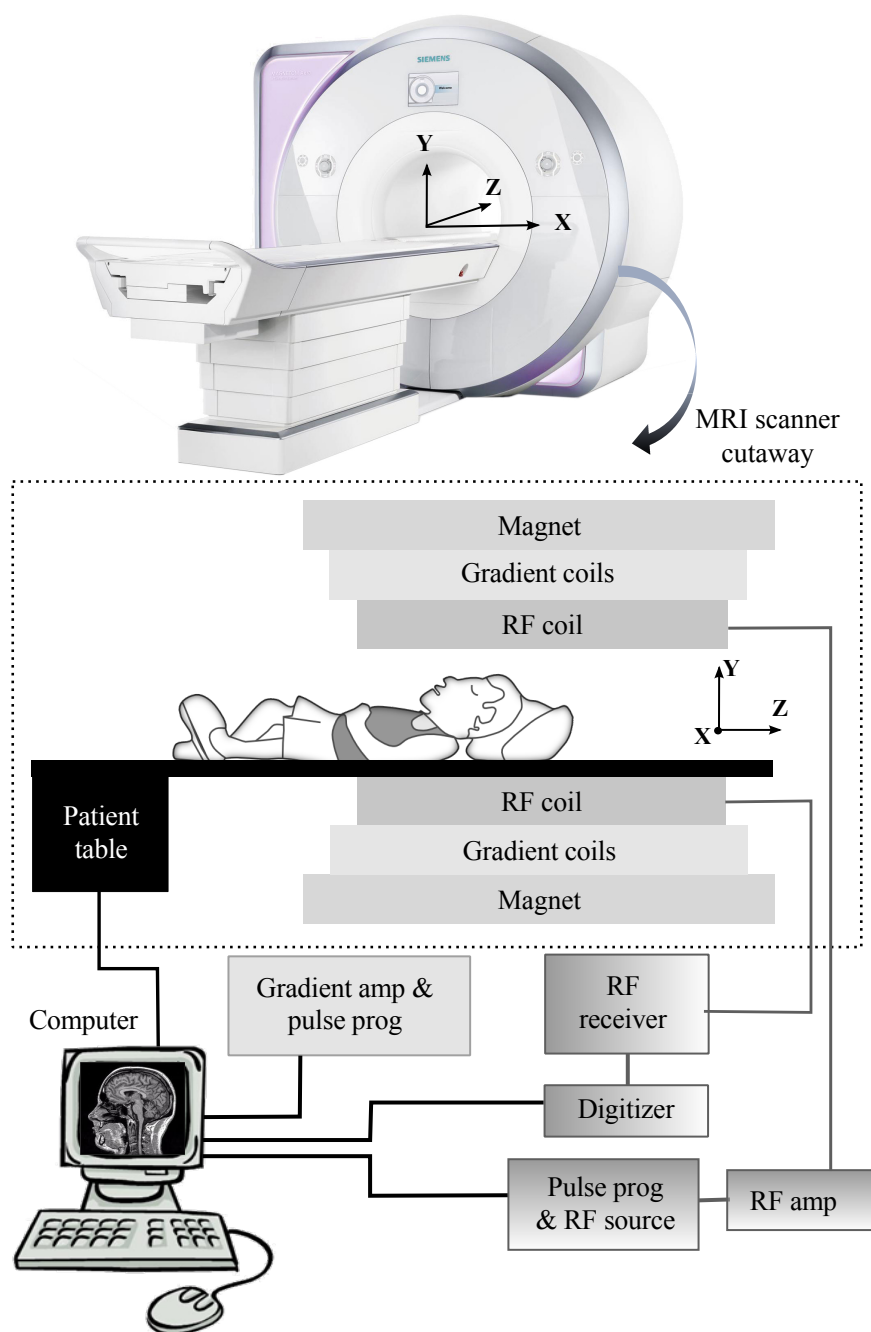


Figure 2.18: The schematic diagram of an MRI scanner system - scanner cutaway.

2.2.3 MRI of the brain

One of the greatest advantages of MRI over other brain imaging techniques is its excellent soft tissue contrast. Standard anatomical brain MRI acquisitions are typically designed to optimize discrimination between three tissue types: gray matter (GM), white matter (WM), and cerebrospinal fluid (CSF), see Fig. 2.19(a). Tissue contrast is produced and optimized by altering several different intrinsic and extrinsic parameters. Intrinsic parameters are related to the chemistry of the tissue and include the relaxation constants T_1 and T_2 . Extrinsic parameters include the flip angle, the repetition time (TR) and the echo time (TE). By manipulating with these parameters, standard MRI modalities such as T_1 -W and T_2 -W, can be obtained.

The two extreme cases in terms of contrast difference in MR are fat and water (CSF). For example, when imaging with a long TE parameter, inherent differences in T_2 times of tissues will become apparent. Tissues with a long T_2 (water) will take longer to decay and their signal will be stronger (or appear brighter in the image) than the signal from tissue with a short T_2 (fat). In a similar manner TR governs T_1 contrast. Tissue with a long TR (water) will take a long time to recover back to the equilibrium magnetisation value, so therefore a short TR interval will make this tissue appear dark compared to tissue with a short T_1 (fat). Therefore, in T_1 -W images the CSF around the cortical areas and within the ventricles is dark and in T_2 -W images bright, Fig. 2.19(a),(b). When TE and TR are chosen to minimise both these weightings, the signal contrast is only derived from the number or density of spins in a given tissue. This type of image is called Proton Density (PD), Fig. 2.19(c). Signal intensities of the adult brain tissues and TR and TE times at T_1 -W, T_2 -W and PD are summarized in Table 2.4.

Additional modalities used in the methods presented in this theses are Fluid Attenuation Inversion Recovery (FLAIR) and Diffusion Weighted Images (DWI). These modalities are very useful for studying of brain injuries. The important property of FLAIR is that the CSF is not enhanced as in the T_2 -W images and the injuries adjacent to the CSF are seen much more earlier, see Fig. 1.2(c). The main property of DWI is that they give local directional information on the diffusivity of water inside the brain tissue. Using these images we can understand how much a water molecule can migrate along each direction in a given location and using that we can detect brain tissue malformations.

Anatomical MRI modalities are formed from 3-D volume elements called voxels. Each voxel is assigned a single value based on the average magnetic resonance characteristics present in the tissue corresponding to that voxel. The size of the voxel determines the spatial resolution, or the fineness of detail that can be distinguished in an image. Voxel sizes vary depending on imaging parameters, magnet strength, the time allowed for acquisition, and other factors, but often in standard MRI studies voxel sizes are on the order of 1-2 mm. Greater spatial resolution can be obtained with a longer scanning time, but this must be weighed against patient discomfort. In adult brain MRI studies image acquisition time is around 20 min, while in pediatric MRI studies image-acquisition time is limited to between 5 and 15 min.

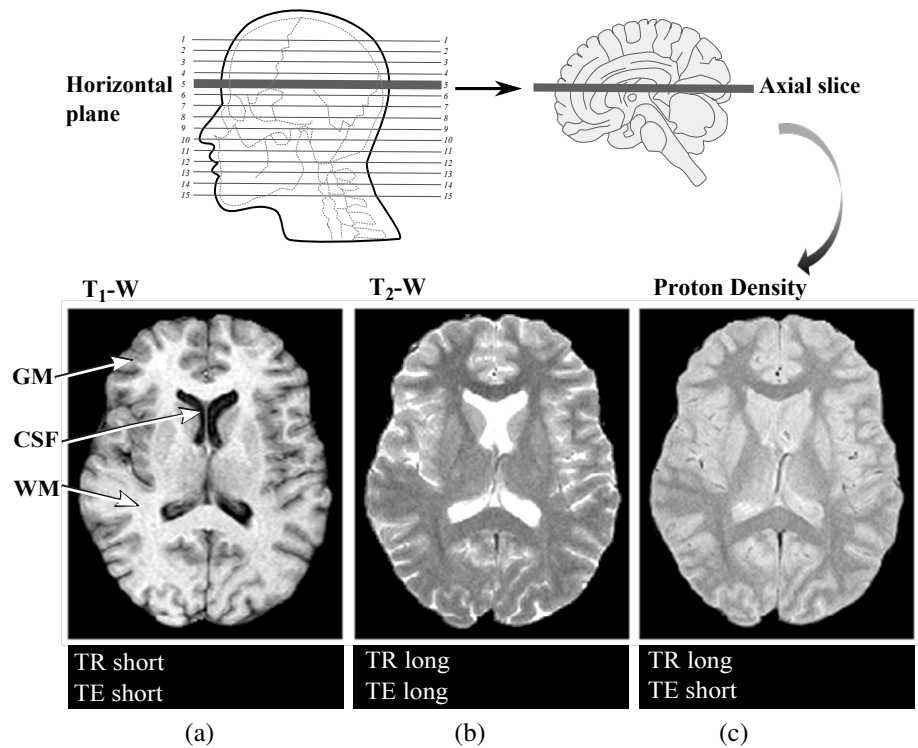


Figure 2.19: Illustration of standard anatomical MRI modalities of the human adult brain in an axial plane: (a) T₁-weighted (T₁-W) image, (b) T₂-weighted (T₂-W) image and (c) Proton Density (PD) image. The combination of RF pulse timing constants (TE and TR), specific for each modality, are given below images.

Table 2.4: Signal intensity of various brain tissues at T₁-W, T₂-W and PD in adults.

Tissue	T ₁ -W	T ₂ -W	PD
Fat	Bright	Bright (less than T ₁ -W)	Bright
Water	Dark	White	Light gray
Gray matter (GM)	Gray	Gray	Gray
White matter (WM)	White	Dark (darker than PD)	Dark
TR values	< 500 ms	> 1500 ms	> 1500 ms
TE values	50-100 ms	> 80 ms	< 50 ms

2.2.3.1 Challenges in brain MRI analysis - imaging artifacts

Different kinds of artifacts affect the analysis of brain MRI and diagnostic quality. Often MR images are deteriorated by noise due to various sources of interference and other phenomena that affect the measurement processes in imaging and data acquisition systems. The small differences that may exist between normal and abnormal tissues are confounded by noise and artifacts, often making direct analysis of the acquired images difficult. Typically, all MRI brain artifacts can be classified in three groups: (1) patient-related, (2) signal processing-related and (3) hardware (machine)-related [Erasmus et al., 2004].

Among patient-related artifacts are those resulting from either voluntary or involuntary motions during MRI acquisition. Patient motion can cause either ghost images or image noise. Periodic movements such blood vessel or CSF pulsation cause ghost images (Fig. 2.20(a)), while non-periodic movement causes image noise. Ghost image intensity increases with amplitude of movement and the signal intensity from the moving tissue. Several methods can be used to reduce motion artifacts, where the most common ones are patient immobilisation and signal suppression of the tissue causing the artifact.

Several signal processing-related artifacts occur frequently in MRI: the Gibbs phenomenon (ringing artifacts), the partial volume effect (PVE) and the aliasing (wrap-around). The Gibbs phenomenon or ringing artifact is caused by the under-sampling of high spatial frequencies at sharp boundaries in the image. The artifact is seen at bright edges or at near sharp boundaries, where high contrast transitions in the tissue occur (like at the skull-brain interface, see Fig. 2.20(b)). The Gibbs artifact is characterized by a series of regularly spaced parallel lines alternating between bright and dark, which slowly fade with distance. The easiest way to reduce this effect is increasing the matrix size at the cost of additional acquisition time.

The partial volume effect manifests itself in the mixing of tissue intensities when more than one tissue is present at the voxel. If an interface between two different tissues occurs within a voxel, the resulting voxel intensity will be proportional to the weighted average of the signals deriving from these tissues, see Fig. 2.20(c). By using a smaller pixel size and/or a smaller slice thickness, this artifact can be reduced.

The aliasing or wrap-around artifact occurs whenever the object being imaged extends beyond the field of view but is still within the sensitive volume of the coil. As a result, the areas extending beyond the field of view boundaries are aliased (wrapped) back into the image on the opposite side to appear at artifactual locations, see Fig. 2.20(d). This phenomenon is usually caused by undersampling of the frequencies contained within the return signal (sampling at a frequency below the Nyquist limit).

Perhaps the most challenging artifact is the intensity inhomogeneity, also called the bias field, which is the most significant hardware-related artifact. The bias field is a smooth low-frequency multiplicative artifact caused by the inhomogeneity of the magnetic field during the scanning process, altering intensities across the image. The degree of inhomogeneity of the magnetic field during scanning strongly depends on

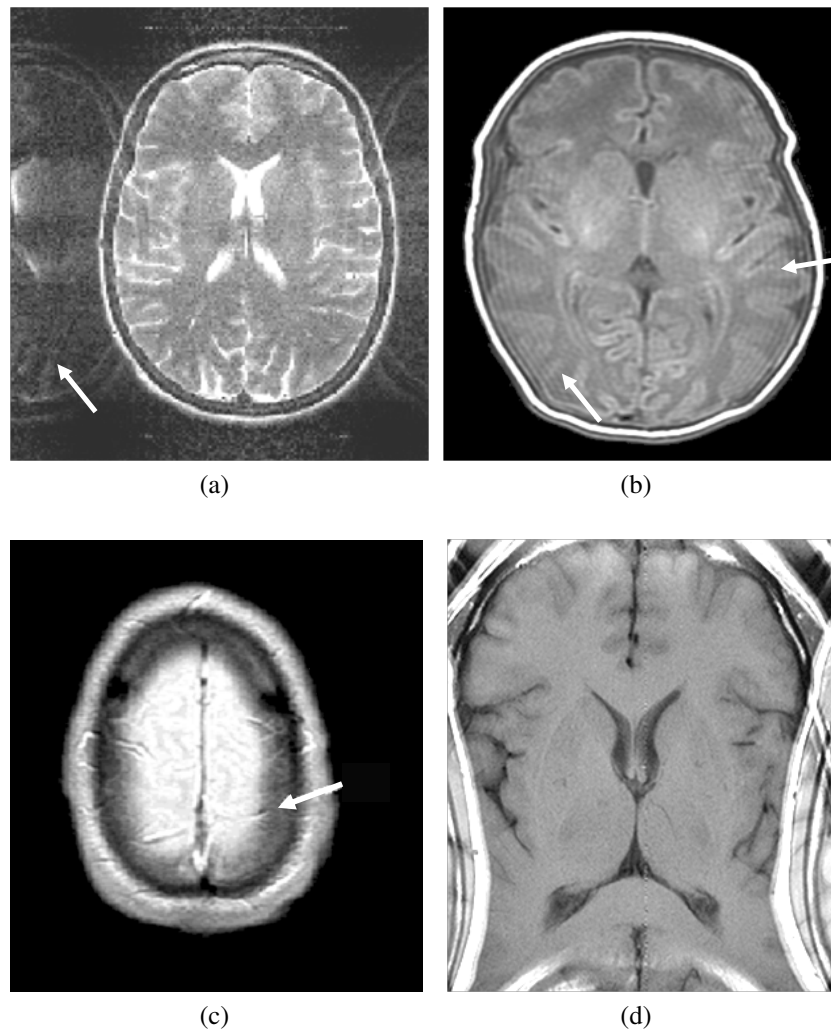


Figure 2.20: MR imaging artifacts: (a) the ghosting effect (caused by the movement of the patient in the scanner), (b) the Gibbs phenomenon (ringing), (c) the partial volume effect (PVE) and (d) the aliasing (wrap-around).

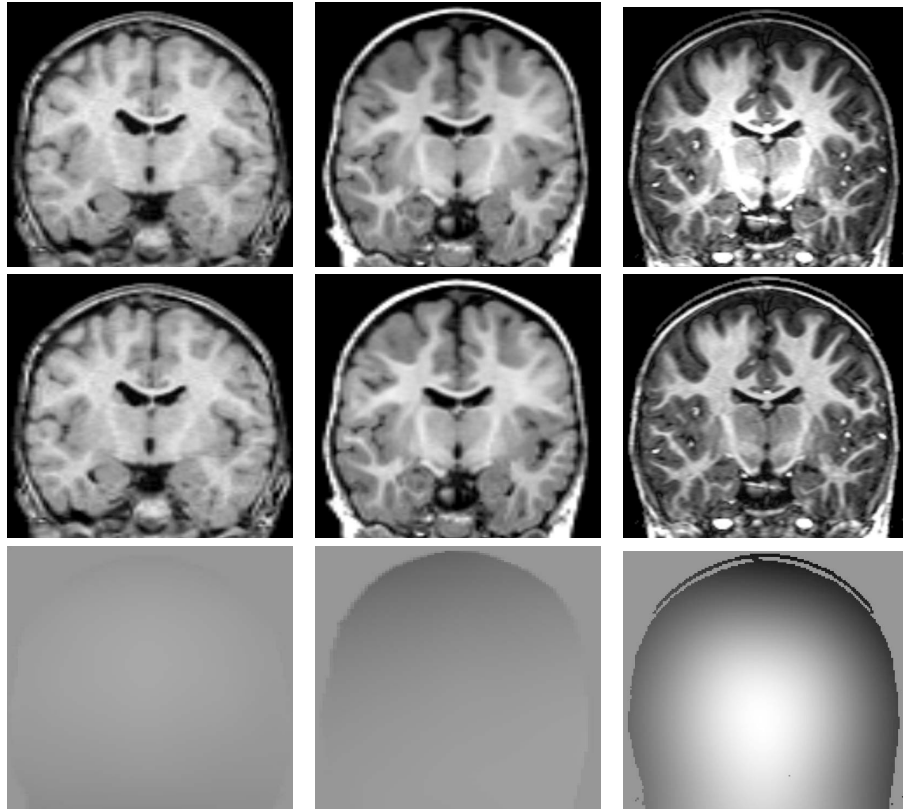


Figure 2.21: T_1 -W MRI scanned at different magnetic field strengths: (a) 0.5T with virtually no bias; (b) 1T with slightly visible bias; (c) 3T with strong bias. First row: original image; second row: corrected image; third row: bias field. From [Murgasova, 2008].

strength of the magnet used, Fig. 2.21. Data scanned at 0.5 T exhibit virtually no bias field and this artifact can be simply neglected. These days MRI is usually acquired on scanners with a magnetic field strength between 1 and 3 T producing an inhomogeneity strong enough to cause problems for the automated MRI analysis.

2.2.3.2 Neonatal brain imaging

MR imaging is an excellent technique for imaging neonates because of the absence of ionizing radiation and the superior contrast of soft tissues and resolution compared with sonography. However, there are certain differences between adult and neonatal imaging and thus, imaging neonatal brains presents set of technical and practical challenges that must be addressed to obtain optimal images [Plaisier et al., 2012].

The most obvious technical difficulty is in obtaining motion-artifact-free images, due to movement of a baby during a long MRI acquisition. This problem will decrease the image quality and often necessitate a repeat MRI to establish a diagnosis. The two main practical difficulties are due to anatomical and developmental issues. Neonates are much smaller than adults. An average term neonate weighs 3.5 kg, with brain 25% of the adult size [Kliegman et al., 2008]. With development and maturation, in addition to growth, there are changes in the appearance of many structures, such as the brain, bones (skull) and cartilage. For instance, the brain sulcation of the cortex and myelination of the white matter tracts develop rapidly in the neonatal period.

All these developmental changes influence the appearance of the available MR signal of the neonatal brain and create the limits of the scan resolution. The immature brain has higher water content than the adult brain and this is associated with a marked increase in T_1 and T_2 values. Appropriate changes in the pulse sequences are required to produce good quality images. For instance, the high water content, and lack of fatty myelin, requires an increase in echo time TE on T_2 -W imaging to around 150-160 ms to improve contrast. T_1 contrast can be flat requiring an increase in repetition time TR to around 1200 ms at 1.5 Tesla (compare this with adult brain MRI in Table 2.4).

The appearance of neonatal and mature adult brains in MRI differs significantly. For instance, if we look at T_1 -W MRI of the neonatal brain (see Fig. 2.22 top row) we can notice that the most prominent differences between the neonatal and adult brain (see Fig. 2.22 bottom row) is the reversed contrast of white matter (WM) and gray matter (GM). This is caused by the presence of unmyelinated WM and higher water content of the brain structures in neonates. Also, MRI of the neonatal brain has lower contrast-to-noise ratio and lower resolution in comparison to the adult brain. As the brain matures, the darker intensities of WM present in the MRI of the neonatal brain gradually increase, eventually exhibiting a bright intensity pattern on T_1 -W MRI. This is caused by a decrease in both T_1 and T_2 times as the water content decreases and myelin sheath forms around the WM tracts.

By the age of one year, the majority of white matter tracts are well defined (see 2.22, second row) and the tissue contrast is very similar to the contrast in the adult brain. The cortical folding has increased, resulting in a more complicated shape of WM and cortical GM than in neonates. The process of myelination is almost complete by the age of two years. However, the refined configuration of the adult brain is not attained until early adolescence [Rutherford, 2001]. As a result, WM and GM of very young children can be very difficult to distinguish in MRI, due to age and location dependent WM/GM contrast.

Even though tissue contrast is already adult-like, brain structures in young children have different shapes and sizes [Wilke et al., 2003]. Also, the smaller size of the brains structures together with the limited resolution of MRI result in an increased number of voxels containing two or more tissue classes, causing mixing of tissue intensities or partial volume effect.

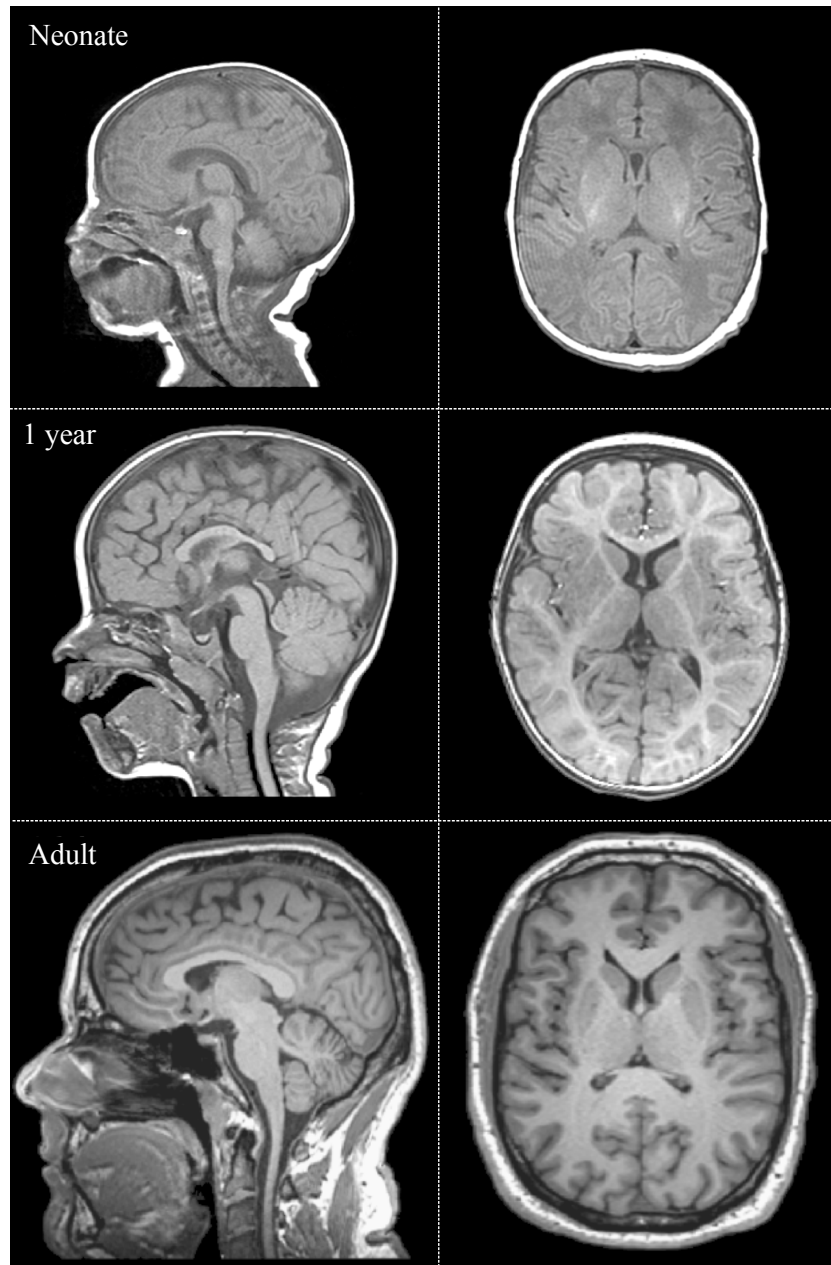


Figure 2.22: Illustration of sagittal (the first column) and axial slices (the second column) of the normal T_1 -W MRI of the human brain. The first row shows the baby's brain at birth, the second row is one year old child and the last row is the mature adult brain.

2.3 Electroencephalography - EEG

Although it was known as early as in the 19th century that living brains have electrical activity, the German psychiatrist Hans Berger was the first to record this activity in humans, in the late 1924 [Berger, 1929]. A recording of electrical signals from the brain is made by attaching the electrodes to the subject's scalp. These electrodes pick up electric signals naturally produced by the brain and send them to galvanometers (instruments that detect and measure small electric currents). The galvanometers are attached to pens, under which graph paper moves continuously. The pens trace the signals onto the graph paper. Berger's invention, commonly known as the EEG or brainwave test, is used today routinely as a non-invasive diagnostic test in neurology, psychiatry and in brain research.

Due to recent advances in EEG recording technology and rapid development of signal analysis methods, EEG has received the status of a true brain-mapping and brain-imaging method that provides spatio-temporal information regarding brain (dys)function [Michel and Murray, 2012]. In fact, EEG measures changes in the brain's electric potential field at the scalp surface. By properly sampling and correctly analyzing this electric field, EEG can provide reliable information about the neuronal activity in the brain and the temporal dynamics of this activity. However, the main drawback of EEG is its low spatial resolution. This is because of the presence of the skull layer between the brain and EEG electrodes. The skull disperses the electrical field making EEG recording relatively ineffective at differentiating specific circuit and regions in the brain.

Although many clinical EEG studies still use the EEG in its traditional way (analyzing the graphs at certain electrodes), nowadays, there is an increased interest in combined multimodal studies. For instance, EEG is increasingly used in the neuroimaging because of the increasing interest in the temporal dynamics of brain networks and compatibility of the EEG with other brain imaging techniques (e.g. MRI, fMRI and PET). The multimodal EEG-MRI studies (e.g. EEG source analysis) are important aid in the diagnosis and management of epilepsy (like focal cortical dysplasia) and other seizure disorders (asphyxia and HIE), as well as in the diagnosis of brain damage related to trauma and diseases such as strokes, tumors, encephalitis, and drug and alcohol intoxication.

2.3.1 Electrical activity of the brain

The main information processing structures in the CNS are neurons, see Fig. 2.1. At rest state neurons are electrically polarized due to an unequal distribution of Na^+ , K^+ and Cl^- ions across the cell membrane. The intracellular environment (inside the cell membrane) is negatively polarized with the respect to the extracellular environment (outside the cell membrane). This potential difference across the cell membrane is called the resting potential and is typically around -70 mV [Schaul, 1998]. If the potential difference grows (the intracellular environment is more negative), the neuron

is hyperpolarized, and if the potential difference lowers (the intracellular environment is more positive, or less negative), the neuron is depolarized.

Neurons have unique capabilities to transmit signals both within the cell (intracellular signaling) and between cells (intercellular signaling). In the intracellular signaling the cell body of a neuron communicates with its own terminals by sending electrical signals (action potentials) along an axon in the process called conduction. In the intercellular signaling the communication between neurons is achieved by releasing chemicals at the synaptic terminals in the process called neurotransmission. Electrical signals in a neuron occur due to the ions movement across the cell membrane (through the ion channels). When the intracellular environment of the neuron is depolarized beyond a critical level or threshold, an action potential is generated that proliferates along the axon until it reaches its axon terminals.

The neurotransmission begins at axon terminals where neuron transmits its electrical signal from presynaptic to postsynaptic regions using neurotransmitters (brain chemicals) to communicate with other neurons. The postsynaptic potentials alter the neuronal membrane potential by several millivolts, which lasts around 10 ms. Since every neuron has many synapses connecting to different neurons, the actual potential over a cell membrane is given by the spatial and/or temporal summation of the postsynaptic potentials. Both depolarisation (an excitatory postsynaptic potential) or hyperpolarisation (an inhibitory postsynaptic potential) is possible. If the potential is excitatory, it is more likely that an action potential will be triggered. When the potential is inhibitory, the generation of action potentials will be suppressed. This complex network of electro-chemical signals controls normal brain function.

2.3.2 EEG recording

The electro-chemical signals travel through the brain and skull, and can be recorded with EEG electrodes attached to the scalp surface. Below each electrode are many thousands of neurons. Slight changes of voltage in the axons of these neurons are called graded potentials, which can only be detected when many neurons synchronously depolarize or hyperpolarize. This occurs mainly in the brain cortex where vertically oriented large pyramidal cells are aligned and amplify each other's extracellular field, Fig. 2.23(a),(b). The currents generated by these neurons sum up in the extracellular space and are attenuated through different head layers such as the CSF, skull and scalp. After attenuation, the sum of electrical brain potentials is still large enough to be detected by EEG electrodes, see Fig. 2.23(c). For instance, when cortical neurons are simultaneously active, the sum of these potentials on the human scalp will be between 10 to 150 μV .

The process of current flow through different head tissues between the electrical sources (generators) and the recording electrode is referred to volume conduction, while the process of retrieving these electrical sources which generate the EEG is called EEG source analysis (or EEG source imaging).

In a typical set-up, EEG electrodes are placed at well-defined positions on the scalp

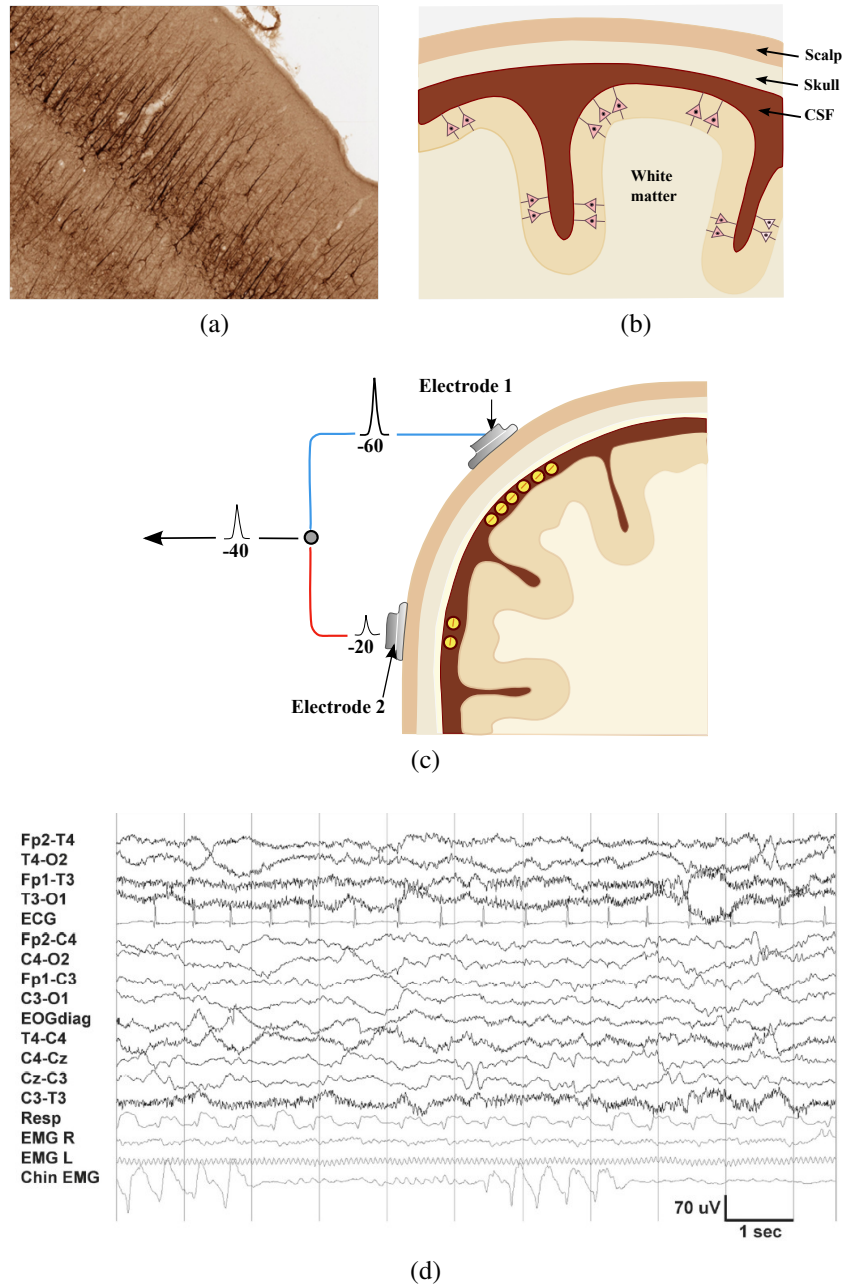


Figure 2.23: (a) An illustration of the cortical slice with the pyramidal neurons which are orthogonal to the surface. From [Hallez, 2008]. (b) A schematic picture of the alignment of the pyramidal neurons in the cortex. (c) The difference of electrical brain potentials measured by electrodes placed on the human scalp. From [De Vos, 2009] (d) An example of an EEG. Potential differences are measured between electrodes, indicated by a label. From [Perumpillichira, 2010].

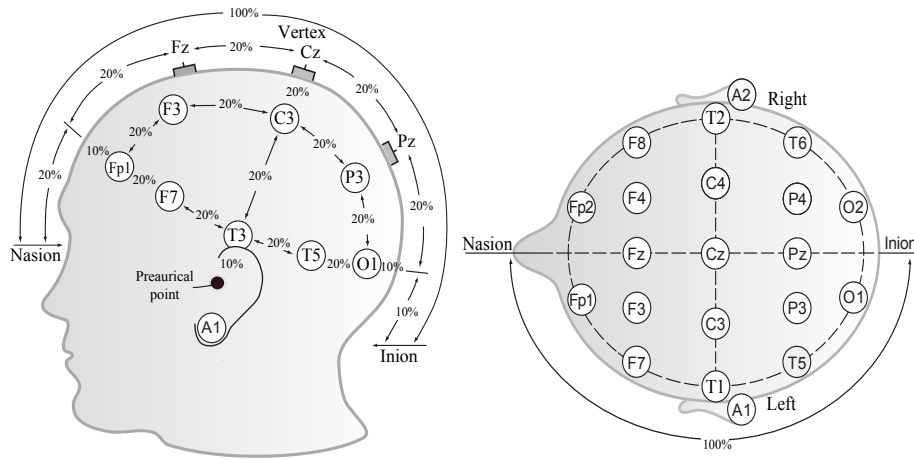


Figure 2.24: Illustration of the standard 10-20 system electrode placement with a side and a top view of the head. The standard 10-20 system uses the distances between bony landmarks (the nasion, inion and preauricular points) of the head to generate a system of lines that run across the head and intersect at intervals of 10% or 20% of their total length. Electrodes are placed at the intersections.

surface. The most common positioning of electrodes that provides a uniform coverage of the entire scalp is given by the international 10-20 system [Wang and Gotman, 2001]. The standard 10-20 system includes 19 electrodes, where each electrode has a name referring to the brain lobe or anatomical point where it is located, see Fig. 2.24. Often in practice, particularly in the neonatal intensive care unit (NICU), the electrodes are attached manually on the scalp using anatomical reference points and 10-20 system measurements. To compromise between the need to obtain high accuracy (more electrodes) and practical applicability in a NICU setting (less number of electrodes), typically 9 or up to 17 scalp electrodes are used for neonatal EEG monitoring. In adults, to avoid the manual electrode montage on the head, an electrode cap consisting of 32, 64, 128 or 256 fixed electrodes is used. However, using the same caps for neonates is challenging because of differences in head size between adults and neonates and greater variation in head geometry among neonates. Today, there are some promising solutions for this problem available in the market, like specially designed EEG head caps for neonates [Vanhatalo et al., 2008], which might have a great potential for clinical use in the near future.

Since EEG recording consists of measuring the potential differences between two electrodes as a function of time, see Fig. 2.23(c) and Fig. 2.23(d), an appropriate reference for this measurement has to be chosen. The most used EEG references are: one electrode on the top of the head such as C_z or F_z , average between two ear electrodes, average of all connected electrodes or bipolar leads between adjacent electrodes. The average reference requires high density recording (~ 128 channels) and is commonly used for visualizing widespread coherent waveforms that occur with similar phase and amplitude. The bipolar reference, where the EEG signals are obtained by subtracting

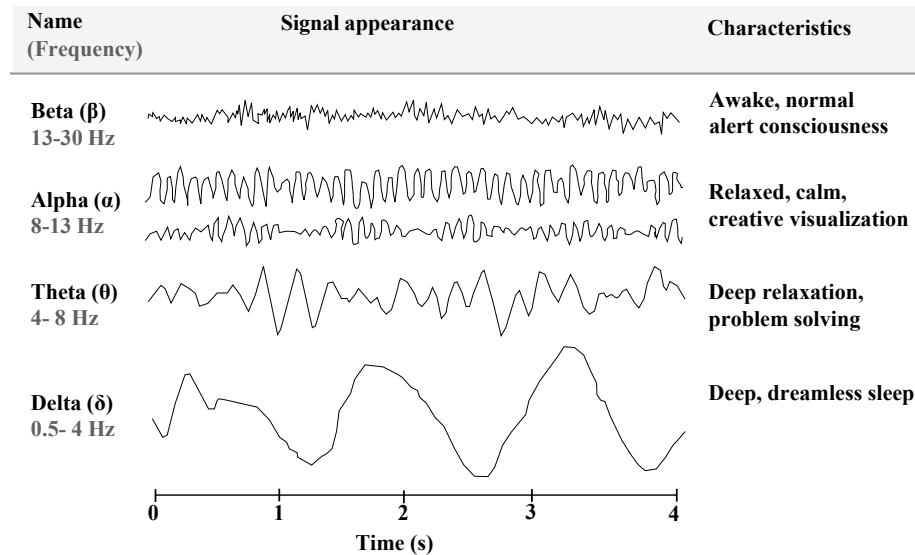


Figure 2.25: Examples of different brain traces, from bottom to top: (1) beta rhythm (13-30Hz), (2) alpha rhythm (8-13Hz), (3) theta rhythm (4-8Hz) and (4) delta rhythm (0.5-4Hz). For each brain wave, the characteristic states of consciousness are listed in the last column.

neighboring electrode signals, is commonly used for visualizing highly localized brain activity.

2.3.2.1 EEG's wave patterns

Every human being has a unique brain wave pattern, and the brain wave characteristics such as the length, height, and rate, vary in different parts of the brain being studied. The normal brain wave pattern is associated with the age (the adult EEG is different from the neonatal EEG) and the state of consciousness, like changes in a person's state of arousal (from being deeply asleep to awake and alert). Analyzing EEG recording, several brain wave patterns can be identified and the EEG signals are typically subdivided in 4 frequency f bands (delta, theta, alpha and beta), as illustrated in Fig. 2.25. Each brain wave pattern is associated with different mental and physiological processes.

Delta waves are in the frequency range from 0.5 Hz up to 4 Hz and are the slowest waves with the highest amplitude. Delta waves are dominant during unconscious states, e.g. during deep sleep, and are normally found in infants and young children. In neonates, delta waves are the most prominent in posterior regions of the brain, while in adults, they occur in frontal regions. In clinical diagnosis, delta waves can be detected with deep midline lesions, with diffuse lesions and with subcortical lesions in frontal region of the brain.

Theta waves are in the frequency range from 4 Hz to 8 Hz and are typically seen in young children. They are associated with deep relaxation, meditative and creative states. Abnormal activity occurs when there is an excess of theta waves. In clinical diagnosis, it can be seen in similar disorders as mentioned with delta waves.

The first rhythmic EEG activity that Hans Berger detected were alpha waves. Alpha waves are in the frequency range from 8 Hz to 12 Hz and are associated with relaxation, closed eyes and a light sleep. Alpha waves can be seen in the posterior regions of the brain. In clinical diagnosis, abnormal alpha waves occur in coma.

Beta waves are the high-frequency waves in the range from 12 Hz up to 30 Hz. They are prevalent during conscious and wakeful activity, such as busy thinking and active concentration, and are most evident frontally. Abnormal rhythmic beta activity is usually linked with drug effect and in patients who are anxious and alert. In the areas of cortical damage the beta activity is reduced or completely absent.

2.3.3 Advantages and limitations of EEG

From a practical point of view, EEG is a low-cost, non-invasive and portable tool to measure in real time brain function. EEG has a high temporal resolution (millisecond temporal resolution) and is able to detect fast changes in neural activity. The temporal resolution is determined by the sampling frequency and in clinical applications EEG is mostly sampled at 256 Hz.

Next to the great advantages of EEG, it is important to understand the limitations of the technique. The first EEG limitation is its low spatial resolution, which limits the amount of brain activity that can be extracted. For instance, using only visual evaluation it is feasible to localize brain activity and define brain lobes of interest, but more precise spatial localization of the brain activity is not possible. To perform the quantitative localization of the brain activity, also referred to as inverse problem or EEG source localization, research have focused on developing mathematical models for electrical sources and volume conductor. However, the source localization problem is highly ill-posed and under-determined. Ill-posed means that the inverse problem is very sensitive to noise and that the solution changes when there is a slight change in the input data. Under-determined means that a multiple number of sources within the brain volume can “fit” one EEG recording. This means that it is theoretically impossible to precisely determine the location of the EEG generator using only EEG scalp recordings. To obtain a unique solution, additional/prior assumptions about the source must be introduced. Today, several different approaches to solve inverse problem exist based on different assumptions [Michel et al., 2004, Hallez et al., 2007]. The most common approach is to assume that a limited number of dipoles generate the measured potentials on the scalp [Scherg and von Cramon, 1985], and that the electrical field generated by a group of pyramidal cells can be approximated sufficiently by a single dipole [de Munck et al., 1988, De Vos, 2009].

The second limitation is that only a portion of underlying brain electrical activity can be recorded using scalp EEG. For instance, it is more difficult to detect the electrical

activity from deep sources than near the skull [Gloor, 1985]. The electrical signals that are generated in the deep brain structures can be greatly modified by time they reach the recording electrode. This is because the voltage field decreases with the square of the distance and the electrical signals are attenuated by different brain layers between the source and the recording electrode (the volume conductor effect). Also, the skull can act as a “low-pass” spatial filter of the brain’s electrical field [DeLucci et al., 1962], where the potentials of interest can be averaged out by different brain layers. It can also happen that the electrical signal can not be recorded due to volume conduction effect and the orientation of the electrical generator (represented by a dipole) to the recording electrode [Gloor, 1985]. Dipole orientations that are “aimed” towards the electrode are better recorded.

Finally, the third and the most challenging problem is to remove EEG artifacts, which hamper the interpretation of the brain activity. All EEG artifacts can be divided in two groups: (1) patient-related or physiological artifacts and (2) hardware (machine)-related artifacts [Fisch, 1999]. Patient-related artifacts are caused by different kinds of body movements (e.g. muscle activity, respiration, movement of the head, eye balls or scalp), skin resistance changes (e.g. due to perspiration) and moving electrical potentials within the body (e.g. heart muscle contraction). Hardware (machine)-related artifacts are caused by electrical malfunctioning of the EEG recording system (e.g. disconnected electrode, malfunctioning of the cables or amplifiers). Many signal processing methods have been developed to remove different EEG artifacts [Jung et al., 2000], especially eye and muscle artifacts which are the most common artifacts in EEG recordings [Joyce et al., 2004, De Vos et al., 2010].

2.3.4 Applications of EEG analysis

EEG is extensively used in many clinical and research applications to study normal and abnormal functioning of the brain. In clinical practice, EEG is typically used to monitor and diagnose neurological disorders, to evaluate the patients’ status in intensive care units (for both adults and neonates), to measure the brain activity after a severe head injuries, to identify cause of sleep disorders and to analyze the changes in behavior. In research applications EEG is used to assess cognitive functions of the brain and to improve our understanding the brain development and maturation.

The most intensively studied application of EEG analysis is in epilepsy, where EEG is still the most important method to determine the epileptic syndrome. In epilepsy the synchronous electrical activity of a focal or large brain area is abnormal and the typical clinical manifestation is an epileptic seizure. The EEG recording during a seizure is called ictal EEG and readings display rhythmic activity with a frequency of 5 to 6 Hz. The signal amplitude during ictal EEG is usually higher than when no seizure occurs. The EEG measured between seizures is called interictal EEG and typically consists of a spike (a fast electrical event) with a time duration of 20 to 70 ms, a sharp wave with a time duration of 70 to 200 ms and a spike-wave-complex, consisting of a spike followed by a wave. In focal epilepsy spikes are detected in only one hemisphere of the brain, while in multi-focal epilepsy spikes spread over both hemispheres.

By visually investigating the ictal or interictal EEG, it is possible to perform a qualitative localization of the electrical source. It is also possible to perform a quantitative localization using EEG source imaging, when a volume conductor model and an electrical source model are introduced. A focal electrical source may be represented by a current dipole with three parameters: two orientation parameters and one magnitude parameter. EEG dipole source analysis aims at retrieving the dipole which best fits the measured EEG. An increasing number of studies demonstrated that EEG source imaging is a powerful tool to non-invasively localize the epileptic focus [Kaiboriboon et al., 2012].

A relatively new field is EEG monitoring of neonates with neurologic disorders (e.g. asphyxia, HIE). It is an important field as seizures occur in 1 up to 3.5 per 1000 births [Volpe, 2008]. Neonatal EEG gives valuable information about brain function and maturation, helps detecting seizures, and complements other clinical examinations. Since some neonatal seizures are subclinical, without clinical symptoms, it is extremely important to monitor them with a full EEG. The expertise needed to interpret neonatal EEGs is not available around the clock in the Neonatal Intensive Care Unit (NICU). Also, EEG monitoring is highly labor intensive as it generates large amounts of data. Because of these reasons, automated analysis and seizure detection methods are needed to assist doctors in reviewing the EEG [Deburchgraeve et al., 2008, Perumpillichira, 2010].

Diagnostic brain-wave patterns of other disorders vary greatly. In the case of severe brain injury, EEG typically shows overall slowing of the brain activity and excess of theta waves (4 to 8 cycles per second). However, a trained medical expert should interpret EEG results in the context of the patient's medical history and other medical test results.

Further readings on the EEG (including EEG source localization and neonatal EEG) can be found in [Perumpillichira, 2010, Restak, 1995, Hallez, 2008, De Vos, 2009].

2.4 Conclusion

Multimodal and non-invasive brain imaging is one of the fastest growing multidisciplinary activity. In the last two decades, enormous progress in assessing brain injury in both adults and neonates has been made using MRI, while EEG has been considered as the gold standard in the diagnosis of neurological dysfunction. By combining both EEG and MRI in multimodal imaging of the brain, important aid in the diagnosis and management of neurological dysfunction of the brain and neonatal seizure phenomena has been achieved.

In this chapter the important background of the human brain anatomy, MR imaging of the brain, and MRI and EEG brain data analysis are explained. Firstly, we introduced the reader with the human brain anatomy including the developmental phases of the brain from fetus till adulthood. Then, we explained the causes and symptoms of the two brain injuries, birth asphyxia (in neonates) and epilepsy with FCD lesions

(in adults). These two brain injuries are the main clinical applications of the thesis. Secondly, we described how the MR images are formed, what they show, how they differ, how we can analyze them and what are the challenges of the brain MRI analysis. Since MRI analysis of the neonatal and adult brain is the central subject of the thesis, we also highlighted and illustrated the differences between neonatal and adult MRI. Finally, we explain the essence of EEG brain data analysis that is necessary for understanding multimodal MRI-EEG brain imaging. We explain electrical brain activity, potentials and limitations of EEG and clinical applications of spatial EEG analysis.

3

Brain MRI segmentation

You don't understand anything unless you understand there are at least 3 ways.
– Marvin Minsky

Image segmentation is an important task in medical image analysis and is often the first and the most critical step in many clinical applications. In brain MRI analysis, image segmentation is commonly used for measuring and visualising the brain's anatomical structures, for analyzing brain changes, for delineating pathological regions and for surgical planing and image-guided interventions. In the last few decades, various segmentation techniques of different accuracy and degree of complexity have been developed and reported in the literature.

In this chapter we review the most popular methods commonly used for MRI brain tissue segmentation. We highlight differences between them and discuss their capabilities, advantages and limitation. We first introduce the basic concepts of image segmentation. Then, we explain different MRI preprocessing steps including image registration, bias field correction and removal of non-brain tissue. Finally, after reviewing different brain MRI segmentation methods, we discuss the validation problem in brain MRI segmentation.

However, despite intensive research, brain MRI segmentation still remains a challenging problem with no unique and general solution and there is a continuous need for developing newer and better segmentation methods. Thus, in Chapter 4, we propose a modification of the standard graph cuts algorithm for more accurate 3D brain MRI segmentation.

3.1 Basic concepts

In the following text we will introduce the basic concepts necessary for understanding brain MRI segmentation. This includes defining 2D and 3D images over a lattice, describing an image segmentation problem and image features, and introducing MRI intensity distributions of the brain tissue.

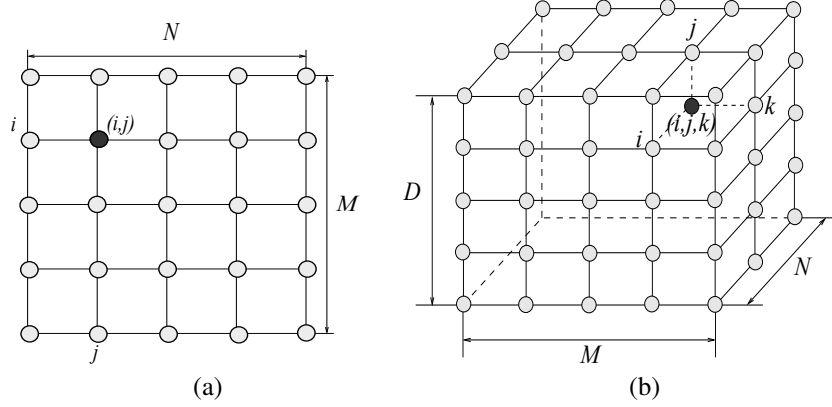


Figure 3.1: Illustration of lattice nodes in 2D and 3D space. (a) 2D lattice with dimensions $M \times N$, where each node is specified with its coordinates (i, j) . (b) 3D lattice with dimensions $M \times N \times D$, where each node is specified with its coordinates (i, j, k) .

3.1.1 2D and 3D images

An image can be defined as a function $I(i, j)$ in 2D space or $I(i, j, k)$ in 3D space, where $i = 0, \dots, M - 1, j = 1, \dots, N - 1$ and $k = 0, \dots, D - 1$ denote spatial coordinates. The values (or amplitudes) of the functions $I(i, j)$ and $I(i, j, k)$ are intensity values and are typically represented by a logical value 0 or 1 for binary images, a gray value $\{0, \dots, 255\}$ for gray scale images, or a color vector for color images. In MRI of the brain, image elements are represented by gray intensity values, see Fig. 3.3. Every image consists of a finite set of image elements called pixels in 2D space or voxels in 3D space. Each image element is uniquely specified by its intensity value and its coordinates (i, j) for pixels and (i, j, k) for voxels, where i is the image row number, j is the image column number and k is the slice number in a volumetric stack.

To describe image data in space a finite rectangular or square point lattice \mathcal{P} is used. A lattice \mathcal{P} is defined as a discrete set of m nodes (or sites) $\mathcal{P} = \{1, \dots, m\}$, where $1, \dots, m$ are indices. Each lattice node is a point in the Euclidean space and represent an image pixel in 2D or an image voxel in 3D. A rectangular lattice for a 2D image of size $M \times N$ can be denoted as $\mathcal{P} = \{(i, j) | 1 \leq i \leq M, 1 \leq j \leq N\}$. In general, the lattice is represented with an orthogonal grid with nodes lying at the intersections of the grid lines as shown in Fig. 3.1. However, to represent image data, an alternative representation of the lattice is used where a node is depicted as a square for an image pixel or a cube for an image voxel. This is illustrated in Fig. 3.2 and Fig. 3.3.

For simplicity of notation, in the following text an image is represented with I and an image pixel (i, j) is represented by a single index $i = 1, \dots, m$ (assuming raster scanning order) where $m = MN$. The dimensionality of an image I will be clear from the context.

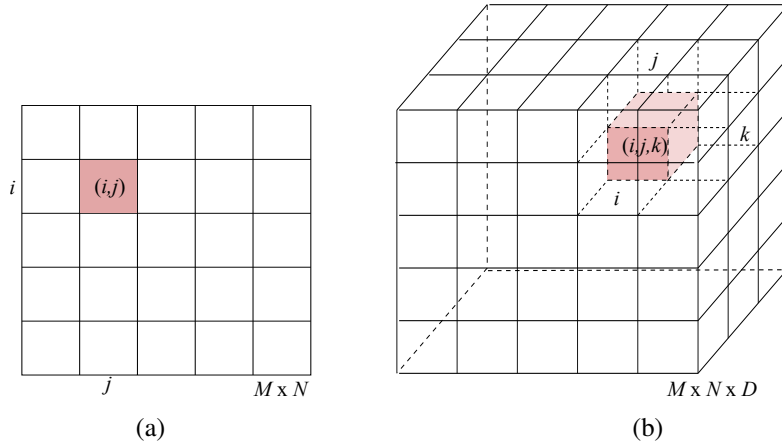


Figure 3.2: Illustration of image elements in 2D and 3D space. (a) In 2D space image elements (pixels) are represented with a lattice nodes depicted as a square. (b) In 3D space image elements (voxels) are represented with a lattice nodes depicted as a cube.

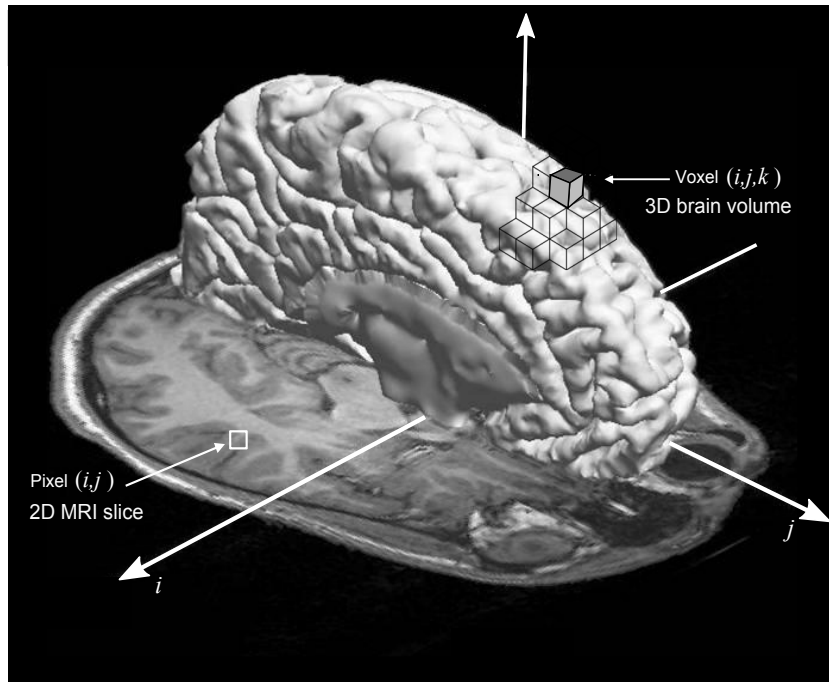


Figure 3.3: Illustration of image elements in the MRI of the brain. An image pixel (i,j) is represented with the square in the 2D MRI slice and an image voxels (x,y,z) is represented as the cube in 3D space.

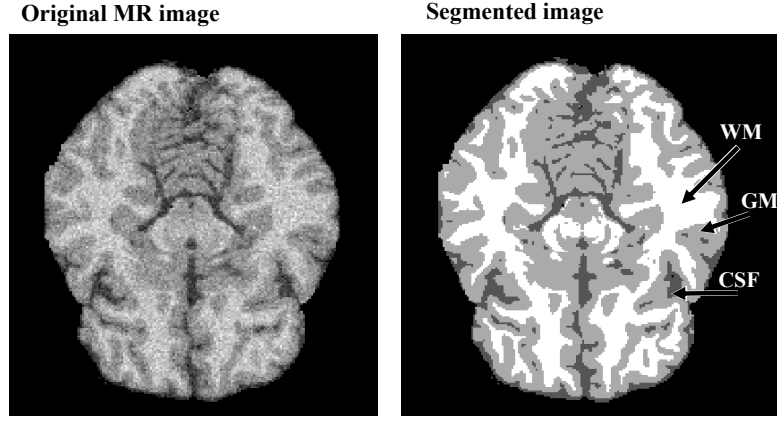


Figure 3.4: An example of the brain MRI segmentation with an original MR image (on the left) and segmented image with three labels: WM, GM and CSF (on the right).

3.1.2 Image segmentation

The goal of image segmentation is to divide an image into a set of semantically meaningful, homogeneous and non-overlapping regions of similar attributes such as intensity, depth, color or texture. The segmentation result is either an image of labels identifying each homogeneous region, or a set of contours which describe the region boundaries. The labeling problem is to assign a label from the set of labels \mathcal{L} to each of the nodes in \mathcal{P} . Since in our work we use pixel/voxel intensities for MR image segmentation, we consider a discrete set of labels $\mathcal{L} = \{1, \dots, L\}$ and the nodes with similar intensities are assigned the same unique label.

Image segmentation can be performed on 2D images, sequences of 2D images or 3D volumetric imagery. Most of the image segmentation research has focused on 2D images. If the data is defined in 3D space, such as obtained from a series of MRI images, then typically, each image “slice” is segmented individually. However, since important anatomical information relevant for segmentation of volumetric imagery also exists in 3D space, the development of integrated 3D segmentation algorithms is desired.

Fundamental components of structural brain MRI analysis include the classification of MRI data into specific tissue types and the identification and description of specific anatomical structures. Classification means to assign to each element in the image a tissue class, where the classes are defined in advance. The problems of segmentation and classification are interlinked because segmentation implies a classification, while a classifier implicitly segments an image. In the case of brain MRI, image elements are typically classified into three main tissue types: white matter (WM), gray matter (GM) and cerebrospinal fluid (CSF), see Fig. 3.4. The segmentation results are further used in different applications such as for analyzing anatomical structures, for studying pathological regions, for surgical planing and for visualization, see Fig. 3.5.

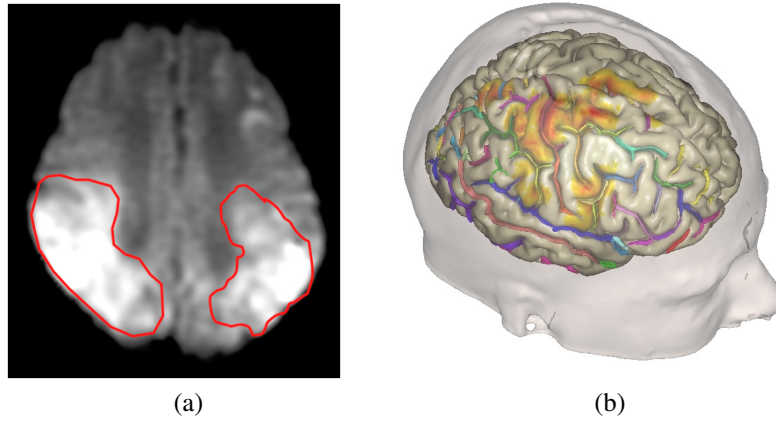


Figure 3.5: Segmentation results. (a) Segmentation of pathological regions and (b) 3D visualization of the cortex anatomy (from [BrainVisa, 2012]).

3.1.3 Image Features

Image features represent distinctive characteristics (signatures) of an object or an image structure to be segmented. Features rely on numerical measurements, including quantitative visual appearance and shape descriptors, that can help to discriminate between the structures of interest and their background. The outcome of image segmentation highly depends on appropriate feature selection (choosing the most relevant features) and accurate feature extraction.

The visual appearance of an object of interest is typically associated with its pixel or voxel intensities (gray values in brain MRI) and spatial interaction between intensities (intensity co-occurrence) in an image. Image segmentation based on individual pixel/voxel intensities is feasible only when intensities of an object of interest and its background differ to a large extent. Then, the complete object or the majority of its pixels/voxels can be separated from the background by simply comparing the intensity values to the threshold (the intensity value that clearly separates the object from the background). The threshold is derived from the overall intensity distribution of the image.

In general, individual intensities are not sufficient for accurate image segmentation and more powerful discriminative features have to be used. This includes spatial interaction between intensities. For instance, the appearance of tumour lesion in brain MRI can be associated with spatial patterns of local pixel/voxel intensity variations or empirical probability distributions of intensity co-occurrences. In the spatial interaction models each intensity depends on a subset of the neighboring intensities, see Fig. 3.6. The most popular models that can capture local spatial interactions between pixels/voxels intensities are Markov Random Field (MRF) models [Li, 1995], which will be explained in Section 3.4.3 and will be used in the graph cuts segmentation algorithm described in Chapter 4.

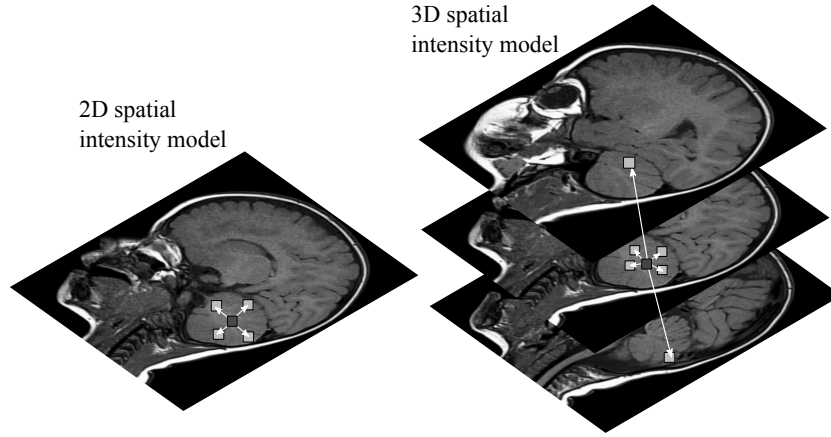


Figure 3.6: Illustration of 2D (on the left) and 3D (on the right) spatial interactions between neighboring pixel/voxel intensities.

In the presence of noise and under poor image resolution, appearance features (pixel/voxel intensities and their spatial interaction) may fail to identify an object of interest in an image. In this case, the segmentation performance can be improved by incorporating shape features such as probabilistic prior shape models, which have been extensively used in medical image segmentation [Yan et al., 2010, Ecabert et al., 2008, Yang and Duncan, 2004, Tao et al., 2002, Duta and Sonka, 1998]. The probabilistic prior shape models specify an average shape and variation of an object of interest and are typically estimated from a population of co-aligned images of the object (training data sets) [Davies et al., 2008].

One of the most popular features for image segmentation are edges. Edges refer to boundaries of an object surface where the intensities change sharply [Gonzalez and Woods, 2008]. Such changes are typically detected by thresholding the first- and second-order spatial derivatives of the intensities (the intensity gradient and Laplacian). However, edges detected in this way are sensitive to image noise [Rogowska, 2000] and often require image smoothing as a preprocessing step [Canny, 1986, Marr and Hildreth, 1980].

Another more robust method for edge detected is the phase congruency method [Kovesi, 1999, Kovesi, 2002], which is a frequency-based method for feature detection. This feature detection method, using local phase and energy, is based on a plausible model of how mammals detect edges suggested by Morrone and Owens [Morrone and Owens, 1987] and successfully explains the psychophysical effect of human feature perception. Instead of searching the pixels/voxels in the image with sharp intensity changes, features such as step edges, lines and corners are detected at points where the Fourier components of the image are maximally in phase (local maximal congruency in the phase values). In our work we use the phase congruency feature detection method to improve image segmentation in Chapter 5.

3.1.4 Intensity distribution in brain MRI

The intensity of brain tissue is one of the most important features for brain MRI segmentation. However, when intensity values are corrupted with MRI artifacts such as image noise, partial volume effect (PVE) and bias field effect (see Section 2.2.3.1), intensity-based segmentation algorithms will lead to wrong results. Thus, to obtain relevant and accurate segmentation results, very often several preprocessing steps are necessary to prepare MRI data. For instance, it is necessary to remove background voxels, extract brain tissue, perform image registration for multimodal segmentation and remove the bias field effect, see Fig. 3.7.

In the case when the bias field, non-brain structures (e.g. the skull and the scalp) and background voxels are removed, the histogram of the adult brain MRI has three main peaks corresponding to the three main tissue classes, see Fig. 3.9(a). In the healthy adult brain, the intensity variation within tissue is small and the intensities inside the brain can be considered to be a piecewise constant intensity function, corrupted with noise and PVE. The PVE describes the loss of small tissue regions due to the limited resolution of the imaging system. It means that one pixel/voxel lie in the interface between two (or more) classes and is a mix of different tissues. This happens because the resolution of the MRI scanner is finite.

To understand intensity distribution in brain MRI, it is important to remember that MRI acquisition is based on acquiring complex k -space data and an MR image is then calculated as the magnitude of the Fourier transform of the k -space data, see Section 2.2.2.3. It has been shown that the noise in the magnitude images is governed by a Rician distribution, based on the assumption that the noise on the real and imaginary channels is Gaussian [Gudbjartsson and Patz, 1995]. The probability density function for a Rician distribution is defined as:

$$f_{\text{Rice}}(x) = \frac{x}{\sigma^2} \exp\left(-\frac{(x^2 + \nu^2)}{2\sigma^2}\right) I_0\left(\frac{x\nu}{\sigma^2}\right), \quad (3.1)$$

where x is the measured pixel/voxel intensity, ν is the image pixel/voxel intensity in the absence of noise, σ is the standard deviation of the Gaussian noise in the real and the imaginary images and I_0 is the zero-order modified Bessel function of the first kind. The Rician probability density function (PDF) is plotted in Fig. 3.8(a) for several values of the signal-to-noise ratio (SNR), where the SNR is defined as ν/σ (the power ratio between the signal and the background noise).

A special case of the Rician distribution is in image regions where only noise is present and $\text{SNR} = \nu/\sigma = 0$ (e.g. in the dark background areas of an MRI where no NMR signal is present). This special case of the Rician distribution where $\nu = 0$ and $I_0 = 1$ is also known as the Rayleigh distribution:

$$f_{\text{Rayleigh}}(x) = \frac{x}{\sigma^2} \exp\left(-\frac{x^2}{2\sigma^2}\right). \quad (3.2)$$

In the image regions where the NMR signal is present and $\text{SNR} \geq 3$, the noise distribution approximates a Gaussian distribution, see Fig. 3.8. Thus, the problem of

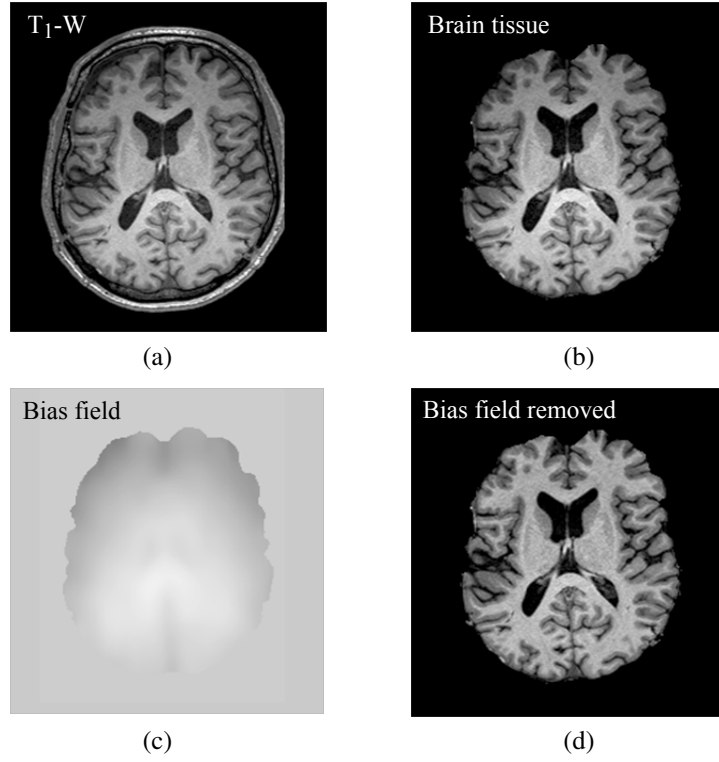


Figure 3.7: Preprocessing steps: (a) the original T_1 -W MR image of the adult brain; (b) the brain tissue image after removing non-brain structures; (c) the bias field ; (d) the brain tissue image after bias field correction.

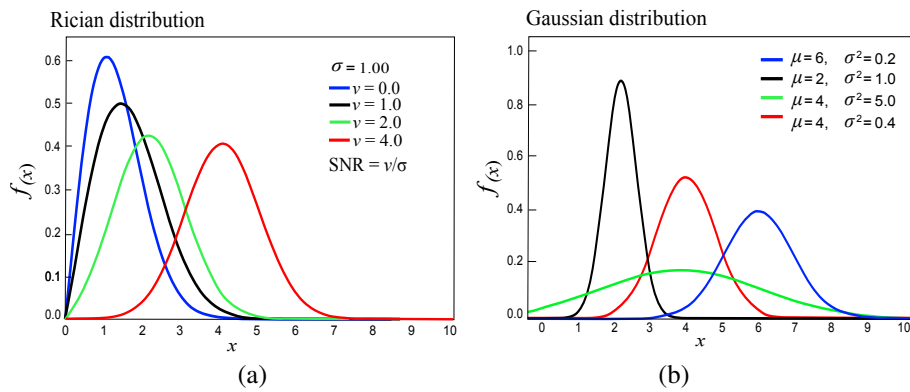


Figure 3.8: (a) The PDF for the Rician distribution. (b) The PDF for the Gaussian distribution.

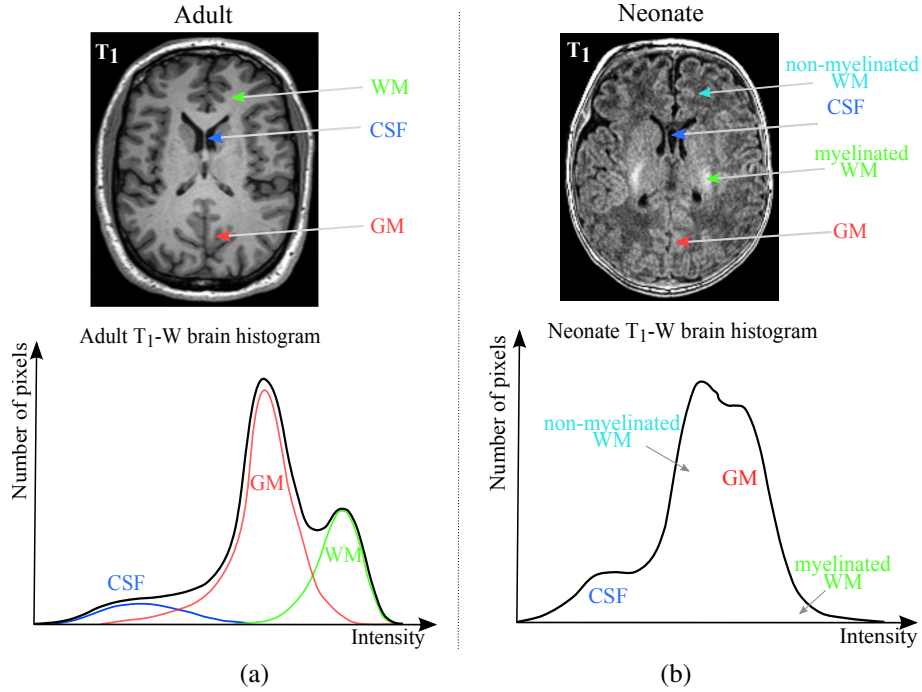


Figure 3.9: (a) Histogram of a bias-corrected T₁-W MRI of an adult brain. Histograms of the tissue classes are based on manual segmentation and distributions slightly differ from Gaussian due to partial volume effect. (b) Histogram of a 1.5 T T₁-W MRI of a neonatal brain. The difference between the neonatal and the adult brain histogram is the existence of the myelinated and non-myelinated WM in neonates, which are separated with GM intensities. Since non-myelinated WM is more dominant than myelinated WM, T₁-W MRI shows an inverted WM/GM intensities in neonates in comparison to adults.

Rician noise in the brain MRI is often simplified in practice by assuming the Gaussian distribution for the noise:

$$f_{\text{Gauss}}(x) = \frac{1}{\sigma\sqrt{2\pi}} \exp\left(-\frac{(x-\mu)^2}{2\sigma^2}\right), \quad (3.3)$$

where x , σ and μ are the intensity, the standard deviation and the mean value respectively. Due to this approximation, the histogram of a bias-corrected brain MRI in the presence of noise can be described with a Gaussian mixture model (GMM), where each tissue class (WM, GM and CSF) is modeled by a Gaussian distribution. However, in the presence of partial volume effects the tissue intensity distributions slightly diverge from a Gaussian distribution, as can be seen from the histogram in Fig. 3.9(a) where histograms of the tissue classes are based on manual segmentation.

The MRI intensity distribution of the neonatal brain is more complex because the intensity variability within-tissue cannot be neglected due to the process of myelination.

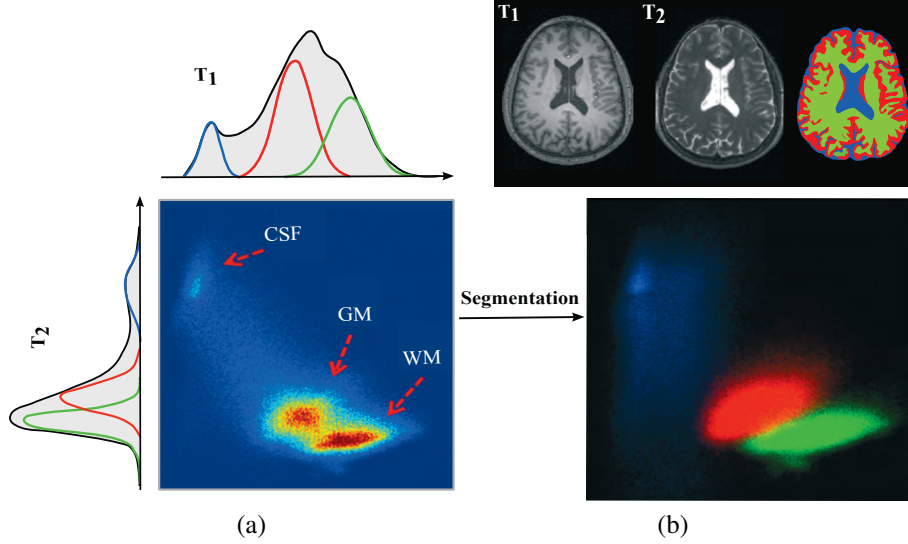


Figure 3.10: (a) Joint 2D intensity histogram of T_1 -W and T_2 -W MRI of the adult brain. The associated 1D histograms of each MRI modality are plotted on the left and top. Both individual histograms consist of three overlapped Gaussian distributions that approximate the expected tissue distribution of GM, WM and CSF. (b) The scatter plot of the tissue intensities after applying tissue segmentation. The horizontal axis represents T_1 -W intensities and the vertical axis represents T_2 -W intensities. The red cloud corresponds to GM, the green to WM, and the blue to CSF.

The histogram of 1.5 T T_1 -W MRI of the neonatal brain is shown in Fig. 3.9(b). The difference between the neonatal and the adult brain histogram is the existence of the myelinated and non-myelinated WM in neonates, which are separated with GM intensities. Since non-myelinated WM is more dominant than myelinated WM, T_1 -W MRI shows an inverted WM/GM intensities in neonates in comparison to adults.

3.1.4.1 T_1 -W and T_2 -W intensity distribution

It can be noted from the 1D histogram of the bias-corrected T_1 -W MRI of an adult brain in Fig. 3.9(a) that there is an overlap between different tissue classes. Also, it can be seen that an overlap between WM and GM tissue is higher than between GM and CSF. This overlap between the class distributions can cause ambiguities in the decision boundaries when intensity-based segmentation methods are used [Fischl et al., 2002]. However, many researchers showed that adding additional MRI sequences with different contrast properties (e.g. T_2 -W MRI, Proton Density MRI) can improve intensity-based segmentation and help separate the class distributions [Maillard et al., 2008, Mayer and Greenspan, 2009, Traynora et al., 2011]. Therefore, to improve the brain MRI segmentation, we developed a new fuzzy clustering method that incorpo-

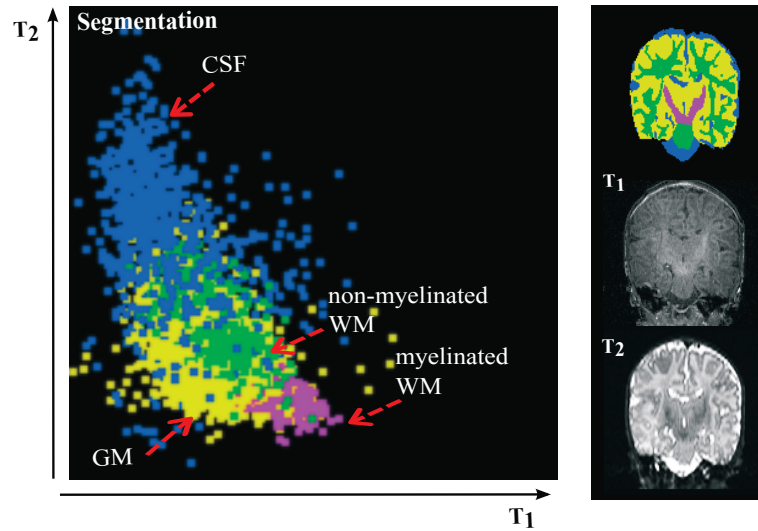


Figure 3.11: The scatter plot of the tissue intensities, including T_1 -W and T_2 -W MRI of the neonatal brain, after manual segmentation. Blue is cerebrospinal fluid, yellow is gray matter, purple is myelinated white matter and green is non-myelinated white matter. The horizontal axis represents T_1 -W intensities and the vertical axis represents T_2 -W intensities. As can be seen from the scatter plot, there is a significant overlap between the intensities of different tissues, and there are ambiguities in the decision boundaries. From [Prastawa, 2007].

rates both T_1 -W and T_2 -W intensity information [Despotovic et al., 2010c]. This method is described in Chapter 5 and is used in Chapter 6 for the neonatal brain segmentation.

The joint 2D intensity histogram of T_1 -W and T_2 -W MRI of the adult brain is shown in Fig. 3.10(a). The shape of the intensity distributions of tissue classes depends on the image quality (the presence of noise, PVE, etc.) and the shape of the classified data depends on the applied segmentation method. In the example in Fig. 3.10(a), there is a small overlap among classes due to the good quality MRI. Thus, the standard k-means clustering method is used to segment the brain tissue probability maps (see 3.3.2.4) and the final clusters are indicated with different colors in the scatter plot of T_1 -W and T_2 -W MRI in Fig. 3.10(b). In general, when MRI artifacts are present and there is a significant overlap among tissue classes, the spatial information of the brain tissue is required to disambiguate the classification problem.

The scatter plot of the tissue intensities including T_1 -W and T_2 -W MRI of the neonatal brain is shown in Fig. 3.11. The brain tissue is manually segmented in four classes: GM, CSF, myelinated WM and non-myelinated WM. In comparison to the scatter plot of the adult brain tissue intensities, the scatter plot in neonates has a significant overlap between the intensities of different tissues, and there are ambiguities in the decision boundaries.

3.2 Preprocessing

After MRI acquisition several preprocessing steps are necessary to prepare the images for segmentation, see Fig. 3.7. The most important steps include MRI bias field correction, image registration (in the case of multimodal image analysis) and removal of non-brain tissue (also called a brain extraction).

3.2.1 Bias field correction

The bias field, also called the intensity inhomogeneity, is a low-frequency spatially varying MRI artifact causing a smooth signal intensity variation within tissue of the same physical properties, see Fig. 2.21 and Fig. 3.7. The bias field arises from spatial inhomogeneity of the magnetic field, variations in the sensitivity of the reception coil and the interaction between the magnetic field and the human body [Collins et al., 2005, Sled et al., 1998]. The bias field is dependent of the strength of the magnetic field. When MR images are scanned at 0.5 T, the bias field is almost invisible and can be neglected. However, when MR images are acquired with modern high-field MR scanners with a magnetic field strength 1.5 T, 3 T or higher, the bias field is strong enough to cause problems and considerably affect MRI analysis. In practice, trained medical experts can make visual MRI analysis to certain levels of intensity inhomogeneity (10%-30%) [Sled et al., 1998]. In contrast, the performance of automatic MRI analysis and intensity-based segmentation methods decreases greatly in the presence of the bias field, see Fig. 3.12. This is because most of the segmentation algorithms assume intensity homogeneity within each class. Therefore, the correction of the bias field is an important step for the efficient segmentation and registration of brain MRI.

The bias field is typically modeled as low-frequency multiplicative field [Lewis and Fox, 2004, Sled et al., 1998]. Suppose that we place all image elements $I(i, j, k)$, $i = 0, \dots, M - 1$, $j = 0, \dots, N - 1$ and $k = 0, \dots, D - 1$ into an $m \times 1$ column vector $\mathbf{x} = (x_1, \dots, x_m)$, where x_i , $i = 1, \dots, m$ represents the observed intensity of the i -th voxel and $m = MND$ is the total number of image elements. The degradation effect of each image voxel x_i can be expressed as:

$$x_i = x_i^l b_i, \quad i = 1, \dots, MND \quad (3.4)$$

where x_i^l is an ideal intensity of the i -th voxel and b_i is an unknown smoothly varying bias field. The problem of eliminating the bias field is the task of estimating b_i .

If the intensities of MRI are logarithmically transformed, the multiplicative bias field becomes an additive bias field as follows:

$$\log(x_i) = \log(x_i^l) + \log(b_i). \quad (3.5)$$

This simplified multiplicative model is used in most state-of-the-art bias correction methods to represent the bias field [Sled et al., 1998, Shattuck et al., 2001, Lewis and Fox, 2004]. However, in reality there are certain limitations to the correctness

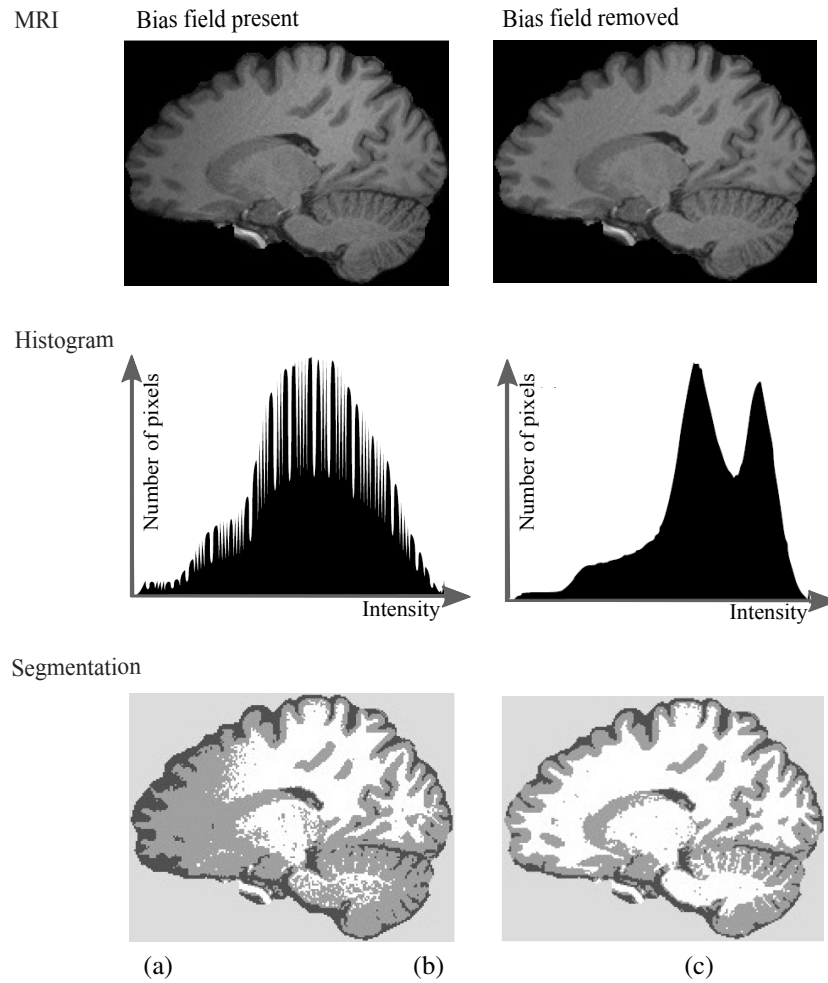


Figure 3.12: Influence of the bias field on brain MRI segmentation. (a) An example of the sagittal brain MRI slice with bias field is shown in the top of the figure. The image histogram is shown in the middle and the three label segmentation in the bottom. (b) The bias corrected MRI slice is shown in the top, the corresponding histogram in the middle and three label segmentation in the bottom.

of this model. Even though the model is consistent with the variations arising from the sensitivity of the receiver coil, the relationship between the measured and true intensities in MRI is more complicated. This is due to non-uniformity of the induced currents and spatial inhomogeneity of the excitation field, which depends on the geometry and electromagnetic properties of the subject as well as the coil polarization and pulse sequence [Sled et al., 1998]. In spite of these difficulties, the multiplicative low-frequency model is successfully used in practice to model the intensity inhomogeneity in brain MRI.

In the literature, various methods have been proposed to correct the bias field in MRI. One of the earliest methods proposed to correct the bias field are based on the manual labeling of the brain tissue voxels, which are then used to reconstruct the bias field in form of a parametric surface. The main disadvantage of this surface fitting method is the need for manual interaction. The bias field can be also estimated and corrected by using a low-pass filtering [Cohen et al., 2000], but this approach can introduce additional artifacts in the image because it also removes the low-frequency component of the true image data. Both the surface fitting method and the low-pass method can be improved and made fully automatic if they are coupled with automatic segmentation of the brain [Wells III et al., 1996b, Van Leemput et al., 1999]. Other approaches for the bias field correction include minimizing the image entropy [Mangin, 2000], fitting the histogram of the local neighbourhood to global histogram of the image [Shattuck et al., 2001], maximizing the high-frequency content of the image [Sled et al., 1998] and using a registered template image [Lewis and Fox, 2004]. Image templates and probabilistic atlases are explained later in the Section 3.2.2.2.

In this thesis we use the non-parametric bias correction method (also called the N3 method - Non-parametric Non-uniform Normalization), which is developed by Sled et al. [Sled et al., 1998]. They tested the method on both real and simulated MR data and showed that the accuracy of brain tissue classification and cortical surface extraction is significantly improved using N3 method as a preprocessing step.

3.2.2 Image registration

Image registration is the process of overlaying (spatially aligning) two or more images of the same content taken at different times, from different viewpoints, and/or by different sensors. Registration is required in medical image analysis for obtaining more complete information about the patient's health when using multimodal images (e.g. MRI, CT, PET, SPECT) and for treatment verification by comparison of pre- and post-intervention images. In medical image registration the term co-registration is used for intra-subject registration (the alignment multimodal images of the same subject), re-alignment is used for motion correction within the same subject, and normalization is used for inter-subject registration when several population groups are studied. Three examples of image registration are shown in Fig. 3.13.

Image registration involves finding the transformation between images so that corresponding image features are spatially aligned. The spatial alignment is typically



Figure 3.13: Three examples of image registration. (a) 3D fusion of a skin and a skull model derived from MRI. (b) Fusion of MR and CT image of the brain. (c) Fusion of 3D MRI and PET brain volumes. From [Vansteenkiste, 2007].

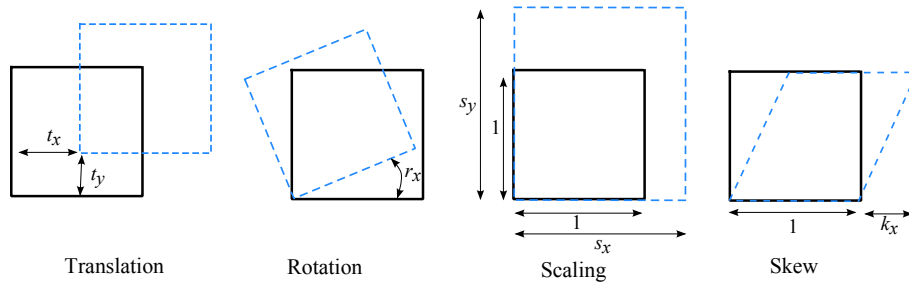


Figure 3.14: Illustration of affine 2D transformation including translation, rotation, scale and skew of a regular square. The solid line square corresponds to the original shape and the dashed line square is the target square.

initialized using rigid or affine transformation [Hajnal et al., 2001]. A rigid transformation is a 6-parameter transformation composed of translation and rotation. If scaling and skewing are allowed, we obtain a 12-parameter affine transformation, see Fig. 3.14. A rigid registration is sufficient for intra-subject registration if the object of interest does not deform. This is a reasonable assumption for images of the brain if these are acquired at the same stage of brain development. However, if the task is to match images belonging to either different subjects (inter-subject registration) or the same subject at different stages of brain development (e.g. growth in children, changes related to ageing, or atrophy due to disease), a non-rigid registration of the images is required to obtain satisfactory results. The non-rigid registration algorithms are typically based either on physical models for transformation such as elastic [Shen and Davatzikos, 2002] or fluid deformation models [D'Agostino et al., 2002], or a linear combination of smooth basis functions [Ashburner and Friston, 1999] or free-form deformations [Rueckert et al., 1999]. However, the problems in inter-subject brain MRI registration will arise when brains include lesions or diseases, because it is not possible to match the same structures between healthy and diseased brains.

3.2.2.1 Similarity measures

The registration problem seeks to find an alignment of a source image I_S and a target image I_T to maximize their similarity. So, the aim is to find a transformation \mathcal{T} which maps each voxel in the target image I_T to its corresponding voxels in the source image I_S and maximizes a similarity measure S :

$$\mathcal{T} = \arg \max_{\mathcal{T}} S(I_T, I'_S), \quad (3.6)$$

where I'_S is the aligned source image. There are different similarity measures available and they can be based on intensity (correlation metrics) or features (points, edges, corners, lines, etc).

The simplest way of defining a similarity measure is to use sum of square differences:

$$S_{SSD} = -\frac{1}{N} \sum_{i=1}^N (x_i - y_i)^2, \quad (3.7)$$

where N is the number of voxels, x_i denotes intensity of the i -th voxel of the target image I_T , and y_i denotes intensity of the i -th voxel of the aligned source image I'_S . This similarity measure assumes that images have the same photometric properties (e.g. similar intensities) and is therefore only suitable when images are acquired with the same MRI protocol. In the case when this assumption is relaxed to deal with linear changes of the intensities in the two images, the cross-correlation can be used as a similarity measure:

$$S_{CC} = \frac{\sum_{i=1}^N (x_i - \bar{x})(y_i - \bar{y})}{\sqrt{\sum_{i=1}^N (x_i - \bar{x})^2 \sum_{i=1}^N (y_i - \bar{y})^2}}, \quad (3.8)$$

where \bar{y} and \bar{x} denote the mean voxel intensity in the source and target images.

When different image modalities are used, such as T₁- and T₂-W MRI or CT and MRI, the intensity relationship is not linear and the intensity pattern does not match among modalities. In these cases it is possible to use a similarity measure called mutual information, which assumes that the statistical dependency between intensities of corresponding voxels in images I_T and I_S is maximal at registration [Wells III et al., 1996a, Viola and Wells, 1997, Pluim et al., 2003].

Mutual information is defined in terms of entropy and joint entropy:

$$S_{MI} = H(I_T) + H(I_S) - H(I_T, I_S), \quad (3.9)$$

where $H(I_T)$ and $H(I_S)$ denote respectively the entropy of image I_T and I_S , and $H(I_T, I_S)$ is the joint entropy of both images. The entropy H of the grayscale MR image I_T with intensity values $i = 0, \dots, 255$ is calculated as:

$$H(I_T) = - \sum_{i=0}^{255} P(i) \log P(i), \quad (3.10)$$

where $P(i)$ is the probability of observing intensity i in image I_T and can be estimated from the histogram of the image. Other methods for estimating this probability distribution include techniques such as Parzen windowing [Wells III et al., 1996b]. Similarly, the joint entropy $H(I_T, I_S)$ is calculated as:

$$H(I_T, I_S) = - \sum_{i=0}^{255} \sum_{j=0}^{255} P(i, j) \log P(i, j), \quad (3.11)$$

where $P(i, j)$ is the joint probability of observing intensity i in the target image and intensity j at the corresponding location in the source image. This joint probability can be estimated from the joint histogram of images I_T and I_S .

Using these definitions, mutual information can be also written as:

$$S_{\text{MI}} = \sum_{i=0}^{255} \sum_{j=0}^{255} P(i, j) \log \frac{P(i, j)}{P(i)P(j)}, \quad P(i) > 0, \quad P(j) > 0. \quad (3.12)$$

When the intensities are one-to-one related, then $P(i) = P(j) = P(i, j)$ and mutual information is maximal. When the intensities are independent, then $S_{\text{MI}} = 0$.

A modified version of this similarity measure which is more robust to variations in image overlap and field of view is the normalized mutual information [Studholme et al., 1999]:

$$S_{\text{NMI}}(I_T, I_R) = \frac{H(I_T) + H(I_S)}{H(I_T, I_S)}. \quad (3.13)$$

Mutual information has been successfully used by many researchers to register multimodal images in various applications [Wells III et al., 1996a, Viola and Wells, 1997, Thevenaz and Unser, 2000, Pluim et al., 2003, Mellor and Brady, 2005]. In this work we use mutual information [Thevenaz and Unser, 2000, Mellor and Brady, 2005] to register T_1 - and T_2 -W images of the neonatal brain in Chapter 6.

3.2.2.2 Templates and probabilistic atlases

The template is an image/volume which encodes the average probability of finding different kinds of tissues at each spatial location. The anatomical template is obtained by normalizing, aligning and averaging of anatomical images from several different subjects. All the images are normalized in a standard stereotaxic space such as the Montreal Neurological Institute (MNI space) [Evans et al., 1993]. MNI is widely used to provide a common reference for the 3D localization of functional activation foci and anatomical structures, enabling the comparison of results obtained across different studies. The standard probabilistic atlas of the human brain consists of a template and three tissue probability maps for WM, GM and CSF [Evans et al., 1993], see Fig. 3.15. The tissue probability maps are obtained by normalizing and averaging a number of segmented subjects. The probabilistic atlas then describes the anatomical variability of the brain.

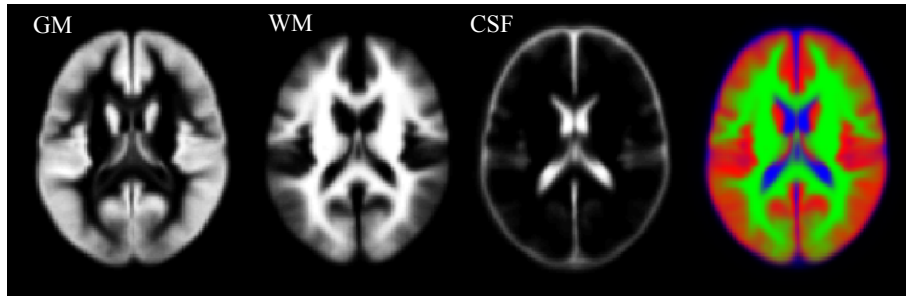


Figure 3.15: Templates for GM, WM and CSF for an axial plane. The last image corresponds to an overlap of the previous tissue probability maps.

Image registration is a necessary step for the inclusion of probabilistic atlases as a prior knowledge of the brain anatomy into the segmentation method. A probabilistic atlas is often used to initialize and constrain the segmentation process. The prior knowledge of the brain anatomical structures can increase the robustness and accuracy of a segmentation method, see Section 3.3.4.

A general review of registration techniques can be found in [Fitzpatrick et al., 2004, Crum et al., 2004, Zitova and Flusser, 2003].

3.2.3 Removal of non-brain tissue

Non-brain tissues such as fat, skull, or neck have intensities overlapping with intensities of brain tissues. Therefore, the brain has to be extracted before brain segmentation methods can be used. This step classifies voxels as brain or non-brain. The result can be either a new image with just brain voxels or a binary mask, which has a value of 1 for brain voxels and 0 for the rest of tissues. In general, the brain-voxels comprises GM, WM, and CSF of the cerebral cortex and subcortical structures, including the brain stem and cerebellum. The scalp, dura matter, fat, skin, muscles, eyes and bones are always classified as non-brain voxels. The Fig. 2.2 can help to visualize brain and non-brain parts.

The common method for brain extraction is to use prior information of the brain anatomy. A deformable template can be registered with an image and non-brain tissue is then removed by transferring the brain mask from the template, [Xue et al., 2007]. However, brain extraction using a probabilistic atlas is usually not very accurate and can cause misclassification around the brain boundary. An alternative method for extracting the brain is the brain extraction tool (BET) [Smith, 2002], which is part of the publicly available software package FSL. This method finds the center of gravity of the brain and then inflates a sphere until the brain boundary is found. It has been proven to work in practice on good-quality T_1 -W and T_2 -W images of the adult brain. An example of the brain extraction is shown in Fig. 3.16.



Figure 3.16: Result of brain extraction on a T_1 MR image in an axial plane. The left image shows the original T_1 -W MRI. The middle image depicts the estimated brain mask. The right image presents an overlap of the brain mask and original MR image.

3.3 Image segmentation methods

The diversity of image processing applications has led to development of various techniques for image segmentation [Pal and Pal, 1993, Chan and Vese, 2001, Boykov and Funka-Lea, 2006, Unnikrishnan et al., 2007, Cai et al., 2007, Prastawa, 2007, Shi et al., 2011]. This is because there is no single method that can be suitable for all images, nor are all methods equally good for a particular type of image. For example, some of the methods use only the gray level histogram, while some integrate spatial image information to be robust for noisy environments. Some methods use probabilistic or fuzzy set theoretic approaches, while some additionally integrate prior knowledge (specific image formation model, e.g. MRI brain atlas) to further improve segmentation performance. Also, some of the methods are suitable only for 2D images, while others are designed to segment 3D volumes.

However, most of the segmentation methods developed for one class of images can be easily applied/extended to another class of images. For example, the theory of graph cuts, although firstly developed for binary images [Greig et al., 1989], can be modified and used for 3D MRI segmentation of the brain tissue, which will be described in more detail in Chapter 4. Also, unsupervised fuzzy clustering [Pal and Pal, 1993, de Oliveira and Pedrycz, 2007] has been successfully applied in different areas such as remote sensing, geology, medical, biological and molecular imaging. In Chapter 5 we will present our new fuzzy C-means clustering solution and demonstrate its applicability in different areas.

The segmentation methods, with application to brain MRI, may be grouped as follows:

- Manual segmentation;
- Intensity-based methods (including thresholding, region growing, classification, clustering);
- Atlas-based methods;
- Surface-based methods (including level sets and deformable models).

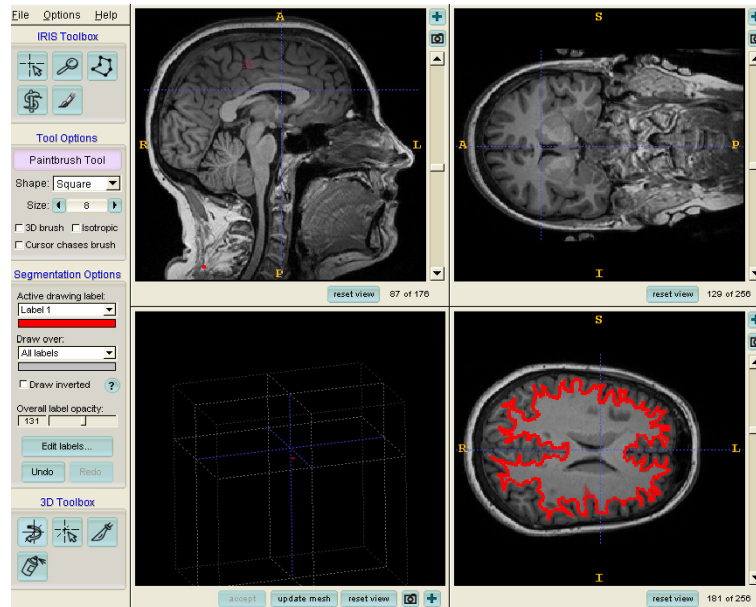


Figure 3.17: Editing tool for manual delineation: ITK-SNAP screen shot [ITK-SNAP, 2009].

3.3.1 Manual segmentation

Manual segmentation refers to the process where a human operator (e.g. expert physician) segments and labels an image by hand. The manual method is believed to be the most accurate because of the difficulty to accurately and reliably delineate structures in medical images. The segmentation difficulties are related to image quality and artifacts, see Section 2.2.3.1.

Given the improvements achieved over the past years by imaging tools (e.g. MR scanners resolve images at millimetric resolution) the manual segmentation has become an intensive and time consuming task. A trained operator typically has to go through around eighty 512×512 images, slice by slice, to extract the contours of the target structures. This manual segmentation is not only tedious but particularly prone to errors, as assessed by various intra- or inter-operator variability studies [Collier et al., 2003, Vansteenkiste, 2007]. Also, manual segmentation results are often difficult and even impossible to reproduce, because even experienced operators show significant variability with respect to their own previous delineation.

However, manual segmentation is still intensively used for defining a surrogate for true delineation (called “ground truth”) and quantitative evaluation of automated segmentation methods. Also, manual segmentation of different brain structures is a fundamental step in brain atlas formation and is used in atlas-based segmentation approaches [Prastawa, 2007, Murgasova, 2008, Shi et al., 2011].

For manual delineation, editing tools such as ITK-SNAP [Yushkevich et al., 2006, ITK-SNAP, 2009] usually display 3D data in the form of a 3 synchronized 2D orthogonal views (sagittal, coronal and axial) onto which the operator draws the contour of the target structure, see Fig. 3.17. The output data therefore consists of a series of 2D contours from which a continuous 3D surface has to be extracted. This is a non-trivial post-processing task and is prone to errors. For instance, due to inter-slice inconsistencies in segmentation, bumps in the reconstructed 3D surface are inevitable. More robust segmentation methods can usually be derived from true 3D structure models in that they can ensure globally smoother and more coherent surfaces across slices.

3.3.2 Intensity-based methods

Intensity-based segmentation methods classify individual pixels/voxels based on their intensity. In the case of the brain MRI, three main tissue classes, WM, GM and CSF, can be distinguished based on intensity, see Fig. 3.4. A more detailed classification is not possible because the intensity profiles of more detailed brain structures overlap. Even separation of the three main tissue classes based on intensity itself requires incorporating tools for dealing with artifacts in MRI, such as intensity inhomogeneity, noise, partial volume, as well as overlap in intensities of brain and non-brain tissue (e.g. the scalp have the same intensities as brain tissues).

Several intensity-based techniques are available for tissue classification. The most common method is the use of intensity histogram of all of the voxels and fitting Gaussian functions to the distribution. The probability of a given intensity corresponding to a given type of tissue can thus be inferred and voxels are assigned to tissue types accordingly. Additionally incorporating neighbourhood information helps to give preference to spatially homogeneous regions in the resulting segmentation. This can significantly decrease misclassification due to random noise in the image [Pham et al., 2000]. Additionally, probabilistic atlases can be included in the classification to inform whether a given location in the brain is likely to contain WM, GM, or CSF voxels [Prastawa, 2007].

3.3.2.1 Thresholding

Thresholding is the simplest image segmentation method. A thresholding procedure uses the intensity histogram and attempts to determine intensity values, called thresholds τ , which separates the desired classes. The segmentation is then achieved by grouping all pixels between thresholds into one class, see Fig. 3.18. The thresholding methods have many variations: global (single threshold) or local threshold (depending on the position in the image), multi-thresholding, adaptive thresholding, etc. In the case of a single global threshold, segmentation of an image $I(i, j)$ is defined as:

$$I^t(i, j) = \begin{cases} 1 & \text{if } I(i, j) > \tau \\ 0 & \text{if } I(i, j) \leq \tau. \end{cases} \quad (3.14)$$

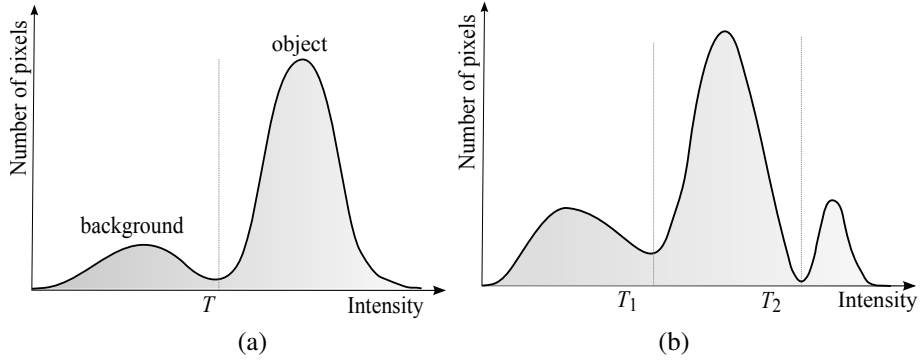


Figure 3.18: (a) Gray level histogram that can be partitioned by a single threshold. (b) Gray level histogram that can be partitioned by multiple thresholds.

where $I'(i, j)$ is a segmented (thresholded) image, where pixels labeled with 1 correspond to object and pixels labeled with 0 correspond to background, see Fig. 3.18(a).

Thresholding is a fast and computationally efficient method, but does not take into account the spatial characteristics of an image (neighborhood information). Thus thresholding is sensitive to noise and intensity inhomogeneities. In low-contrast images it tends to produce scattered groups of pixels rather than connected regions and requires connectivity algorithms as a post-processing step.

In general, threshold-based segmentation methods are not suitable for textured images. This is because the perceptual qualities of textured images are based on higher order interactions between image elements or objects in the scene. However, in brain MRI segmentation, thresholding can be used to separate background voxels from the brain tissue or for initializing the tissue classes in iterative segmentation methods such as fuzzy C-means clustering, see Chapter 5. A survey on thresholding techniques is provided in [Sezgin and Sankur, 2004].

3.3.2.2 Region growing

Region growing (also called region merging) is a technique for extracting a connected region of the image which consists of groups of pixels/voxels with similar intensities [Haralick and Shapiro, 1985]. In its simplest form, region growing starts with a seed point (pixel/voxel) that belongs to the object of interest. The seed point can be manually selected by an operator or automatically initialised with a seed finding algorithm. Then, region growing examines all neighboring pixels/voxels and if their intensities are similar enough (satisfying a predefined uniformity or homogeneity criterion), they are added to the growing region. This procedure is repeated until no more pixels/voxels can be added to the region.

Region growing is suitable for segmentation of volumetric images which are composed of large connected homogeneous regions. Thus, it is successfully used in med-

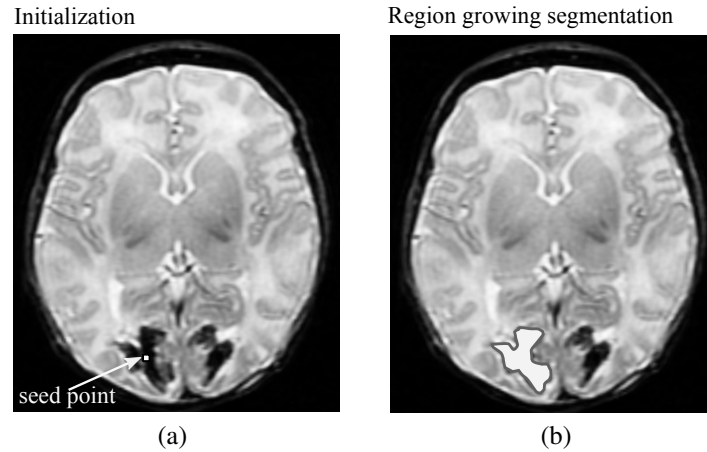


Figure 3.19: An example of a region growing segmentation of a brain lesion. (a) In the initialization step, a seed point is manually selected in the lesion area. (b) The final segmentation result is a connected region and represents the lesion.

ical image analysis to segment different tissues, organs or lesions from MR images. For example, it is used in brain MRI analysis for segmentation of brain vessels [Passat et al., 2005], brain tumour segmentation [Weglinski and Fabijanska, 2011] or extraction of brain surface [del Fresno et al., 2009]. See an example of region growing segmentation in Fig. 3.19.

The main disadvantage of the region growing method is its sensitivity to the initialization of seed point. By selecting a different seed point, the segmentation result can be completely different. If seed point and homogeneity criterion are not properly defined, the growing region can leak out and merge with the regions that do not belong to the object of interest. Also, region growing is sensitive to noise and segmented regions in the presence of noise can become disconnected or have holes. On the other hand, separate regions can become connected in the presence of partial volume effects.

3.3.2.3 Classification methods

Classification methods use data with known labels to partition image feature space. Image features are typically intensity values, but can be also related to texture or other image properties. Classification methods can be both supervised and unsupervised. Supervised classification require training images, which are manually segmented and then used as references for automatic segmentation of new images. Next to the manual interaction that is laborious and time consuming, another disadvantage of supervised classification methods is that they generally do not take into account the neighborhood information and thus, they are sensitive to noise. Also, the use of the same training set for a large number of images can lead to biased results, which do not take into account anatomical and physiological variability between different subjects.

kNN classifier

One of the simplest classifiers is the nearest-neighbor classifier [Duda et al., 2001], where each pixel/voxel is classified in the same class as the training datum with the closest intensity. A generalization of this approach is the k-nearest-neighbor (kNN) classifier, where the pixel/voxel is classified according to the majority vote of the closest training data. The kNN classifier is considered a non-parametric classifier because it makes no underlying assumption about the statistical structure of the data. It is especially suitable if a large number of training data is available.

The kNN classification method was adapted for brain MRI segmentation by Warfield et al. [Warfield et al., 1998]. In addition to image intensities, Warfield used spatial localization of brain structures (classes) in form of a non-rigidly registered template as an additional feature to enhance the classification process. The segmentation is then calculated in an iterative process by interleaving the segmentation refinement with updating the non-rigid alignment to the template. This procedure requires manual selection of a large number of training samples for each tissue class to train the kNN classifier. Due to the manual interaction in the training phase, the method is not fully automatic and the results depend on particular choice of the training set. Cocosco et al. [Cocosco et al., 2003] developed a method for the robust selection of training samples to make the kNN classification process fully automatic. This method is reported to deal well with anatomies which differ from the probabilistic atlas. However, it does not deal with the problem of natural intensity variation within each tissue class. Both methods require correction of the bias field as a pre-processing step.

Bayesian classifier

One of the most commonly used parametric classifiers is the Bayesian classifier [Wells III et al., 1996b]. The Bayesian classifier models the probabilistic relationships between the attribute set and the class variables, which are then used for estimating the class probability of the unknown variable. This model involves Bayesian inference such as maximum a posteriori (MAP) estimation, where the goal is to estimate the label output image $\hat{\mathbf{x}}$ given the observed image \mathbf{y} by minimizing the *posterior* distribution $P(\mathbf{x}|\mathbf{y})$ of the possible labels \mathbf{x} :

$$\hat{\mathbf{x}} = \arg \max_{\mathbf{x}} P(\mathbf{x}|\mathbf{y}). \quad (3.15)$$

The Bayesian framework consists of three probability distributions: the *prior* distribution $P(\mathbf{x})$, the *posterior* distribution $P(\mathbf{x}|\mathbf{y})$ and the *conditional* distribution $P(\mathbf{y}|\mathbf{x})$ (also called the *likelihood*). The prior distribution embodies the knowledge of likely configurations before an actual image is observed. The posterior distribution is derived after an observation has been made and the likelihood is defined as the probability of obtaining a particular observation given a set of model parameters.

The Bayes rule describes the relation between the posterior probability $P(\mathbf{x}|\mathbf{y})$, prior probability $P(\mathbf{x})$, and likelihood $P(\mathbf{y}|\mathbf{x})$ as follows:

$$P(\mathbf{x}|\mathbf{y}) = \frac{P(\mathbf{y}|\mathbf{x})P(\mathbf{x})}{P(\mathbf{y})}. \quad (3.16)$$

Using this definition (3.16), the MAP estimate can be written as:

$$\begin{aligned}\hat{\mathbf{x}} &= \arg \max_{\mathbf{x}} (P(\mathbf{y}|\mathbf{x})P(\mathbf{x})/P(\mathbf{y})) \\ &= \arg \max_{\mathbf{x}} (P(\mathbf{y}|\mathbf{x})P(\mathbf{x})),\end{aligned}\tag{3.17}$$

where $P(\mathbf{y})$ can be omitted because it is a constant in the case when \mathbf{y} is known. Since in many cases the probability distributions have exponential functions, this computation can be simplified by using a logarithmic transform:

$$\hat{\mathbf{x}} = \arg \max_{\mathbf{x}} (\log P(\mathbf{y}|\mathbf{x}) + \log P(\mathbf{x})).\tag{3.18}$$

More details about the Bayes' theory can be found in [Therrien, 1989].

In the case of the brain MRI segmentation, the classifier assumes that the pixel intensities are independent samples from a mixture of Gaussian probability distributions, see Section 3.1.4 and Fig. 3.10(a). Training data is collected by obtaining representative samples from each component of the Gaussian mixture accordingly. Classification of new data is obtained by assigning each pixel to the class with the highest posterior probability.

Bayesian classifiers are used in the expectation-maximization (EM) segmentation methods which have been successfully implemented in several software packages used in the medical imaging community: SPM [Ashburner and Friston, 2005], FAST [Zhang et al., 2001], FreeSurfer [Fischl et al., 2002] and 3DSlicer [Pohl et al., 2006]. All these methods implement a segmentation and bias correction in the EM framework. They also include various additional improvements, such as non-rigid alignment of atlas [Ashburner and Friston, 2005] and including neighbourhood information in the form of Markov Random Fields [Li, 1995, Zhang et al., 2001].

In general, the EM segmentation framework can be described as follows:

EM approach for brain MRI segmentation

Firstly, initialize the EM algorithm. In the case of brain MRI segmentation, the GMM is used to initially estimate model parameters. Then, iterate between expectation step (**E-step**) and maximization step (**M-step**) until convergence:

E-step: Estimate the brain tissue segmentation given the current estimate of model parameters. This step can include the use of neighbourhood information (e.g. in the form of MRF modeling).

M-step: Estimate the model parameters. This step can consist of a combination of the following steps:

1. Estimate the intensity distribution parameters for each tissue class.
2. Estimate the bias correction parameters.
3. Estimate the registration parameters for alignment of probabilistic atlas with the image.

3.3.2.4 Clustering methods

Clustering methods are unsupervised segmentation methods that partition an image into clusters of pixels/voxels with similar intensities without using training images. In fact, clustering methods use the available image data to train themselves. The segmentation and training is done in parallel by iterating between two steps: data clustering and estimating the properties of the each tissue class. The most commonly used clustering methods are the k-means clustering [Coleman and Andrews, 1979], the fuzzy C-means clustering [Dunn, 1973, Bezdek, 1981] and the expectation-maximisation (EM) method [Pham et al., 2000].

The k-means clustering method partitions the input data into k classes by iteratively computing a mean intensity for each class (also called centroid) and segmenting the image by classifying each pixel/voxel in the class with the closest centroid. The k-means clustering is also known as a hard classification method because it forces each pixel/voxel to belong exclusively to one class in each iteration. The fuzzy C-means clustering is soft classification method based on fuzzy set theory [Zadeh, 1965]. It is a generalization of the k-means clustering because it allows each pixel/voxel to belong to multiple classes with different membership degrees in each algorithm iteration and the final classification decision is made at the end (when the convergence criteria is reached). The EM method has the same soft classification principle but typically assumes that MRI intensities of different brain tissues can be represented with a Gaussian mixture model, see Section 3.1.4. Even though clustering methods do not require training images, they do require some initial parameters and the EM method has shown the highest sensitivity to initialization in comparison to fuzzy C-means and k-means methods [Pham et al., 2000].

As it is the case with classification methods, clustering methods do not incorporate spatial neighborhood information and thus, they are sensitive to noise and intensity inhomogeneities. To improve the clustering performance for images corrupted with noise, we developed a new spatially coherent fuzzy C-means clustering method for noise-robust image segmentation [Despotovic et al., 2013c, Despotovic et al., 2010c]. Our method is described in Chapter 5.

3.3.3 Atlas-based methods

If an atlas or template of the human brain for a specific population of interest is available (see Section 3.2.2.2), then atlas-based methods can be a powerful tool for brain MRI segmentation. The atlas contains information about the brain anatomy (e.g. contains the information about the location of different brain structures) and it is used as a reference (a prior knowledge) for segmenting new images. The main advantage of these methods is the possibility to segment any brain structure available in the atlas without any additional cost. Conceptually, atlas-based approaches are similar to classifier methods, except that they are implemented in the spatial domain rather than in the feature space.

Before a probabilistic atlas can be used as a prior knowledge, it has to be aligned with the image to be segmented. Since the segmentation labels and the “ground truth” are known for the atlas, all atlas information is transferred to the target image after registration. Therefore, the performance of atlas-based methods is directly dependent on quality of the registration method used.

The traditional way of aligning the probabilistic atlas with the image is to use affine registration. Unfortunately, an affine alignment may not be sufficient if the brain anatomy of interest differs significantly from the average atlas anatomy. Pohl et al. therefore suggest aligning the atlas using non-rigid registration [Pohl et al., 2002]. However, in their later work Pohl reports difficulties in registering anatomical template with the image to be segmented using standard registration methods [Pohl, 2005]. D’Agostino developed a special similarity measure for registering probabilistic maps directly to the new image [D’Agostino et al., 2004]. Recently, several methods have been developed which aim to overcome this problem by iteratively refining the segmentation and non-rigid registration of the probabilistic atlas at the same time. Ashburner developed a method for simultaneous segmentation, bias correction and non-rigid registration of a probabilistic atlas [Ashburner and Friston, 2005].

However, even with non-rigid registration methods, accurate segmentations of complex structures is difficult due to anatomical variability. Also, atlas-guided segmentation in patients with brain deformations can be difficult and prone to errors, because the probabilistic atlas is based on a population of healthy subjects. For instance, in patients with brain lesions or a brain-anatomy that significantly differs from the atlas template, the atlas alignment and the corresponding segmentation of the brain will fail or give inaccurate results. In these cases an atlas-based approach is not a suitable method for image segmentation.

An aligned probabilistic atlas can be also used as a good initial estimate of the segmentation, which is especially important for EM-based methods, as EM algorithm is guaranteed to converge to local, not global, maxima. In addition, most EM-based methods, [Ashburner and Friston, 2005, Pohl et al., 2006] use the probabilistic atlas to constrain the segmentation process where again, the correct alignment of the probabilistic atlas is crucial for a successful and accurate segmentation.

3.3.4 Surface-based methods

In addition to intensity-based and atlas-based methods, there are a number of alternative brain segmentation approaches. These approaches include surface-based methods, such as level sets and deformable models.

Deformable models, also called active contours or snakes in 2D and active surfaces or active balloons in 3D, were introduced in [Kaas et al., 1988] and were further developed in [Cohen and Cohen, 1993, Terzopoulos et al., 1998]. Deformable models use closed parametric curves or surfaces for delineating region boundaries. The parametric curves and surfaces deform under the influence of external (or image) forces (controlled by the image attributes) and the internal forces, which control the surface

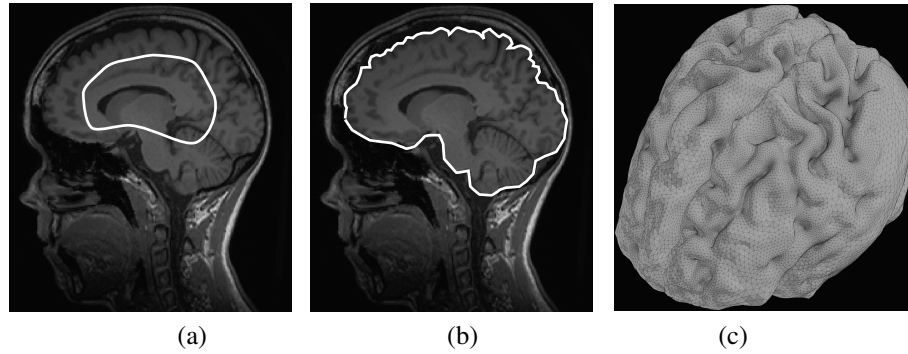


Figure 3.20: Segmentation of the brain surface using deformable models. (a) A closed curve is initialised inside the brain. (b) The segmentation result of the brain surface in 2D. (c) 3D surface of the brain.

regularity. In general, deformable models represent the fusion of geometry, physics and approximation theory. Geometry is used to represent the shape of the object, physics defines constraints on how the shape may vary over time and space, and approximation theory provides mechanisms for fitting the models to measured data.

To delineate a boundary of an object, first a closed curve or surface is placed near the desired boundary in an image. Then, internal and external forces are deforming the curve or surface in an iterative relaxation process. Internal forces are computed from within the curve or surface to keep it smooth throughout the deformation. External forces are usually derived from the image to deform the curve or surface towards the desired feature of interest. In traditional deformable models, image forces come primarily from edge information (i.e., significant image intensity). However, such reliance on edge information makes deformable models sensitive to noise and highly dependent on the initial estimate. There have been significant efforts to integrate region information into deformable models. For instance, Chan and Vese [Chan and Vese, 2001] present a level-set method based whose main idea is to consider the information inside the regions, and not only at their boundaries. We use this level-set method in Chapter 6 to refine and delineate the surface of the brain and scalp in newborn infants.

Sometimes the image data are not sufficient to delineate the region of interest and thus, prior knowledge has to be introduced. Also, a noise model can be added to the shape prior. A general review on deformable models in medical image analysis can be found in [Montagnat et al., 2001].

3.4 Modeling the spatial context

The use of spatial context or neighborhood information is of great importance in brain MRI segmentation. Unless the image is simply random noise, the intensity of an image pixel/voxel is highly statistically dependent on the gray intensities of its neighbors (surrounding pixels/voxels). Markov Random Field (MRF) theory provides a basis for modeling local properties of an image, where the global image properties follow the local interactions. MRF models have been successfully integrated in various brain MRI segmentation methods to decrease misclassification errors due to image noise [Pham et al., 2000, Zhang et al., 2001, Ashburner and Friston, 2005]. Here we introduce the basic concepts of MRF models that we use later to formulate the energy function of the 3D graph cut method for brain MRI segmentation.

3.4.1 Neighborhood system

First, let us introduce some notations. As has been described in Section 3.1.1, every pixel (or voxel) in an image can be represented with one node in the lattice \mathcal{P} . Let x_i represent an intensity value of a single pixel (or voxel) with a position i in an image $\mathbf{x} = (x_1, \dots, x_m)$ defined over a finite lattice \mathcal{P} , where m is the total number of image elements ($m = MN$ for a 2D image and $m = MND$ for a 3D image). Let $\mathcal{N} = \{\mathcal{N}_i | \forall i \in \mathcal{P}\}$ denote a neighboring system for a lattice \mathcal{P} , where \mathcal{N}_i represent a small neighborhood around i , not including x_i .

The nodes (pixels/voxels) in a lattice \mathcal{P} are related to one another via neighborhood system \mathcal{N} that can be defined as:

$$\mathcal{N} = \{\mathcal{N}_i | \forall i \in \mathcal{P}\}. \quad (3.19)$$

The neighboring relationship has the following properties:

- a node i does not belong to its own neighborhood: $i \notin \mathcal{N}_i$;
- the neighboring relationship is mutual: $i \in \mathcal{N}_{i'} \iff i' \in \mathcal{N}_i$.

The set of neighbors of i can be defined as the set of surrounding nodes within a radius of \sqrt{r} from the center i

$$\mathcal{N}_i = \{i' \in \mathcal{P} | [\text{dist}(\text{pixel}_i, \text{pixel}_{i'})]^2 \leq r, i' \neq i\}, \quad (3.20)$$

where $\text{dist}(a, b)$ is the Euclidean distance between neighboring pixels a and b and $r \in \mathbb{Z} : r \geq 0$ is an integer number.

The first and the second order neighborhoods are the most commonly used neighborhoods in image segmentation. The first order neighborhood consists of 4 nearest nodes in a 2D image and 6 nearest nodes in a 3D image, while the second order neighborhood consists of 8 nearest nodes in a 2D image and 18 nearest nodes in a 3D image, see Fig. 3.21.

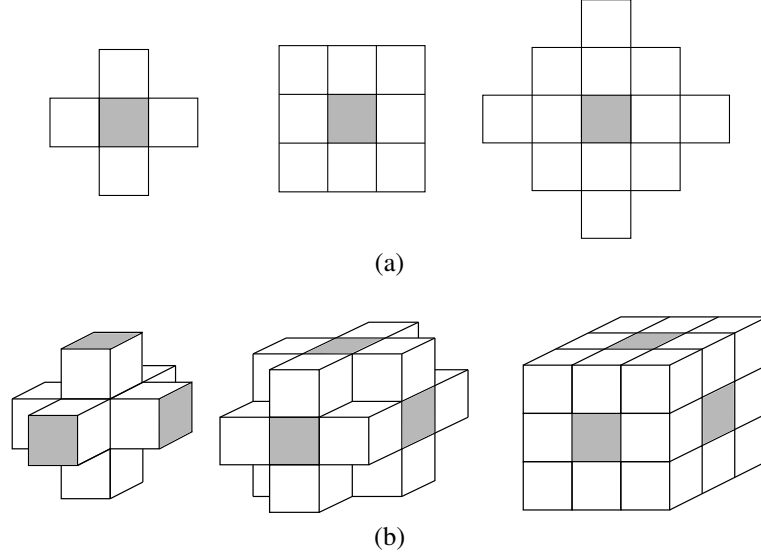


Figure 3.21: (a) 2D and (b) 3D neighborhood configuration for the first, second and third order respectively.

3.4.1.1 Cliques

A clique c , defined over a lattice \mathcal{P} with respect to a neighborhood system \mathcal{N} is a subset of nodes in \mathcal{P} such that c is either a single-node, or a pair of two neighboring nodes, or a collection of n neighboring nodes.

The collection of all cliques for a lattice \mathcal{P} and a neighborhood system \mathcal{N} is denoted by \mathcal{C} . Let \mathcal{C}_n be the set of all cliques containing n nodes. Then, the single-node clique \mathcal{C}_1 , the two-node clique \mathcal{C}_2 and the three-node clique \mathcal{C}_3 can be formulated as:

$$\mathcal{C}_1 = \{i | i \in \mathcal{P}\}, \quad (3.21)$$

$$\mathcal{C}_2 = \{\{i, i'\} | i' \in \mathcal{N}_i, i \in \mathcal{P}\}. \quad (3.22)$$

$$\mathcal{C}_3 = \{\{i, i', i''\} | i, i', i'' \in \mathcal{P} \text{ are neighbors to one another}\}. \quad (3.23)$$

The types of 2D cliques occurring in the first and the second order neighborhoods containing up to 4 nodes are illustrated in Fig. 3.22(a). The cliques \mathcal{C}_2 containing only two nodes for the first, second and third order 3D neighborhoods are illustrated in Fig. 3.22(b). The number of possible cliques increases significantly as the lattice dimensions and the neighborhood order increase, so usually \mathcal{C} is constrained to be a set of pairwise (two-node) cliques.

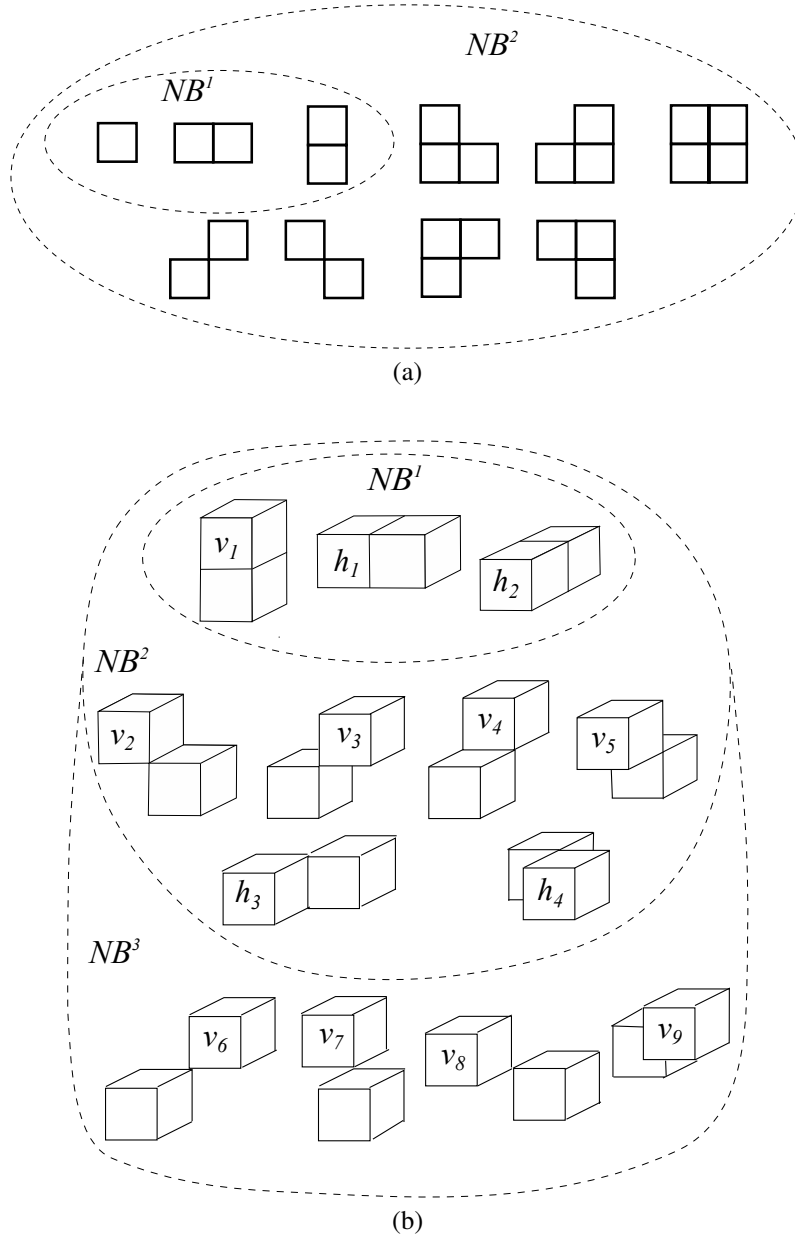


Figure 3.22: (a) 2D clique types occurring in the first (NB^1) and the second (NB^2) order neighborhoods. (b) 3D pairwise cliques for the first (NB^1), the second (NB^2) and the third order (NB^3) neighborhood. There are 13 such cliques indexed as $v_i, i = 1, \dots, 9$ for the vertical and $h_i, i = 1, \dots, 4$ for the horizontal ones.

3.4.2 Markov Random Field models

Markov random field model can be represented with a graph $\mathcal{G} \triangleq (\mathcal{P}, \mathcal{N})$, where \mathcal{P} represents the nodes and \mathcal{N} determines the links (also called edges) that connect the nodes according to the neighborhood relationship. Such graph structure corresponds to an image, where nodes correspond to pixels (or voxels) and the links connecting the nodes represent the contextual dependency between pixels (or voxels).

To define Markov property, let $\mathbf{x}_{\mathcal{P} \setminus i}$ denote the vector of all gray values in the image without x_i , and let $\mathbf{x}_{\mathcal{N}_i}$ denote the neighborhood vector containing gray intensities from a small neighborhood \mathcal{N}_i around i , not including x_i . Using these notations, Markov models assume the following property:

$$P(x_i | \mathbf{x}_{\mathcal{P} \setminus i}) = P(x_i | \mathbf{x}_{\mathcal{N}_i}). \quad (3.24)$$

Expressed in words, this property states that knowing all the intensity values in the image without x_i , gives no extra information on x_i over knowing only the intensity values in the local neighborhood \mathcal{N}_i around i .

According to the well known Hammersley-Clifford theorem [Clifford, 1990], the joint prior distribution of all image elements x is always a Gibbs distribution $P(\mathbf{x})$ if the MRF property in (3.24) is correct:

$$P(\mathbf{x}) = \frac{1}{Z} \exp \left(-\frac{1}{T} U(\mathbf{x}) \right) \text{ where } U(\mathbf{x}) = \sum_{c \in \mathcal{C}} V_c(\mathbf{x}). \quad (3.25)$$

where Z is a positive normalizing constant known as the partition function and T is the constant called the temperature of the field. The temperature controls the sharpness of the distribution and is typically assumed to be 1. If the temperature is high, all configurations tend to be equally distributed. Near the zero temperature, the distribution concentrates around the global energy minima. $U(\mathbf{x})$ is the energy function, which is a sum of clique potentials $V_c(\mathbf{x})$ over all possible cliques \mathcal{C} .

The Hammersley-Clifford theorem establishes the important connection between the local and global specifications of an MRF. It gives theoretical justification to the design of an MRF via local or global properties depending on their availability in a specific application context. The theorem's relevance in the image processing community was established by Geman and Geman [Geman and Geman, 1984]. Its original proof was developed in 1971, but was published in 1990 [Clifford, 1990].

The importance of the theorem in practice is that it provides a simple way of specifying the joint probability. This can be done by defining the clique potential functions. Thus, any a priori knowledge or preference about the interactions between the sites can be embraced. How to properly select the parameters controlling the strength of spatial interactions for an effective model is a major topic in MRF theory and practice. Computation time is also often an issue.

For more reading and details about MRF see [Li, 1995].

3.4.3 Energy functions and optimization criteria

MRF theory is often merged with estimation theory and is used to formulate energy functions to find an optimal solution to the segmentation problem. Often, the energy function is formulated to define the minimal solution. The main issues are how to formulate the energy function and how to choose the optimization technique for its minimization. The formulation of the energy function describes how various image properties (e.g. pixel intensities and their contextual properties) are encoded into the function. It maps a solution to a real number, which indicates the quality of the solution in terms of a cost or goodness. The optimization of the energy function addresses the problem of local or global minima and the efficiency of methods in time and space.

The most popular optimisation criteria that is used with MRF modeling is Maximum a posteriori (MAP) probability. This MAP-MRF framework is a special case of Bayesian approach (see Section 3.3.2.3) and has been successfully used in different image segmentation problems to decrease misclassification error due to random noise in the image [Pham et al., 2000]. In medical imaging, MRF is used to model the prior probability $P(\mathbf{x})$, which takes into account the fact that most pixels belong to the same tissue class as their neighboring pixels. Then, the segmentation is obtained by maximizing a posterior probability $P(\mathbf{x}|\mathbf{y})$ of the segmentation given the image data [Zhang et al., 2001, Ashburner and Friston, 2005]. This maximization problem from Eq. (3.18) becomes an energy minimization $\hat{\mathbf{x}} = \arg \min E(\mathbf{x}|\mathbf{y})$ problem. This is because if $P(\mathbf{x})$ is a Gibbs distribution (3.25), then it can be shown that $P(\mathbf{x}|\mathbf{y})$ is a Gibbs distribution with posterior energy $E(\mathbf{x}|\mathbf{y})$ and $P(\mathbf{x}|\mathbf{y}) \propto \exp(-E(\mathbf{x}|\mathbf{y}))$.

The posterior energy is represented as a sum of clique potentials $V_c(\mathbf{x})$ and the smoothness data term (or likelihood) $D_i(y_i|x_i)$

$$E(\mathbf{x}|\mathbf{y}) = \sum_i D_i(y_i|x_i) + \sum_{c \in \mathcal{C}} V_c(\mathbf{x}). \quad (3.26)$$

In the case of MRF model with pairwise cliques, the energy function is

$$E(\mathbf{x}|\mathbf{y}) = \sum_i D_i(y_i|x_i) + \sum_{i,i'} V_{i,i'}(x_i, x_{i'}), \quad (3.27)$$

where $V_{i,i'}(x_i, x_{i'})$ is the pairwise potential representing the interaction of neighboring labels.

Next to Bayesian approach, graph cut is another powerful optimization method that aims to find the optimal solution of the segmentation problem by minimizing the energy function [Greig et al., 1989, Boykov et al., 2001]. Generally, graph cuts based segmentation has become an attractive approach in computer vision because it addresses segmentation in a global optimization framework and gives exact solutions for sub-modular MRF problem described in (3.27) [Greig et al., 1989]. In Section 4 we focus on graph cuts based segmentation and propose its modification for more accurate and automatic 3D brain MRI segmentation.

3.5 Validation of brain MRI segmentation

Validation and comparison of different segmentation methods is a general problem in medical image analysis. It requires a “ground truth” or gold standard to which the outcome of the segmentation method can be compared. Unfortunately, the “ground truth” does not exist for the analysis of in vivo acquired data in humans. Thus, the “ground truth” of the real patients is typically generated after image acquisition.

In brain MRI analysis, the “ground truth” for the real patient data is usually made by one or more expert physicians who need to manually analyze and segment anatomical structures of interest, see Section 3.3.1. Although this is the only way to validate the real patient MRI data, this validation must be critically considered because the manual segmentation is prone to errors, highly subjective and difficult to reproduce (even by the same expert) [Vansteenkiste, 2007]. Also, this type of validation is not always available because it is time-consuming and depends on the human operator. Therefore, few alternative validation methods evolved in the praxes to validate the accuracy of the segmentation algorithms. The most popular validation methods include the use of software simulations and phantoms.

In software simulations, the artificial MR images are generated with computer programs that simulate the real acquisition process. In this way the “ground truth” is known and the influence of different acquisition parameters and imaging artifacts can be controlled and examined independently. This type of validation is very flexible, easily accessible by different researchers and can be performed with little effort. However, a drawback of this validation is that software simulators can not take into account all factors that might influence the real image acquisition and the simulated images are only and approximate of the real images.

Since software simulations have certain limitations, validation of new segmentation methods can be done using human-like phantoms, whose physical properties (e.g. geometry of the tissue structures, material properties) are known and are similar to the in vivo properties. The phantom images are generated using the MRI scanner and are more realistic than images generated with software simulations. On the other hand, the phantom images do not offer the flexibility of the software simulations and imaging is more expensive and labour intensive.

The most popular simulated images used for validation of brain MRI segmentation methods are designed by Collins et al. [Collins et al., 1998] and are also known as a realistic digital brain phantom or simply BrainWeb. Images are freely available on-line and easily accessible for all researcher to test the performance of the new segmentation methods. In our work, we used this simulated brain database to test the outcome of our segmentation methods and to compare it with other state-of-the-art methods. We also validated our segmentation methods on real patients where the “ground truth” segmentation is done manually by an expert physician (or it is corrected and approved by an expert physician when it is done by less experienced researcher).

3.6 Conclusions

Image segmentation is an important step in many medical applications involving 3D visualization, measurements, registration and computer-aided diagnosis. This chapter has provided a brief introduction to the fundamental concepts of MRI segmentation of the human brain and methods that are commonly used.

In Section 3.1, we have defined the basic concepts necessary for understanding MRI segmentation methods, such as 2D and 3D image definition over a lattice, image features and brain MRI intensity distributions. Following this, pre-processing steps necessary to prepare images for MRI segmentation have been described in Section 3.2. The most important steps include bias field correction, image registration and removal of non-brain tissues or brain extraction. The correction of intensity inhomogeneity is an important step for the efficient segmentation and registration of brain MRI. Image registration is required in brain MRI segmentation for the alignment of multimodal images of the same subject or several population groups taken at different times and from different viewpoints.

Due to the rapid development of medical image modalities, new application-specific segmentation problems are emerging and new methods are continuously explored and introduced. Selection of the most appropriate technique for a given application is a difficult task. In many cases, a combination of several techniques may be necessary to obtain the segmentation goal. Very often integration of multimodal information (acquired from different modalities or over time) can help to segment structures that otherwise could not be detected on single images.

The most popular image segmentation methods that are used for brain MRI segmentation have been reviewed and discussed in Section 3.3. Newer methods are usually designed to bring more accurate results by incorporating neighborhood information and prior information from atlases. As a consequence, the segmentation process often becomes more complex and time consuming. The likely future research will still focus on developing more accurate and noise-robust methods, but also on improving the computational speed of segmentation methods. Computational efficiency will be particularly important in real-time processing applications such as computer guided surgery.

Probably one of the most important questions concerning medical image segmentation is its use in real clinical settings. It is undeniable that computerized segmentation methods have shown their potentials and applicability in computer-aided diagnosis and therapy planning. It is expected that in the near future they will also become essential tools in real clinical settings, particularly in qualitative diagnosis and where 3D reconstruction and visualisation of the anatomical structures is important.

4

Three-label graph cut for 3D brain MRI segmentation

The science of today is the technology of tomorrow.
– Edward Teller

The increasing importance of 3D medical imaging leads to a growing demand for volumetric image analysis and automatic 3D MRI segmentation of the brain tissue. This automatic segmentation is a challenging problem because MRI imperfections and degradations such as the bias field and noise can highly influence the accuracy of segmentation methods. To improve segmentation performance and correct erroneous data, it is often necessary to use some additional knowledge about the image structure and contextual constraints. Since the intensity of a pixel/voxel in an image is highly statistically dependent of its neighboring pixels/voxels, the common solution is to integrate the spatial interaction between neighboring elements directly into the image segmentation algorithm.

One of the most consistent and convenient ways to model local spatial properties of an image is using the Markov Random Field (MRF) theory. To establish optimal solutions, MRF theory is often merged with estimation theories and used to formulate energy functions. Graph cut is a powerful optimization method for a wide class of binary and non-binary energies that aims to find the optimal solution of the segmentation problem by minimizing the objective or the energy function [Boykov et al., 2001, Song et al., 2006, Wolz et al., 2010]. Graph cut method provides an efficient and flexible approach for image segmentation that can enforce image smoothness while preserving important image discontinuities [Boykov et al., 2001]. In some cases, such as a sub-modular MRF problem described in Eq. (3.27), it can produce globally optimal solutions, as it was shown by Greig et. al. [Greig et al., 1989]. The computational efficiency of this sub-modular optimization problem is improved by using the combinatorial s - t min-cut method on graph, which was proposed by [Boykov et al., 2001].

In this chapter, we address the problem of 3D brain MRI segmentation, where we focus on multi-label min-cut graph cut segmentation and propose its modification for

more accurate and automatic 3D brain MRI segmentation. The main contribution of our work is that we extended s - t min-cut/max-flow graph cut method for automatic 3D brain MRI segmentation using three-label graph and performed comparison study between this and several state-of-the-art brain MRI segmentation methods. First, we describe the basic concepts of the graph cut approach. Then, we propose an improved 3D graph-cut method that is designed to use three labels and segment brain MRI in three brain tissues: WM, GM and CSF. Following this, we study the performance of the automatic 3D graph cut method on simulated and real brain MRI, and we present the comparison results with other popular 3D brain MRI segmentation methods. Next, we apply the proposed method to automatic brain cortex segmentation in patients with focal cortical dysplasia (FCD). Finally, we draw general conclusions and give future directions for improving 3D brain MRI segmentation.

This work is done in collaboration with my master thesis student Ief Segers [Segers et al., 2010] who implemented the proposed segmentation algorithm in C++, created the graphical user interface (GUI) and did an initial testing of the method on patients with FCD lesions.

4.1 Graph cut approach - background

First, let us introduce some basic terminology. Let $\mathcal{G} \triangleq (\mathcal{V}, \mathcal{E})$ represent a graph, where \mathcal{V} is a set of nodes and \mathcal{E} is a set of links (or edges) that connect neighboring nodes. A set of nodes $\mathcal{V} = \mathcal{P} \cup \{t, s\}$ consists of all nodes in a lattice $p \in \mathcal{P}$ and two additional terminal nodes, which are called the source s and the sink t . A set of edges $\mathcal{E} = \mathcal{N} \cup \{(s, p), (p, t)\}$ consists of two type of edges: n-links and t-links. Edges that connect two lattice nodes are called n-links and a set of all n-links correspond to a neighborhood system \mathcal{N} for a lattice \mathcal{P} . Edges that connect a node p from a lattice \mathcal{P} with a terminal node s or t are called t-links. Note that a neighborhood system can be arbitrary and may include diagonal or any other kind of n-links.

A non-negative weight w (also called a cost) is assigned to all edges in a graph $e \in \mathcal{E}$. For simplicity, we will concentrate on directed graphs where each pair of connected nodes p and q (neighboring nodes in \mathcal{P}) is described by a single link $e_{pq} = (p, q) \in \mathcal{E}$ and a single weight w_{pq} . Generally, in directed graphs, a cost of a direct edge is not equal to the cost of the reverse edge $w_{pq} \neq w_{qp}$. A simple 2D example of an undirected graph that can be used for image segmentation is shown in Fig. 4.1, where n-links are represented with blue lines, t-links with red and green lines and edge weights with the line thickness.

4.1.1 The min-cut and max-flow problems

Let C denote an s - t cut that partitions the graph nodes into two disjoint subsets \mathcal{O} and \mathcal{B} , where $s \in \mathcal{O}$ and $t \in \mathcal{B}$. The cut is a curve (or a hyper-surface in N-dimensional space) that separates the source s from the sink t . The min-cut problem is to search for

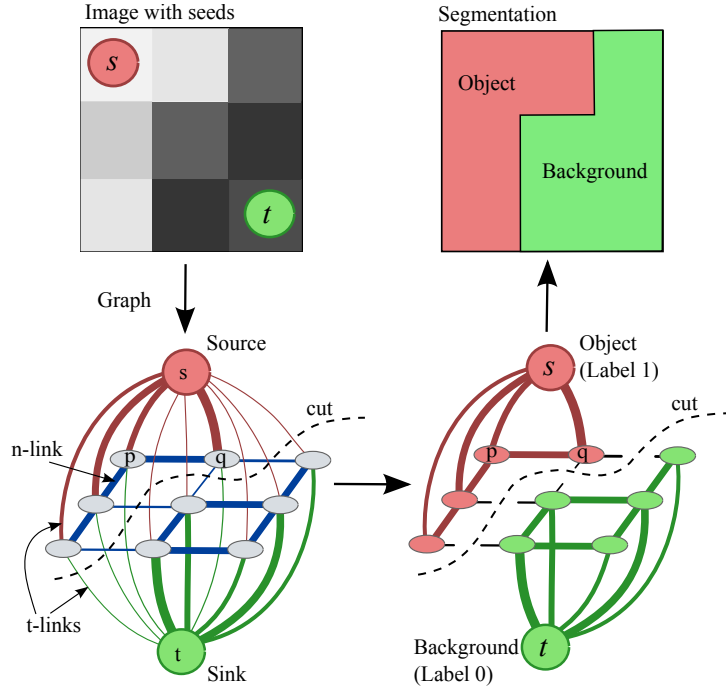


Figure 4.1: Illustration of a graph with two terminal nodes s and t and a simple 2D segmentation example for a 3×3 image. The cost of each edge is represented by the line thickness, n-links are shown in blue color and t-links in red and green color. An s - t cut is represented with a dashed line. After the cut, the nodes are connected either to s or t , meaning they are assigned with one of the two labels: object or background.

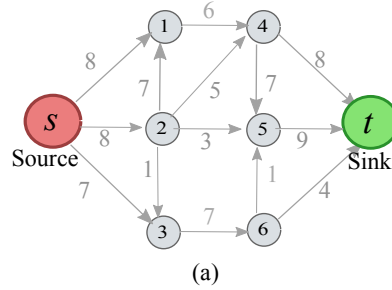
an s - t cut with the minimum cost among all cuts, where the cost of a cut $C = \{\mathcal{O}, \mathcal{B}\}$ is the sum of costs of edges traversed by the cut $e \in C$:

$$|C| = \sum_{e \in C} w_e. \quad (4.1)$$

Note that a cut in Fig. 4.1 divides the nodes between the terminals and corresponds to a binary partitioning of an underlying image into “object” and “background” segments.

A min-cut problem can be also solved by finding a max-flow from the source terminal s to the sink terminal t . The max-flow method can be easily explained with the “quantity of water” that can flow from the source to the sink, while considering graph edges as “water pipelines” of the size proportional to edge weights [Ford and Fulkerson, 1962]. The idea is to push as much “flow” as possible through the directed graph from the source to the sink and there must be at least one saturated edge on any path from source to sink (otherwise we could push more flow). The set of saturated edges separate the source and sink in two disjoint parts $\{\mathcal{O}, \mathcal{B}\}$ which correspond to min-cut. Thus, the max-flow value is equal to the min-cut cost and Fig. 4.2 shows a simple example of max-flow cut in a given two-terminal graph.

Step 1: Define graph edges and assign their weights



Step 2: Saturate edges with a max-flow and find min-cut

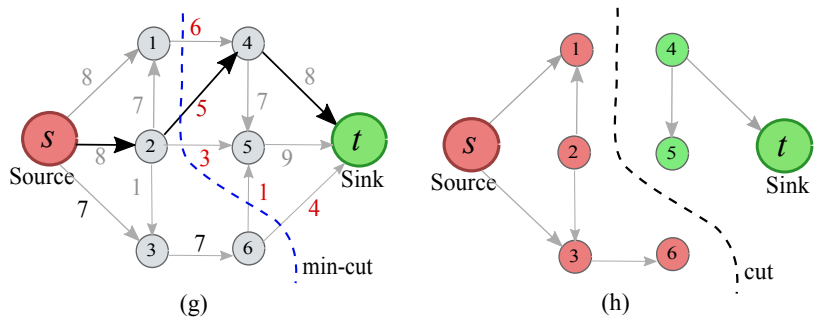
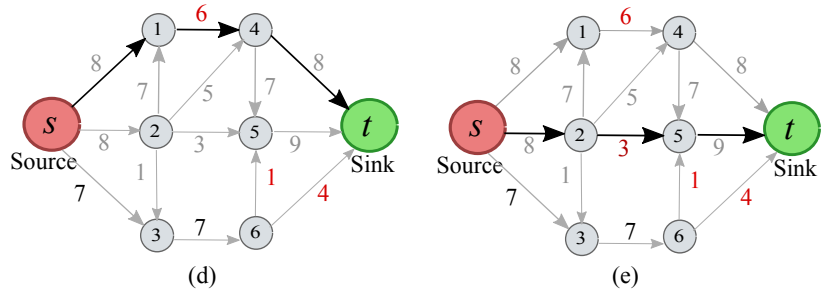
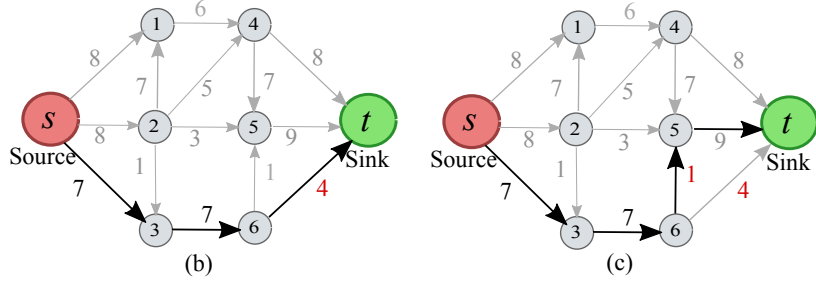


Figure 4.2: A simple example of the min-cut/max-flow in a given two-terminal graph.

4.1.2 Energy function for binary optimization

In general, graph representation shown in Fig. 4.1 is used for a binary labeling problems, where non-terminal nodes $p \in \mathcal{P}$ represent pixels or voxels, while terminal nodes t and s represent binary labels 0 and 1, where $t = 0$ denote a background label L_{bkg} and $s = 1$ denote an object label L_{obj} . Assume that x_p is the intensity value of pixel p and \mathcal{N}_p is a small neighborhood around p , not including x_p . Then, q denotes a neighboring node of p and $q \in \mathcal{N}_p$. Let $\mathbf{f} = (f_1, \dots, f_p, \dots, f_{|\mathcal{P}|})$ be a binary vector whose components $f_p \in \{L_{\text{bkg}}, L_{\text{obj}}\}$ specify assignments to pixel p , where each pixel p can be either “obj” or “bkg”. Vector \mathbf{f} defines a segmentation. The global energy function that integrates region and boundary properties of \mathbf{f} is defined in the same way as in Eq. (3.27):

$$E(\mathbf{f}) = \underbrace{\lambda \sum_p D_p(f_p)}_{\text{data term}} + \underbrace{\sum_{p,q} V_{p,q}(f_p, f_q)}_{\text{smoothness term}}. \quad (4.2)$$

The coefficient $\lambda \geq 0$ specifies a relative importance of the region properties term versus the boundary properties term. A regional term is also called a data term because it is derived from the observed data and it expresses the label preference for each node p . A boundary term is also called a smoothness term where the interaction (pairwise) potential $V_{p,q}(f_p, f_q)$ expresses the prior knowledge about the optimal labeling \mathbf{f} and is derived from the neighborhood interaction (e.g. MRF).

The data term $D_p(f_p)$ assumes that the individual penalties for assigning pixel p to “object” and “background”, correspondingly $D_p(L_{\text{obj}})$ and $D_p(L_{\text{bkg}})$, are given. For example, the data penalty $D_p(f_p)$ can represent how x_p (the intensity of pixel p) fits into given intensity models (e.g. histograms) of the object and background:

$$\begin{aligned} D_p(L_{\text{obj}}) &= -\ln P(x_p | L_{\text{obj}}) \\ D_p(L_{\text{bkg}}) &= -\ln P(x_p | L_{\text{bkg}}). \end{aligned} \quad (4.3)$$

This definition of the data term is motivated by the MAP-MRF formulations in [Greig et al., 1989]. Defined in this way, the smaller the value of $D_p(f_p)$ the more likely is the label f_p for node p .

The smoothness term describes a penalty for a discontinuity between neighboring elements p and q , where the interaction potential $V_{p,q} \geq 0$. The cost of $V_{p,q}$ is close to zero when the neighboring elements p and q are very different (e.g. in their intensity), and $V_{p,q}$ is large when p and q are similar. The penalty $V_{p,q}$ can also decrease as a function of distance between p and q . Often, the costs $V_{p,q}$ is calculated as follows:

$$V_{p,q} \propto \exp\left(-\frac{(x_p - x_q)^2}{2\sigma^2}\right) \frac{1}{\text{dist}(p, q)}. \quad (4.4)$$

The pairwise potential $V_{p,q}(f_p, f_q)$ expresses the prior knowledge about the optimal labeling \mathbf{f} .

This function penalizes a lot for discontinuities between pixels of similar intensities when $|x_p - x_q| < \sigma$. However, if pixels are very different, $|x_p - x_q| > \sigma$, then the

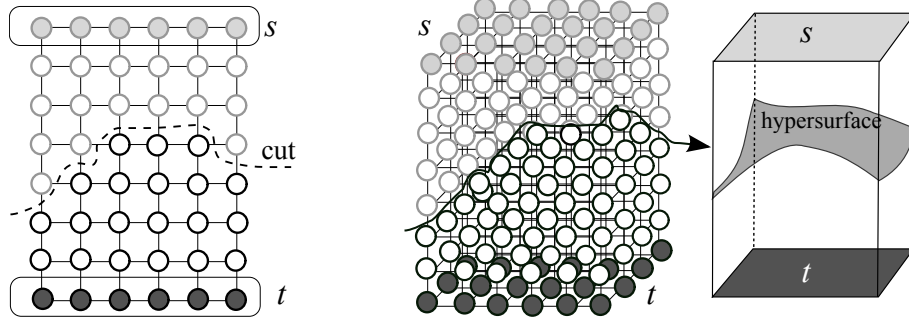


Figure 4.3: Illustration of a 2D graph cut with a curve (on the left) and a 3D graph cut with a surface (on the right).

penalty is small. This function corresponds to the distribution of noise among neighboring pixels of an image. Since in brain MRI the noise distribution approximates a Gaussian distribution (see Section 3.1.4), σ^2 can be calculated as:

$$\sigma^2 = \sum_{i=1}^n \left(\frac{(x_i - \mu)^2}{n} \right). \quad (4.5)$$

In the case of binary energy minimization in Eq. (4.2), it is possible to get a globally optimal labeling \mathbf{f} if and only if the pairwise interaction potential $V_{p,q}(f_p, f_q)$ satisfies the regularity condition

$$V_{p,q}(0,0) + V_{p,q}(1,1) \leq V_{p,q}(0,1) + V_{p,q}(1,0). \quad (4.6)$$

The theoretical proof of this regularity condition can be found in [Kolmogorov and Zabih, 2004].

This s - t graph cut segmentation method with binary labels is not restricted to only 2D images and can compute globally optimal segmentation on volumetric 3D images as well as on volumetric images of any dimension. This was shown in the work of Boykov et al. [Boykov and Kolmogorov, 2004, Boykov and Funka-Lea, 2006]. In the case of 2D images, a graph cut can be represented with a curve and for N-D images a cut is a hyper-surface, see illustration for 2D and 3D case in Fig. 4.3.

Although the s - t graph cut approach is computationally feasible for many tasks, its straightforward implementation for high-resolution images and 3D volumes is limited both by the supra-linear time complexity and the intense memory requirements [Boykov and Funka-Lea, 2006]. Recent results in Lombaert et al. [Lombaert et al., 2005] showed that multi-level and banded techniques can mitigate the problem.

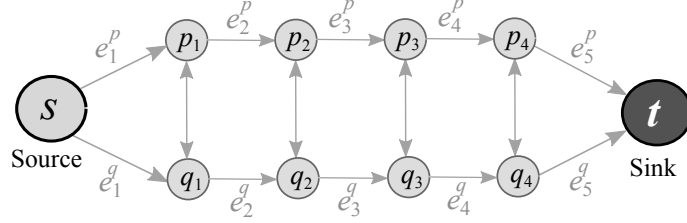


Figure 4.4: Part of the graph construction for multi-label energy minimization with 5 labels.

4.1.3 Multi-label optimization

Graph cuts can also be used for multi-label energy minimization where $|\mathcal{L}| > 2$. In certain cases the minimization of the multi-label energy can be exact, but more often only approximate minimization is possible.

The exact minimum can be found efficiently via graph cuts only if \mathcal{L} is a finite 1D set, the labels are linearly ordered and the interaction potential is $V_{p,q}(f_p, f_q) = |f_p - f_q|$ [Boykov et al., 2001]. In this case the energy function is:

$$E(\mathbf{l}) = \lambda \sum_p D_p(f_p) + \sum_{p,q} w_{p,q} |f_p - f_q|. \quad (4.7)$$

In this multi-label case a graph $\mathcal{G} = (\mathcal{V}, \mathcal{E})$ is constructed as follows. Graph nodes \mathcal{V} contain terminals s and t and for each node p a set of nodes p_1, p_2, \dots, p_{k-1} is created. All nodes are connected with edges $\{e_1^p, \dots, e_k^p\}$, where $e_1^p = \{s, p_1\}$, $e_j^p = \{p_{j-1}, p_j\}$, and $e_k^p = \{p_{k-1}, t\}$. Each edge e_j^p has a weight $K_p + D_p(j)$, where $K_p = 1 + (k-1) \sum_{q \in \mathcal{N}_p} w_{p,q}$. For each pair of neighboring nodes p, q and for each $j = \{1, \dots, k-1\}$ create an edge (p_j, q_j) with weight w_{pq} .

Fig. 4.4 illustrates the part of the graph \mathcal{G} which corresponds to two neighbors p and q . For each node p , a cut on the graph \mathcal{G} separates at least one edge e_i^p . The weights for e_i^p are assigned sufficiently large so that the min-cut separates exactly one of them for each p . This creates a correspondence between the min-cut and an assignment of a label to p . If the min-cut separates edge e_i^p , then a label i is assigned to p .

4.1.3.1 Approximate optimization

In the majority of cases, only the approximate optimization of the multi-label energy function is possible. The major restriction is that the smoothness term in the energy function must only involve pairs of pixels. The most popular approximation methods that efficiently find a local minimum for an arbitrary set of labels \mathcal{L} are the α -expansion and the $\alpha\beta$ -swap algorithms proposed by Boykov et al. [Boykov et al., 2001], which are also called the move-making algorithms.

Both the expansion and the swap algorithms find a local minimum of the energy function defined as in Eq. (4.2) with respect to very large moves. These large moves allow

a group of image elements to change their label simultaneously, which is in contrast to the standard moves where only one pixel can change one label at the time. The standard moves are used in methods such as Iterated Conditional Modes (ICM) [Besag, 1986] and simulated annealing [Geman and Geman, 1984], which sometimes give results that are far from the global optimum as demonstrated in [Greig et al., 1989]. The move-making algorithms find good approximate solutions by iteratively running min-cut/max-flow algorithms on appropriate graphs [Boykov et al., 2001, Boykov and Kolmogorov, 2004]. Boykov et al. proved in their work [Boykov et al., 2001] that by using α -expansion moves any labeling locally is within a known factor of global minimum.

The main idea behind these two methods is to decompose the segmentation problem with multiple labels into a set of problems defined over a set of binary labels. In this case the binary labels make decision whether the node keeps already assigned label or it takes the new proposed label. The algorithms start with some initial labeling and then iteratively find the optimal subset of nodes (i.e. giving the largest energy decrease) to switch to the new proposed label. The expansion algorithm performs an iteration for every label $\alpha \in \mathcal{L}$, and the swap algorithm for every pair of labels $\alpha, \beta \in \mathcal{L}$. The algorithm stops when no further decrease of the energy is possible. Both algorithms terminate in a finite number of steps.

Since in this thesis we use only α -expansion algorithm for three-label graph cut optimization, we will explain it in more detail.

4.1.3.2 α -expansion algorithm

Let \mathbf{f} denote a given labeling (an input labeling) and \mathbf{f}' a new labeling. A labeling \mathbf{f} uniquely defines an image partition $\mathbf{P} = \{\mathcal{P}_l | l \in \mathcal{L}\}$, where $\mathcal{P}_l = \{p \in \mathcal{P} | f_p = l\}$ is a subset of nodes assigned label l . A new labeling \mathbf{f}' defines a new partition \mathbf{P}' . Given a label α and an input labeling \mathbf{f} , the goal is to find a labeling $\hat{\mathbf{f}}$ that minimizes the energy E over all labelings within one α -expansion of \mathbf{f} .

The outline of the α -expansion algorithm is:

1. Start with an arbitrary labeling \mathbf{f} .
2. Set success:=0.
3. For each label $\alpha \in \mathcal{L}$:
find $\hat{\mathbf{f}} = \arg \min E(\mathbf{f}')$ among \mathbf{f}' within one α -expansion of \mathbf{f} .
4. If $E(\hat{\mathbf{f}}) < E(\mathbf{f})$, then set $\mathbf{f} := \hat{\mathbf{f}}$, success:=1 and go to the step 2.
5. Return labeling \mathbf{f} .

The structure of the α -expansion graph $\mathcal{G}_\alpha = (\mathcal{V}_\alpha, \mathcal{E}_\alpha)$ is illustrated in Fig. 4.5 on the case of a 1D image for simplicity. The set of nodes includes two terminals α and $\bar{\alpha}$

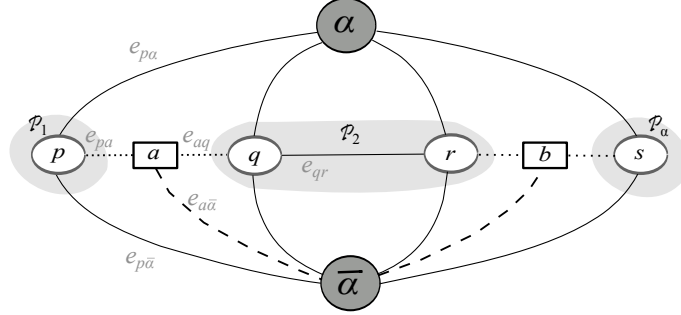


Figure 4.5: An example of the graph structure for α -expansion on the case of a 1D image. The set of pixels in an image are represented with nodes $\mathcal{P} = \{p, q, r, s\}$ and there are two auxiliary nodes $a = a_{pq}$ and $b = a_{rs}$. The current partition is $\mathbf{P} = \{\mathcal{P}_1, \mathcal{P}_2, \mathcal{P}_\alpha\}$, where $p \in \mathcal{P}_1$, $\{q, r\} \in \mathcal{P}_2$ and $s \in \mathcal{P}_\alpha$.

and all image elements $p \in \mathcal{P}$. Additionally, an auxiliary node a_{pq} is created for each pair of neighboring nodes $\{p, q\} \in \mathcal{N}$ that are separated in the current partition (e.g. such that $f_p \neq f_q$), where the set of all auxiliary nodes is denoted by \mathcal{A} . Auxiliary nodes are introduced at the boundaries between partition sets \mathcal{P}_l for $l \in \mathcal{L}$. Then, we can write the set of all nodes \mathcal{V}_α as:

$$\mathcal{V}_\alpha = \{\alpha, \bar{\alpha}, \mathcal{P}, \mathcal{A}\}. \quad (4.8)$$

Each node p is connected to the terminal nodes α and $\bar{\alpha}$ by t-links $e_{p\alpha}$ and $e_{p\bar{\alpha}}$ respectively, where the set of all t-links is denoted by $\mathcal{E}_{\text{t-links}}$. Each pair of neighboring nodes, which are not separated by partition \mathbf{P} ($f_p = f_q$), is connected by n-link \mathcal{E}_{pq} , where the set of all n-links is denoted by $\mathcal{E}_{\text{n-links}}$. Additionally, for each pair of neighboring nodes $\{p, q\} \in \mathcal{N}$ which are separated by partition \mathbf{P} ($f_p \neq f_q$), three edges are defined $\mathcal{E}_{pq} = \{e_{pa}, e_{aq}, e_{a\bar{\alpha}}\}$, where $a = a_{pq}$ is the auxiliary node. The set of all triplet of edges is denoted by \mathcal{A}_{pq} . Then, we can write the set of all edges \mathcal{E}_α as:

$$\mathcal{E}_\alpha = \{\mathcal{E}_{\text{t-links}}, \mathcal{E}_{\text{n-links}}, \mathcal{A}_{pq}\}. \quad (4.9)$$

Any cut C on graph \mathcal{G}_α must separate one t-link for any pixel $p \in \mathcal{P}$. An image element p keeps its old label f_p if the cut C separates the t-link $e_{p\bar{\alpha}}$ and p is assigned a new label α if the cut C separates the t-link $e_{p\alpha}$. The cut C also separates n-links e_{pq} if and only if the cut C connects nodes p and q to different terminals. In the case of the triplet set of edges \mathcal{E}_{pq} , the cut C can be defined in 4 different ways:

1. If $e_{p\alpha}, e_{q\alpha} \in C$, then $C \cap \mathcal{E}_{pq} = \emptyset$, see Fig. 4.6(a);
2. If $e_{p\bar{\alpha}}, e_{q\bar{\alpha}} \in C$, then $C \cap \mathcal{E}_{pq} = e_{a\bar{\alpha}}$, see Fig. 4.6(b);
3. If $e_{p\bar{\alpha}}, e_{q\alpha} \in C$, then $C \cap \mathcal{E}_{pq} = e_{pa}$, see Fig. 4.6(c);
4. If $e_{p\alpha}, e_{q\bar{\alpha}} \in C$, then $C \cap \mathcal{E}_{pq} = e_{aq}$

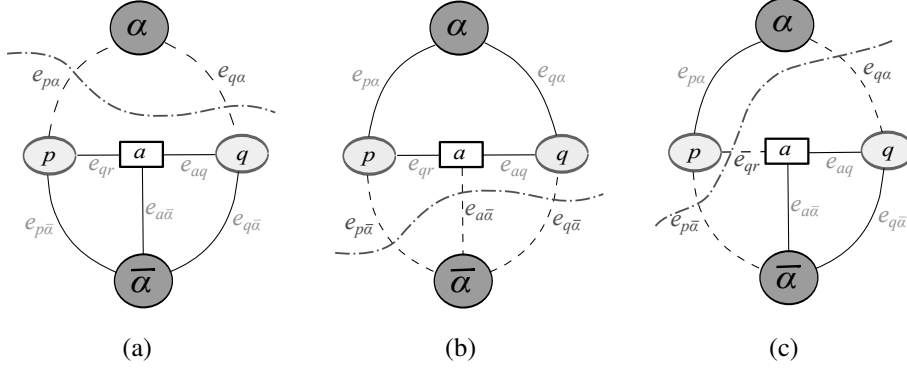


Figure 4.6: An illustration of the possible cuts on a graph \mathcal{G}_α for two nodes p, q , where $f_p \neq f_q$. (a) $C \cap \mathcal{E}_{pq} = \emptyset$; (b) $C \cap \mathcal{E}_{pq} = e_{a\bar{a}}$; (c) $C \cap \mathcal{E}_{pq} = e_{pa}$.

According to the study in [Kolmogorov and Zabih, 2004] the α -expansion algorithm may be used whenever $V_{p,q}(\alpha, \alpha) + V_{p,q}(\beta, \gamma) \leq V_{p,q}(\alpha, \gamma) + V_{p,q}(\beta, \alpha)$, for all $\alpha, \beta, \gamma \in \mathcal{L}$, which is also called the expansion inequality.

4.2 Three-label graph for brain segmentation

In this section we describe our graph cut 3D brain MRI segmentation method, which is based on the multi-label α -expansion graph cut algorithm proposed by Boykov et al. [Boykov et al., 2001, Boykov and Kolmogorov, 2004].

To segment brain MRI data we create an extended 3D graph cut method with three labels $\mathcal{L} = \{L_{WM}, L_{GM}, L_{CSF}\}$ and three terminal nodes WM, GM, CSF, which refer to the three brain tissue types: WM, GM and CSF. First, we define the MRF-based energy function in the same way as in Eq.(4.2). Then, we define the data term and the smoothness term based on the intensity and boundary information of the observed MRI data. The fusion of intensity and boundary properties and definitions of data and smoothness terms are described in the following sections.

4.2.1 Data term

The data term $D_p(l_p)$, $l_p \in \{L_{WM}, L_{GM}, L_{CSF}\}$ defines t-links and is derived from the observed MRI data assuming a Gaussian mixture model (GMM) as an intensity model, where each tissue class (WM, GM and CSF) is modeled by a Gaussian distribution, see Section 3.1.4. A GMM is fitted to intensity histogram using the expectation-maximization (EM) algorithm as described in [D'Souza, 2004] and in Section 3.3.2.3. In this way, the partial volume effects, which occur at the boundaries between tissues, are also taken into account.

After the Gaussians are calculated, we have for each intensity value the probabilities of belonging to the three tissues $P(x_p|L_{WM})$, $P(x_p|L_{GM})$ and $P(x_p|L_{CSF})$. Since adding a constant to $D_p(l_p)$ does not change the energy formulation [Boykov et al., 2001], we assume without loss of generality that all $D_p(l_p)$ are non-negative. Following this, we define the data term $D_p(l_p)$ for each label as the maximum penalization constant K_{\max} minus the sum of the negative log-likelihoods of the probabilities that voxel p belongs to the other two labels:

$$\begin{aligned} D_p(L_{WM}) &= K_{\max} - ((-\ln P(x_p|L_{GM}) + (-\ln P(x_p|L_{CSF}))), \\ D_p(L_{GM}) &= K_{\max} - ((-\ln P(x_p|L_{WM}) + (-\ln P(x_p|L_{CSF}))), \\ D_p(L_{CSF}) &= K_{\max} - ((-\ln P(x_p|L_{WM}) + (-\ln P(x_p|L_{GM}))). \end{aligned} \quad (4.10)$$

The constant K_{\max} is chosen large enough to keep $D_p(l_p)$ positive.

4.2.2 Smoothness term

The smoothness term $V_{p,q}$ defines n-links and is based on two terms: the intensity $V_{p,q}^I$ term and the boundary term $V_{p,q}^B$:

$$V_{p,q} = cV_{p,q}^I + (1 - c)V_{p,q}^B, \quad (4.11)$$

The intensity term depends on the intensity information and the distance between the neighboring elements p and q ($q \in \mathcal{N}_p$), while the boundary term depends on the boundary information. The parameter c controls the contribution of the boundary and intensity terms. When $c = 1$, only the intensity discontinuity part has an influence and when $c = 0$, only the boundary term has an influence.

The boundary information is derived from image gradients, which have been often used as a measure of image sharpness and an indication of image boundaries. First, the gradient g_p is computed for each image voxel p as the derivative of the intensity values of the neighboring voxels in the chosen 3D neighborhood \mathcal{N}_p , see Section 3.4.1. Then, the mean gradient \bar{g}_p for the considered voxel is calculated to reduce the noise influence. For each voxel p , the boundary information is calculated as:

$$B_p = 1 - \exp(-\bar{g}_p/\sigma_g), \quad 0 < B_p < 1, \quad (4.12)$$

where σ_g is the normalization factor. In the computation of the boundary information B_i between two neighbouring voxels p and q , the maximum mean gradient is used from the set of local maxima along the line joining elements p and q , denoted as $M_{p,q}$ [Malik et al., 2001]. The gradient-based boundary term is defined as $V_{p,q}^B = (1 - \max_{i \in M_{p,q}}(B_i))$. B_i is nearly 1 whenever the gradient is maximum at i , which means that there is a strong local maximum along $M_{p,q}$ and that elements p and q have weak connection between them. On the contrary, if only the weak local maxima exist along $M_{p,q}$, then B_i is nearly 0 and the connection between the two pixels will be strong, w_B will be nearly 1. For example, this will happen in a constant brightness region.

Following these definitions, the smoothness term $V_{p,q}$ can be calculated as:

$$V_{p,q} = \underbrace{c \left(\exp \left(-\frac{(x_p - x_q)^2}{2\sigma^2} \right) \frac{1}{\text{dist}(p, q)} \right)}_{\text{intensity term}} + \underbrace{(1 - c) \left(1 - \max_{i \in M_{p,q}} (B_i) \right)}_{\text{boundary term}}. \quad (4.13)$$

The intensity term penalizes intensity discontinuities and is based on the MRF. Each node in the lattice \mathcal{P} corresponds to a voxel in the brain MRI volume and n-links between nodes are created using the same neighborhood system \mathcal{N}_p as in the boundary term. The edge (n-links) weights are defined by the first term in Eq. (4.13), which consists of the squared intensity difference between the two voxels $(x_p - x_q)^2$, the intensity variance σ^2 over the whole volume and the distance $\text{dist}(p, q)$ between both voxels. When the intensity difference is small, the weight will be large and vice versa. Consequently, the voxels with similar intensity values will less likely be separated from each other because the cost will be higher. Similarly, the voxels with largely differing intensities will be faster separated. The variance σ^2 is included to adapt between images with overall strongly differing intensity values and those with overall less differing intensity values. Finally, taking the spatial distance between into account ensures that voxels that are further away contribute less to the neighbourhood system of the considered voxel.

4.2.3 Graph construction and energy minimization

The construction of the three-label graph $\mathcal{G} = (\mathcal{V}, \mathcal{E})$ and a simple example of 2D image segmentation are illustrated in Fig. 4.7. For simplicity, an example is given for a 2D image with 3×3 pixels. The set of nodes consists of three terminals WM, GM, CSF and lattice nodes $p \in \mathcal{P}$, where each lattice node represent one image pixel.

The first step in Fig. 4.7 involves the creation of the graph with two different set of edges: n-links and t-links. Each node p is connected to the terminal nodes WM, GM, CSF by t-link. The weights of t-links are defined by a GMM model and are represented in the energy function as the data term $D_p(l_p)$, $l_p \in \{L_{\text{WM}}, L_{\text{GM}}, L_{\text{CSF}}\}$. Each pair of neighboring nodes $\{p, q\} \in \mathcal{N}$ is connected by n-link e_{pq} according to the predefined neighborhood system \mathcal{N}_p . The weights of n-links are defined by a MRF model and a gradient image, and are represented in the energy function as the smoothness term $V_{p,q}$.

The created graph is a three-label graph, as shown in the second step. An optimal segmentation will be achieved by minimizing the energy function for all possible segmentations. The minimization of the energy function is achieved by decomposing the three-label problem into a set of problems defined over a set of binary labels, using α -expansion algorithm, see Section 4.1.3.2. The third step presents the final result of this minimization that consists of a multi-way cut and a final label assignment to pixels. The resulting graph can be denoted by $\mathcal{G} = (\mathcal{V}, \mathcal{E} - C)$, where the cost of the cut $|C|$ is the sum of its edge weights in the edge set C .

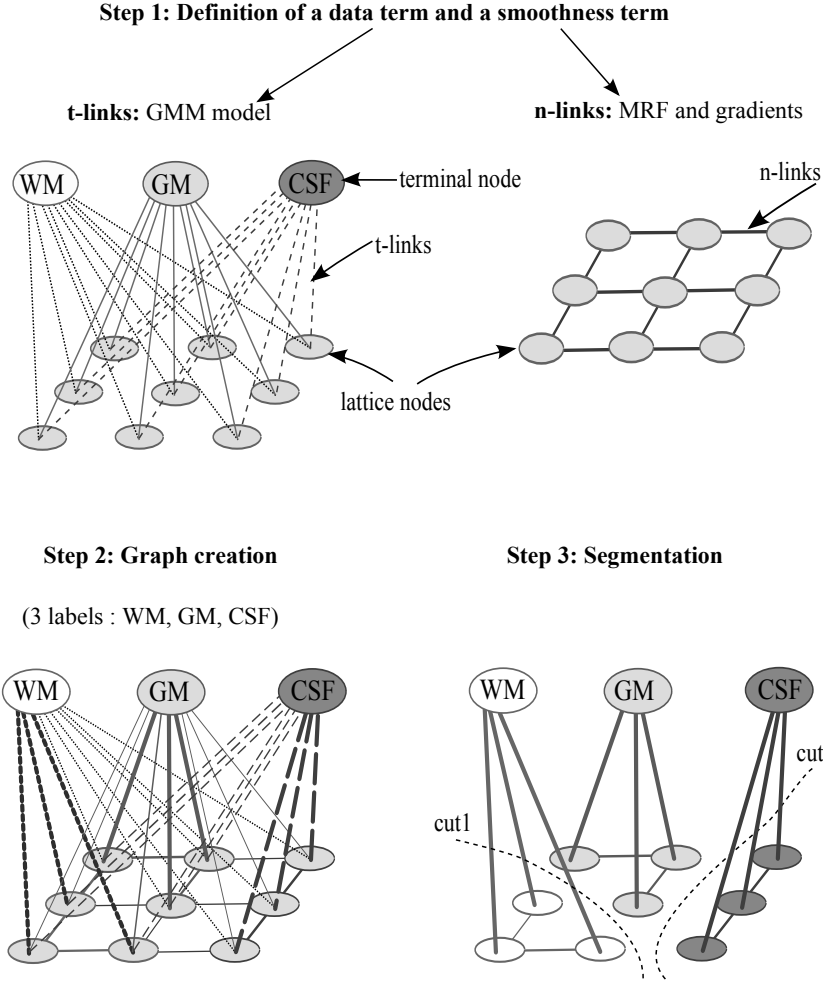


Figure 4.7: Overview of the three-label graph cut segmentation for a 2D image with 3×3 pixels. In the first step, the two different types of edges of the graph are presented. The second step shows the complete graph. The edges between lattice nodes $p \in \mathcal{P}$ are initialized with weights that are calculated based on the smoothness properties (MRF and gradients). The weights for the edges between lattice nodes and terminal nodes (labels) are based on the data properties (intensity model). The third step presents the final result of the energy minimization and a final label assignment to pixels.

The major problem with energy minimization of the large 3D volumetric data using graph cuts is in the computational cost. Graph cut implementation for high-resolution volumetric MRI of the brain such as $256 \times 256 \times 120$ or even higher $512 \times 512 \times 120$ is limited both by the supra-linear time complexity and the intense memory requirements. One of the solutions is to split the 3D volume into a number of volumes. In our

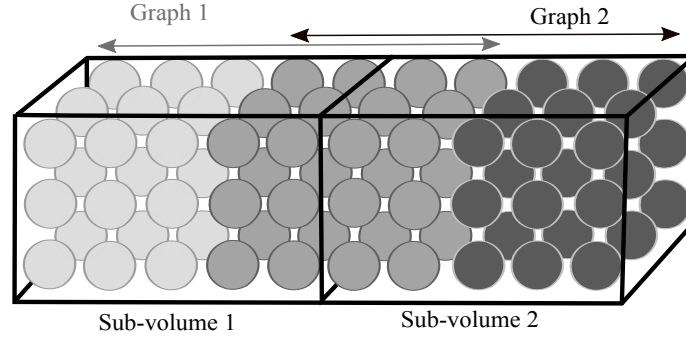


Figure 4.8: Illustration of a 3D volume splitting into two overlapping parts on a simplified example. Let's assume that all balls together make the entire 3D volume and that each ball represents one image voxel. The light gray balls represent the voxels from the first sub-volume, the dark gray balls represent the voxels from the second sub-volume and the mid-gray balls represent the overlapping voxels that belong to both the first and the second sub-volume. To do 3D segmentation we use 2 graphs, each for one sub-volume. The segmentation results are stored for the first and the second sub-volume to the middle of the overlap.

implementation we split the 3D volume into two overlapping sub-volumes. This overlap between sub-volumes is important because we want to keep continuity of the 3D edge information and the spatial context information that are included in the energy function. We use an overlap of 20 voxels wide and the segmentation results are stored for the first and the second sub-volume to the middle (10th voxel) of the overlap. This 3D volume splitting is illustrated in simplified example in Fig. 4.8.

4.3 Experimental results

In this section we present the performance of the proposed three-label graph cut method for 3D brain MRI segmentation (from hereon termed as 3DGC). The method was validated both quantitatively and qualitatively on a realistic digital brain phantom MRI data (BrainWeb) and real MRI data. The simulated brain MRI data were downloaded from the BrainWeb Database [BrainWeb, 2013, Collins et al., 1998] and the real MRI data were downloaded from the Internet Brain Segmentation Repository (IBSR) [IBSR, 2013]. The IBSR provides real patient MRI data and manually guided expert segmentation results, which are used as a “ground truth” segmentation in this study.

In all experiments we used T_1 -W MRI volumes and we performed a comparison study to other 3D brain MRI segmentation methods. Our quantitative results indicated that the 3D graph cut segmentation performs well in comparison with other state-of-the-art methods without the use of a prior knowledge of a preregistered statistical brain phantom.

4.3.1 Simulated brain MRI data - BrainWeb

To validate the method quantitatively, we need images with known “ground truth” because the gold standard for the analysis of real MR images does not exist, see Section 3.5. Thus, we used the simulated MRI from the realistic brain phantom, BrainWeb [Collins et al., 1998] ($181 \times 217 \times 181$ voxel matrix with a resolution of $1mm \times 1mm \times 1mm$), where the “ground truth” segmentation is provided. The BrainWeb data is available for different additive noise levels. The noise level (expressed in percentages) is relative to the average real and imaginary values of the overall brightness of the tissue class. The noise is generated using a pseudorandom Gaussian noise, which is added to both real and imaginary components before the final magnitude value of the simulated MR image is computed.

In the following experiments, we use the Dice coefficient ρ_i [Dice, 1945] as a similarity measure to quantify the overlap between the automated segmentation and the given “ground truth” for each tissue type i :

$$\rho_i = \frac{2|A_i \cap B_i|}{|A_i| + |B_i|}, \quad (4.14)$$

where A_i and B_i denote the set of pixels labeled into i by the “ground truth” and 3DGC segmentation respectively, and $|A_i|$ denotes the number of elements in A_i .

The Dice coefficient is in the range $0 \leq \rho_i \leq 1$ and has value 0 if there is no overlap between the two segmentations and 1 if both segmentations are identical. The average Dice coefficient ρ_{avr} , considering the Dice coefficients of all three brain tissues ρ_{WM} , ρ_{GM} and ρ_{CSF} , is calculated as follows:

$$\rho_{avr} = \frac{\rho_{WM} + \rho_{GM} + \rho_{CSF}}{3}. \quad (4.15)$$

4.3.1.1 Quantitative results

In Fig. 4.9 we show the results of different experiments where we tested the performance of the proposed 3DGC method for different noise levels 3%, 5%, 7% and 9%. First, in Fig. 4.9(a) we show comparison results between the proposed three-label graph cut method implemented in 3D and in 2D (slice by slice). The results show that the 3D implementation of the method has better performance for all noise levels. Then, in Fig. 4.9(b) we show the performance of the 3DGC method considering a different number of neighbors which are used to model the spatial contextual information. The best results are obtained for 18 neighbors for all noise levels. Following this, we experimentally searched for the values of the parameters λ and c , for which the 3DGC gives the best segmentation. Both parameters are strongly dependent on the noise level and are plotted in Fig. 4.9(c) and Fig. 4.9(d) respectively. The parameter λ is decreasing and the parameter c is increasing with the higher noise levels. Finally, we show in Fig. 4.9(e) the comparison between the two-label graph cut method presented in Section 4.1.2 and the proposed three-label graph cut method, for GM and

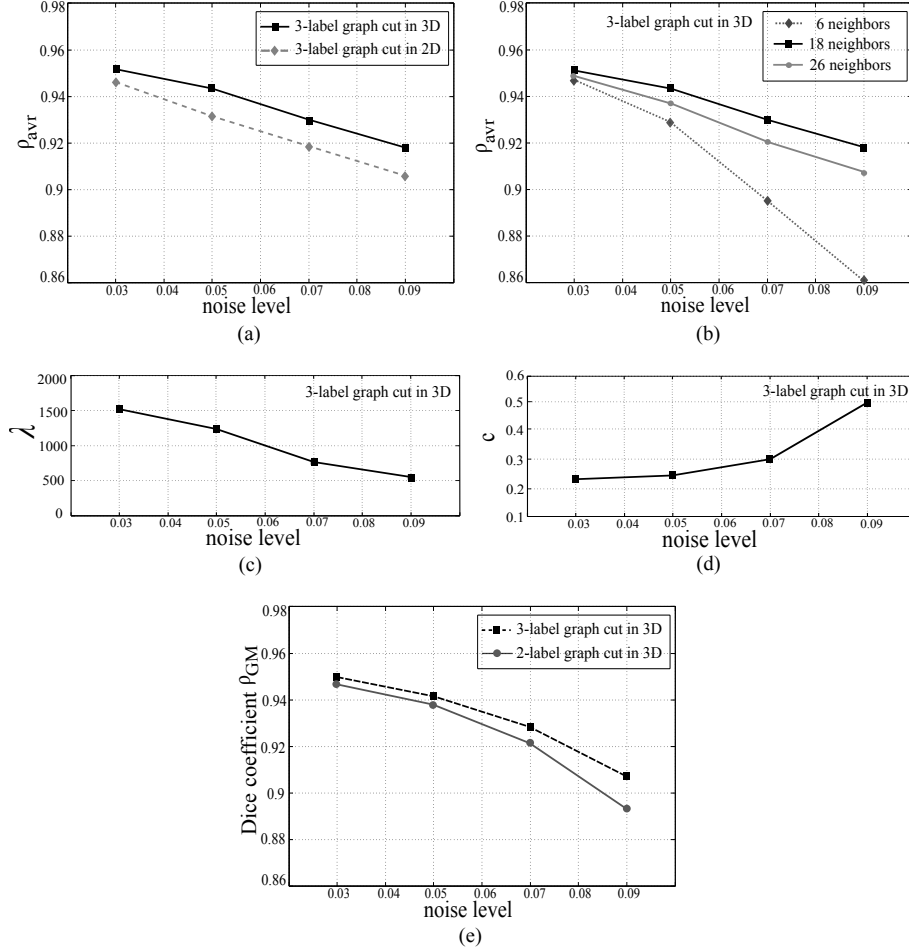


Figure 4.9: (a) The average similarity measure ρ_{avr} of the proposed graph cut method in 2D (slice by slice and using 8 neighbors) and in 3D (using 18 neighbors). (b) Sensitivity of the 3DGC method to a different number of neighbors. (c) The parameter λ for different noise levels and 18 neighbors. (d) The parameter c for different noise levels and 18 neighbors. (e) The similarity measure for the gray matter ρ_{GM} in the case of the 3DGC method and the two-label graph cut presented in Section 4.1.2 and implemented in 3D.

both implemented in 3D. In the two-label graph cut the first label is the gray matter and the second label is the rest of the brain.

Considering these experimental results, in the following experiments we use 18 neighbors for the 3DGC segmentation and depending on the noise level, we choose the appropriate parameters λ and c to obtain the optimal segmentation.

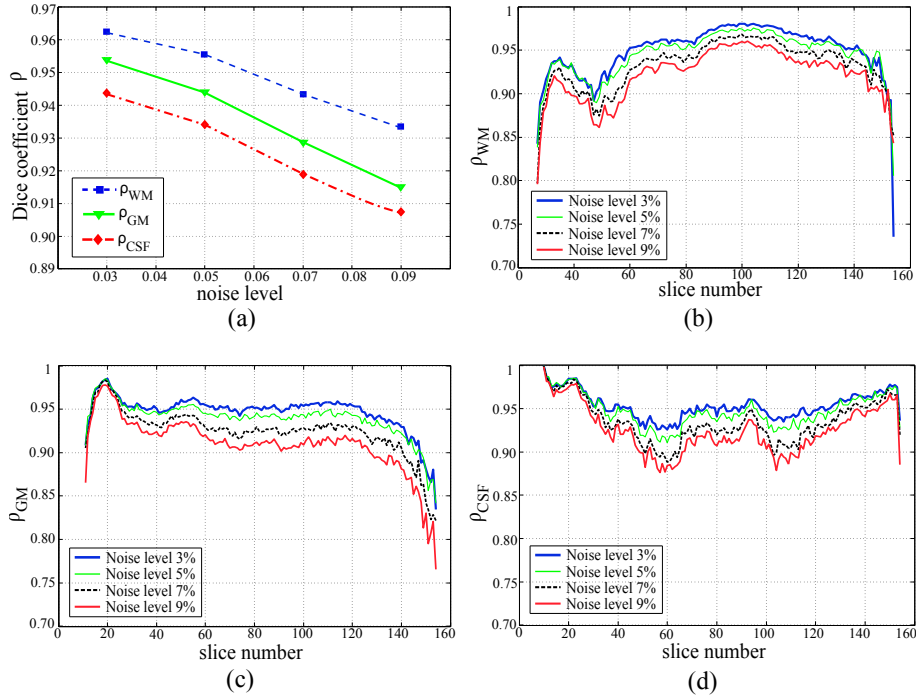


Figure 4.10: Segmentation performance of the 3DGC method for different noise levels. (a) The average similarity measure ρ_{avr} of the slices of the phantom volume in the range $[30 - 150]$, for different tissue types. The similarity measure of all individual slices per tissue type are show in (b) for WM, (c) for GM and (d) for CSF.

More detailed segmentation results of the 3DGC method for different noise levels are shown in Fig. 4.10. The results are presented for each tissue type individually ρ_{WM} , ρ_{GM} , ρ_{CSF} (for all BwainWeb data slices) and as the average Dice coefficient ρ_{avr} . Typically, only the slices in the range $[20 - 150]$ are taken into account for a quantitative evaluation and the average Dice coefficient ρ_{avr} calculation, because the slices outside this range do not contain the brain tissue. From the results we can see that the best results are obtained for the WM segmentation and the lowest results for the CSF segmentation. Considering individual Dice coefficients, we can see that ρ_{GM} is stable over a wide range of slice numbers, but drops in the higher regions of the brain. In contrast, ρ_{WM} is showing the better results in the higher than in the lower regions of the brain. In the case of ρ_{CSF} , the best performance is at the very low and high regions of the brain, while there are some decreases in the performance in the middle regions.

The segmentation results of the 3DGC method using BrainWeb data are compared with seven popular methods for 3D brain MRI segmentation: (1) FMRIB's Automated Segmentation Tool (FAST-FSL) [Zhang et al., 2001], (2) Statistical Parametric Mapping (SPM) [Ashburner and Friston, 2005], (3) Histogram-Based method with

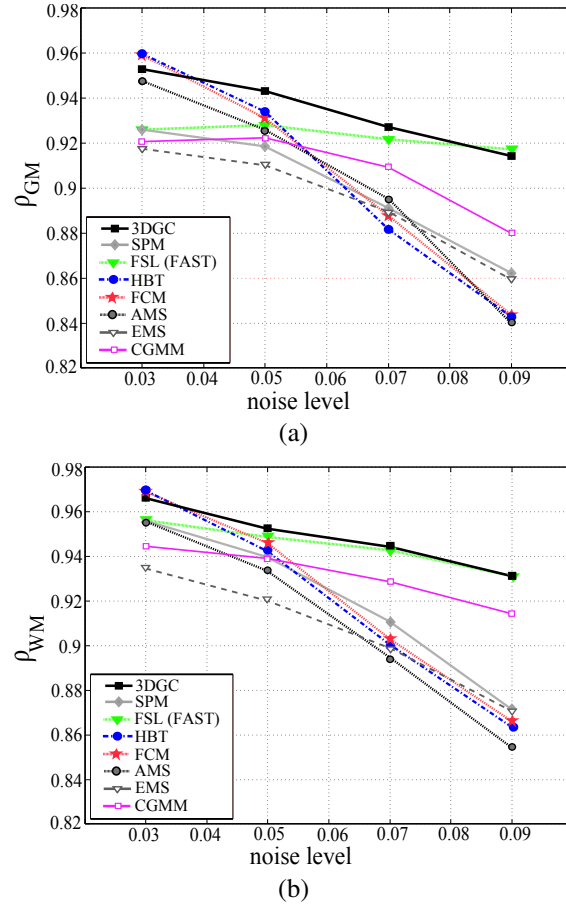


Figure 4.11: Comparison analysis of the 3DGC method with seven popular brain MRI segmentation methods. (a) The similarity measure for the gray matter ρ_{GM} . (b) The similarity measure for the white matter ρ_{WM} . For all segmentation methods the existing parameters were chosen to give the highest similarity measure.

automated Threshold (HBT) [Antel et al., 2002], (4) Fuzzy C-Means (FCM) [Bezdek, 1981], (5) EM-based Segmentation method (EMS) [Van Leemput et al., 1999], (6) Constrained Gaussian Mixture Model method (CGMM) [Greenspan et al., 2006] and (7) Adaptive Mean-Shift method (AMS) [Mayer and Greenspan, 2009]. The comparison results are presented in Fig. 4.11.

Results show that for the lowest noise level of 3%, HBT and FCM give the best results but for the higher noise levels, the accuracy of these methods decrease rapidly. For other noise levels, the 3DGC method outperforms other segmentation methods, except for the highest noise level of 9%, where the best performance in segmenting the GM was achieved using the FSL method. In all experiments, the parameters of the segmentation methods were selected to give the best segmentation result.

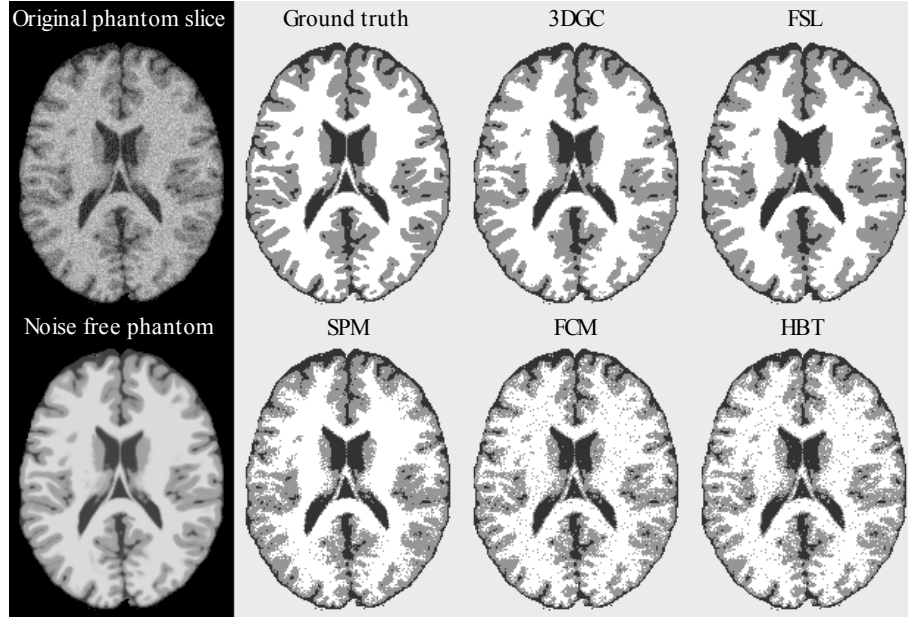


Figure 4.12: Segmentation results of the phantom slice 90 with the highest noise level 9% for the 4 different methods. In the upper left corner is the MRI image with the 9% noise and in the lower left corner is the original simulated MRI image without noise. The “ground truth” segmentation image is showing three tissue types: WM in white, GM in light gray and CSF in dark gray. The 3DGC and FSL segmentation results show the closest resemblance to the “ground truth” image, while the HBT, FCM and SPM retain more noise artifacts.

4.3.1.2 Qualitative results

To illustrate the quantitative results, in Fig. 4.12 we show the qualitative results on the BrainWeb phantom slice number 90 with the highest noise level 9%. In this representative example, we can see how different segmentation methods including the 3DGC, FSL, SPM, FCM and HBT are performing in the presence of noise. It is clear from Fig. 4.12 that the HBT and FCM have a lot of noise artifacts, which are especially visible in the white matter regions. This is because these two methods are very sensitive to image noise and deal with image pixels as separate points, without integrating the spatial contextual information. The SPM segmentation shows less noise artifacts, but still lacks in accurate labeling of the neighboring voxels and do not preserve the homogeneous regions. Finally, the FSL and 3DGC methods show the best segmentation performance and the highest robustness to noise. They both succeed to enforce the spatial coherence and correctly label the neighboring voxels in the noisy areas. Judging on these visual results, it is difficult to say which method performs better in this particular example. However, the benefit of the 3DGC method in comparison to FSL is that we do not use the spatial priors based on the atlas information, which are used in FSL method and still, we obtain a high segmentation accuracy.

4.3.2 Real MRI data - IBSR

In this section we demonstrate the performance of the 3DGC on real MRI datasets for the brain gray matter segmentation. A set of 20 normal T₁-W MRI brain data was downloaded from the IBSR repository [IBSR, 2013] together with the manually guided expert segmentation results, which are used as a “ground truth” segmentation. Each MRI volume consists of about 60 coronal T₁-W slices with the inter-slice resolution of 3.1 mm (thickness between consecutive slices). We also downloaded from the IBSR repository segmentation overlap index of the several brain MRI segmentation methods, which are available for a comparison study. The overlap index between the manual expert segmentation (the “ground truth” segmentation) and the automatic segmentation is measured with the Tanimoto coefficient $\mathcal{T}(i)$ (also known as Jaccard index) for each tissue type i

$$\mathcal{T}_i = \frac{|A_i \cap B_i|}{|A_i| + |B_i| - |A_i \cap B_i|}, \quad (4.16)$$

where A_i and B_i denote the set of pixels labeled into i by the “ground truth” and the segmentation method respectively, and $|A_i|$ denotes the number of elements in A_i . Note that $\mathcal{T}(i) \leq \rho(i)$ and $0 \leq \mathcal{T}(i) \leq 1$.

Before we tested the performance of the 3DGC method on the IBSR data, we did the bias field correction of all MRI scans using the method proposed by [Sled et al., 1998]. We skipped the brain extraction step, because we downloaded MRI scans where the non-brain structures were previously removed. For more details about the bias field correction and the brain extraction see Section 3.2.

4.3.2.1 Quantitative results

Quantitative results of the 3DGC method along with results of six other segmentation methods from the IBSR website and literature are shown in Fig. 4.13 for all 20 volumes. The six segmentation methods that we used in this comparison study are: (1) Adaptive Mean-Shift method (AMS) [Mayer and Greenspan, 2009], (2) Adaptive MAP method (AMAP) [Rajapakse et al., 1997], (3) Biased-MAP method (BMAP) [Rajapakse and Kruggel, 1998], (4) Fuzzy C-Means (FCM) [Bezdek, 1981], (5) Bayesian method for automatic segmentation of brain MRI (MPM-MAP) method [Marroquin et al., 2002] and (6) MLC method [Duda et al., 1973].

The proposed 3DGC method competes favorably with the other considered methods. This trend is most evident in the first six volumes, which are quoted in the literature as being particularly difficult scans, of low contrast and relatively large spatial inhomogeneities. The IBSR brain volumes have been roughly ordered by their difficulty to be segmented, ordered in decreasing level of difficulty. The 3DGC results are consistent across the varying brain data, whereas the alternate segmentation methods exhibit a strong decrease in performance in the more difficult cases.

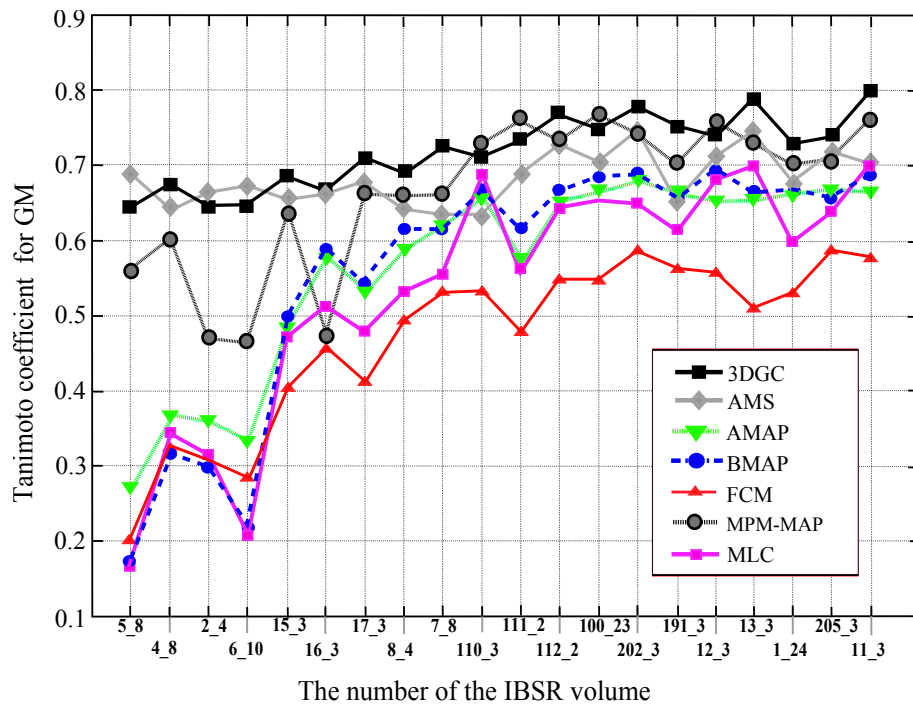


Figure 4.13: Comparison analysis of the 3DGC method with six popular brain MRI segmentation methods. The graph shows the Tanimoto similarity measure for the gray matter \mathcal{T}_{GM} . For all segmentation methods the existing parameters were chosen to give the highest similarity measure.

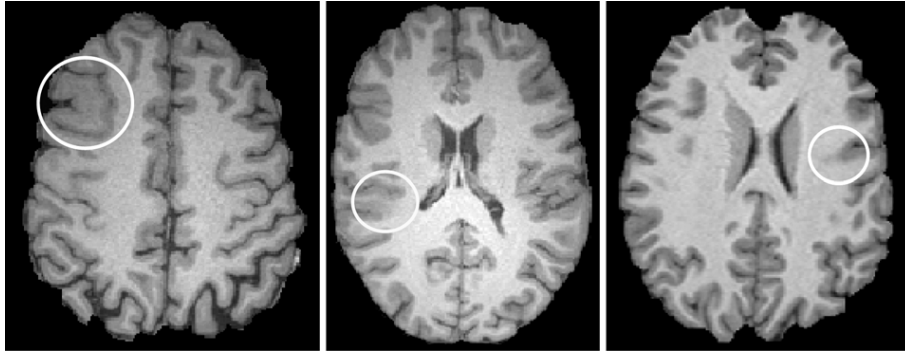


Figure 4.14: Three examples of T_1 -W MRI with FCD lesions. The lesions are indicated with a circle. They are characterized by increased cortical thickness and blurring of the cortical gray matter and white matter border.

4.4 3D brain cortex segmentation in patients with FCD

In patients with intractable epilepsy, focal cortical dysplasia (FCD) is the most frequent malformation of cortical development. The latest studies have indicated that one out of two hundred adults suffer from recurrent epilepsy [Rajan et al., 2009] and 30% of them are due to FCD. In clinical treatment, the FCD lesions often have to be removed by surgery and before this can be done, it is necessary to detect and delineate the lesions. However, FCD detection is a very challenging task and standard radiological MRI evaluation of the lesions still fails in many cases, because of the complexity of the cortex and subtle behavior of the lesions. Therefore, developing an automatic algorithm for FCD detection would be a very useful tool for clinical diagnosis and surgical planning.

On MRI scans, FCD lesions are typically characterized with the increased cortical thickness, blurring of the gray-white matter interface and hyperintensity signal in the lesion area. Examples of T_1 -W MR images with FCD lesions are shown in Fig. 4.14.

To date, several methods have been reported for detection and visual improvement of FCD lesions [Bernasconi et al., 2001, Antel et al., 2002, Colliot et al., 2005, Besson et al., 2008]. Often, the T_1 -W MRI scans are first preprocessed by removing skull, lipid layers and intensity inhomogeneity. Then, the maps of the three main FCD features for a lesion detection are calculated: cortical thickness map, gradient map and relative intensity map. The cortical thickness map is derived from a cortical thickness measurement, which requires MRI segmentation of the brain cortex as a preprocessing step. However, the choice of the selected segmentation method and its segmentation accuracy can highly affect the cortical thickness map and final FCD lesion detection. For instance, in the approach of [Bernasconi et al., 2001], the main problem is a large false positive rate where many non-lesion areas are detected as lesions. This is mainly due to the limitations of the cortical thickness model, which does not evaluate the gray matter thickness with enough accuracy. The overview of the FCD lesion detec-

tion steps is shown in Fig. 4.15.

In general, accurate MRI brain cortex segmentation is a challenging task, not only because of the complicated structure of the brain and the anatomical variability between subjects, but also because of the presence of noise and often low contrast between brain tissues in MRI. This is even a more difficult problem in the patients with subtle brain lesions which might be hard to visualize on brain MRI. Since manual segmentation is time-consuming, prone to errors and subjective, automated and accurate tissue segmentation is needed. Currently, the most popular methods used for brain cortex segmentation in FCD patients are the histogram-based method with automated threshold (HBT) [Antel et al., 2002], FMRIB's Automated Segmentation Tool (FAST-FSL) [Zhang et al., 2001], Statistical Parametric Mapping (SPM) [Ashburner and Friston, 2005] and Fuzzy C-Means (FCM) [Bezdek, 1981]. The comparative segmentation results of these methods on the healthy brain are shown in Section 4.4.1.

While most of these methods are suitable for general brain tissue segmentation, HBT is used in the vast majority of FCD detection techniques because of its simplicity and good computational efficiency. The main disadvantage of the HBT method (as well as of the standard FCM method) is its high sensitivity to noise and other imaging artifacts. In contrast, the FSL, SPM and graph cuts methods are less sensitive to noise because they include the spatial contextual information in the image segmentation.

In this Section we use an improved three-label 3D graph cut segmentation framework, which integrates intensity and boundary information, to segment brain cortex in 3D in FCD patient. The boundary information is used to constrain the shape of the cortex with a goal to achieve more precise cortex segmentation. The performance of the method is tested on real patients with FCD lesions. The location and the size of all FCD lesions is manually indicated by an expert physician in all patients. This manual segmentation was used as a "ground truth" for the qualitative evaluation of the experimental segmentation results.

Our results showed that the proposed method is effective, robust to noise and achieves good segmentation of the brain cortex. The qualitative validation, visually verified by a medical expert, showed that the FCD lesions were segmented well as a part of the cortex, indicating increased thickness and cortical deformation. The results of our segmentation can be further used for a cortical thickness measurement and lesion detection.

4.4.1 Qualitative validation

The qualitative validation was performed on MR images of 8 real patients with FCD lesions. The MRI data were recorded at Ghent University Hospital on a Siemens 3T MRI scanner ($256 \times 256 \times 176$ voxel matrix with a resolution of $1\text{mm} \times 1\text{mm} \times 1\text{mm}$). The MRI were preprocessed by removing skull, lipid layers and bias field. The cortex segmentation is visually evaluated by expert physician. In all cases the segmentation was successful and the lesions were segmented as part of the cortex. The segmentation results are shown in Fig. 4.16 for four patients. The original MRI slice is shown on

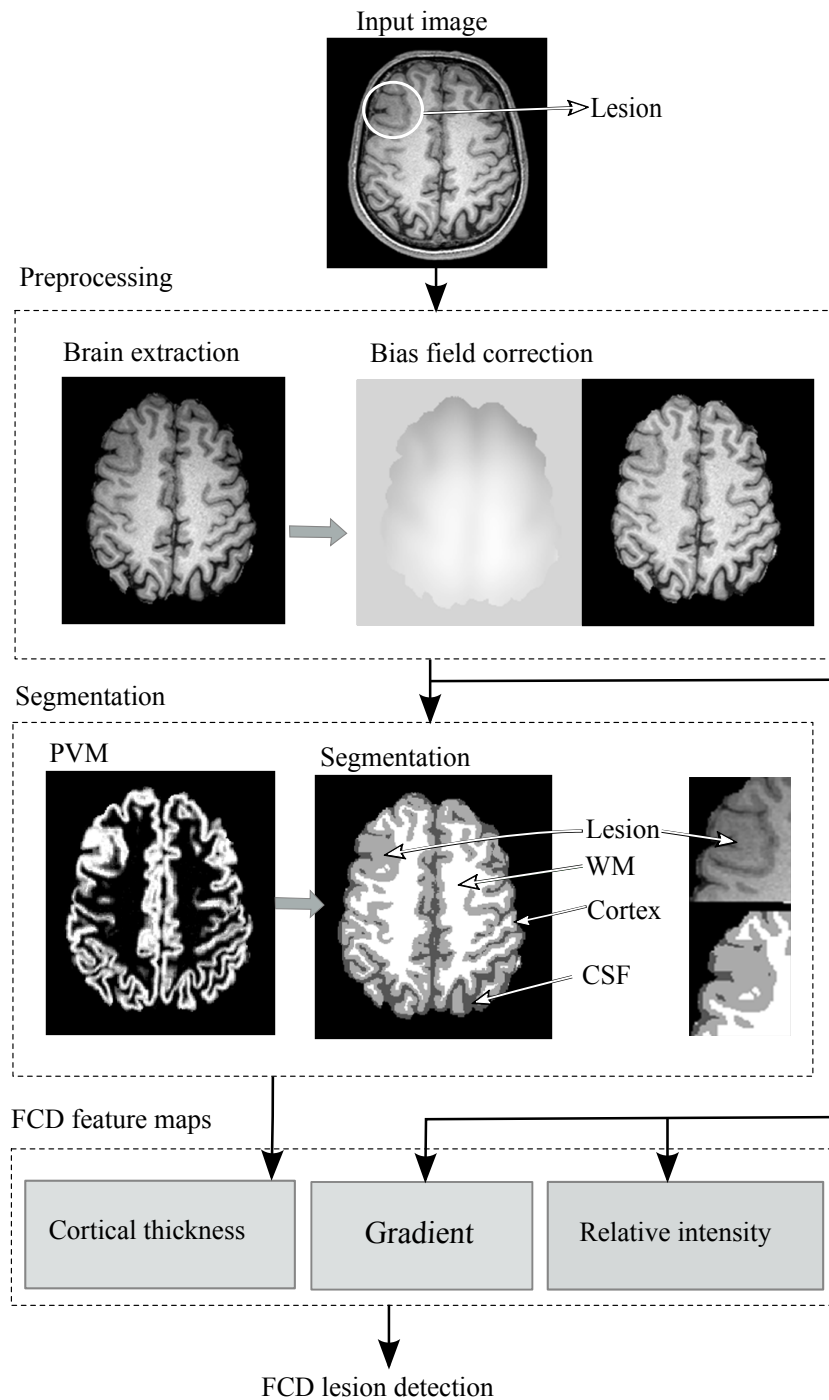


Figure 4.15: An overview of the steps for automatic FCD lesion detection.

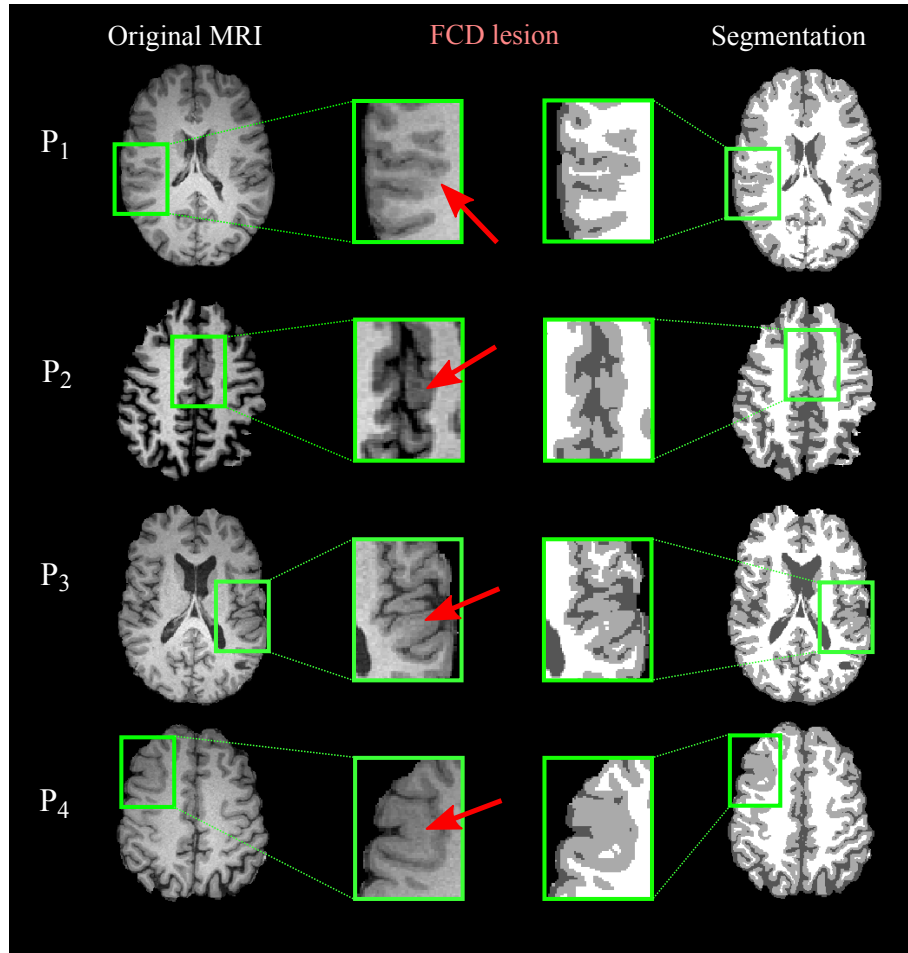


Figure 4.16: The cortex segmentation results for four different patients are shown in each row. The original MRI slice is shown at the left and the resulting slice after segmentation with the 3DGC is shown at the right.

the left with a rectangle around the lesion. On the right is the segmentation result.

For all patients we use the 3DGC method with 18 neighbors and the parameters $c = 0.3$ and $\lambda = 2040$. The parameters are experimentally determined and since the segmentation results highly depend on the choice of the parameter λ we performed additional experiments. In Fig. 4.17 and Fig. 4.18 we show two examples on how different values of the parameter λ influence the segmentation results [Segers et al., 2010]. We use four different values of the parameter λ : (a) $\lambda = 510$, (b) $\lambda = 1020$, (c) $\lambda = 1530$ and (d) $\lambda = 2040$. In these two examples, as well as for the other six FCD patients, the worst segmentation result is obtained for $\lambda = 510$, where the brain cortex is over-segmented. Considering the opinion of the expert physician, the

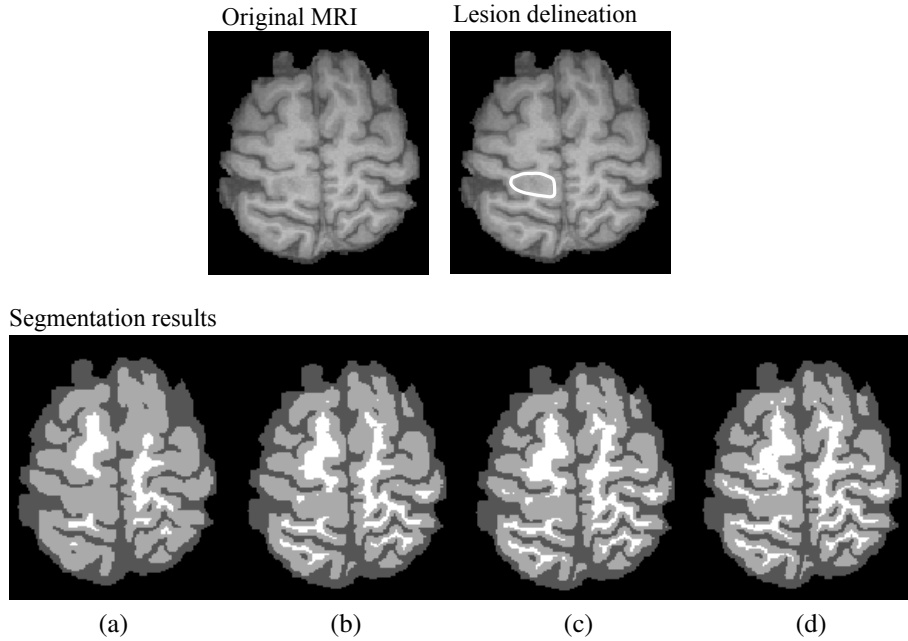


Figure 4.17: Illustration of the 3DGC performance on real FCD patient's MRI for different values of the parameter λ [Segers et al., 2010]: (a) $\lambda = 510$, (b) $\lambda = 1020$, (c) $\lambda = 1530$ and (d) $\lambda = 2040$.

best segmentation of the cortex is obtained for $\lambda = 2040$, where both the cortex and lesions are well delineated together.

4.5 Computational efficiency

The final implementation of the automatic 3DGC method and the graphical user interface is done in C++ by my master student Ief Segers [Segers et al., 2010]. The graphical user interface (GUI) is implemented in Qt. The visualisation of the segmentation results in 2D and 3D is done using the Visualization Toolkit (VTK) [Schroeder et al., 2006]. The Insight Toolkit (ITK) is used for the lesion annotation and for calculating the bias field using the N4ITK method [Sled et al., 1998].

The execution time of the 3DGC method for $181 \times 217 \times 181$ brain volume is about 3 min. This execution time is calculated without taking into account preprocessing steps such as the brain extraction and the bias field estimation. The execution time of the bias field alone is about 1 hour, for the same brain volume. This means that the 3DGC segmentation method is fast, but preparing MR images for segmentation is time-consuming and highly influence the computational complexity of the complete segmentation process.

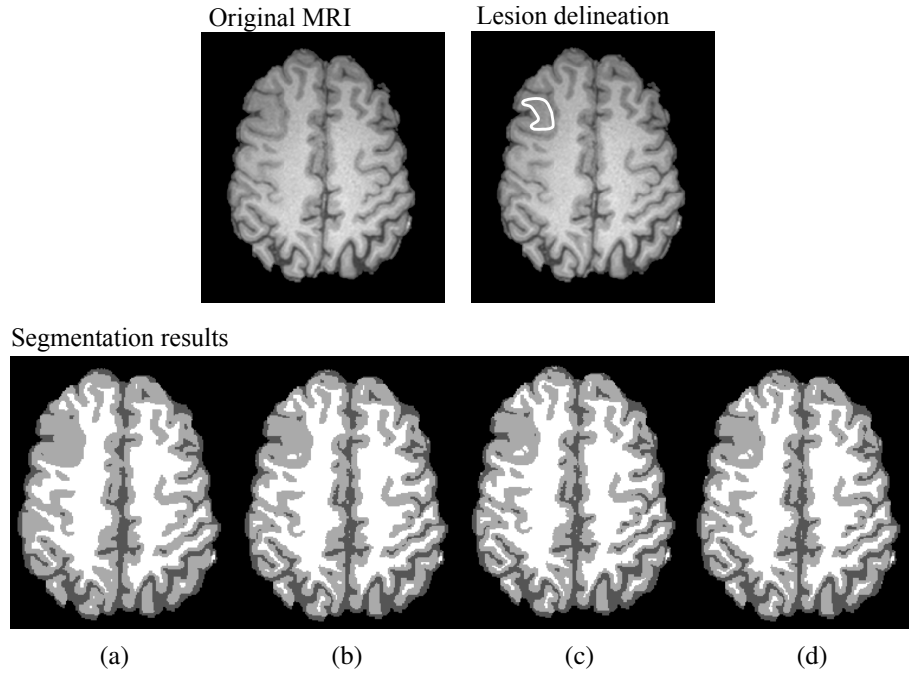


Figure 4.18: Illustration of the 3DGC performance on real FCD patient's MRI for different values of the parameter λ [Segers et al., 2010]: (a) $\lambda = 510$, (b) $\lambda = 1020$, (c) $\lambda = 1530$ and (d) $\lambda = 2040$.

4.6 Discussion

The segmentation performance of the 3DGC method was extensively validated in this study. Both quantitative and qualitative validation for different noise levels was done using the brain phantom MRI data. The quantitative validation was also done on real MRI data, while the qualitative validation is performed on real MRI data of the patients with FCD lesions. In the following text we will discuss the segmentation results in more detail.

The quantitative validation indicated that the 3DGC method using three labels and 18 nearest neighbors gives the best segmentation results. To obtain the best possible segmentation, we also needed to experimentally adjust the values of the parameters λ and c . The parameter λ controls the relative importance of the data term versus the smoothness term in the energy function, while the parameter c controls the relative importance of the boundary versus the intensity properties in the smoothness term.

At higher noise levels, we found better segmentation performance for the lower values of the parameter λ . A lower value of λ gives more importance to the smoothness term, which uses the spatial neighborhood information (integrates MRF) to attract neighboring voxels to the same tissue class. In this way, the smoothness term is eliminating

noise and small isolated artifacts, but at the same time is smoothing and removing some important anatomical details of the brain cortex. For instance, the smoothing can eliminate tiny cortical fissures in the brain surface (called sulcus) which are filled with CSF, see Section 2.1.1. These fissures are very important for a cortical thickness measurement because if they are over-smoothed and not segmented well, the cortical thickness in that area will increase and indicate a false cortical lesion.

To avoid tissue over-smoothing and over-segmentation we integrated the boundary information in the smoothness term, which is controlled with the parameter c , see Section 4.2.2. If the parameter $c = 1$, then the boundary information has no influence and only the intensity discontinuity part controls the smoothness term. But when $c = 0$, the boundary term has the highest influence. In our experiments, the parameter c was tested for several different values and in average the best segmentation performance was obtained for $c = 0.3$. Different values of the parameter c did not show a high impact on the final Dice coefficient values. This is because the Dice coefficient is calculated for the whole 3D volume, which is much bigger than the tiny fissures in the brain cortex. Thus, the best way to see an improvement in the fissure segmentation is by qualitative validation.

The 3DGC method is compared quantitatively with seven different segmentation methods, see Section 4.3. For the lowest noise level of 3%, HBT and FCM gave good results, but for the higher noise levels, the accuracy of these methods decreased rapidly. For higher noise levels, the quantitative results indicated that the 3DGC method with three classes and 18 neighbors outperformed other segmentation methods. Only for the highest noise level of 9%, the best performance in segmenting the GM was achieved using the FSL method. In the case of real MRI data, the proposed 3DGC algorithm is shown to competes favorably with the set of algorithms tested for GM tissue. The first six brains of the dataset are known to be particularly difficult to segment as they correspond to “older” scans with the strong bias field. In all experiments, the 3DGC method was able to enforce the spatial coherence and correctly label the neighboring voxels in the noisy areas.

The performance of the 3DGC method was also tested on 3D MRI data of the patients with FCD lesions. The qualitative results showed that in all eight patients the FCD lesions were segmented well together with the brain cortex, indicating an increased cortical thickness. The segmentation performance was highly influenced by the parameters λ and c . As it was the case with the qualitative results, the quantitative results showed that the changes in the parameter λ influenced the final segmentation more than the changes of the parameter c . However, even for a wide range of λ and c values, the lesions were segmented as a part of the cortex. These results suggest that the 3DGC method is suitable for calculating the cortical thickness map and can be further integrated in the FCD lesion detection framework, see Fig. 4.15.

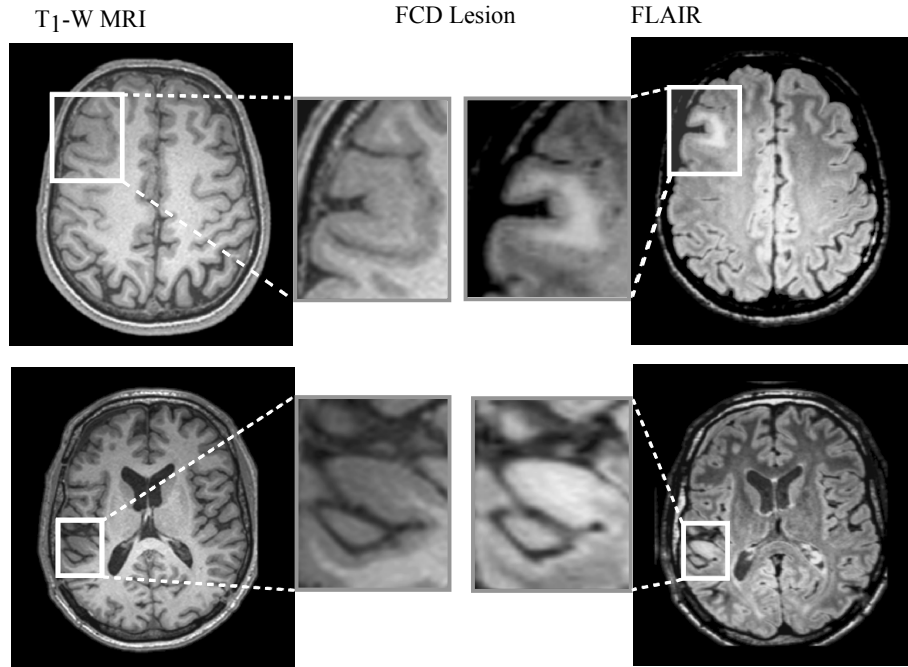


Figure 4.19: FCD lesion on T_1 -W and Core Flair MRI. By integrating both MRI modalities in a segmentation framework can improve the FCD lesion detection.

4.7 Future directions

In the future work, several different possibilities can be considered for improving the performance of the 3DGC method. The first possibility is to extend the graph cut algorithm to deal with multimodal image information. For instance, by integrating T_1 -W and FLAIR MRI of the brain, it is possible to obtain additional features for FCD lesion detection and to create more accurate multimodal brain cortex segmentation. In some cases, FCD lesions are hardly visible on T_1 -W images, but they can be detected on FLAIR scans. Two examples of T_1 -W and FLAIR images with FCD lesions can be seen in Fig. 4.19.

The second possibility is to include the prior knowledge of the probabilistic brain atlas or the training data of the patients with FCD lesions into the segmentation framework. It has been show by several studies that atlas-based MRI segmentation of the healthy brain is more accurate and can deal with several MRI artifacts. However, it has been also noticed that atlas-based MRI segmentation fails when the segmentation deals with the brain with certain deviations and lesions which are not captured by the atlas database. In those cases, it is possible to create a training subset of MRI data with expert-delineated brain deviations of interest and include it in the segmentation framework as a prior knowledge, where the training data is not used for the perfor-

mance evaluation.

The third possibility is to improve the gradient-based boundary information in the smoothness term to be more robust to image noise. Since the gradients are very sensitive to noise, in this work we used an average image gradient to suppress the noise problem. However, when MRI sequences are corrupted by higher noise levels, the problem of determining the accurate spatial gradients becomes challenging and often certain boundary information is over-smoothed by averaging. One of the solutions is to use more sophisticated methods that can successfully deal with image noise (e.g. phase congruency method [Kovesi, 2000]) or to improve the spatial gradient calculation.

The fourth possibility is to automatically determine the optimal parameters λ and c . In this work we did an experimental study on how different values of the parameters influence the segmentation results. We found a strong relationship between the parameters and image noise. The higher the noise level is in the image, the lower λ and the higher c are needed. The lower λ gives more importance to the smoothing term and the higher c gives more importance to the boundary term (if the boundary information is properly determined).

Finally, the validation of the method on more FCD patients and further improvements in both speed and accuracy of the 3DGC can be also considered in the future work.

4.8 Conclusion

In this chapter we presented an improved technique for 3D brain MRI volume segmentation based on the graph cut algorithm. In Section 4.1, we explained the basic concepts necessary for understanding graph cut segmentation methods. This included the explanation of the min-cut and max-flow problems, definition of the energy function for binary optimization and definition of the problem for multimodal energy minimization. Then, we explained in more detail the α -expansion algorithm for approximate energy optimization that we used for energy minimization of the proposed three-label graph cut approach. Following this, we explained an improved three-label graph cut method for 3D brain MRI segmentation in Section 4.2. We defined the data and the smoothness term of the energy function using intensity, boundary and spatial neighborhood information.

In Section 4.3 we presented the experimental results. The proposed method was validated both qualitatively and quantitatively on simulated and real brain MRI datasets, and the results were compared with the state-of-the-art algorithms for 3D brain MRI segmentation. The performance of the 3DGC algorithm was also demonstrated on the real MRI data of the patients with FCD lesions. Based on the quantitative validation, the proposed 3D graph cuts method with 18 neighbors outperforms the popular brain segmentation techniques for a wide range of noise levels. Experimental results with different neighbourhood systems showed that the 3D segmentation outperforms the 2D slice-by-slice segmentation. The qualitative validation indicated the ability of the

3DGC to successfully segment the FCD lesions as a part of cortex, even when the λ parameter is not precisely tuned to the image. Also, the results showed that using the 3DGC method, segmentation of the normal tissues is not degraded by the presence of abnormal tissues. In all experiments, the proposed method was able to enforce the spatial coherence and correctly label the neighboring voxels in the noisy areas. Although the results presented in this chapter are preliminary and further clinical evaluation is required, they are very encouraging and suggest that the 3DGC method can improve the FCD lesion detection and can be successfully applied in many other clinical applications.

In future research, different ways to improve the current algorithm's limitations can be examined. In particular, the selection of the appropriate parameters λ and c . Also, integrating noise robust boundary detection method could help in more accurate definition of the regions corresponding to different tissue types. The performance of the 3DGC method can be potentially improved by including multimodal intensity information from T₁-W and FLAIR MRIs and using probabilistic atlases in the segmentation framework.

5

Noise-robust FCM clustering

There is a way to do it better - find it.
– Thomas Edison

Segmentation of noisy images is one of the most challenging problems in image analysis and any improvement of segmentation methods can highly influence the performance of many image processing applications. In automated image segmentation, the fuzzy c-means (FCM) clustering has been widely used because of its ability to model uncertainty within data, its applicability to multimodal data and its fairly robust behavior. However, the standard FCM algorithm does not consider any information about the spatial image context and is highly sensitive to noise.

In this chapter, we present a new FCM-based method for spatially coherent, noise-robust image segmentation. The contribution of our method is twofold: (1) the spatial information of local image features is integrated into both the similarity measure and the membership function to compensate for the effect of noise; and (2) an anisotropic neighborhood, based on phase congruency features, is introduced to avoid edge smoothing and retain image details. The performance of the proposed algorithm is tested on synthetic images with different noise levels and on real images. The segmentation results demonstrate that our method efficiently preserves the homogeneity of the regions, without smoothing the line features and important details, and is more robust to noise than related FCM-based methods.

Following this we also present an extension of the new FCM method to multimodal image segmentation, where we integrate multimodal image information into the spatial contextual information to overcome the noise problem. The performance of the proposed algorithm is tested on simulated and real adult MR brain images with different noise levels, as well as on neonatal MR brain images with the gestational age of around 40 weeks. Experimental results show that the proposed multimodal method is effective and robust to noise and can be successfully used for complex and noisy image segmentation of the neonatal brain.

5.1 Introduction

Fuzzy clustering is an iterative, soft classification method. While hard classification methods (such as k-means) force each pixel to belong exclusively to one class in each iteration, fuzzy clustering allows pixels to belong to multiple classes with different membership degrees, where a final classification decision (defuzzification) is made at the end. In this way fuzzy clustering can retain more information about the original image properties through all iterations, leading to a more accurate classification. This is very important in applications where uncertainty, poor contrast, limited spatial resolution and noise are present (for example medical and satellite images). Among fuzzy clustering methods, the fuzzy c-means (FCM) algorithm, initially developed by Dunn [Dunn, 1973] and later generalized by Bezdek [Bezdek, 1981], is the most popular one. Although this conventional FCM algorithm works well on noise-free images, it is highly sensitive to noise because it classifies pixels in the feature space without considering their spatial distribution in the image.

To overcome misclassification errors due to noise, many extensions of the FCM algorithm have been proposed [Ahmed et al., 2002, Xue et al., 2003, Chen and Zhang, 2004, Shen et al., 2005, Chuang et al., 2006, Cai et al., 2007, Wang et al., 2009, Li et al., 2011]. The most common approach is to include feature information (e.g. intensity values) of the neighboring pixels into the modified FCM objective function [Ahmed et al., 2002, Chen and Zhang, 2004] or into a similarity measure between cluster centers and image elements [Shen et al., 2005]. Ahmed *et al.* [Ahmed et al., 2002] modified the objective function of the standard FCM algorithm to allow the immediate neighbours of the pixel to influence its labeling. Chen and Zhang [Chen and Zhang, 2004] proposed two improvements of the Ahmed *et al.* algorithm to reduce the computational time. On the other hand, to keep the continuity from the FCM algorithm, Shen *et al.* [Shen et al., 2005] introduced a new similarity measure that depends on spatial neighbourhood information, where the degree of the neighbourhood attraction is optimized by a neural network. The FCM performance can also be enhanced by combining pixel-wise fuzzy classification with pre-processing (noise cleaning in the original image) [Xue et al., 2003, Cai et al., 2007] and post-processing (noise cleaning on the classified data) [Xue et al., 2003].

However, these methods have certain limitations. They can not deal with very noisy images and can not accurately segment at the same time coarse homogeneous regions and finer image elements such as edges and lines. Also, some of the methods have increased complexity [Ahmed et al., 2002, Wang et al., 2009] and some of them introduce image smoothing [Xue et al., 2003, Cai et al., 2007]. Image smoothing together with using an isotropic neighborhood model for integrating the neighborhood information are often the main causes for loss of important image elements during segmentation. For instance, the loss of line elements, such as roads and rivers in remote sensing images or brain sulci (fissures in the surface of the brain) in brain MRI.

In this chapter, we present an improved FCM clustering algorithm for accurate and noise-robust image segmentation. The two main novelties with respect to related approaches are: (1) our algorithm integrates spatial neighborhood information of local

image features into both the similarity measure and the membership function and (2) an anisotropic neighborhood is introduced using the properties of the phase congruency features [Kovesi, 1999, Kovesi, 2002]. With the first improvement we obtain a method that is highly robust to noise and can successfully segment coarse homogeneous regions. With the second improvement, using an anisotropic neighborhood, we improve the segmentation accuracy and designed the method that is also able to segment line elements and step edges without smoothing and with more accuracy. To identify phase congruency features (such as edges, lines, corners, etc.) and obtain their location, orientation and confidence factor, we use an improved noise-robust phase congruency method [Kovesi, 2002], which was designed to provide good feature localization. The efficiency of our segmentation method is tested on synthetic and real images with different noise levels. Experimental qualitative and quantitative results indicate that our method successfully reduces the effect of noise, preserves image details and biases the algorithm toward homogeneous clustering. Following this, we also present an extension of the improved FCM method to multimodal brain MRI segmentation.

This chapter is organized as follows. In Section 5.2 the basic principles of the standard FCM algorithm are reviewed and in Section 5.3 the phase congruency feature detection method is explained. Our modified noise-robust FCM algorithm is explained in Section 5.4. Experimental and comparison results are presented and discussed in Section 5.5. Next, in Section 5.6 we explain the multimodal FCM segmentation with experimental results. Finally, we give hints for the future work in Section 5.8 and conclude this chapter in Section 5.9.

5.2 FCM algorithm

Let $X = \{\mathbf{x}_j, j = 1, 2, \dots, N \mid \mathbf{x}_j \in \mathbb{R}^q\}$ represent feature vectors of the image with N pixels that needs to be partitioned into C classes, where every component of the vector \mathbf{x}_j represents a feature of the image at position j , and q is the dimension of the feature vector. The FCM clustering algorithm is based on minimizing the following objective (or energy) function:

$$J_{\text{FCM}}(U, V) = \sum_{i=1}^C \sum_{j=1}^N u_{ij}^m D_{ij} \quad , \quad (5.1)$$

where u_{ij} is the membership degree of the feature vector \mathbf{x}_j with respect to the i -th cluster, U is the partition matrix $[u_{ij}]_{C \times N}$, V is the set of the cluster prototypes $\{\mathbf{v}_i\}_{i=1}^C$, m is the weighting exponent that controls the fuzziness of the resulting partition (most often $m = 2$), D_{ij} is the similarity index which measures the distance between \mathbf{x}_j and the i -th cluster center \mathbf{v}_i . The most commonly used similarity measure is the squared Euclidean distance and then $D_{ij} = \|\mathbf{x}_j - \mathbf{v}_i\|^2$. Low membership degree values are assigned to pixels far from the cluster centroid, and high membership degree values to pixels close to the cluster centroid.

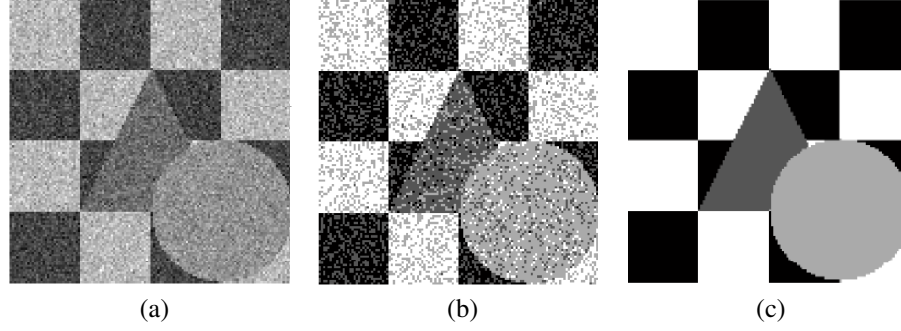


Figure 5.1: An example for the FCM segmentation: (a) noisy image, (b) segmentation result using standard FCM algorithm and (c) “ground truth”(desirable segmentation).

The objective function $J_{\text{FCM}}(U, V)$ (Eq. (5.1)) is minimized under the following constraints:

$$u_{ij} \in [0, 1], \forall j : \sum_{i=1}^C u_{ij} = 1 \text{ and } \forall i : 0 < \sum_{j=1}^N u_{ij} < N. \quad (5.2)$$

Considering these constraints and calculating the first order partial derivatives of $J_{\text{FCM}}(U, V)$ with respect to u_{ij} and \mathbf{v}_i and setting them to zero, results in the following two conditions for minimizing $J_{\text{FCM}}(U, V)$:

$$u_{ij} = \left[\sum_{k=1}^C \left(\frac{D_{ij}}{D_{kj}} \right)^{\frac{1}{m-1}} \right]^{-1} \quad (5.3)$$

and

$$\mathbf{v}_i = \frac{\sum_{j=1}^N u_{ij}^m \mathbf{x}_j}{\sum_{j=1}^N u_{ij}^m}, (i = 1, 2, \dots, C) . \quad (5.4)$$

The FCM algorithm iteratively optimizes $J_{\text{FCM}}(U, V)$, by evaluating Eq. (5.3) and Eq. (5.4), until the following stop criterion is satisfied:

$$\max_{i \in [1, C]} \|\mathbf{v}_i^{(l)} - \mathbf{v}_i^{(l+1)}\|_{\infty} < \epsilon, \quad (5.5)$$

where l is the iteration index and $\|\cdot\|_{\infty}$ is the L_{∞} norm. Once a membership value u_{ij} for each class i is assigned to each pixel j , a defuzzification of the fuzzy clusters $\{F_k\}_{k=1}^C$ into their crisp version $\{H_k\}_{k=1}^C$ is done by assigning each pixel to the class with the highest membership value as follows:

$$\max_{i \in [1, C]} (u_{ij}) = u_{kj} \implies \mathbf{x}_j \in H_k \quad (5.6)$$

The main drawback of the standard FCM for image segmentation is that the objective function does not take into account neighborhood information and deals with the pixels as the separate points. Therefore, the standard FCM algorithm is sensitive to noisy

pixels (or outliers) and very often those pixels are wrongly classified. An example of the FCM segmentation on a noisy synthetic image with its “ground truth” (desirable segmentation) is shown in Fig. 5.1.

The most logical approach to improve the FCM performance and eliminate noise problem is to include spatial and feature information of the neighboring pixels into the algorithm. In most of the cases, including an isotropic neighborhood configuration will give satisfactory results, but in the cases where it is important to accurately segment line features and edges, we need to use an anisotropic neighborhood configuration. To define the anisotropic neighborhood configuration in our method, we used location, orientation and confidence factor of the image features defined with the phase congruency method, which is described in Section 5.3.

5.3 Phase congruency, local phase and energy

Phase congruency is a frequency-based method for feature detection, where features are detected at points where the Fourier components of the image are maximally in phase (local maximal congruency in the phase values). This feature detection method, using local phase and energy, is based on a plausible model of how mammals detect edges suggested by Morrone and Owens [Morrone and Owens, 1987] and successfully explains the psychophysical effect of human feature perception. Originally, the concepts of local phase and energy were developed for analyzing one-dimensional (1D) signals and are later successfully extended to two dimensions (2D) [Kovesi, 1999, Kovesi, 2002].

Initially, phase congruency of the signal $f(x)$ at the location x (proposed by Morrone and Owens [Morrone and Owens, 1987]) is defined by:

$$PC(x) = \max_{\bar{\phi}(x) \in [0, 2\pi]} \frac{\sum_n A_n \cos(\phi_n(x) - \bar{\phi}(x))}{\sum_n A_n}, \quad (5.7)$$

where A_n is the amplitude and ϕ_n is the local phase at position x of the n^{th} Fourier component of the signal $f(x)$ and $\bar{\phi}(x)$ is the amplitude-weighted mean local phase angle of all the Fourier terms at position x . The cosine of the difference between the local phase ϕ_n and the weighted mean local phase $\bar{\phi}(x)$ is a quantity approximately equal to one minus half this difference squared (the Taylor expansion of $\cos(x) \approx 1 - x^2/2$ for small x). This means that finding a maximum of the phase congruency is approximately equivalent to finding a minimum of the weighted standard deviation of phase angles. Defined in this way, phase congruency is a rather inelegant quantity to calculate. Thus, an alternative interpretation of phase congruency is proposed by Venkatesh and Owens [Venkatesh and Owens, 1990], based on the analytical signal and the local energy function $E(x)$:

$$E(x) = \sqrt{F(x)^2 + H(x)^2}, \quad (5.8)$$

where $F(x)$ is the input signal $f(x)$ without its DC component and $H(x)$ is the Hilbert transform of $F(x)$ (90° phase shifted version of $F(x)$). Components $F(x)$ and $H(x)$

are typically calculated by convolving the signal with a quadrature pair of 1D filters (one even- and one odd-symmetric filters that have zero mean, identical L^2 norm and are orthogonal). Venkatesh and Oens showed that calculating points of maximum phase congruency is equivalent to searching for peaks in the local energy function and that phase congruency can be defined as:

$$PC(x) = \frac{E(x)}{\sum_n A_n}. \quad (5.9)$$

Note that phase congruency at location x is significant only in the case when it occurs over a wide range of frequencies.

The phase congruency function $PC(x)$ is directly proportional to the local energy function $E(x)$ scaled by the sum of the Fourier component amplitudes $\sum_n A_n$. Since local energy is a measure of signal change, it can be interpreted as a feature detector for different feature types. The local phase indicates the type of the feature that energy corresponds to (line or step edge). By dividing the local energy function with $\sum_n A_n$ we obtain the phase congruency function which is dimensionless and takes values between 0 (no congruency) and 1 (perfect congruency). Calculated in this way, phase congruency provides a dimensionless measure of feature significance (confidence factor, $PC \in [0, 1]$), which is invariant to variations in image illumination and/or contrast. In certain applications, these phase congruency characteristics gives advantage to the phase congruency method over the gradient-based methods [Canny, 1986, Marr and Hildreth, 1980, Gonzalez and Woods, 2008], which are very sensitive to image illumination and sometimes fail in feature localization.

Since 1D phase congruency is initially defined as a normalized quantity in Eq. 5.7 and 5.9, then it is sensitive to noise, ill-conditioned when nearly all Fourier amplitudes are small and feature localization is not always good. All these problems are addressed in the phase congruency method proposed by Kovese [Kovese, 2002], which is designed to provide noise-robust and accurate feature localization. The new noise-robust phase congruency function $PC_{nr}(x)$ is defined as:

$$PC_{nr}(x) = \frac{W(x)\langle E(x) - T \rangle}{\sum_n A_n + \varepsilon}, \quad (5.10)$$

where $W(x)$ is a phase congruency weighting function, T is the radius of the noise circle (see Fig. 5.2a), ε is a small positive constant (to avoid division by zero) and $\langle \rangle$ here denotes that the enclosed quantity is equal to itself when its value is positive and zero otherwise. To solve the noise problem, phase congruency is calculated using the amount by which $E(x)$ exceeds the radius of the noise circle and the appropriate noise threshold T is determined from the statistics of the filter responses to the image. A small positive constant ε is addressing the problem when all the Fourier amplitudes are very small. For more details on how W , T and A_n are calculated see [Kovese, 2002]. The geometrical relationship between phase congruency, local energy and the sum of Fourier amplitudes is shown in Fig. 5.2a. The local Fourier components are plotted as complex vectors adding head to tail. The total energy $E(x)$ is the magnitude of the vector from the origin to the end point.

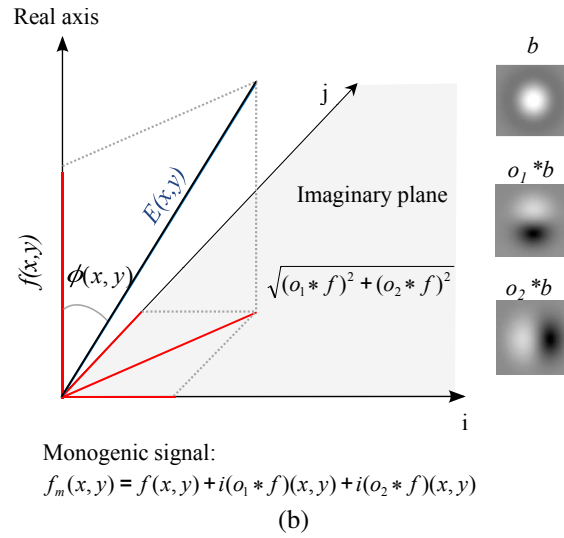
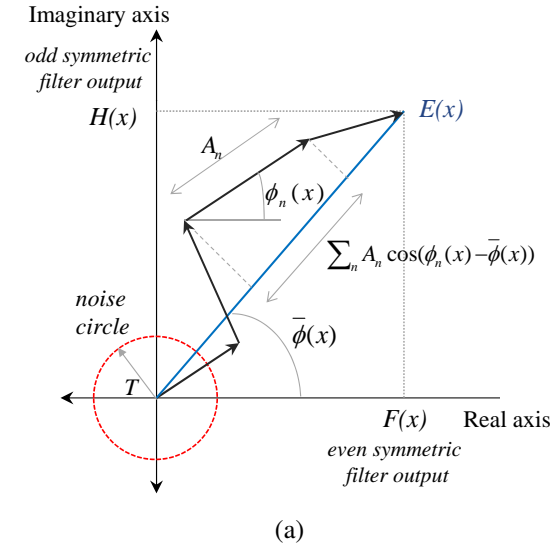


Figure 5.2: Geometrical representation of the local energy for 1D and 2D signals. (a) Polar diagram shows the geometrical relationship between the sum of Fourier amplitudes $\sum_n A_n$, local energy $E(x)$ and phase congruency $PC(x)$. The noise circle represents the level of $E(x)$ one can expect from the noise in the signal. If $E(x)$ falls within this circle, the confidence of phase congruency value falls to 0. (b) Geometrical representation of the monogenic signal and 2D local energy. The convolution is written using an asterisk *. On the right side of the graph are examples of three filters that might be used to find the monogenic signal (b is the difference of Gaussians bandpass even filters, o_1 and o_2 are two odd filters antisymmetric to the even part).

There are a few ways to extend the definition of local phase and energy to 2D. One possibility is to use steerable filters [Freeman and Adelson, 1991] to estimate the phase of 1D signal in the direction of maximal local energy. Another way, proposed by Kovesei [Kovesei, 1999, Kovesei, 2000, Kovesei, 2002], is to use the 2D log-Gabor filters with different scales and orientations (e.g. 6 orientations and 4 scales). For this paper, the local phase $\phi(x, y)$ and energy $E(x, y)$ were estimated using the monogenic signal, which is a multi-dimensional extension of the analytical signal theory developed by Felsberg and Sommer [Felsberg and Sommer, 2001]. This choice is mainly made because of the computational speed and simplicity.

The monogenic signal consists of three quantities: local energy, local phase, and local orientation (discussed in more detail in [Felsberg and Sommer, 2001, Boukerroui et al., 2004] and illustrated in Fig. 5.2b). The computation of the monogenic signal for a 2D image proceeds as follows. First, a rotationally symmetric, zero-mean filter is applied to the image to form a bandpass image I_b , which constitutes the even component of the signal. Then, the odd component is composed of the response of two anti-symmetric filters to the even part. These two filters, o_1 and o_2 are described in the Fourier domain as:

$$O_1(u, v) = \frac{u}{\sqrt{u^2 + v^2}}, \quad O_2(u, v) = \frac{v}{\sqrt{u^2 + v^2}}, \quad (5.11)$$

where u, v are the Fourier domain coordinates. Local phase $\phi(x, y)$, local orientation $\theta(x, y)$, and local energy $E(x, y)$ are calculated using these filter responses and the bandpass (even) image I_b in the space domain as follows:

$$\phi(x, y) = \tan^{-1}\left(\frac{I_b}{\sqrt{(o_1 * I_b)^2 + (o_2 * I_b)^2}}\right), \quad (5.12)$$

$$\theta(x, y) = \tan^{-1}\left(\frac{o_1 * I_b}{o_2 * I_b}\right), \quad (5.13)$$

$$E(x, y) = \sqrt{I_b^2 + (o_1 * I_b)^2 + (o_2 * I_b)^2}, \quad (5.14)$$

where o_1 and o_2 are the inverse Fourier transforms of O_1 and O_2 . The geometrical representation of the monogenic signal $f_m(x, y)$, 2D local energy $E(x, y)$, local phase $\phi(x, y)$ and an example of a quadrature triple filters are shown in Fig. 5.2b. Note that an extension of the Hilbert transform to multiple dimensions in Eq. 5.11 is known as the Riesz transform.

Three examples of the phase congruency feature map obtained from the corresponding intensity image is shown in Fig. 5.3. The first row illustrates the difference between Canny edge detection and phase congruency feature detection. Note the difference at the line features. The Canny detects two edges at the both sides of the line, while phase congruency detects exactly one line feature. The second row illustrates the robustness of the phase congruency to image contrast and illumination. For instance, the low contrast square in the circle at the top right corner of the image is almost invisible with the Canny edge detector, while using phase congruency is clearly marked. Finally, the last row illustrates the noise-robust phase congruency feature detection.

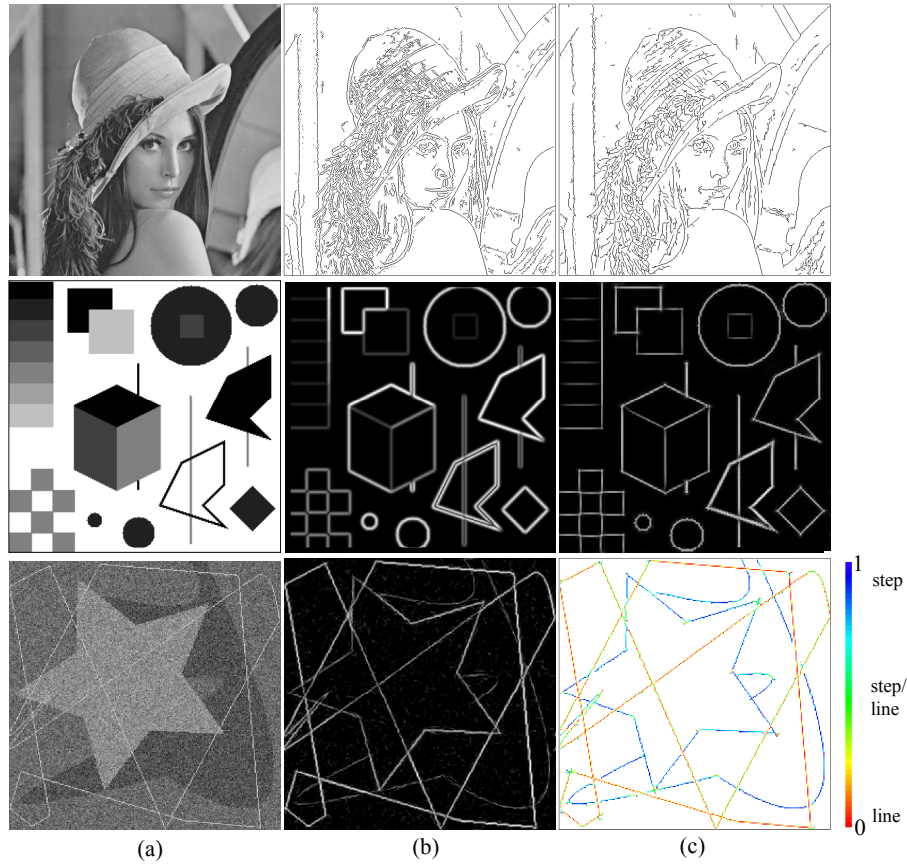


Figure 5.3: Illustration of three examples of the phase congruency maps. The first row illustrates the difference between phase congruency and Canny edge detection: (a) original image Lena, (b) Canny edge detection and (c) phase congruency feature map. The second row illustrates the robustness of phase congruency to changes in image contrast and illumination variations: (a) original image, (b) Canny edge detection and (c) phase congruency. The third row illustrates: (a) noisy image, (b) phase congruency and (c) feature map (red color represents the line feature and blue color represents the step (edge) feature).

5.4 Accurate and noise-robust image segmentation

One of the important characteristics of an image is that neighbouring pixels tend to have similar feature values and the probability that they belong to the same cluster is high. Therefore, to improve the performance of the standard FCM algorithm, we integrate information of the neighboring pixels in our method. We used both intensity information and membership degree values of the neighboring pixels to overcome noise problem during segmentation. Furthermore, to obtain more accurate segmentation, we use phase congruency features (such as step edges and lines) to define isotropic or anisotropic neighborhood configuration.

5.4.1 Neighborhood configuration

The location (x, y) , orientation θ , local phase ϕ and confidence factor PC of the phase congruency features are used to define a neighborhood configuration.

In homogeneous regions, where phase congruency is zero or a very small value almost equal to zero ($PC \simeq 0$), an isotropic neighborhood is used. In the regions where lines and edges are detected (PC is greater than zero), an anisotropic neighborhood is used. This is illustrated in Fig. 5.4, where on the left top side is an image segment with different 3×3 neighborhoods (highlighted with different symbols and colors) and on the right bottom side is a table describing each of those neighborhoods in a separate row and illustrating their isotropic or anisotropic configuration.

The type of the feature is defined with the local phase, see example in Fig. 5.3(c). In our method the local phase ϕ is normalized between 0 and 1 as follows. First, the negative phase angles $\phi < 0$ are mapped to the range $[0 - \pi]$ where, for example, $-\pi/3$ is mapped to $\pi/3$. Following this, all $\phi > \pi/2$ are mapped in the range $[0 - \pi/2]$ as $\pi - \phi$. Finally, the normalization of the phase is done as $\phi_{\text{norm}} = (\pi/2 - \phi)/(\pi/2)$, where $\phi_{\text{norm}} \in [0 - 1]$.

If the phase ϕ_{norm} is closer to 0 we have a line feature. The orientation of the line is defined with an orientation θ and only the neighbours lying on the same line are considered for an anisotropic neighborhood configuration (see the 6th row of the table in Fig. 5.4(b) for the line pixel). If ϕ_{norm} is closer to 1, the feature is an edge and the neighbors lying on the same side of the edge are selected for an anisotropic neighborhood configuration (see the 5th row of the table in Fig. 5.4(b) for the edge pixel). In the case that the central element belongs to a region ($0 < PC < 1$) and some of the neighboring elements belong to a line, an anisotropic neighborhood is defined excluding all elements within the line, see the last row of the table in Fig. 5.4(b).

5.4.2 Integrating neighborhood information

If we look back at the FCM objective function in Eq. (5.1) and its two necessary conditions for the convergence Eq. (5.3) and Eq. (5.4), we can conclude that the

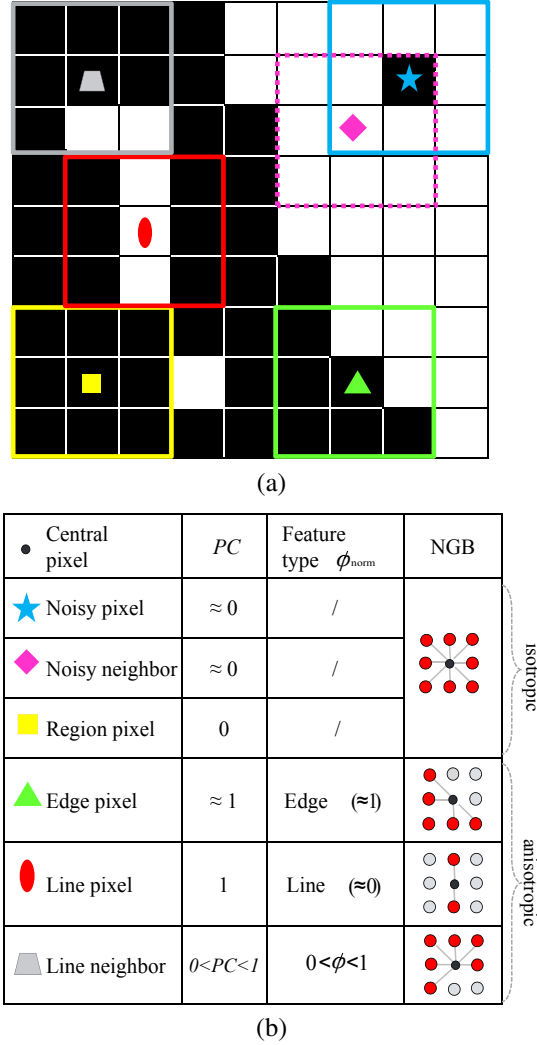


Figure 5.4: Neighborhood configuration. (a) An illustration of 6 different 3×3 neighborhoods (delineated in different color) with the central pixel defining the specific neighborhood configuration; (b) The table describes all 6 neighborhoods (indicated on the image on the left side). The second column shows the confidence factor PC and the third column shows type of the feature (local phase values ϕ). The last column shows the appropriate isotropic or anisotropic neighborhood configuration (NGB), where the important neighbors are highlighted in red color. Note that the neighborhood configuration (isotropic or anisotropic) is determined for each image pixel in advance using phase congruency features as described here.

segmentation result is significantly influenced by the choice of the similarity measure D_{ij} , which is used for computing the membership degree values u_{ij} in Eq. (5.3), and u_{ij} are further used for computing the cluster centers v_i in Eq. (5.4). Considering that, in each iteration of the algorithm we adjust both the similarity measure and the membership degree values in two separate steps using the information of the neighboring pixels. By using only one of these two steps, we can successfully segment noisy images till certain noise level, but for images with higher noise levels both steps are needed for accurate segmentation. We explain now these two steps in more detail.

In the first step we define the new neighborhood weighted similarity measure as follows:

$$D_{ij}^* = w_{ij} \|\mathbf{x}_j - \mathbf{v}_i\|^2 = (1 - \alpha S_{ij}) \|\mathbf{x}_j - \mathbf{v}_i\|^2, \quad (5.15)$$

where $w_{ij} \in [0, 1]$ is the similarity measure weight, which depends on the local neighborhood attraction weight $S_{ij} \in [0, 1]$ and the parameter $\alpha \in [0, 1]$ that controls the relative importance of the neighbourhood attraction. If $\alpha = 0$ or $S_{ij} \simeq 0$, then $w_{ij} = 1$ and $D_{ij}^* = D_{ij}$, and we have the standard FCM.

The local neighborhood attraction weight S_{ij} is defined as:

$$S_{ij} = \frac{\sum_{r \in \mathcal{N}_j} u_{ir} a_{jr} d_{jr}^{-1}}{\sum_{r \in \mathcal{N}_j} a_{jr} d_{jr}^{-1}}, \quad (5.16)$$

where \mathcal{N}_j is a set of neighbors with index r in a $n \times n$ square window, surrounding the study element with index j , u_{ir} is the membership degree of the neighbouring element r to the cluster i , a_{jr} is the intensity attraction and d_{jr} is the distance attraction. The intensity attraction a_{jr} is defined as the absolute intensity difference between the study pixel j and its neighbor r :

$$a_{jr} = |x_j - x_r|. \quad (5.17)$$

The distance attraction d_{jr} can be defined in different ways, but for this study we used the Manhattan distance to equally include the influence of the first and the second order neighborhood into the weight calculation. The Manhattan distance between the element j with coordinates (p_j, q_j) and its neighbor r with coordinates (p_r, q_r) is defined as:

$$d_{jr} = \max(|p_j - p_r|, |q_j - q_r|). \quad (5.18)$$

The number of neighbors N_r depends on the neighborhood configuration. In homogeneous regions where the neighborhood configuration is isotropic we have $N_r = n^2 - 1$ and in the regions where line and edges are detected and the neighborhood is anisotropic we have $0 < N_r < n^2 - 1$.

After calculating the new similarity measure D_{ij}^* , we update the membership values using Eq. (5.3) where instead of D_{ij} we use D_{ij}^* .

Then, to further improve the segmentation performance, in the second step we use again the neighbourhood information to adjust the updated membership values in the

following way:

$$u_{ij}^* = \frac{u_{ij} M_{ij}^\beta}{\sum_{k=1}^C u_{kj} M_{kj}^\beta}, \quad M_{ij} = \frac{\sum_{r \in \mathcal{N}_j} u_{ir} d_{jr}^{-2}}{\sum_{r \in \mathcal{N}_j} d_{jr}^{-2}}, \quad (5.19)$$

where u_{ij}^* is the new membership value ($u_{ij}^* \in [0, 1]$, $\sum_{i=1}^C u_{ij}^* = 1 \forall j$ and $0 < \sum_{j=1}^N u_{ij}^* < N \forall i$), C is the number of clusters, M_{ij} is the spatially weighted membership degree mean and $\beta \in \mathbb{Z}_+$ is the parameter that controls the relative importance of M_{ij} . The squared reciprocal distance d_{jr}^{-2} is used in Eq. (5.16) and Eq. (5.19) because the neighbours r close to the central element j should influence the result more, while more distant neighbours should have a lower weight.

The idea behind this new integration of neighborhood information in the FCM algorithm is as follows. Consider the local $n \times n$ neighbourhood where the central element \mathbf{x}_j is corrupted with noise and hence has large intensity differences with the closest neighbouring elements \mathbf{x}_r , which in turn have intensities similar to that of the cluster center \mathbf{v}_i (see Fig. 5.4, noisy pixel). After running the standard FCM algorithm, the neighbouring elements will be classified in a cluster i , while the central element will be in a different cluster. However, in this case the local neighbourhood attraction weight S_{ij} will be large and the expression $(1 - \alpha S_{ij})$ will be small for $\alpha \neq 0$. Therefore, the new spatially dependent similarity measure will be smaller than the one in the standard approach. That means that after one iteration of the algorithm the central element \mathbf{x}_j will be attracted to the neighbouring cluster i . Next, if we calculate M_{ij} and update the membership values using Eq. 5.19, the new membership values u_{ij}^* will stay unchanged in homogeneous regions, but for a noisy pixel they will be influenced by the labels of its neighbouring pixels. In our case, the central element \mathbf{x}_j is then even stronger attracted to the cluster i . If the neighbourhood attraction is continuously large till the end of the algorithm, the central element \mathbf{x}_j will be forced to belong to the cluster i despite being dissimilar to it. More precisely, this property biases the algorithm towards homogeneous clustering and suppresses the noise problem.

5.4.2.1 Parameters α and β

Note that if $\alpha = \beta = 0$, we have the standard FCM algorithm. If $\alpha = \beta = 1$ the neighborhood attraction is maximal and it decreases for $\alpha < 1$ or $\beta > 1$. The optimal values of α and β depend on the image noise level.

In the case when an isotropic neighborhood model is used, we experimentally found that the higher the image noise is, the higher parameter α and $\beta = 1$ are needed for the best segmentation performance. This result is also intuitive, because it shows that in the case of higher noise levels, the neighborhood attraction is more important to eliminate isolated noisy pixels in the image. Similarly, for lower noise levels, the parameter α should be lower and $\beta > 1$. The exact values of the parameters can be experimentally determined and their values depend not just on the image noise but also on the image content as well (e.g. MRI image, satellite image, etc.).

The relationship between the parameters and noise is a little bit different when an anisotropic neighborhood model is used. In this case, if an anisotropic neighborhood is accurately defined (e.g. a noise robust method is used to determine a neighborhood configuration), then the resulting method does not appear to be highly sensitive to parameter settings. This means that α and β optimization is not critical anymore. We experimentally found that the best segmentation is achieved when the neighborhood attraction is maximal $\alpha = \beta = 1$. Intuitively, this is because only important neighbors (see Fig. 5.4) are used to calculate the weights S_{ij} and M_{ij} and even when the noise level is low the maximal neighborhood attraction will not smooth image edges and lines as it is the case with an isotropic neighborhood models.

5.4.3 Algorithm steps

The outline of the proposed noise-robust FCM algorithm is:

Step1. Set the number of clusters C , degree of fuzziness m , stop criterion ϵ and neighborhood size.

Step2. Calculate phase congruency features and define the neighborhood configuration for each pixel.

Step3. Initialize the centers of the clusters $\mathbf{v}_i | i = 1, 2, \dots, C$.

Step4. Calculate the new similarity measure D_{ij}^* , see Eq. (5.15).

Step5. Calculate u_{ij} using D_{ij}^* , see Eq. (5.3).

Step6. Calculate the new membership values u_{ij}^* , see Eq. (5.19).

Step7. Update \mathbf{v}_i using u_{ij}^* , see Eq. (5.4).

Repeat steps 4-7 until the stop criterion is satisfied, see Eq. (5.5).

As with all clustering algorithms, the segmentation performance and the computation speed may highly depend on the initialization step such as the initialization of the cluster centers and the membership degrees of each pixels to different cluster. The existing methods very often rely on the random assignment of the cluster centers in the initialization process, which can produce inconsistent and non-reproducible clustering results. It can happen that in multiple runs of the same data and for different initial cluster seeds, the method does not converge to the same final set of clusters. This can happen due to the convergence of the objective function to different local minima. However, by having a good initialization of the FCM's parameters, which can be estimated from an initial segmentation, we can obtain faster convergence and more accurate segmentation results. In this way, the initial segmentation constructs the training set of classified voxels in the original image and ensures the convergence of the energy function to an optimal minimum. Therefore, to mitigate the initialisation problem, we use intensity-based thresholding [Reddi et al., 1984] (as an initial segmentation) to initialize the cluster centers and to generate a fast and reliable convergence of the FCM's objective function.

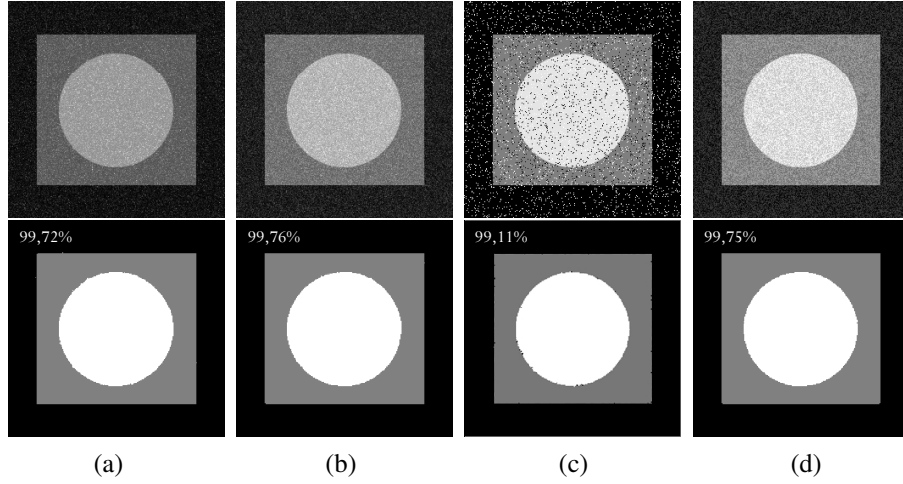


Figure 5.5: Segmentation results for different types of noise (SNR = 16 dB): (a) gamma; (b) Rayleigh; (c) salt-and-pepper; (d) uniform. The similarity between the segmented image and the “ground truth” is shown in percentage.

5.5 Experimental results

In this section, we present experimental results of our algorithm using three different types of images: (1) synthetic images with different noise levels, (2) phantom Magnetic Resonance Images (MRI) of the human brain, and (3) real images. We present qualitative results for all three image types and the quantitative results are only computed for the first two image types where the “ground truth” segmentation is available. In all experiments we set the weighting exponent to $m = 2$, the stop criterion to $\epsilon = 0.01$ and the parameter which controls the effect of the neighbors to $\alpha = 1$.

5.5.1 Synthetic images

Firstly, we investigate the sensitivity of our method to different types of noise: gamma, Rayleigh, salt-and-pepper and uniform. For this purpose we use a simple synthetic image (size 256×256) shown in Fig. 5.5, which contains three different homogeneous classes and known “ground truth” segmentation. In this example Signal to Noise Ratio between the original and noisy images is 16 dB for all noise types. Both qualitative and quantitative segmentation results using 5×5 neighborhood size are shown in Fig. 5.5 (second row). The results indicate that our method can successfully deal with different types of image noise and give satisfactory segmentation.

Secondly, we investigated the segmentation performance of our method on a synthetic image (size 256×256) shown in Fig. 5.6i, which contains a four-class pattern with three different homogeneous classes and a line as the fourth class. We tested the

sensitivity of our method to different levels of the zero mean Gaussian noise and how the size of the chosen neighborhood influence the segmentation result (e.g. 3×3 , 5×5 or 7×7 neighborhood). The quantitative comparison results are plotted in Fig. 5.7. The first graph Fig. 5.7(a) shows the segmentation performance of our method using different neighborhood sizes, where the best performance is achieved using 7×7 neighborhood. The comparison results with other methods (using 5×5 neighborhood for our method and the best segmentation result for other methods) are plotted in the next three graphs.

In all experiments, we use the Dice coefficient ρ_i as the similarity measure to quantify the overlap between the automated segmentation and the given “ground truth”, where i indicates different clusters. The definition of the Dice coefficient is given in the previous Chapter 4 in Eq. 4.14.

The graph in the Fig. 5.7(b) shows the results of the average Dice coefficient (ρ_{avr}) over all four clusters:

$$\rho_{avr} = \frac{\rho_1 + \rho_2 + \rho_3 + \rho_4}{4}, \quad (5.20)$$

where ρ_1 , ρ_2 and ρ_3 are the Dice coefficients of 3 homogeneous clusters and ρ_4 is the Dice coefficient of the line cluster. The lower-left graph (Fig. 5.7(c)) shows the Dice coefficient of the line cluster (ρ_4 or ρ_{line}), while the lower-right graph (Fig. 5.7(d)) shows the average Dice coefficient of the three homogeneous regions excluding the line cluster (ρ_{hom}):

$$\rho_{hom} = \frac{\rho_1 + \rho_2 + \rho_3}{3}. \quad (5.21)$$

From the graphs we can clearly see that the FCM method shows the worst performance for all noise levels. The methods by Cai et al. [Cai et al., 2007] and Shen et al. [Shen et al., 2005] give an improved performance of ρ_{avr} for all noise levels compared to the FCM method. However, their segmentation performance starts rapidly to decrease for very noisy images (SNR < 14 dB). The method by Shen et al. gives better result in segmenting the line cluster, while the method by Cai et al. has good performance in segmenting homogeneous regions, but fails in segmenting line cluster, especially for higher noise levels. The results of our method, without using phase congruency and anisotropic neighborhoods, indicate that this method is good for segmenting homogeneous regions (good performance for very noisy images), but it is not efficient in segmenting line elements. However, by including anisotropic neighborhoods in our method, we obtained the best segmentation performance for all noise levels and for both homogeneous and line clusters.

In Fig. 5.6 we show the qualitative comparison results of our method with other FCM-based methods [Bezdek, 1981, Shen et al., 2005, Xue et al., 2003, Cai et al., 2007, Despotovic et al., 2010d], where Signal-to-Noise Ratio (SNR) between the original and noisy image is 14 dB. As can be seen in Fig. 5.6(b), the standard FCM algorithm can not classify correctly four classes. The method by Shen et al. [Shen et al., 2005] shows the improved segmentation performance compared to the standard FCM algorithm, but it is not effective for the higher noise levels shown in Fig. 5.6(c). The method from Xue et al. [Xue et al., 2003], which is using image pre-processing and

SNR = 14 dB

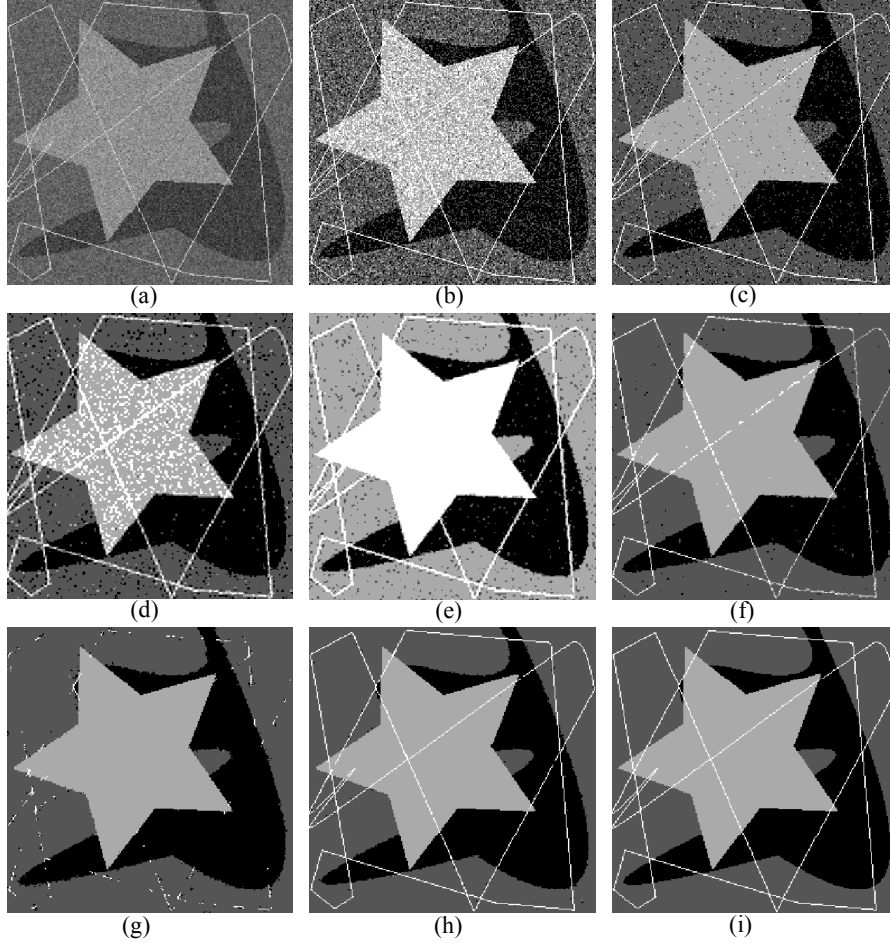


Figure 5.6: Comparison of the segmentation results: (a) noisy image SNR=14 dB; (b) FCM [Bezdek, 1981]; (c) Shen et al. [Shen et al., 2005]; (d) Xue et al. [Xue et al., 2003] without post-processing; (e) Xue et al. [Xue et al., 2003] with post-processing; (f) Cai [Cai et al., 2007]; (g) our method without phase congruency (isotropic neighborhood); (h) our proposed method (anisotropic neighborhood); (i) original image (“ground truth”).

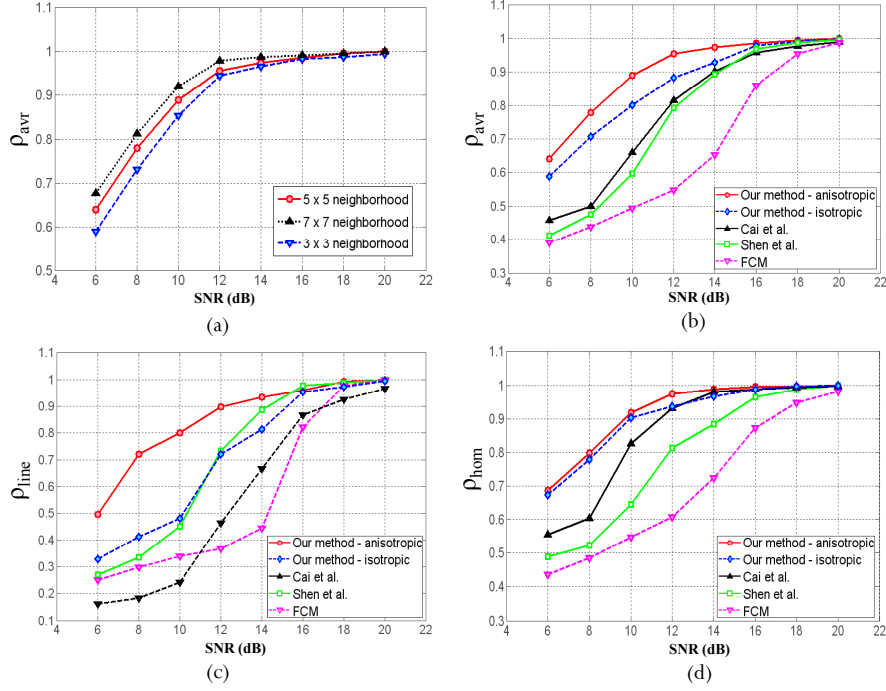


Figure 5.7: Quantitative validation results for different noise levels (SNR): (a) segmentation performance using different neighborhood sizes; (b), (c) and (d) comparison results of FCM, Shen et al., Cai et al. and our proposed algorithm using isotropic and anisotropic neighborhood configuration. The upper-right graph shows the average Dice coefficient ρ_{avr} . The lower-left graph shows the Dice coefficient for the line class ρ_{line} and the lower-right graph shows the average Dice coefficient for the homogeneous classes excluding line ρ_{hom} . In all three cases our method shows the best performance.

post-processing to improve the segmentation performance, shows blurring artifacts after pre-processing (Fig. 5.6(d)) and wrong classification (merging the line with another class) after post-processing (Fig. 5.6(e)). The method from Cai et al. [Cai et al., 2007], which is using image filtering before applying the fast version of the FCM, shows better performance (Fig. 5.6(f)) than previous methods, but still causing blurring, data misclassification and lost of line elements for the higher noise levels. Finally, the results of our method using only isotropic neighborhood configuration in Fig. 5.6(g) is very efficient in segmenting homogeneous regions, but not in preserving the line feature. By adding phase congruency and anisotropic neighborhood configuration to the algorithm, we get the best segmentation result, see Fig. 5.6(h).

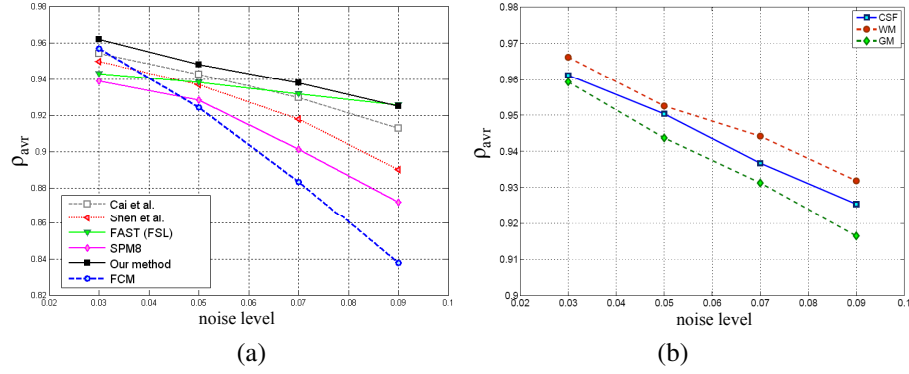


Figure 5.8: Quantitative validation results for different noise levels (3%, 5%, 7% and 9%): (a) comparison results of FCM, Shen et al., Cai et al., SPM, FSL and our proposed algorithm using anisotropic neighborhood configuration and 3×3 neighborhood size; (b) segmentation performance of our methods for white matter, gray matter and CSF. Both graphs show the average Dice coefficient ρ over all MRI slices.

5.5.2 Simulated brain MRI data - BrainWeb

In this experiment, we use simulated MR images from the realistic brain phantom with known “ground truth”, which are obtained from the BrainWeb (Simulated Data Base at the McConnell Brain Imaging Centre of the Montreal Neurological Institute) and described in [Collins et al., 1998].

The quantitative segmentation results for four different noise levels (3%, 5%, 7% and 9%) are shown in Fig. 5.8. The Dice coefficient (see Eq. (4.14)) is also used here as the similarity index ρ between the segmented and “ground truth” images. For all graphs the plotted similarity measure ρ is the average similarity measure over all slices of the MRI brain phantom. The first graph in Fig. 5.8(a) shows the comparison results between our method, FCM and two FCM-based methods (Shen et al. and Cai et al.) and two popular MRI segmentation methods - not FCM-based (Statistical Parametric Mapping (SPM) [Ashburner and Friston, 2005] and FMRIB’s Automated Segmentation Tool (FAST-FSL) [Zhang et al., 2001]). The experimental results indicate that our method has the highest accuracy in segmentation compared to other methods. The segmentation results of our algorithm for each of the three classes (WM, GM and CSF) are plotted in the second graph Fig. 5.8(b).

The qualitative segmentation result of the brain MRI with 9% noise (slice 70) are shown in Fig. 5.9. The original noisy image is shown in Fig. 5.9(a) and the “ground truth” segmentation image in Fig. 5.9(f). Here, the goal was to segment the brain into three classes: white matter, gray matter and cerebrospinal fluid (CSF) (which can be identified as white, light gray and dark gray class in the “ground truth” image). The best segmentation results plotted in Fig. 5.9 are obtained using 3×3 neighborhood.

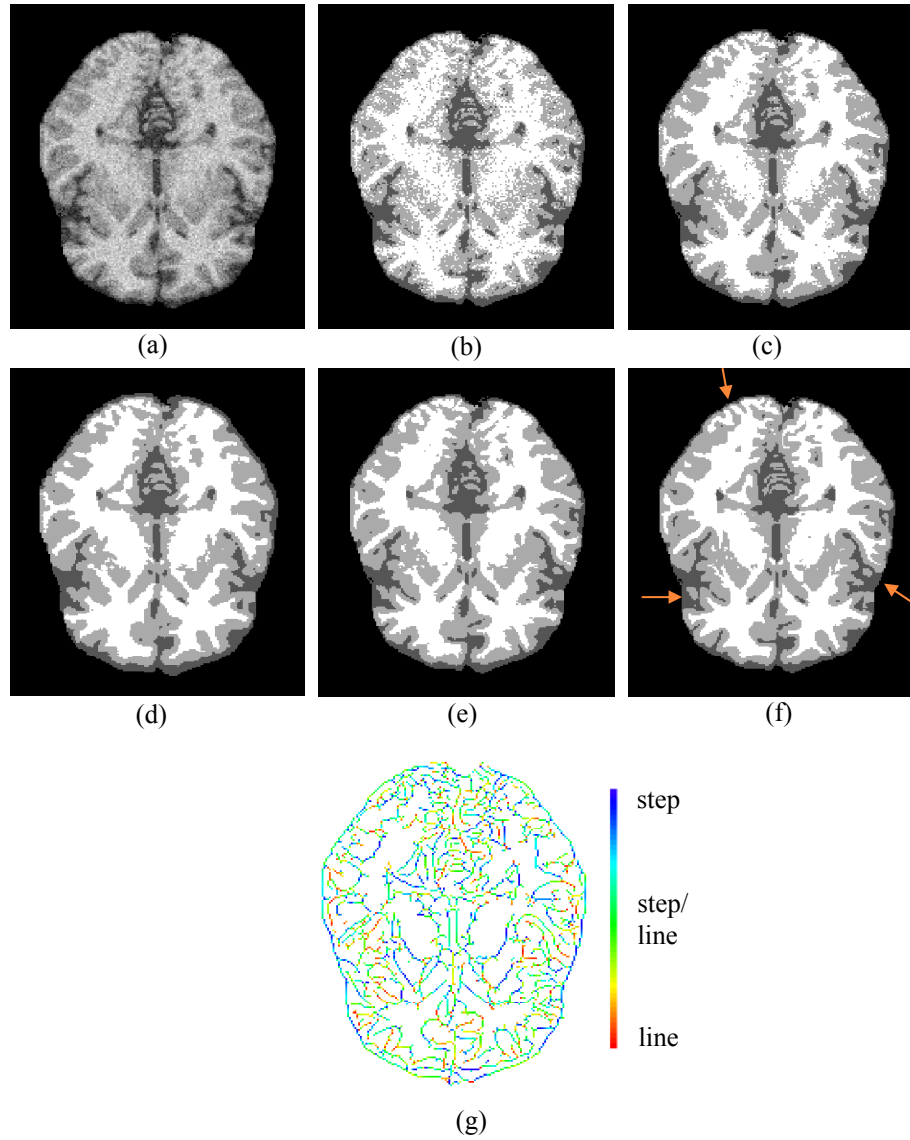


Figure 5.9: Segmentation result using T1-W MRI BrainWeb phantom image, slice 70: (a) noisy image corrupted with 9% noise; (b) FCM [Bezdek, 1981]; (c) Shen et al. [Shen et al., 2005]; (d) Cai et al. [Cai et al., 2007]; (e) our segmentation result; (f) “ground truth” image and (g) the phase congruency feature map indicating line and step edge features in color. Compared to the “ground truth” image (look at the areas indicated with the arrows), our segmentation is robust to noise and preserves image details the best.

We compare our segmentation results with the results of the standard FCM [Bezdek, 1981], Shen et al. [Shen et al., 2005], Cai et al. [Cai et al., 2007] methods. The segmentation result of the standard FCM algorithm in Fig. 5.9(b) shows the worst performance and high sensitivity to image noise. Although a better result is obtained using the algorithm of Shen et al. Fig. 5.9(c), their method is still not enough efficient to deal with higher noise levels. This drawback is improved in the algorithm of Cai et al. Fig. 5.9(d), which is able to remove all noise artifacts and give nice homogeneous regions, but it is not able to perceive line elements (like sulci, folded brain cortex regions filled with CSF). The phase congruency feature map indicating step edges and sulci of the brain is shown in Fig. 5.9(g). Compared to the “ground truth” in Fig. 5.9(f) and other segmentation results, our method successfully segments both homogeneous regions and brain sulci as shown in Fig. 5.9(e).

5.5.3 Real images

The performance of our algorithm is also demonstrated on four real images: (1) a Computer Tomography (CT) image of the skull, (2) a satellite image of the airport, (3) a fingerprint image and (4) a CT image of the liver with tumor lesion. The qualitative results for all four images are shown in Fig. 5.10. Images in the left column are the original images. The segmentation results using the standard FCM method are shown in the second column and the results using the proposed noise-robust FCM segmentation are shown in the right column.

For the first image, a CT image of the human skull, the goal was to segment the bone structures of the skull which have a light gray or white intensity on the original CT image. For this purpose, we segmented the image in two clusters: the bone structures as the first cluster and the rest of the tissue plus background in the second cluster. Since the original image is corrupted with noise artifact the segmentation result using the standard FCM segmentation was not successful and isolated noisy pixels appeared all over the image. The noise problem is successfully eliminated and the segmentation result is visibly improved by using our noise-robust FCM method. The skull is precisely segmented as a one homogeneous structure and the noisy pixels in the background are removed.

For the second and third images the goal was to accurately segment line elements of the airport tracks and fingerprint curves respectively. Also, in these two examples, we segmented images in two clusters. In the satellite image of the airport, we segmented the airport tracks and nearby roads in the first cluster (appears white in the segmentation image -white label) and the rest of the image in the second cluster (black label). In the example of a fingerprint image, we segmented the fingerprint friction ridges in the first cluster (black label) and the rest in the second cluster (white label). These two image examples have less noise artifacts than the first image and the FCM segmentation gives better result than in the first case. However, still some noise artifacts are present, especially in the fingerprint image. The results using our method again show the segmentation improvements by efficiently removing noise pixels but at the same time preserving line elements without blurring or over-segmenting them.

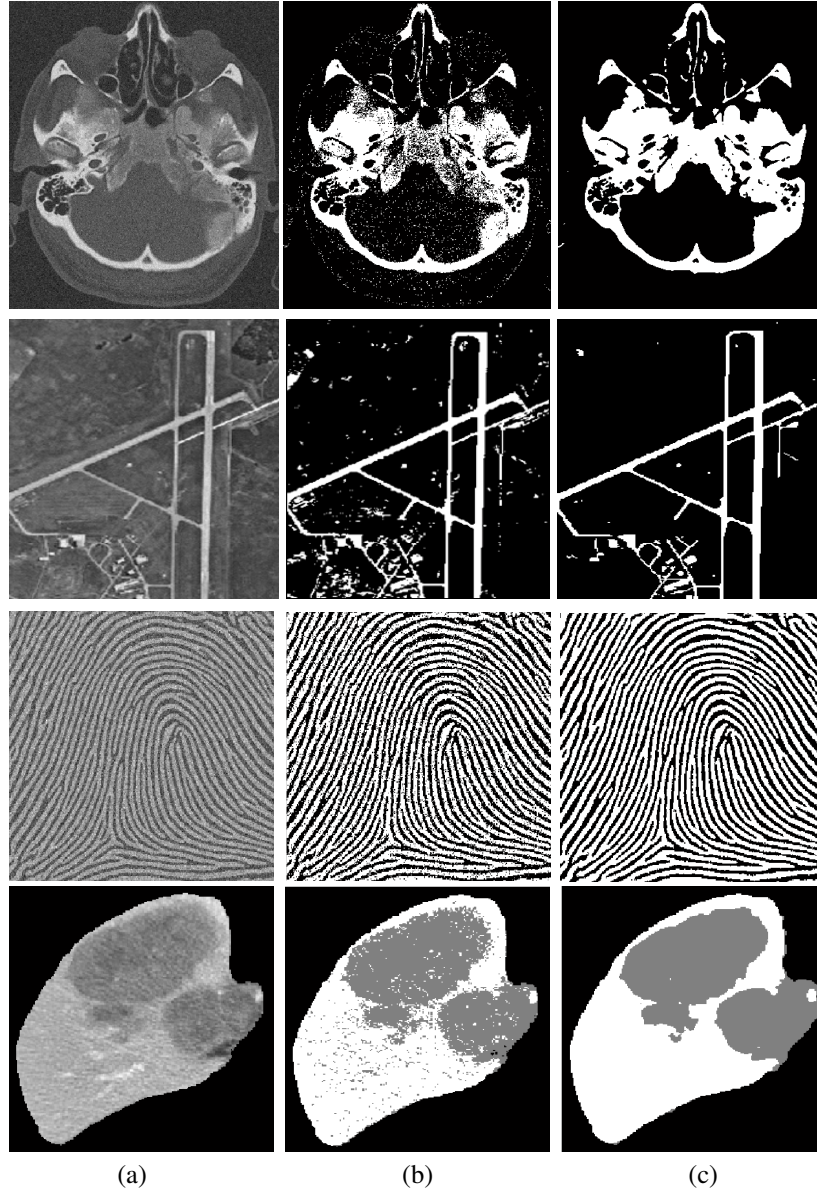


Figure 5.10: Segmentation results of the standard FCM and our proposed method on four real images. The first row represents a CT image of the skull, the second row shows a satellite image of the airport, the third row shows a fingerprint image and the last row shows a CT image of the liver with a tumor lesion. In the first column (a) we have original images. The second column (b) shows the results of the FCM segmentation and the last column (c) shows the results of our proposed segmentation.

For the last image, a CT image of the liver, the goal was to separate the tumor lesion, which appears as darker tissue in comparison to the rest of the liver tissue. In this example we segmented the image in three clusters: the tumor tissue as the first cluster, the rest of the liver tissue as the second cluster and the image background in the third cluster. The noise artifacts are again present after the FCM segmentation, while the result using our segmentation algorithm removes noise and shows more homogeneous regions.

5.6 Multimodal spatially constrained FCM clustering

In this Section we propose the multimodal extension of the FCM method for more accurate and spatially constrained multimodal brain MRI segmentation, from hereon termed as SCFCM. To preserve the homogeneity of different brain tissues, we combined information from both T_1 -W and T_2 -W MRI scans into the spatial neighborhood information. Here, we used an isotropic multimodal neighborhood model. The performance of the proposed algorithm is tested on simulated and real adult MR brain images with different noise levels, as well as on neonatal MR brain images with the gestational age of 39 weeks. Experimental quantitative and qualitative segmentation results show that the proposed method is effective and robust to noise. Also, SCFCM appears as a very promising tool for complex and noisy image segmentation of the neonatal brain.

5.6.1 SCFCM algorithm

The new SCFCM clustering aims to improve the robustness of the FCM algorithm and the accuracy of MRI brain segmentation. In this multimodal clustering method, we modify the distance measure of the FCM, similarly as in Eq. (5.15), by including the multimodal spatial contextual information \mathcal{M}_{ij} as follows:

$$D_{ij}^{**} = w_{ij} \|\mathbf{x}_j - \mathbf{v}_i\|^2 = (1 - \alpha \mathcal{M}_{ij}) \|\mathbf{x}_j - \mathbf{v}_i\|^2, \quad (5.22)$$

where $\alpha \in [0, 1]$ is a parameter to control the relative importance of the neighborhood attraction and \mathbf{x}_j is a two-dimensional feature vector consisting of the pixel intensities from T_1 -W and T_2 -W images at position j . If $\alpha = 0$, D_{ij}^{**} is the squared Euclidean distance and we have the standard FCM.

The multimodal spatial contextual information \mathcal{M}_{ij} depends on the feature attraction a_{jr} (pixel intensities in our case) and the distance attraction d_{jr} (spatial position of the pixels), and is defined as the average of the neighborhood contributions from both the T_1 -W and T_2 -W images:

$$\mathcal{M}_{ij} = \frac{1}{2} \left(\frac{\sum_{r=1}^{\mathcal{N}_r} u_{ir} a_{jr}^{(T_1)} d_{jr}^{-1}}{\sum_{r=1}^{\mathcal{N}_r} a_{jr}^{(T_1)} d_{jr}^{-1}} + \frac{\sum_{r=1}^{\mathcal{N}_r} u_{ir} a_{jr}^{(T_2)} d_{jr}^{-1}}{\sum_{r=1}^{\mathcal{N}_r} a_{jr}^{(T_2)} d_{jr}^{-1}} \right), \quad (5.23)$$

where \mathcal{N}_r is the number of neighbors surrounding the element \mathbf{x}_j and u_{ir} is the membership degree of the neighboring element \mathbf{x}_r to the cluster i . Feature attractions $a_{jr}^{(T_1)}$ and $a_{jr}^{(T_2)}$ are defined as the absolute intensity differences between \mathbf{x}_j and its neighbor \mathbf{x}_r in respectively the T_1 -W and T_2 -W image as

$$a_{jr}^{(T_1)} = |[\mathbf{x}_j]_1 - [\mathbf{x}_r]_1| \quad \text{and} \quad a_{jr}^{(T_2)} = |[\mathbf{x}_j]_2 - [\mathbf{x}_r]_2| . \quad (5.24)$$

The distance attraction d_{jr} between the coordinates of elements $\mathbf{x}(p_j, q_j)$ and $\mathbf{x}(p_r, q_r)$ could be defined in different ways, but for this study we use the squared Euclidean distance

$$d_{jr} = (p_j - p_r)^2 + (q_j - q_r)^2 , \quad (5.25)$$

where a different weight is assigned to the first and the second order neighborhood.

This is slightly different than in the case of the Manhattan distance, defined in Eq. (5.18), where the distance weight is the same for the first and the second order neighborhood. The Manhattan distance is more appropriate in the case when the image consists of broad homogeneous regions of a simpler geometric structure as it is the example in Fig. 5.6(a) or when an anisotropic neighborhood is used. However, in the case when the image consists of more complex structures, such as the brain tissue, it is desirable to assign different weights to further neighbors to avoid the smoothing or even elimination of some important smaller anatomical structures (e.g. the brain cortex fissures).

In Eq. (5.23), the reciprocal of the distance d_{jr}^{-1} reflects the fact that neighbors \mathbf{x}_r closer to the element \mathbf{x}_j should have more influence on the result, while further neighbors should be less important.

The outline of the proposed SCFCM algorithm is:

Step1. Set the number of clusters C , degree of fuzziness m , stop criterion ϵ and neighborhood size.

Step2. Initialize the centers of the clusters \mathbf{v}_i and using FCM calculate u_{ij} .

Step3. Calculate the modified multimodal distance D_{ij}^{**} , see Eq. (5.22).

Step4. Update u_{ij} using the modified distance D_{ij}^* , see Eq. (5.3).

Step5. Update \mathbf{v}_i using u_{ij} , see Eq. (5.4).

Repeat steps 3-5 until the stop criterion $\max_{i \in [1, C]} \|\mathbf{v}_i^{(l)} - \mathbf{v}_i^{(l+1)}\|_\infty < \epsilon$ is satisfied.

As it has been already noted in Section 5.4.3, the segmentation performance and the computational speed of the clustering methods highly depend on the initialization step. Here, we also use intensity-based thresholding [Reddi et al., 1984] (as an initial segmentation) to initialize the cluster centers and to generate a fast and reliable convergence of the FCM's objective function.

5.6.2 Experimental results - simulated brain MRI data

In this section, the experimental results of applying the multimodal SCFCM algorithm to simulated BrainWeb MRI [BrainWeb, 2013] is presented for different noise levels. The method is compared with the segmentation performance of the standard FCM [Bezdek, 1981] (including intensities of both T_1 -W and T_2 -W MRI into the feature vector) and SCFCM with only T_1 -W MRI. For all experiments, we set the number of clusters $C = 3$, the weighting exponent $m = 2$, $\epsilon = 0.001$ and the neighborhood size 3×3 . The parameter α , which controls the effect of the neighborhood attraction in SCFCM, is experimentally determined. Since the lower signal-to-noise ratio (SNR) of the MRI signal requires a higher value of the parameter α , it changes with the noise level for the simulated data. In the following experiments we use $\alpha = 0.8$ for 9% noise, $\alpha = 0.7$ for 7% noise, $\alpha = 0.4$ for 5% noise and $\alpha = 0.1$ for 3% noise.

The quantitative comparison results for different noise levels between the 3DGC method that we proposed in the previous chapter, the standard FCM which includes both T_1 -W and T_2 -W MRI intensities in the feature vector, the noise-robust FCM that we introduced in the previous section, the SCFCM using only T_1 -W MR image (SCFCM T1) and both T_1 -W and T_2 -W MR images (SCFCM T1&T2) are presented in Fig. 5.11(a). We used the Dice similarity index ρ for the comparison and quantitative evaluation. In our experiment, the results for ρ are averaged over slices with indices 30, 60 and 90. From Fig. 5.11(a) we can clearly see that the SCFCM T1&T2 gives better results than the SCFCM T1, 3DGC and FCM for lower noise levels. However, the noise-robust FCM method outperforms all methods in this example. For the highest noise level, the 3DGC gives equally good result as the SCFCM T1&T2. Detailed results for SCFCM T1&T2 in terms of anatomical structures are depicted in Fig. 5.11(b). For any of the three brain tissues, the maximum difference between two noise levels is less than 2% in similarity index ρ . This experiment on simulated brain MRI is very interesting to quantitatively compare the segmentation performance of our different segmentation methods: the automatic 3DGC, the noise-robust FCM clustering and the unsupervised SCFCM clustering.

For the qualitative comparison results, we use the three representative slices with indices 60, 90 and 120 from the BrainWeb data and corrupted with 9% Gaussian noise. The qualitative segmentation results of the standard FCM, SCFCM T1 and SCFCM T1&T2 for different noise levels are showed in Fig. 5.12 for the slice 60, Fig. 5.13 for the slice 90 and Fig. 5.14 for the slice 120. In all three examples, results show that the standard FCM method, although including multimodal intensity information, can not deal with noisy images and gives the worst segmentation result. The SCFCM method using only T_1 -W MRI gives better result by eliminating isolated noisy pixels. The best segmentation result is achieved using the multimodal SCFCM method, which highly agrees with the “ground truth” segmentation and this can be visually noted.

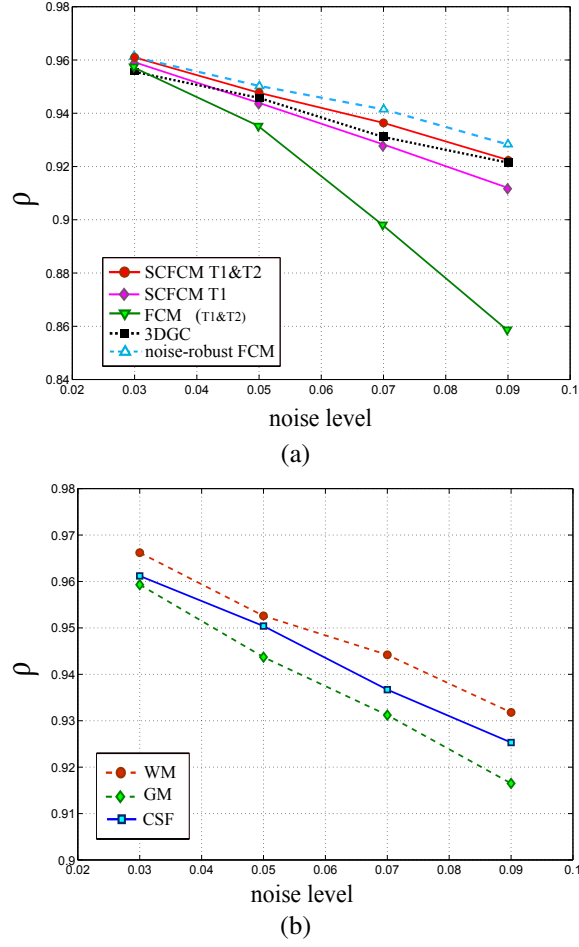


Figure 5.11: Quantitative validation result for different noise levels. (a) Comparison results between: the 3DGC method that we proposed in the previous chapter, the standard FCM method, the noise-robust FCM with anisotropic neighborhood, the SCFCM using only T_1 -W MR image (SCFCM T1) and using multimodal T_1 -W and T_2 -W MR images (SCFCM T1&T2). The similarity index ρ is the average value of the similarity indexes for WM, GM and CSF tissue over the slices with indices 30, 60 and 90. (b) Segmentation performance of the multimodal SCFCM (SCFCM T1&T2) for WM, GM and CSF.

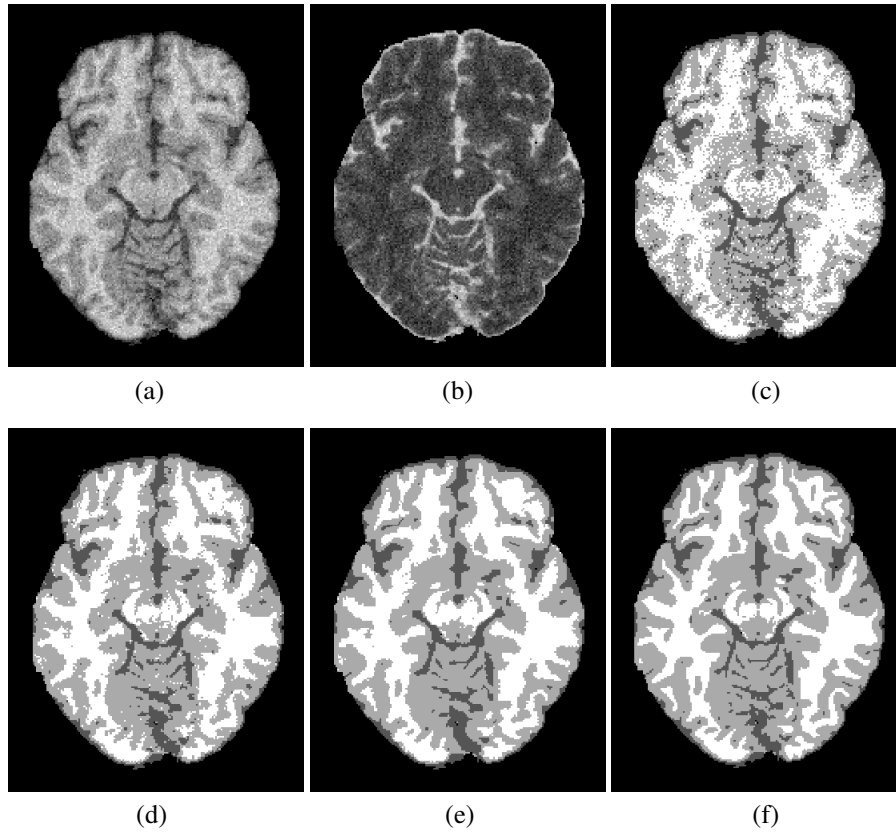


Figure 5.12: Comparison of the segmentation results on the 60th BrainWeb brain slice: (a) the original T_1 -W MR image with 9% noise; (b) the original T_2 -W MR images with 9% noise; (c) the segmentation result obtained with the FCM algorithm; (d) the segmentation result of the SCFCM method using only T_1 -W image; (e) the segmentation result of the multimodal SCFCM method using T_1 -W and T_2 -W MR images; (f) the “ground truth” segmentation .

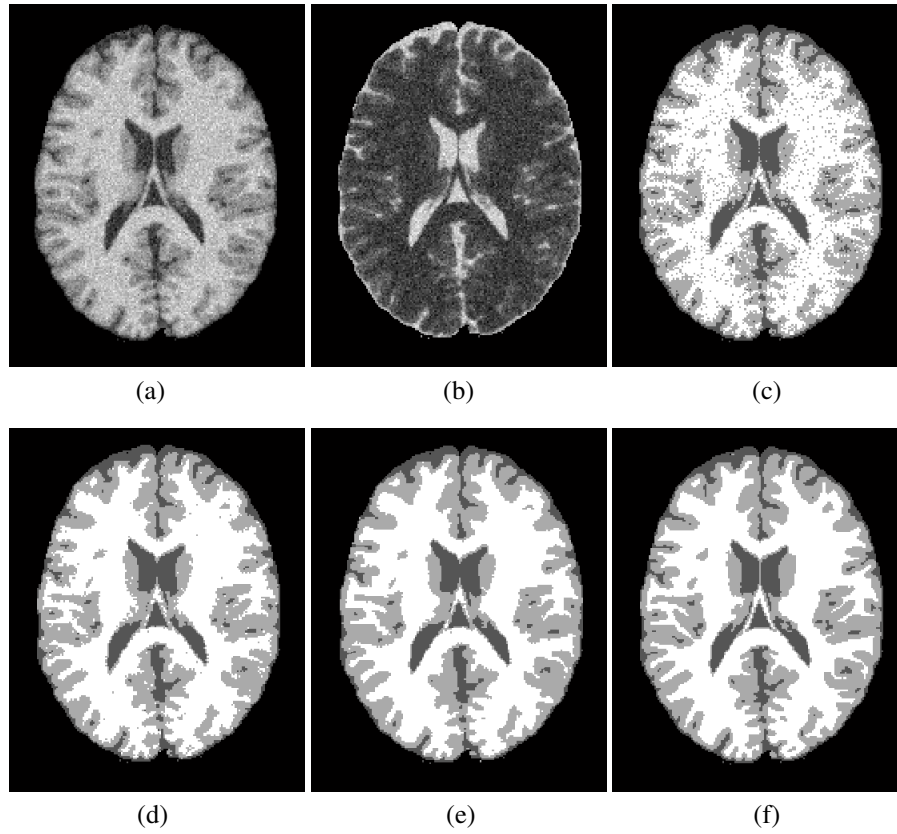


Figure 5.13: Comparison of the segmentation results on the 90th BrainWeb brain slice: (a) the original T₁-W MR image with 9% noise; (b) the original T₂-W MR images with 9% noise; (c) the segmentation result obtained with the FCM algorithm; (d) the segmentation result of the SCFCM method using only T₁-W image; (e) the segmentation result of the multimodal SCFCM method using T₁-W and T₂-W MR images; (f) the "ground truth" segmentation .

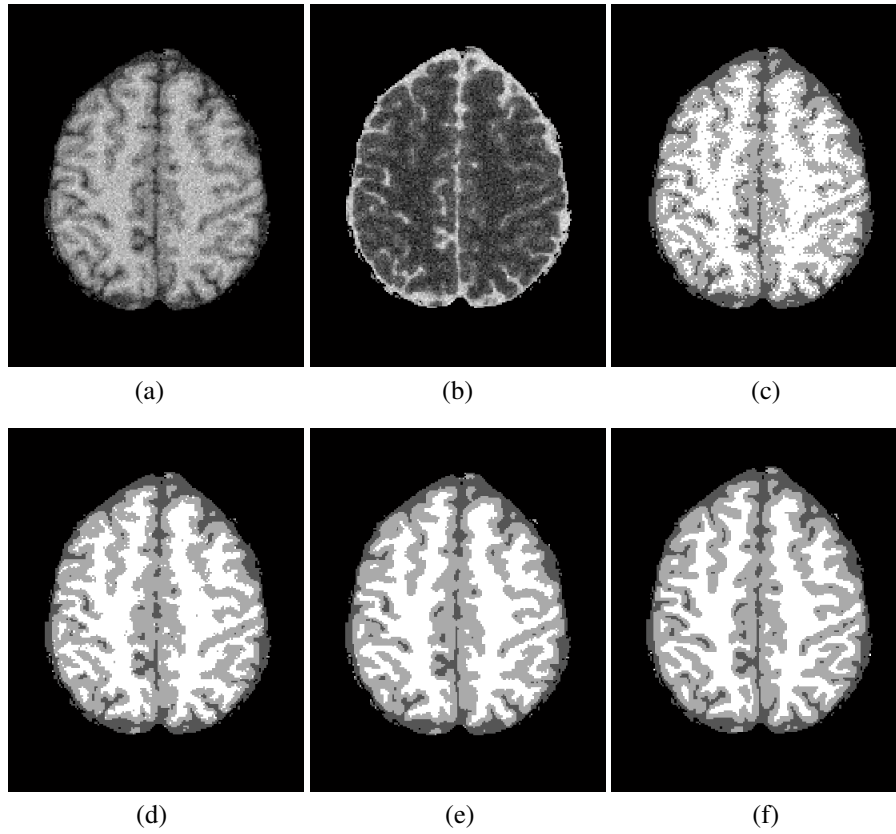


Figure 5.14: Comparison of the segmentation results on the 120th BrainWeb brain slice: (a) the original T_1 -W MR image with 9% noise; (b) the original T_2 -W MR images with 9% noise; (c) the segmentation result obtained with the FCM algorithm; (d) the segmentation result of the SCFCM method using only T_1 -W image; (e) the segmentation result of the multimodal SCFCM method using T_1 -W and T_2 -W MR images; (f) the “ground truth” segmentation .

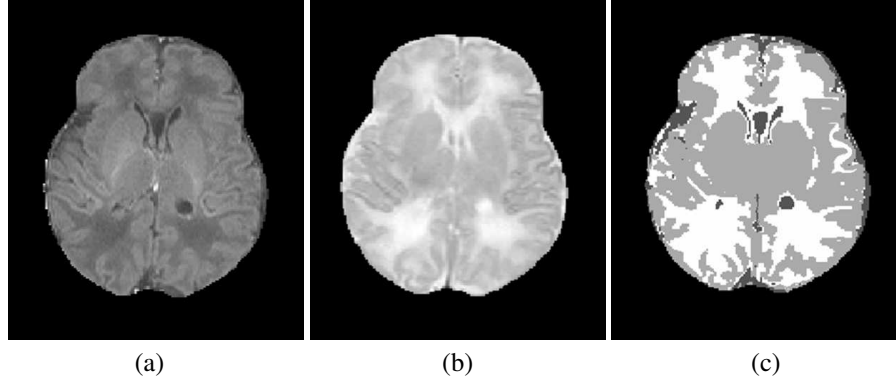


Figure 5.15: Real neonatal MR brain image: (a) and (b) original T_1 -W and T_2 -W MR images respectively; (c) the multimodal SCFCM segmentation of the neonatal brain in three tissues: WM (white segment), GM (light gray segment) and CSF (dark gray segment).

In addition to synthetic brain MRI we also demonstrate the performance of our multimodal SCFCM algorithm on real neonatal MRI images. Due to lack of ground truth, the real neonatal MR brain scans are used only for qualitative validation. The neonatal MR brain data in Fig. 5.15 was recorded at Sophia Children's Hospital (Erasmus Medical Center, Rotterdam, the Netherlands), on a newborn preterm (born at 39 weeks of gestation) subject to asphyxia. Both T_1 -W and T_2 -W MR images were acquired on a Siemens 1.5T MRI scanner ($256 \times 256 \times 20$ voxel matrix with a resolution of $0.7mm \times 0.7mm \times 4mm$). Before segmentation, the T_1 -W and T_2 -W neonatal images are registered and the non-brain tissue is eliminated.

We use this multimodal SCFCM method in Chapter 6 for multimodal MRI segmentation of the neonatal brain tissue.

5.7 Computational efficiency

The final implementation of the proposed fuzzy segmentation methods is done in Matlab. The execution time of the noise-robust FCM clustering for 256×256 image, 3×3 neighborhood and 3 labels (clusters) is less than 1 min. Note that this execution time also includes the calculation of the phase congruency features. Typically, the convergence of the noise-robust FCM energy function is reached after less than 15 iterations.

The execution time of the multimodal FCM clustering for two-modal 256×256 images, 3×3 neighborhood and 3 clusters is also less than 1 min. Note that in this multimodal FCM method we only used isotropic neighborhood (there are no phase congruency features). The convergence of the multimodal FCM energy function is reached after less than 10 iterations. Additional image preprocessing steps that are necessary in brain MRI segmentation were not included in the calculation time.

In comparison with the 3DGC method, both the noise-robust FCM and the multimodal SCFCM are slow. However, the 3DGC method is fully implemented in C++ and we believe that implementation of the FCM methods in C++ can reduce running time by more than a half.

5.8 Future directions

From a methodological point of view, future work can focus on few different improvements of the proposed fuzzy segmentation method. The first improvement can be an extension of the method to deal with volumetric 3D images by incorporating 3D neighborhood information. The second improvement can include bias field correction of MR images directly into the FCM objective function. This will allow the labeling of an image element to be influenced by the neighboring labels and at the same time compensate for intensity inhomogeneities. The third possibility is to include the prior knowledge (in the case of brain MRI - the probabilistic brain atlas) into the segmentation framework. The fourth possibility is to automatically determine the optimal parameters α and β for isotropic neighborhood models and in the case of multimodal image segmentation. The fifth improvement is to automatically determine the optimal number of clusters, because in our work the number of clusters is determined manually. Finally, further improvements in both speed and accuracy of the spatially-coherent and noise-robust FCM should be also considered in the future work.

5.9 Conclusion

In this chapter, we have presented a spatially-coherent fuzzy C-means clustering method for segmentation of noisy images. To enable accurate and noise-robust image segmentation, we integrated both intensity and spatial contextual information of the neighboring pixels into the segmentation algorithm using anisotropic neighborhood configuration. The phase congruency method is used to determine significant image features (edges and lines) and define anisotropic neighborhood. In this way, the proposed method is designed to accurately segment fine image elements and coarse homogeneous regions at the same time. Next to this, we have also presented a multimodal modification of the FCM method for unsupervised segmentation of three brain tissues (CSF, GM, WM) in MRI. To enable noise-robust multimodal segmentation we integrated intensity information from both T_1 -W and T_2 -W images and local spatial contextual constraint into the segmentation algorithm.

The quantitative and qualitative experimental results for synthetic and real images showed a good segmentation performance, especially for very noisy images, and demonstrate an encouraging future of practical applications of the proposed method. For example, our method could be useful in applications such as image texture segmentation, medical image segmentation and multispectral image segmentation, where

spatial contextual information is important. The performance of the multimodal spatially constrained FCM algorithm is tested on simulated and real adult MR brain images with different noise levels, as well as on neonatal MR brain images with the gestational age of 39 weeks. The experimental results showed that the SCFCM method is effective and more robust to noise than other FCM-based methods and can be used for a complex and noisy image segmentation of the neonatal brain.

6

Developing a realistic head model in neonates

If an elderly but distinguished scientist says that something is possible, he is almost certainly right; but if he says that something is impossible, he is very probably wrong.

– Arthur C. Clarke

Developing a realistic volume conductor head model is an important step towards a non-invasive investigation of neuro-electrical activity in the brain. For adults, different volume conductor head models have been designed and successfully used for EEG source analysis. However, creating an appropriate neonatal volume conductor head model is a challenging task mainly due to the more complex anatomy of the developing newborn brain in comparison to adults and insufficient knowledge of head tissue conductivities.

In this chapter we present a pipeline for modeling a realistic volume conductor model of the neonatal head, where we address the modeling challenges (particularly neonatal brain MRI segmentation challenges) and propose our solutions. We explain the necessary MRI segmentation steps for neonatal realistic head modeling including MRI preprocessing, brain volume segmentation, reconstruction of the neonatal skull and final 3D reconstruction. Further on, in Chapter 7 we use this realistic head modeling pipeline to create personalized realistic head models for neonatal EEG source localization.

6.1 Introduction

The rapid development of non-invasive brain imaging techniques has opened new horizons in the study of brain structure and function. In studies of brain pathology, such as epilepsy, birth asphyxia or strokes, the most important diagnostic tools are MRI and EEG. They can capture features of brain anatomy and function, and map neuronal dynamics and degenerative processes. Since individual analysis of EEG and

MRI have its strengths and weaknesses, there is an increasing demand for multimodal EEG-MRI brain analysis, such as EEG source analysis, to synthesize the strengths inherent in each technique [Michel et al., 2004]. However, one of the most important steps in EEG source analysis is a volume conductor head modeling.

The first volume conductor models of the human head were modeled as a homogeneous sphere [Frank, 1952]. Soon it was noticed that different head structures such as the skull, scalp and brain tissue have significantly different conductivities and a new three-shell concentric spherical head model was introduced. In this model, the outer layer represented the scalp, the middle layer represented the skull and the inner layer represented the brain tissue. However, since the spherical head model is just a simplified model of a real human head, further improvements were necessary for more accurate EEG source analysis [Vatta et al., 2010].

New possibilities in the human head modeling came with the development of modern medical imaging techniques such as MRI and CT, which allow in vivo study of the human brain by providing detailed anatomical images of the brain's structure. Nowadays, a more realistic head modeling is possible by segmenting volumetric 3D MRI and CT images of the human head in different anatomical structures. Segmented skull, scalp and brain tissue are then used to reconstruct a 3D realistic volume conductor model. Typically, CT images are used for the skull segmentation, while MRI scans are used for the soft tissue segmentation such as the brain tissue and the scalp. Thus, to appropriately reconstruct a 3D head model, MRI and CT images must be registered prior to image segmentation. However, CT imaging is not allowed in neonates due to its invasive nature and the neonatal head tissue segmentation must rely only on acquired MRI scans. This causes difficulties for the neonatal skull segmentation, which is hardly visible on MRI scans.

In general, realistic head modeling is a more challenging task in neonates than in adults. This is because the appearance of the neonatal and mature adult brains differs significantly on MRI scans and the anatomy of the developing newborn brain is more complex in comparison to adults, see Section 2.2.3.2. Furthermore, there is insufficient knowledge of head tissue conductivities, which, to our knowledge, have never been measured in neonates. Due to these reasons, it is not possible to use the same methods and parameters in neonates that are used for creating an adult realistic head model.

However, the main framework for creating a realistic volume conductor model is still the same in both adults and neonates and includes three equally important steps:

1. MRI segmentation of the head in different head structures such as the scalp, skull and brain tissue;
2. Selection of appropriate conductivities for each head structure;
3. Appropriate placement of the EEG electrodes on the scalp surface.

In this chapter we will address MRI segmentation step, while the steps (2) and (3) will be discussed in more detail in the next Chapter 7.

The chapter is organized as follows. In Section 6.2 we present the main steps of our integrated method for MRI segmentation of the neonatal head that is used for a realistic head modeling. First, we explain preprocessing steps that are used to prepare neonatal MRI for segmentation. Then, we propose the new brain extraction method for neonates and explain methods for MRI segmentation of the neonatal brain tissue. The neonatal skull and scalp segmentation is explained in Section 6.2.4. We also present experimental results of the brain extraction method and compare qualitatively with the manual expert segmentation. In Section 6.3 we summarize and explain the steps for a realistic head modeling. Finally, we conclude this chapter in Section 6.4.

6.2 MRI segmentation of the neonatal head

Head tissue segmentation in newborns is more complex than in adults due to fast growth process, complex anatomy of the developing brain and often poor MRI quality, see Section 2.1.2. Next to the often unavoidable artifacts such as the motion of a non-sedated subject, neonatal brains exhibit different signal intensity characteristics than mature adult brains, see Section 2.2.3.2. Due to these differences, MRI segmentation techniques developed for adults are not applicable for neonates or require additional corrections.

MRI segmentation of the neonatal brain has become a research focus in recent years [Xue et al., 2007, Shi et al., 2011, Weisenfeld and Warfield, 2009]. The existing methods are mainly focused on the problem of neonatal brain tissue segmentation (e.g. brain cortex, myelinated and non-myelinated white matter), and are not developed to segment head structures such as skin, skull, and cranial cavity. Also, the existing methods rely on probabilistic atlases that contain the spatial variability of the tissue structure. However, a good atlas of the newborn brain is difficult to obtain because of the great anatomical variations between subjects and subjective ground truth manual segmentation from which the atlas is derived. Also, an atlas-based segmentation is prone to errors in non-healthy babies due to the existence of brain lesions. Thus, to segment different head structures of the neonatal head, we propose an integrated atlas-free segmentation algorithm based on multimodal T_1 -W and T_2 -W MRI.

All MRI data in this study were recorded at the Sophia Children's Hospital (Erasmus Medical Center, Rotterdam, the Netherlands), on newborn preterms with gestational ages between 37-41 weeks. Both T_1 -W and T_2 -W MRI were acquired on a Siemens 1.5T MRI scanner, $256 \times 256 \times 20$ to 25 voxel matrix, with a resolution of $0.7 \text{ mm} \times 0.7 \text{ mm} \times 4 \text{ mm}$. In few patients, T_2 -W images were acquired at lower in-plane resolution and are later up-sampled to match the higher resolution T_1 -W images. Note that the original MRI scans have low inter-slice resolution to reduce scanning time.

For the purpose of realistic head modeling, we propose an integrated segmentation method that combines active contours, noise-robust FCM clustering and mathematical morphology and is able to segment four head structures in neonates: scalp, skull, cerebrospinal fluid (CSF) and brain tissue. To prepare MRI data for segmentation, we

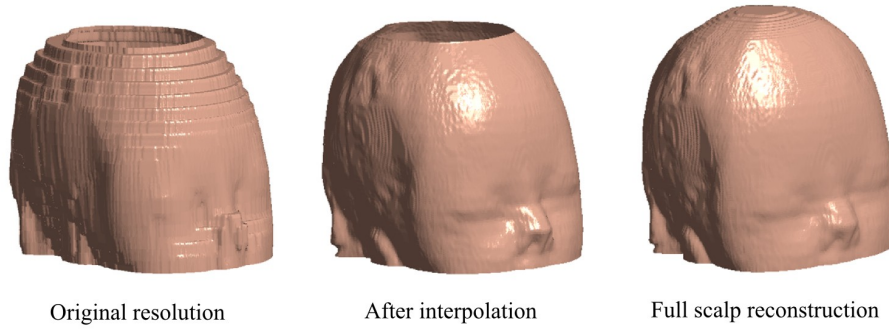


Figure 6.1: 3D reconstruction of low-resolution MRI scans and the result after interpolation. The final results (on the right) shows the appropriate inter-slice resolution.

used several preprocessing steps. First we use cubic spline interpolation to interpolate low resolution MRI scans and obtain the inter-slice resolution of 0.7 mm. Then, we perform bias field (intensity inhomogeneity) correction [Sled et al., 1998] and multimodal T_1 -W and T_2 -W MRI registration [Mattes et al., 2001, Thevenaz and Unser, 2000]. After preprocessing, to identify and segment different head structures (scalp, CSF and brain), we used our brain extraction algorithm [Despotovic et al., 2009a] that will be explained in Section 6.2.2 and an algorithm that combines mathematical morphology and multimodal fuzzy c-means clustering [Despotovic et al., 2010c], see Section 5.6. To reconstruct the neonatal skull, we use mathematical morphology and segmentation results of the brain and the scalp tissue. All these steps will be explained in more detail in the following sections.

To summarize, the proposed algorithm is implemented in the six following steps:

1. Preprocessing of the multimodal T_1 -W and T_2 -W MRI: image interpolation, bias field correction and multimodal image registration;
2. MRI segmentation of the head tissue and the image background;
3. Brain extraction - segmentation of the brain volume;
4. Segmentation of the neonatal brain into two clusters: brain tissue and CSF;
5. Reconstruction of the skull and the scalp;
6. 3D realistic head modeling;

Note that due to the low inter-slice resolution, MRI segmentation is performed in 2D (slice by slice) and the neonatal head is segmented into four labels: scalp, skull, cerebrospinal fluid and brain tissue. White and gray matter are segmented as one class (brain tissue), because of the same conductivity for the neonatal brain.

6.2.1 Preprocessing steps

Several preprocessing steps are necessary before segmenting the neonatal brain into different anatomical structures.

Image interpolation

First, we need to interpolate (up-sample) the original low resolution MRI data to obtain the appropriate inter-slice resolution. It is common in neonatal MRI acquisition that the resolution in the slice direction is much lower than the in-plane resolution because of the short scanning time. This low inter-slice resolution causes disturbing visual artifacts of 3D surfaces of a reconstructed head model. Thus, to obtain smoother surfaces, we need an isotropic resolution of the MRI data. Using the interpolation step we can compute the “missing” voxels in an MRI volume and make that up-sampled 3D volume surface looks better and more realistic than a rough staircase surface of the originally acquired MRI data with a poor inter-slice resolution, see Fig. 6.1. The smooth surfaces of the head structures are important for accurate attachment of EEG electrodes and more precise 3D EEG source localization inside the brain. Note that the interpolation step does not add new information to the original image content.

The goal of interpolation is to estimate the information of missing pixels/voxels in an image based on the information given by existing pixels/voxels, so that the new interpolated image is as close to the original one as possible. The given information can be color, gray level or density and in our case it is gray level intensity of the existing pixels/voxels. There are different interpolation methods such as nearest neighbor, linear, quadratic, cubic spline, and so on. An illustration of different interpolation methods is shown in Fig. 6.2. The nearest neighbor interpolation causes jaggedness or staircase effect, while linear interpolation causes image blurring [Ledda, 2007]. Cubic spline interpolation is considered as a good solution for close to ideal interpolation in many cases and provides attractive properties such as smooth behavior, sufficient regularity and easy implementation [Gotchev et al., 2000]. It also offers a good compromise between computational complexity and accuracy. Thus, in this work we use cubic spline interpolation for the purpose of a realistic head modeling.

Bias field correction

Second, after image interpolation we need to remove the intensity inhomogeneity from the original MRI data. For this purpose we use the non-parametric bias correction method (also called the N3 method - Non-parametric Non-uniform Normalization) proposed by Sled et al. [Sled et al., 1998]. For more details about the bias field correction see Section 3.2.1.

Image registration

After intensity inhomogeneity correction a registration algorithm is required to align T_1 -W and T_2 -W MR images. To do so, we use affine transformation and mutual information metrics [Mattes et al., 2001, Thevenaz and Unser, 2000], where the lower

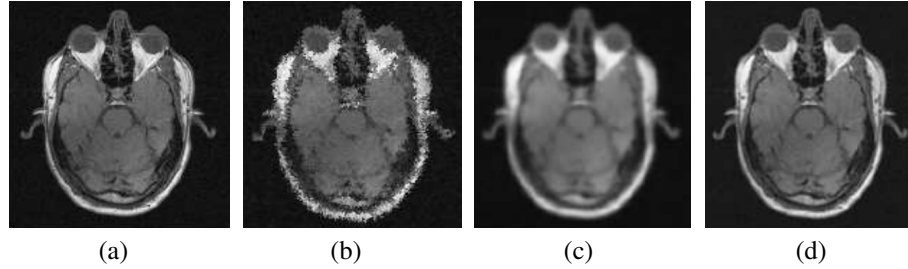


Figure 6.2: Illustration of three commonly used interpolation methods. (a) Original image; (b) Nearest neighbor interpolation; (c) Linear interpolation; (d) Cubic-spline interpolation.

resolution T_2 -W images are up-sampled with cubic spline interpolation to match the higher resolution T_1 -W images. In few neonates, automatic image registration failed or did not give satisfactory results due to the different position angles of the neonatal head during acquisition. In those cases we used supervised registration method where we manually indicated the matching anatomical points (also called landmarks) on both T_1 -W and T_2 -W MRI prior to registration. For more details about image registration see Section 3.2.2.

Brain extraction

Finally, the last and probably the most challenging preprocessing step in neonates is the brain extraction. This step classifies voxels as brain or non-brain. The result can be either a new image with just brain voxels or a binary mask, which has a value of 1 for brain voxels and 0 for the rest of tissues. In general, the brain-voxels comprises GM, WM, and CSF of the cerebral cortex and subcortical structures, including the brain stem and cerebellum. The scalp, dura matter, fat, skin, muscles, eyes and bones are always classified as non-brain voxels. The Fig. 2.2 can help to visualize brain and non-brain parts. This step is challenging because the brain extraction methods proposed for adults do not give satisfactory results when applied to neonates. Thus, we developed a new brain extraction algorithm for neonates, which is explained in the following Section 6.2.2.

6.2.2 Brain volume segmentation

To date, existing brain/non-brain segmentation methods have been mainly developed for adult brain [Shattuck and Leahy, 2002, Smith, 2002, Battaglini et al., 2008]. Among them, BET (Brain Extraction Tool) [Smith, 2002] is the most popular one and is used in SIENA (Structural Image Evaluation, using Normalisation, of Atrophy), which is a robust approach to quantifying brain volume change [Bartsch et al., 2007]. Recently, Battaglini *et al.* [Battaglini et al., 2008] proposed an extension of BET to remove segmentation imperfections (e.g. incorrect inclusion of eyes, periorbital fat and other non-brain structures). However, BET is not designed to segment the neonatal brain.

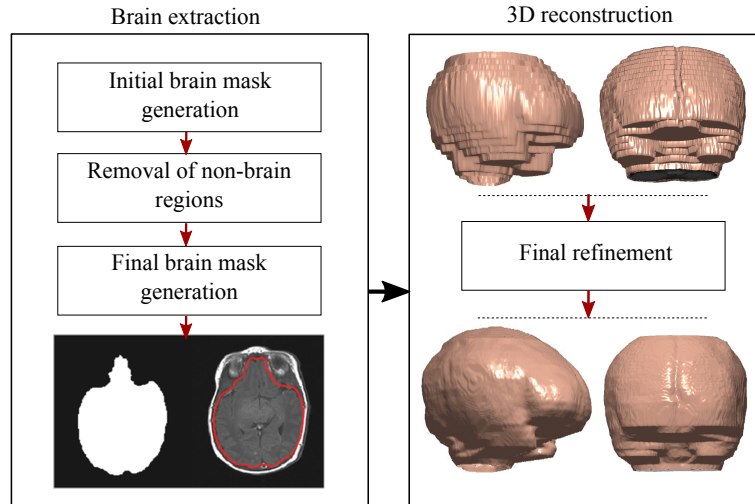


Figure 6.3: A framework representing brain extraction algorithm for neonates using multi-modal MRI images.

Since manual MRI segmentation of the brain is time-consuming, it is desirable to develop a fast and robust computerized method for automatic or semi-automatic brain extraction in neonates. In this Section we propose a hybrid segmentation method for brain volume extraction in neonates using both T_1 -W and T_2 -W MRI, which can also have a low inter-slice resolution. Our method starts with a thresholding step, which generates a binary brain mask. The threshold for an initial segmentation is computed automatically by applying an anisotropic diffusion filter to the image and using the resulting voxel intensity histogram. This is followed by a set of morphological filters: erosion, dilation and closing. Erosion is used to remove small connections between the brain and surrounding tissue such as eyes, muscles and fat. After removing eyes and other non-brain structures, a morphological dilation is performed to recover some of the eliminated tissue. Then, a morphological closing is used to fill in the remaining holes and create a homogeneous brain mask. A final refinement of the brain contour is achieved using active contours proposed by Chan and Vese [Chan and Vese, 2001]. This active contour method is suitable for our application because it can detect objects whose boundaries are not necessarily defined by the gradient, which is often the case in the neonatal brain MRI. An algorithm overview is shown in Fig. 6.3.

The experimental segmentation results of our brain volume segmentation method on real neonatal MRI show that the method achieves performance comparable to manual segmentation and is effective and more accurate than segmentation methods originally developed for adults. Next to a realistic head modeling and 3D volume reconstruction, brain volume segmentation offers the possibility of exploring the developmental changes, measuring the brain growth and detecting early disorders.

6.2.2.1 Image smoothing

To enhance poor MRI quality (e.g to reduce noise, motion artifacts), the registered MR images are filtered using non-linear anisotropic diffusion [Perona and Malik, 1990, Gerig et al., 1992], as modified by Black *et al.* [Black et al., 1998]. The anisotropic diffusion filter is a diffusion process that facilitates intra-region smoothing and inhibits inter-region smoothing, without removing significant parts of the image information that are important for the image interpretation (like edges and lines). The equations that we use for filtering are given as follows:

$$\frac{\partial I(x, y, t)}{\partial t} = \text{div} [g(||\nabla I||)\nabla I], \quad (6.1)$$

$$g(x) = \begin{cases} \frac{\left[1 - \left(\frac{x}{\rho}\right)^2\right]^2}{2} & \text{if } |x| \leq \rho, \\ 0, & \text{otherwise,} \end{cases} \quad (6.2)$$

where $||\nabla I||$ is the gradient magnitude, $g(||\nabla I||)$ is the “edge-stopping” function (Tukey’s biweight) [Black et al., 1998], t is the number of iterations and ρ is a scale parameter. In this method we consider 4 nearest neighbours for diffusion conduction.

6.2.2.2 Brain mask generation

The brain mask generation consists of three main steps. Firstly, we calculate automatic thresholds from the diffused T₁-W and T₂-W MRI histograms to generate an initial brain mask. Then, we use morphological operations to remove the non-brain regions. Finally, we use an active contour model [Chan and Vese, 2001] to refine the brain mask. The brain segmentation steps are illustrated in Fig. 6.5.

Initial brain mask

After anisotropic diffusion, the MRI histogram of a brain is smoother and it allows us to generate automatic thresholds much easier. To obtain initial brain mask, we generate three thresholds (head/background (τ_{bkg}), lower brain (τ_l) and upper brain (τ_u)) using T₁-W and T₂-W MRI histograms, that provide us with different intensity information of the same anatomical structure. The highest peak of the histogram corresponds to the image background and can be approximated by a Rayleigh distribution

$$\rho_R(x) = \frac{x}{\sigma^2} \exp\left(-\frac{x^2}{2\sigma^2}\right), \quad (6.3)$$

where x is the intensity and σ is the standard deviation. Other peaks in the histogram correspond to the head and brain regions and can be approximated with a Gaussian distribution

$$\rho_G(x) = \frac{1}{\sigma\sqrt{2\pi}} \exp\left(-\frac{(x - \mu)^2}{2\sigma^2}\right), \quad (6.4)$$

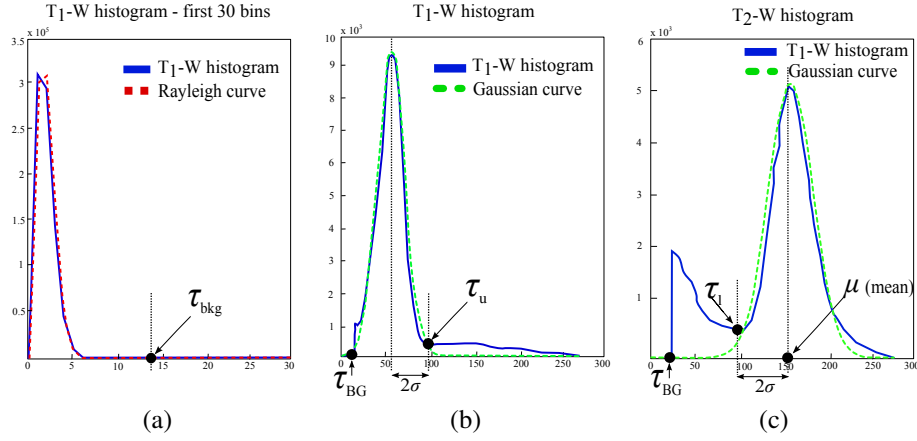


Figure 6.4: Histograms of the T_1 -W and T_2 -W MRI: (a) selecting the head/background threshold τ_{bkg} by fitting the Rayleigh distribution to the first peak of the histogram, (b) setting the upper brain threshold $\tau_u = \mu + 2\sigma$ from the T_1 -W MRI histogram (c) setting the lower brain threshold $\tau_l = \mu - 2\sigma$ from the T_2 -W MRI histogram.

where x , σ and μ are the intensity, the standard deviation and the mean values respectively.

In our algorithm, we firstly calculate the head/background threshold (τ_{bkg}) and the upper brain threshold (τ_u) using T_1 -W MRI histogram and generate binary mask of the head without the eye optic nerves and fat (which are very bright regions in T_1 -W MR images). Then, we apply the obtained head mask on T_2 -W MR images and disconnect the eyes and some of the non-brain tissue from the brain. Next, we calculate the lower brain threshold (τ_l) from the T_2 -W MRI histogram to remove the air and the rest of the non-brain tissue. To select τ_{bkg} , we fit the best Rayleigh curve to the first histogram peak and search for the closest histogram minimum on the right, see Fig. 6.4(a). Similarly, to obtain τ_l and τ_u , we fit the best Gaussian curve to the proper histogram and set thresholds about 2σ below and above the mean value respectively, see Fig. 6.4(b) and Fig. 6.4(c).

Removal of the non-brain regions

In this stage it may still happen that the non-brain tissue is not completely separated from the brain in the initial brain mask. Therefore, before the brain volume is associated with the largest connected component in the binary mask, we apply a sequence of morphological operations to break any remaining attachments. This is normally achieved by morphological filtering in the following way: the bright regions in the binary image are eroded away until any links between brain and non-brain are eliminated, the largest single cluster is then chosen, and this is then dilated by the same extent as the erosion, resulting in a brain mask. At the end, a morphological closing operation is used to fill small holes inside the mask.

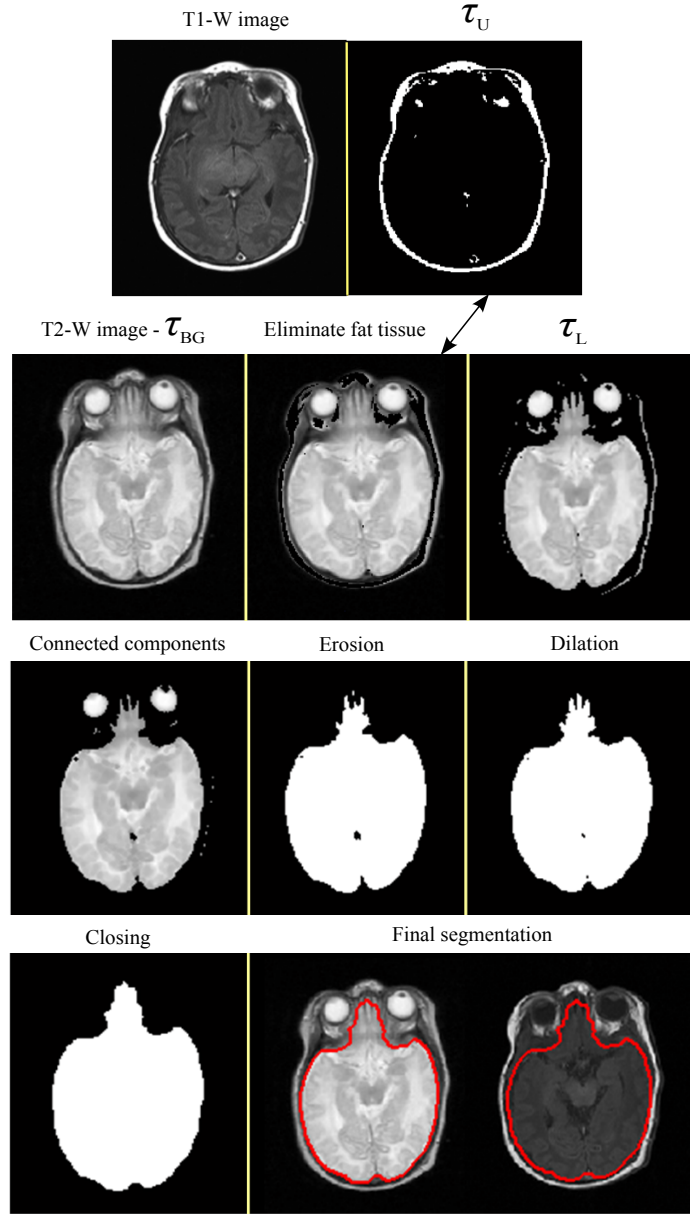


Figure 6.5: An overview of the brain extraction steps. The first row shows the results after applying the three thresholds: head/background τ_{bkg} , upper brain τ_u and lower brain τ_l . The second row shows the results after erosion, finding the biggest connected component and dilation. The third row shows the result after closing and final brain delineation.

Since our brain mask is a binary image $b(i, j)$, it can be described in terms of sets of pixels with coordinates (i, j) assuming the value 1 or 0. To filter these images we need to use binary mathematical morphology, which is based on two basic operators, dilation and erosion. Both operators are defined in terms of a structuring element $h(i, j)$. The structuring element can be thought of as an image, although much smaller in size than the whole image. By much smaller we mean an image with sides below 10 pixels, while the input image can have sides of hundreds of pixels. The shape of this structuring element can be different and reveals what kind of shapes are important in the following morphological operation. In our method we use a structuring element with a spherical shape.

The binary erosion of $b(i, j)$ by structuring element $h(i, j)$ is denoted as $(b \ominus h)(i, j)$ and the dilation is denoted as $(b \oplus h)(i, j)$. The erosion removes bright noisy spots in the image (called bumps), while dilation removes dark noisy spots (called pits). Mathematical opening and closing are combinations of mathematical erosion and dilation. Mathematical opening consists of erosion with a structuring element $h(i, j)$ followed by dilation with the mirrored structuring element $h(-i, j)$, while mathematical closing is dilation followed by erosion. Opening removes bumps and closing removes pits.

Mask refinement

Due to morphological operations, brain mask may have rough surface after removing the non-brain tissue. The refinement of the brain mask is achieved with an active contour [Chan and Vese, 2001] where its initial condition is the previously obtained binary brain mask. We run the active contour on T₂-W images (max 10 iterations) to achieve smoother brain shape.

We use T₂-W images because the brain tissue is more visible (has better contrast in comparison to the surrounding non-brain tissue) than on T₁-W images.

6.2.2.3 Brain extraction results

In this Section, we present both qualitative and quantitative experimental results of the proposed brain extraction algorithm on real neonatal brain MRI.

To validate our method quantitatively, manually segmented images (approved by the expert physician) are used as a “ground truth”, because the gold standard for the analysis of newborn brain MRI does not exist. For manual delineation we used the ITK-SNAP [Yushkevich et al., 2006, ITK-SNAP, 2009] editing tool which displays 3D data as a three synchronized 2D orthogonal views (sagittal, coronal and axial) onto which the operator draws the contour of the target structure, see Fig. 6.6. The output data therefore consists of a series of 2D contours from which a continuous 3D surface has to be extracted. This is a non-trivial post-processing task and is prone to errors. For instance, due to inter-slice inconsistencies in segmentation, bumps in the reconstructed 3D surface are inevitable.

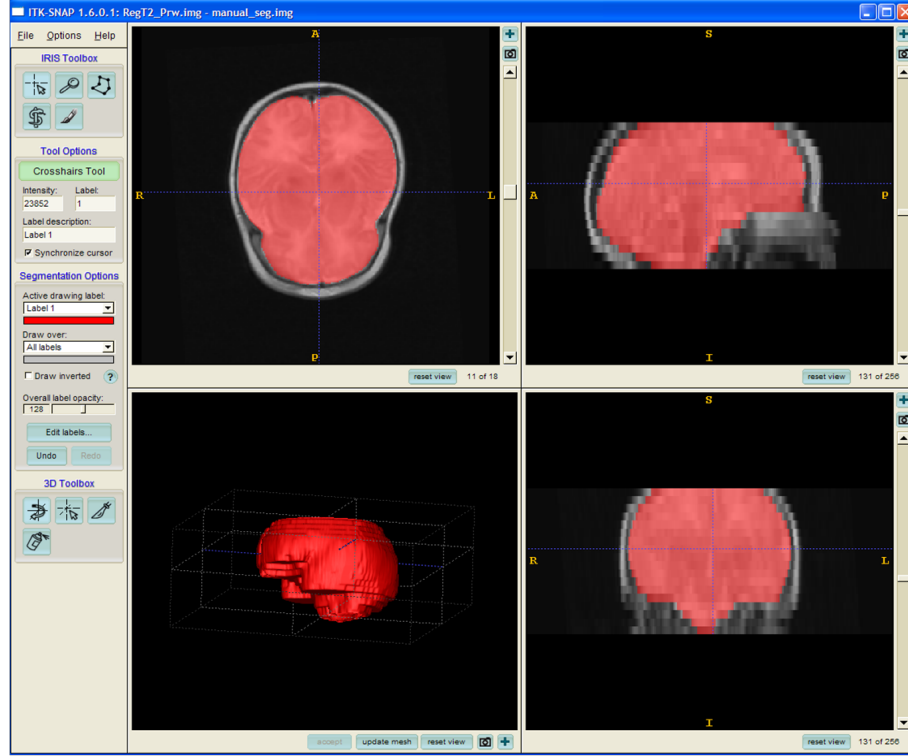


Figure 6.6: The screen shot of the ITK-SNAP editing tool that was used for the manual delineation of the neonatal brain [ITK-SNAP, 2009].

Since a manual delineation is labour-intensive and time-consuming, we have performed only a limited validation of our results. The similarity index used for the comparison and quantitative evaluation is the Dice coefficient ρ_i [Dice, 1945], defined in Eq. (4.14), where i indicates the number of neonates. The average similarity measure for each of the 10 neonates and for the whole brain volume, including all MRI slices that contain the brain tissue, is $\rho_i \geq 0.90$.

The qualitative segmentation results are presented in Fig. 6.7. The first and the second columns show the brain delineation results on T_1 -W and T_2 -W MRI respectively, while the manual segmentation obtained with ITK-SNAP tool is showed in the third column. In the same Fig. 6.7 we show in different figure rows the performance of the method on different brain slices from the top, middle and bottom parts of the brain. We can see that the method is efficient in eliminating non-brain structures and nicely preserves the shape of the brain tissue comparing to the “ground truth” manual segmentation.

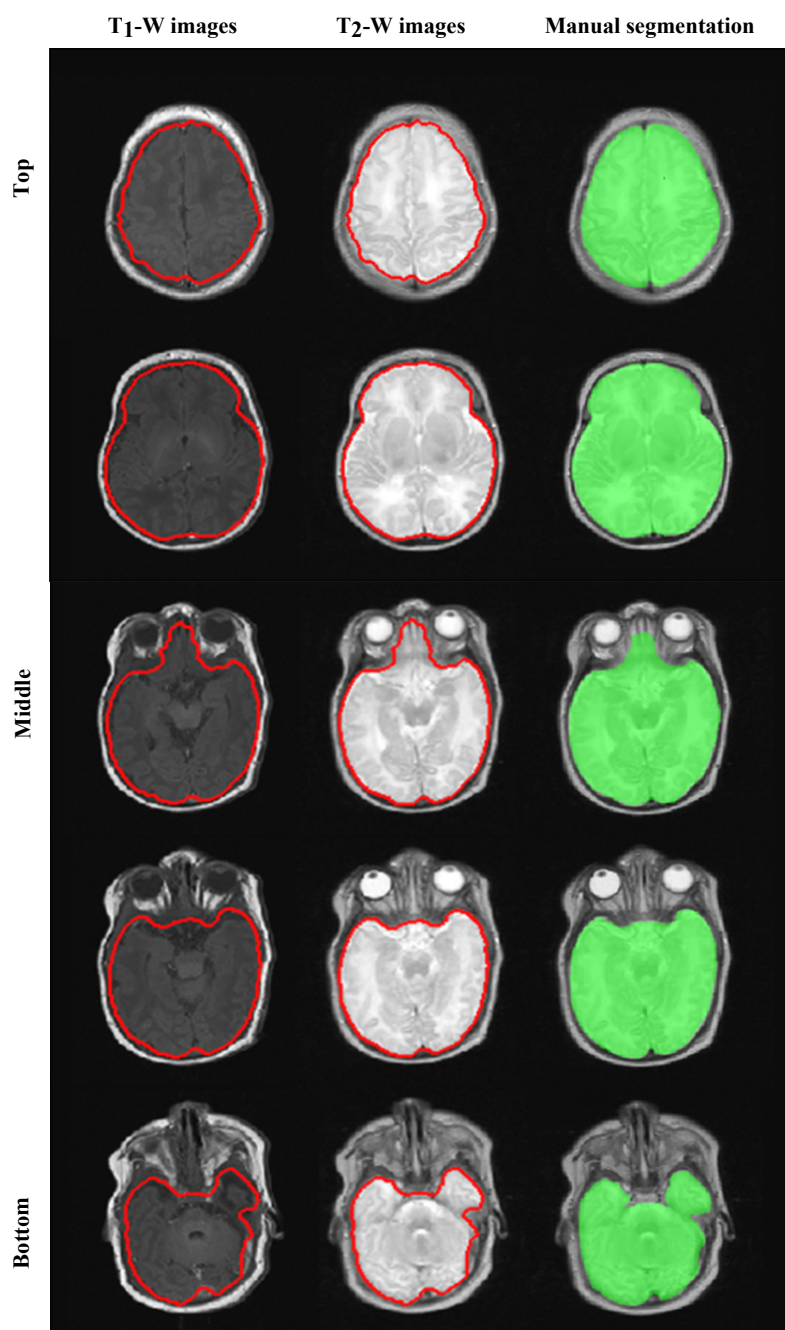


Figure 6.7: Comparison of the segmentation result of the proposed algorithm (delineated with the red contour) with the manually segmented mask (green).

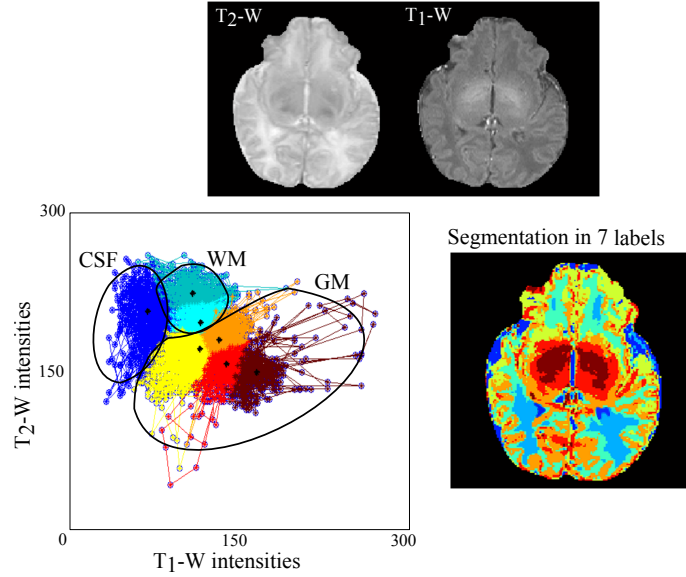


Figure 6.8: Illustration of the multimodal FCM segmentation of the neonatal brain using T_1 -W and T_2 -W MRI. Since there is a great intensity overlap between different tissues we segmented MRI into more than 3 clusters to differentiate between CSF, WM and GM. Afterwards, we merge several clusters into one to obtain desired segmentation. For the purpose of realistic head modeling we need two final clusters: CSF and the brain tissue consisting of both WM and GM.

6.2.3 Brain tissue segmentation

After brain extraction, MR images are prepared for the brain tissue segmentation. For the purpose of a realistic head modeling, we need only to separate CSF from the brain tissue, because these two structures have significantly different conductivities. White and gray matter are segmented as one structure due to the same conductivity in a realistic head model.

For the brain tissue segmentation, we use our multimodal extension of the FCM method for spatially constrained MRI segmentation described, which is described in more detail in Section 5.6. To preserve the homogeneity of different brain tissues, we combined information from both T_1 -W and T_2 -W MRI scans into the spatial neighborhood information. Since there is a great intensity overlap between different tissues in the neonatal brain, we segmented MRI into more than 3 clusters to differentiate between CSF, WM and GM. Afterwards, we merge several clusters into one to obtain desired segmentation into CSF and the brain tissue consisting of both WM and GM. The number of clusters is determined experimentally by visual evaluation for each neonate. In most of the cases, segmentation in 7 clusters successfully separated CSF from the brain tissue, where the clusters are grouped into two final clusters. One example of the multimodal brain MRI segmentation on neonatal MR brain image with the gestational age of 39 weeks is shown in Fig. 6.8.

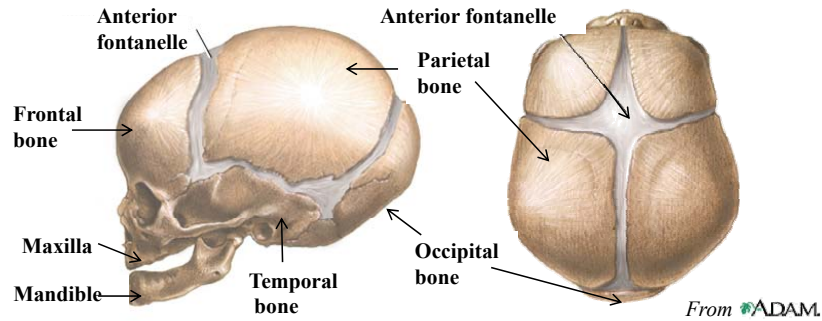


Figure 6.9: Anatomy of the neonatal skull from the side view (left) and top view (right).

6.2.4 Scalp and skull segmentation

Segmentation of the neonatal scalp is obtained using combination of the multimodal FCM clustering (described in Section 5.6) and active contours [Chan and Vese, 2001]. Here, we use the MRI scans where the brain tissue is removed as described in Section 6.2.2. The scalp can be recognized as a bright region on T_1 -W MRI. To segment the scalp from the rest of the head structures, first we use multimodal FCM clustering with two labels, where the first label corresponds to the bright region of the scalp and the second label to the rest of the head. Consequently, when the scalp mask is obtained, the outer surface of the scalp is refined using active contours in the same way as it is done for the refinement of the brain surface.

The most challenging head structure to segment was the neonatal skull because it is not easily visualized on MRI scans, contains structural inhomogeneities and partial volume voxels. For the skull reconstruction, we used the remaining voxels between the brain and the scalp, which resulted in a skull layer that completely surrounds the brain. The anterior fontanelle was modeled as a part of the skull, where the skull layer is eroded at the top of the head, using mathematical morphology and manual landmarks, to reach the maximum possible thickness of one voxel size. The fontanelle was approximately 2-3 cm wide and 3-4 cm long. The anatomy of the neonatal skull and location and shape of the fontanelle are illustrated in Fig. 6.9.

6.3 Realistic head modeling

Finally, all segmented structures are used to generate a cubic grid with a cube side of 0.7 mm. The segmented skull, based on individual MRI, was 1.4-2.1 mm thick (two to three voxels), but sometimes also reaching 2.8 mm in the occipital lobe. The fontanelle thickness was set to 0.7 mm. These values fitted well in the realistic skull thickness range of 1.1-2.9 mm, which was determined by an expert pediatric radiologist, based on manual skull thickness measurements using all patients in this study. An overview of the steps necessary for a realistic head modeling is shown in Fig. 6.10

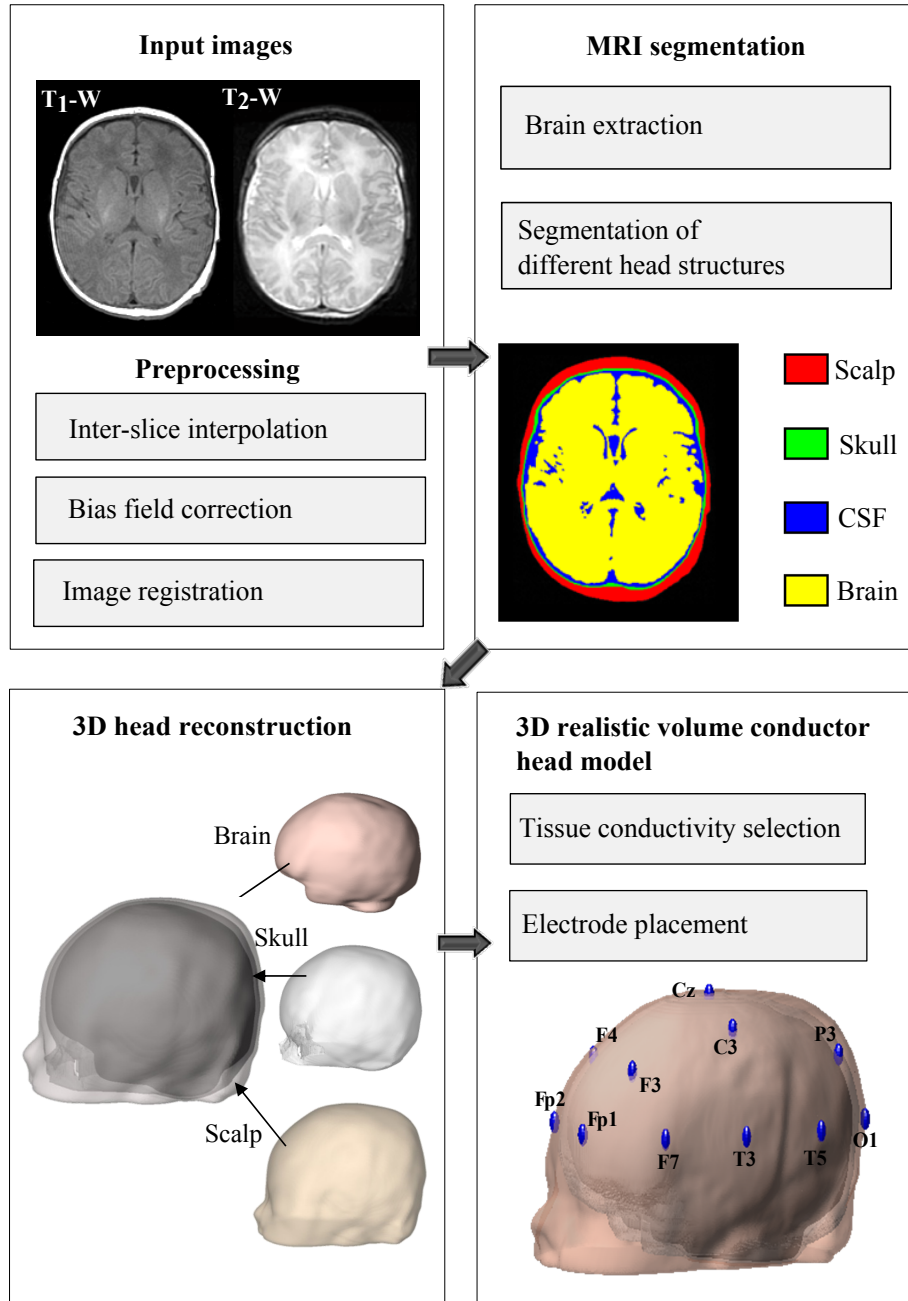


Figure 6.10: An outline of a realistic head modeling method. We use both T₁-W and T₂-W MRI sequences as an input. Firstly we do image preprocessing including bias field correction and image registration. Then, we do brain extraction and MRI segmentation into four compartments: brain tissue, cerebrospinal fluid (CSF), scalp and skull. Finally, 3D head reconstruction is followed with the tissue conductivity selection and electrode placement.

6.4 Conclusion

The aim of this chapter was to present a framework for a realistic head modeling in newborn infants without using atlases and probability maps of the brain. Our method relies on two multimodal MRI information, T_1 -W and T_2 -W images, and has been tested on real neonatal brain MRI. This integrated method combines active contours, FCM clustering and mathematical morphology and is able to segment four head structures in neonates: scalp, skull, cerebrospinal fluid (CSF) and brain tissue.

As a part of a realistic head modeling, we have proposed a new neonatal brain extraction method. This method has three sequential steps: background removal, generation of the initial brain mask and a final brain mask refinement. In the first step, the head tissue is separated from the background using simple thresholding and histogram analysis. The second step includes an anisotropic diffusion filter and an automated threshold to produce an initial brain mask. The anisotropic diffusion filter is used to remove noise artifacts and generate smoother image histogram, which is further used for an automated threshold calculation. The third step involves the refinement of the previously defined brain mask and generates the final brain boundary using active contours. Our brain extraction method is designed for low-resolution MRI data and is robust to partial volume voxels. Experimental results demonstrated good correlation with a “ground truth” manual delineation, with a similarity index above 90%, and yield a good segmentation performance even in noisy and poor quality MRI. Also, our segmentation more closely approximates the “true” brain volume by compensating the missing slices.

Future work may include further refinement of the algorithm and testing on a variety of gestational ages.

7

Neonatal EEG source imaging

*A fact is a simple statement that everyone believes.
It is innocent unless found guilty.
A hypothesis is a novel suggestion that no one wants to believe.
It is guilty, until found effective.*
– Edward Teller

Even though it is known that neonatal seizures are associated with acute brain lesions, the relationship of EEG seizures to acute perinatal brain lesions visible on MRI has not been objectively studied. In the past EEG source localization was successfully used for this purpose in adults, but it has not been sufficiently explored in neonates. In this chapter we propose an integrated method for ictal EEG dipole source localization based on a realistic head model to investigate the utility of EEG source imaging in neonates with postasphyxial seizures. We describe our method and compare the dipole source localization results with acute perinatal lesions seen on brain MRI in 10 full-term infants with neonatal encephalopathy. Through experimental studies, we also explore the sensitivity of our method to the electrode positioning errors and to variations in neonatal skull geometry and conductivity. The localization results of 45 focal seizures from 10 neonates are compared with the visual analysis of EEG and MRI data, scored by expert physicians. In 9 of 10 neonates, dipole locations showed good relationship with MRI lesions and clinical data. Our experimental results also suggest that the variations in the used values for skull conductivity or thickness have little effect on the dipole localization, whereas inaccurate electrode positioning can reduce the accuracy of source estimates. The performance of our fused method indicates that ictal EEG source imaging is feasible in neonates and with further validation studies, this technique can become a useful diagnostic tool.

This work is done in cooperation with Erasmus MC-Sophia Hospital in Rotterdam, MEDISIP group from Ghent University and ESAT-STADIUS division from KU Leuven. Erasmus MC-Sophia Hospital provided us with the necessary MRI and EEG

data, clinical diagnosis of the patients and validations of the experimental results. The MEDISIP group provided us with the source localization method (initially developed for adults), which has been modified in this research for the purpose of neonatal EEG source imaging. Finally, the EEG data analysis and automatic EEG seizure detection is done by the ESAT-STADIUS division, whose results we used as an input for EEG source localization.

7.1 Introduction

7.1.1 Neonatal seizures and their diagnosis

Neonatal encephalopathy is a syndrome characterized by neurological dysfunction in central nervous system in newborns born at term or late preterm (≥ 36 weeks gestation). Seizures are a common manifestation of neurological dysfunction in neonates [Volpe, 2008] and are attributed to biochemical imbalances within the central nervous system (CNS), intracranial damages and infections. The newborn brain is very susceptible to seizures because term infants have well developed excitatory mechanisms and poorly developed inhibitory mechanisms [McBride et al., 2000]. This explains the greater incidents of seizures in the neonatal period than at any other time in life [Patrizi et al., 2003]. In the last decade, an increasing number of studies have shown that neonatal seizures cause lasting changes in the CNS [Koh et al., 1999, Ben-Ari and Holmes, 2006] and are powerful predictors of long-term cognitive and developmental impairment [Miller et al., 2002]. Also, subtle seizures are more common in full-term than in premature infants.

There are two major types of seizures:

1. Primary generalized seizure - this seizure type affects the entire cerebral cortex;
2. Partial (focal) seizure - the abnormal signals of brain cells begins in one region of the brain and remains in that region (Fig. 7.1).

Most seizures in the neonate are focal, although generalized seizures have been described in rare instances. Perinatal asphyxia and hypoxic-ischemic encephalopathy (HIE) are the most common causes of seizures in newborns. Seizures require early detection to enable prompt treatment with the aim to prevent further brain injury.

Confirmation by video EEG is considered the gold standard in the diagnosis of neonatal seizures, while MRI is mainly used to diagnose structural brain damage. The majority of seizures occurring in sick neonates are subtle or subclinical and can be detected only by continuous EEG (cEEG) monitoring [Murray et al., 2008]. Electrographic neonatal seizures are claimed to be independently associated with poor outcome [McBride et al., 2000]. It is also known that the majority of newborns with neonatal seizures have acute brain lesions visible on MRI [Cowan et al., 2003] and that certain MRI patterns of brain injury like thalamus and basal ganglia injury are

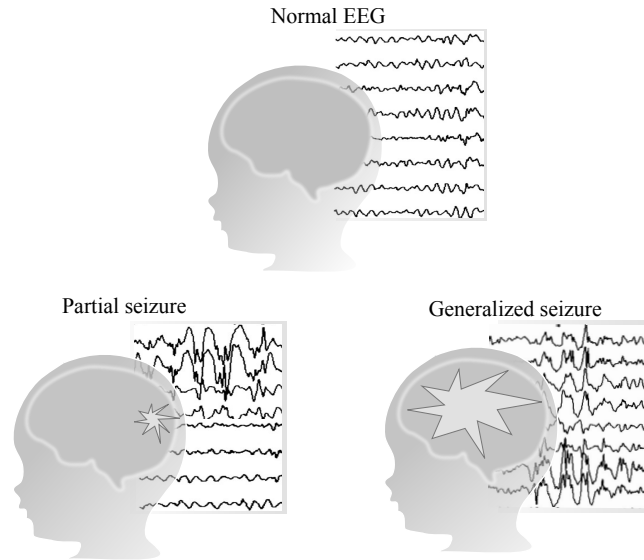


Figure 7.1: Illustration of the normal EEG activity on the top and partial and generalized seizure activities in the bottom. The brain on the top indicates the position of four brain lobes, highlighted with different colors.

strongly predictive of poor outcome in HIE [Barkovich et al., 1998]. Though a few studies have tried to relate brain lesions seen on MRI and specific EEG patterns [Scher et al., 1993, Biagioni et al., 2001, Leijser et al., 2007], an objective study of the relationship between the localization of neonatal seizures and associated MRI patterns of brain injury, using quantitative techniques, has not yet been done. The combination of these modalities by means of 3D source localization might provide further insight into the pathophysiology of neonatal seizure phenomena.

7.1.2 Challenges in neonatal EEG source imaging

EEG source localization estimates the active anatomical zones of the brain using EEG signals measured on the scalp. Two sub problems are involved: (1) the forward problem, which is to calculate the electrode potentials in a head model for a given source (usually a current dipole) and (2) the inverse problem, which is to find the dipole parameters that best represent the measured potentials at the scalp electrodes. The accuracy of source solutions highly depends on the selection of a volume-conductor head model, including the selection of head tissue conductivities. The earliest head models, used for adult source localization, model a head as a set of concentric spheres representing different conductive layers like scalp, skull and brain, to simplify the calculation of the forward and inverse problems. However, the human head is not a sphere and using a spherical instead of a realistic head model results in a dipole location error [Roth et al., 1993, Yvert et al., 1997, Cuffin, 1996, Silva et al., 1999]. This



Figure 7.2: Illustrations of the high density EEG cap for adults (left), promising solution of the EEG cap for neonates (middle, from [Tokarieva et al., 2012]) and the standard 10-20 manual electrode placement (right).

is particularly important when studied sources are located in the temporal or occipital lobes [Vatta et al., 2010].

To perform EEG source localization and compare the results directly with MRI lesions, accurate electrode placement and co-registration of EEG and MRI data are required. The most common methods for placing the electrodes on the scalp are using EEG head caps or using the standard 10-20 International System that requires manual electrode placement based on anatomical landmarks and relative distances (see Fig. 7.2). In adults, standard EEG head caps with fixed electrode positions are often used, but using the same caps for neonates is challenging because of differences in head size and greater variation in head geometry among neonates. Although there are some promising solutions for this problem available in the market, like specially designed EEG head caps for neonates [Vanhatalo et al., 2008], which might have a great potential for clinical use in the near future, the standard 10-20 system is still the most commonly used method in clinical practice in neonates. In source localization studies that employ a realistic head model, the exact electrode positions on the scalp need to be projected on the surface of the head model. This can be solved by using a 3D digitizer, which transforms coordinates of electrode locations to the MRI coordinates. However, this method is not available in most EEG laboratories. Therefore, a common solution is to place the electrodes on the scalp using the standard 10-20 positions and anatomical landmarks (like theinion and nasion points). As a consequence, such an approximation can introduce errors in the source modeling procedure [Khosla et al., 1999, Wang and Gotman, 2001].

Although EEG dipole source analysis is widely used in adults to localize epileptic sources [Michel et al., 2004], it is still not well explored in neonates because of the unknown conductivity values of the neonatal head. Additional challenges in neonatal source localization using a realistic head model are due to significant anatomical differences between newborn and adult heads. For instance, head tissue segmentation in newborns is more complex than in adults because of the lower MRI resolution (due to the short scanning period and small size of the newborn brain), lower contrast-to-noise

ratio (due to the higher water content and ongoing myelination of the white matter) and imaging artifacts (like ghosting effects, ringing and noise). The most difficult structure to segment is the skull, because it is hardly visible on MRI scans. Also, the skull is thinner in neonates and contains more inhomogeneities due to the fontanelles.

7.1.3 Goals and implementation overview

The aim of this pilot study was to explore the utility of neonatal ictal EEG source imaging and study its relationship to anatomical lesions, visible on MRI. For this purpose, we developed an integrated method for ictal EEG dipole source localization in neonates based on a realistic head model. We applied this method on 45 electrographic seizures recorded by cEEG from 10 neonates with presumed perinatal asphyxia and HIE, and we attempt to verify the identified ictal sources by relating them to acute perinatal MRI lesions. We segmented MRI scans from each patient to construct personalized 3D realistic head models with four compartments: scalp, skull, cerebrospinal fluid (CSF) and brain tissue. Using personalized MRI in this study is important to directly relate 3D localization of the active sources in the brain with MRI lesions and to minimize the dipole position errors due to different head shapes in neonates and distinctive anatomical features. For each neonate, we built five personalized 3D realistic head models to experimentally evaluate the sensitivity of the method to variations in skull conductivity and skull geometry (including skull thickness and the presence of the anterior fontanelle). Also, we experimentally evaluated the sensitivity of the method to electrode mislocalization. After constructing the head model, the spatial distribution of seizures over scalp electrodes are extracted with previously developed algorithms [Deburchgraeve et al., 2008, Deburchgraeve et al., 2009] and the optimal dipole position is estimated with EEG source localization method based on the finite difference method [Hallez et al., 2005]. We used the equivalent current dipole as a representative model for a group of synchronously active neurons. For all patients we analyzed only seizures with an unequivocal focal onset as determined by visual inspection of cEEG data.

7.2 Materials

7.2.1 Studied patients

Ten full-term newborns (6 females and 4 males) with gestational ages between 37-41 weeks, admitted to the neonatal intensive care unit (NICU, from Erasmus MC-Sophia, Rotterdam, The Netherlands), were included in this study. All 10 neonates displayed features of perinatal asphyxia and HIE. The selection of these patients was based on both the presence of recorded electrographic seizures on cEEG and acute perinatal brain lesions [Cowan et al., 2003] on MRI. They are part of an ongoing study of utility of long-term cEEG monitoring in neonates with presumed perinatal asphyxia and encephalopathy. Selection for cEEG was based on criteria for asphyxia and/or a

high degree of suspicion of seizures [Perumpillichira et al., 2011]. The medical ethics committee of Erasmus University Medical Center Rotterdam approved this study.

In all patients, we selected and studied focal electrographic seizure discharges with clear focal onsets. All patients had brain lesions visible on MRI. Half of the patients had predominantly unilateral, focal brain injury (like a stroke), while the other half had bilateral brain lesions (due to HIE). Details about the patients and their lesions detected on MRI are shown in Tables 7.1 and 7.4. All EEG and MRI data were recorded at the Sophia Children's Hospital (part of the Erasmus University Medical Center Rotterdam, the Netherlands). cEEG registrations were started mostly within the first 24 hours after birth and MRI scans were done within the first 10 days. This time difference in acquiring EEG and MRI data is important for a reliable diagnosis because EEG changes after asphyxia are best studied in the acute phase and the rate of recovery gives an indication of the severity and duration of the presumed hypoxic insult, while the pattern of brain injury is most easily seen in MRI few days after birth, when brain swelling is lower [Biagioni et al., 2001], and helps to better predict the outcome [Rutherford et al., 1998].

7.2.2 Data acquisition

cEEG registrations were made using a NervusTM monitor (Taugagreining hf, Reykjavik, Iceland). We used silver-silver chloride electrodes applied on the scalp according to the 10-20 International System (17 electrodes: $F_{p1,2}$, $F_{3,4}$, $C_{3,4}$, C_z , $P_{3,4}$, $F_{7,8}$, $T_{3,4}$, $T_{5,6}$, $O_{1,2}$) using conductive paste and fixed with collodion. The F_z electrode was used as the reference. The impedances were kept below 5 k Ω . The polygraphy included ECG, respiration, electro-oculogram (EOG), chin EMG and limb movements. The EEG sampling frequency was 256 Hz. The band-pass filter was between 0.3 - 70 Hz. EEGs were reviewed in their entirety by an experienced clinical neurophysiologist and the background activity was classified according to an in-house developed eight-grade classification system, emphasizing the severity and evolution of discontinuity and recovery of sleep-wake cycles [Perumpillichira et al., 2011].

We defined seizures as ictal-appearing electrographic discharges that showed a clear variation from background activity, displaying a repetitive pattern of sinusoidal oscillations or sharp waves, or a mixture of both, lasting 10 s, with evolution in amplitude and frequency over time [Bye and Flanagan, 1995, Perumpillichira et al., 2011] whether they had clinical correlates or not. Seizures were visually scored for their onset location, frequency, amplitude, duration, morphology and spread (see Table 7.1).

MRI scans of the brain were acquired in the first week post partum (PP) in all 10 patients with seizures. All scans included conventional T_1 -weighted (T_1 -W) and T_2 -weighted (T_2 -W) spin echo sequences, 3D spoiled gradient recalled (3D- T_1 -SPGR) sequence and diffusion weighted imaging (DWI) and were acquired on a 1.5 T MRI scanner (Siemens, Germany), $256 \times 256 \times 20$ to 25 voxel matrix with a resolution of $0.7 \text{ mm} \times 0.7 \text{ mm} \times 4 \text{ mm}$. All MRI scans were scored by a pediatric neuroradiologist according to well-described patterns of neonatal brain injury [Swarte et al., 2009].

No.	Sex	GA (wk)	Birth wt. (g)	Start EEG (h, PP)	Dur. (h)	EEG grade	Total sz. no.	Selected sz. no.	Sz. onset	Spread	MRI (d, PP)	Outcome (year)
1	M	40	2900	24	25	1	53	4	O-R	PTO-R	9	Normal (3)
2	F	41.4	3525	21.5	45	2	57	5	C, O-R	PT-R	4	L-inattention (2)
3	F	38	2910	64.5	41	2	18	5	C-bil	P-bil	4	Dev. delay (3)
4	M	37	2700	8.5	58.5	4	50	5	CP-bil	TO-bil	5	Normal (3)
5	F	41.3	3025	20.5	68	1	46	5	C-bil, F-L	T-bil	7	Epilepsy, lang delay (4)
6	F	39.1	2780	26	46.5	4	26	4	O-L	O-R	4	Died (day 7)
7	F	41.2	3540	37.5	47	2	32	5	C-bil	PT-bil	3	West syndrome, severe PMR (4)
8	F	41	3250	17.5	77	1	63	5	CP-R	O-R	2	L-hemiparesis (1)
9	M	41	3390	47	69	2	24	5	CT-bil, O-R	F-L	4	Normal (2)
10	M	37.6	3280	21.5	77.5	1	3	2	C-L	T-L	5	Normal (3)

Table 7.1: Clinical, EEG, and radiological characteristics and outcome of the 10 neonates. GA: gestational age in weeks; Birth wt.: weight in grams; Start EEG: time of start EEG monitoring; h: hours; PP: post partum; Dur.: duration of cEEG; EEG grade: background activity classified as 8 grades; Total sz. no.: number of seizures recorded during EEG monitoring; Selected sz. no.: number of focal seizures selected for this study; Sz. onset and spread: seizure location as visually scored; MRI: day (d) of MRI scan PP; Outcome: clinical outcome and the year of follow-up; PMR: psychomotor retardation; Dev. delay: mild motor and cognitive developmental delay; F: frontal; C: central; P: parietal; T: temporal; O: occipital; R: right; L: left; bil: bilateral.

7.3 Multimodal data fusion for EEG source imaging

Our method for neonatal EEG ictal dipole source localization consists of three key components: (1) 3D realistic head modeling; (2) automatic extraction of the spatial distribution of the selected seizure over electrodes; and (3) solving the forward and inverse problems for source localization (see Fig. 7.3).

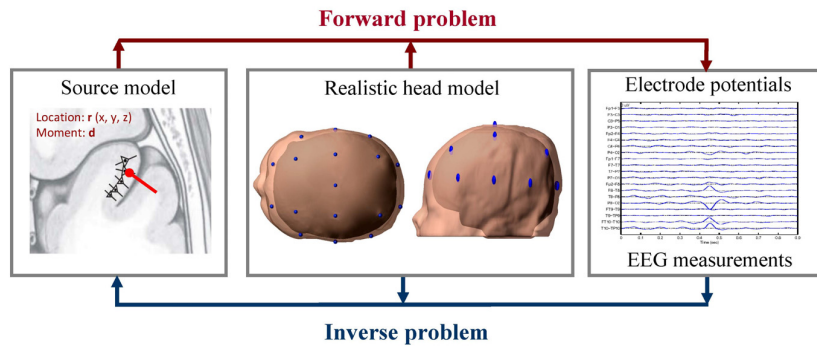


Figure 7.3: An outline of the EEG dipole source localization algorithm with three main components: realistic head model, EEG event detection (automatic seizure detection) and solving the forward and inverse problems using an equivalent current dipole for source localization. Forward problem calculates the electrode potentials given the source and the head model. Inverse problem quantitatively estimates the source parameters in the head model for a given set of EEG measurements.

7.3.1 Head modeling

Modeling a realistic head model as a volume conductor is not a trivial task because it requires three equally important steps: (1) segmentation of the various head structures (such as scalp, skull, and brain tissue), (2) selection of the correct tissue conductivities and (3) appropriate electrode placement.

7.3.1.1 Head MRI segmentation

Segmentation of the neonatal head for the purpose of a realistic head modeling is described in more detail in Chapter 6. Here we will only briefly summarise the most important segmentation steps.

In this study we used an atlas-free segmentation algorithm based on T_1 -W and T_2 -W MRI scans that is able to segment four head structures: scalp, skull, cerebrospinal fluid (CSF) and brain tissue. Before segmentation, we used cubic spline interpolation to interpolate low resolution MRI scans and obtain the inter-slice resolution of 0.7

mm. Then, we did bias field (intensity inhomogeneity) correction [Sled et al., 1998] and multimodal T_1 -W and T_2 -W MRI registration [Mattes et al., 2001, Thevenaz and Unser, 2000]. After preprocessing, to identify and segment different head structures (scalp, CSF and brain), we used a brain extraction algorithm [Despotovic et al., 2009a] and an algorithm that combines multimodal fuzzy c-means clustering [Despotovic et al., 2010c] and mathematical morphology.

The most challenging head structure to segment was the neonatal skull because it is not easily visualized on MRI scans, contains structural inhomogeneities and partial volume voxels. For the skull reconstruction, we used the voxels between the brain and the scalp, which resulted in a skull layer that completely surrounds the brain. The anterior fontanelle was modeled as a part of the skull, where the skull layer is eroded at the top of the head (using mathematical morphology) to reach the maximum possible thickness (one voxel size). The fontanelle was approximately 2-3 cm wide and 3-4 cm long. The anatomy of the neonatal skull and location and shape of the fontanelle are illustrated in Fig. 6.9.

Finally, all segmented structures are used to generate a cubic grid with a cube side of 0.7 mm. The segmented skull, based on individual MRI, was 1.4-2.1 mm thick (two to three voxels), but sometimes also reaching 2.8 mm in the occipital lobe. The fontanelle thickness was set to 0.7 mm. These values fitted well in the realistic skull thickness range of 1.1-2.9 mm, which was determined by an expert pediatric radiologist, based on manual skull thickness measurements using all patients in this study.

7.3.1.2 Head conductivity selection

When different compartments of the brain are obtained, the appropriate conductivities have to be attached to them. Since head conductivities, to our knowledge, have never been measured for neonates, in this work we estimated the conductivity values based on available studies for adults and small animals [Thurai et al., 1984, Geddes and Baker, 1967, Baumann et al., 1997, Gibson et al., 2000, Oostendorp et al., 2000, Akhtari et al., 2002, Gonçalves et al., 2003, Lai et al., 2005, Roche-Labarbe et al., 2008]. The neonatal scalp and CSF conductivities were assumed to be the same as in adults with the values 0.43 S/m and 1.79 S/m respectively [Geddes and Baker, 1967, Baumann et al., 1997], while the neonatal brain conductivity is set to 0.33 S/m [Gibson et al., 2000, Roche-Labarbe et al., 2008]. To estimate the conductivity of the neonatal skull, we used the previous study of Murray [Murray, 1981] where it was reported that the conductivity of the neonatal skull should be between 0.033 and 0.2 S/m (the adult skull conductivity is in the range from 0.0067-0.015 S/m [Oostendorp et al., 2000, Akhtari et al., 2002, Lai et al., 2005]). Since the conductivity of the brain and the scalp is considerably higher than the conductivity of the skull, we used 0.033 S/m as the “true” conductivity value of the neonatal skull, where the brain-to-skull conductivity ratio is 10. Furthermore, since wrong estimation of the skull conductivity can lead to source mislocalization, in the experimental study (Section 7.4.2) we estimated different source localizations based on different plausible values of human skull conductivities as given in Table 7.2.

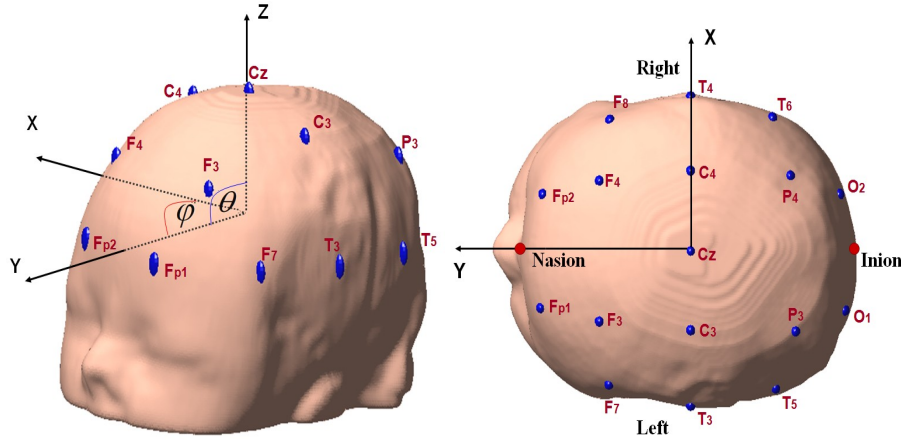


Figure 7.4: The two images (side view on the left and top view on the right) show the example of our reconstructed 3D head model with 17 electrodes. Nasion and inion points together with T_3 , T_4 electrodes form the equatorial plane and the electrode Cz represents the north pole. The x -axis points to the right side of the head (through T_4), the y -axis points to the front of the head (through the nasion point), and z -axis passes through Cz . The coordinates θ (the azimuth) and φ (the latitude) are used to describe the electrode positions.

Component	Adult(S/m)	Neonate(S/m)
Brain	0.2-0.48	0.33
CSF	1.79	1.79
Skull	0.0067-0.015	0.033-0.2
Scalp	0.43	0.43

Table 7.2: Head tissue conductivities

7.3.1.3 Electrode placement

Finally, 17 electrodes were placed on the scalp using the standard 10-20 system [Wang and Gotman, 2001]. An illustration of the standard 10-20 system electrode positions mapped on a head is shown in Fig. 2.24. The nasion and inion points were manually defined on each segmented head volume and were used as anatomical markers for electrode placement. For each patient, electrode positions were adapted regarding the shape of the head and the segmented scalp, which led to subject-dependent electrode placement. The coordinates of the electrodes were described using two parameters: the azimuth θ (angle with the vertical z -axis where $0^\circ \leq \theta < 180^\circ$) and the latitude φ (contra-clockwise angle with the x -axis in the horizontal x - y plane where $0^\circ \leq \varphi < 360^\circ$). An example of the 3D realistic head model with 17 electrodes projected on the scalp is illustrated in Fig. 7.4. All steps for the realistic head modeling are summarized in Fig. 6.10.

7.3.2 EEG event detection

Two to five focal seizures, that were considered to be representative of the expressed seizure patterns in each neonate, were visually selected by a clinical neurophysiologist. The selected seizures were then reviewed by two experienced clinical neurophysiologists and a consensus was reached about the identified seizure characteristics. From a signal processing point of view, the neonatal seizures could be classified in three morphological types with respect to their EEG characteristics: the spike train seizure type (Fig. 7.5(a)), the oscillatory seizure type (Fig. 7.5(b)) and the combination of the previous two types (mixed pattern, Fig. 7.5(c)). The major difference between the spike train type and the oscillatory type is that the spike train type consists of isolated spikes appearing on a background of lower voltage EEG, whereas the oscillatory type is a fluent, continuous seizure. The oscillatory type also has a continuous kind of repetitiveness and a lower frequency content, while the spike train type is a discontinuous, high-frequency seizure. In this study, all analyzed seizures were spike trains or mixed patterns with a large spiky component.

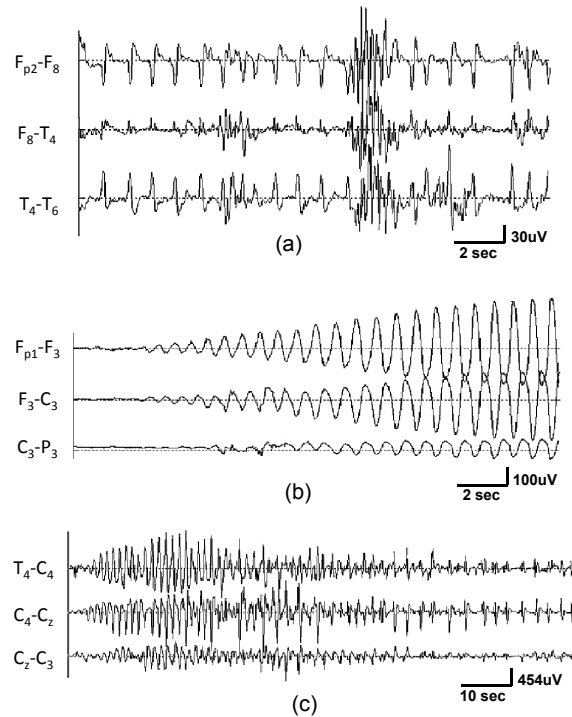


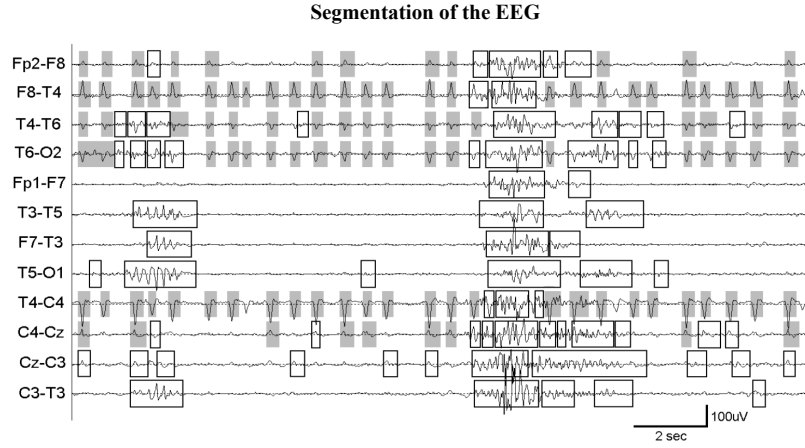
Figure 7.5: (a) Example of a spike train type seizure; (b) example of an oscillatory type seizure; (c) example of a seizure consisting of both morphologies, starting with oscillatory activity and ending with a spike train. From [Deburchgraeve et al., 2008].

7.3.2.1 Automatic seizure detection and localization

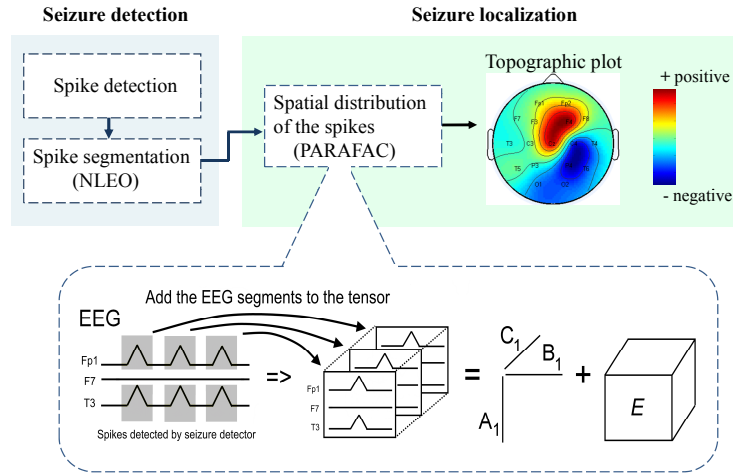
To automatically and objectively extract the spatial topography of the selected seizures, we applied a two-step method consisting of (1) automatic seizure detection and (2) automatic seizure localization.

The first step (automatic seizure detection) is the application of the recently developed automated spike train detector [Deburchgraeve et al., 2008, De Vos et al., 2011], which detects highly similar, high energetic spikes in a seizure. This spike train detection algorithm consists of three consecutive steps. In the first step, high energetic parts of the EEG are segmented using a non-linear energy operator (NLEO) [Kaiser, 1990]. This operator is proportional to the square of both the instantaneous frequency and amplitude. Because of these properties, the NLEO amplifies the high-frequency spikes of the spike train relative to the background EEG, facilitating the segmentation. The second step analyzes the spikiness of the detected high energetic segments. This spikiness defines that the spikes need to be 'isolated' in the EEG by comparing the energy of the detected segment with its immediate background activity. The third step is the correlation analysis that grows a set of highly correlated segments to detect the occurrence of a repetitive pattern of segments. If more than 8 inter-correlated segments can be found in a 30s window (with average correlation > 0.8), a spike train type seizure is detected. The output of the first step is a set of highly correlated, high energetic spike-like segments corresponding to the spikes of the neonatal seizure (see Fig. 7.6(a)).

In the second step (automatic seizure localization), the detected spikes are aligned and grouped into a tensor, which is modeled with a trilinear structure using Parallel Factor Analysis (PARAFAC) [De Vos et al., 2007, Deburchgraeve et al., 2009]. Note that in this study, we consider stationary seizures, but for an extension of the method that takes into account the evolution of the seizure, we refer to [Deburchgraeve et al., 2010]. As a result, the spatial distribution vector of the spikes over the EEG channels is obtained and is used as an input for source localization (Fig. 7.6(b)). The advantage of this preprocessing step is that the signal to noise ratio of the input for source localization is increased compared to raw topographies of single spikes. We have also shown previously that the PARAFAC localization is more robust and less sensitive to added noise as compared to simple spike averaging [Deburchgraeve et al., 2009]. The automated detections and localizations of all the 45 seizures were subsequently checked by the clinical neurophysiologist to ensure that they corresponded to the visual interpretation.



(a)



(b)

Figure 7.6: (a) Example of spike train detection. All marked segments (gray shaded + marked by rectangle) are those detected by segmentation step. After the spikiness operator and correlation analysis only the shaded segments remain. As a result, only those segments with a high correlation with previous segments (shaded) are kept and are detected as being part of a spike train type seizure. (b) Algorithm outline for automatic seizure detection and localization. Firstly, we detect and segment all spikes by the seizure detector. Then, using a PARAFAC decomposition we calculate the spatial distribution of the spikes over the EEG channels, which can be plotted as a topographic plot. Positive and negative brain regions are indicated with red and blue color respectively. Parts of the figure from [Perumpillichira, 2010] and [Deburchgraeve et al., 2009].

7.3.3 EEG dipole source localization

Using a topographic plot as a graphical representation of the spatial distribution of the spikes over the EEG electrodes is suboptimal to relate EEG spatial information with 3D brain anatomy. However, the combination of EEG and MRI data for 3D source localization can provide a representation of electrical generators inside the 3D anatomical space of the brain and enable exploring their relationship with underlying lesions. To achieve this goal, three input elements are required: the electrical fields modeled with an equivalent current dipole, a realistic head model (Section 7.3.1) and the spatial distribution of the seizure over the EEG electrodes (Section 7.3.2). Since all events in this study were assumed to be focal activities, we used a single rotating current dipole for the dipole fit.

7.3.3.1 The current dipole

A neuron cell is modeled as an element that withdraws current I from the extracellular space (a so-called current sink) and injects a current with the same intensity (current source). The current flow causes both electric and potential fields inside the human head, which extends to the scalp. A large group of electrically active neuron cells, located in a small piece of cortex, can be represented as one equivalent current dipole on macroscopic level [He et al., 2002, de Munck et al., 1988]. It is very difficult to estimate the extent of the active area of the cortex because the potential distribution on the scalp is almost identical to that of an equivalent dipole [Hara et al., 1999].

The current dipole is characterized with two parameters: the dipole position \mathbf{r}_{dip} and the dipole moment \mathbf{d} (see illustration in Fig. 7.7(a).

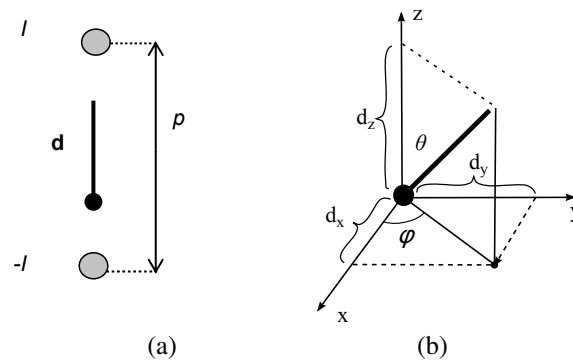


Figure 7.7: (a) Illustration of the current dipole for a given current source and current sink configuration. (b) The dipole as a vector with 6 parameters: 3 for the dipole location (d_x, d_y, d_z) and 3 for the vector components of the dipole ($\mathbf{e}_x, \mathbf{e}_y, \mathbf{e}_z$). These vector components can also be transformed into spherical components: an azimuth θ , elevation φ and magnitude d of the dipole. From [Vanrumste, 2001].

The dipole position parameter \mathbf{r}_{dip} is typically chosen half way between the source and sink. The dipole moment \mathbf{d} is defined by a unit vector \mathbf{e}_d (which is directed from the current sink to the current source) and a magnitude given by $d = \|\mathbf{d}\| = Ip$ where p is the distance between the source and the sink and d_x, d_y, d_z are the dipole components along the three Cartesian axes (Fig 7.7b).

7.3.3.2 Solving the forward and inverse problem

The dipole source localization consists of solving forward and inverse problems. The forward problem starts from a given current source and then calculates the resulting potentials in the volume conductor. These potentials can be obtained by solving the following Poisson's differential equation, which gives a relationship between the potentials at any position in a volume conductor V and the applied current sources:

$$\nabla \cdot \mathbf{J} = \nabla \cdot (\sigma(x, y, z)V(x, y, z)) = \underbrace{I\delta(\mathbf{r} - \mathbf{r}_2)}_{\text{current source density}} + \underbrace{(-I\delta(\mathbf{r} - \mathbf{r}_1))}_{\text{current sink density}}, \quad (7.1)$$

where $\nabla \cdot \mathbf{J}$ is the current density, $\sigma(x, y, z)$ is the location dependent conductivity tensor and $V(x, y, z)$ is the potential distribution inside the head model due to a dipole with current source and sink at positions $\mathbf{r}_2(x_2, y_2, z_2)$ and $\mathbf{r}_1(x_1, y_1, z_1)$ respectively and a scalp measurement point $\mathbf{r}(x, y, z)$. The current density can be also written as the sum of the current source density and the current sink density. The negative sign in front of the current sink density indicates that current is removed from the extracellular volume and the delta function indicates that current is removed at one point in space.

Poisson's equation 7.1 can be solved using an analytical expression for spherical head models, while numerical solutions are needed for realistic inhomogeneous head models. In this study we used a finite difference method (FDM) [Hallez et al., 2005, Hallez, 2008] for numerical solution, where a cubic computational grid is defined to the vertices at the edges of the labeled voxels in the realistic head model (Fig. 7.8).

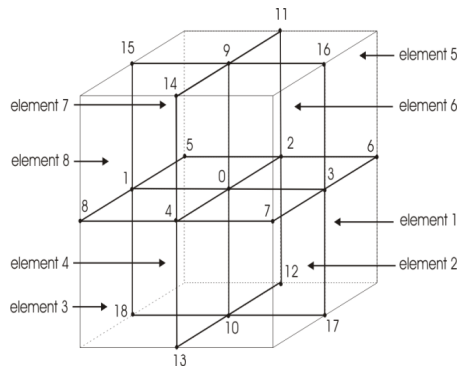


Figure 7.8: The 3D cubic grid with 18 potential points. From [Hallez, 2008].

Differentiating equation (7.1) in anisotropic media leads to the following finite difference formulation at each vertex $V(\mathbf{r}_0)$:

$$I = \sum_{i=1}^{18} A_i V(\mathbf{r}_i) - \left(\sum_{i=1}^{18} A_i \right) V(\mathbf{r}_0), \quad (7.2)$$

where $V(\mathbf{r}_0)$ is the potential at the central discrete point, $V(\mathbf{r}_i)$, $i = a, \dots, h$ is the potential at the i -th neighboring point and A_i is a coefficient depending on the conductivity tensors of the elements (cubes) shown in Fig. 7.8. Note that the cubes indicate the conductivity tensors and the geometry of the head model, but the potential values are computed at the nodes between the voxels. I denotes the current depending on the position of the center node. If the center node is at a monopole of the current source or sink, then $I = 1$ or $I = -1$, respectively, else $I = 0$. To each node, we can assign an equation according to (7.2). This results in a system of equations with N unknowns, with N equal to the number of nodes in the head model. To solve the linear system of equations, we used successive over-relaxation (SOR). Furthermore, reciprocity was used to speed up the forward calculation in the inverse problem [Vanrumste et al., 2001].

Solving the inverse problem consists of finding the parameters of the dipole source that best explain the set of measured potentials at the scalp electrodes consisted of the preprocessed EEG-spike trains. This is an iterative procedure where the source parameters are adjusted until a cost function (indicating the difference between the measured electrode potentials and those caused by the estimated source) is minimal. We find the optimal dipole position \mathbf{r}_{opt} and components \mathbf{d}_{opt} for the input potentials V_{in} at 17 scalp electrodes. This was done by minimizing the relative residual energy (RRE):

$$RRE = \frac{\|V_{in} - V_{model}(\mathbf{r}, \mathbf{d})\|_2^2}{\|V_{in}\|_2^2} + C(\mathbf{r}), \quad (7.3)$$

where V_{in} are the preprocessed spike trains and V_{model} are the electrode potentials obtained by solving the forward problem with a dipole source position \mathbf{r}_{dip} and components \mathbf{d} . $\|\cdot\|_2$ indicates the L_2 -norm. $C(\mathbf{r})$ is zero for dipole positions in the brain compartment and is set to a high value elsewhere. This additional term will constrain the solution of the inverse solver to the brain compartment. The non-gradient based Nelder-Mead simplex method [Nelder and Mead, 1965] is used to find the minimum of the RRE, which is a measure of the goodness of fit (GOF). A reasonable GOF was assumed if the RRE was ≤ 0.20 .

To examine the relationship between EEG seizures and MRI brain lesions, for each patient we performed source localization for each selected event (seizure) using personalized head model obtained from patient's MRI data. The source reconstruction solutions (equivalent dipoles) were projected onto the original T₁-W, T₂-W and DWI MRI volumes. To delineate the lesions on MRI, we used MRI sequences where the lesion was best visualized (like DWI or SPGR) and the distance between the dipole and the nearest lesion margin was measured using 3D Euclidean distance. The manual delineation of the lesions was checked and approved by a pediatric neuroradiologist.

7.4 Experimental setup

Although the main goal of this study was to explore the relationship of acute perinatal brain lesions visible on MRI to estimated EEG sources of neonatal seizures, we also needed to explore the influence of different parameters on these estimates. Since EEG source localization results may be affected by the skull reconstruction errors (including skull thickness and the presence of the fontanelle), the wrong estimation of the skull conductivity and the errors in electrode placement, we performed experimental studies to better understand the influence of these elements on ictal EEG source localization in neonates.

7.4.1 Conductivity and geometry of the skull

For the experimental study, for each patient we built five head models: “normal”, “maxcond”, “mincond”, “no fontanelle” and “thick”, to test the sensitivity of the source localization to variations in skull conductivity and geometry. The “normal” head model is the first head model obtained after the MRI segmentation and the initial head conductivity estimation, where the skull conductivity is set to 0.033 S/m and the segmented skull thickness is 1.4-2.1 mm, containing the anterior fontanelle (0.7 mm thick). This head model was used as the reference (true) head model in this study.

Head model	Skull cond. (S/m)	Skull thick. (mm)	Fontanelle yes/no	Font. thick. (mm)
1. “Normal”	0.033	1.4-2.1	Yes	0.7
2. “Maxcond”	0.2	1.4-2.1	Yes	0.7
3. “Mincond”	0.0067	1.4-2.1	Yes	0.7
4. “Thick”	0.033	2.1-2.8	Yes	0.7
5. “No fontanelle”	0.033	1.4-2.1	No	-

Table 7.3: Five head models used for the experimental study. Skull cond.: skull conductivity; Skull thick.: skull thickness; Font thick.:fontanelle thickness.

The second and the third head models, “maxcond” and “mincond”, were used to test the influence of differences in estimation of the skull conductivity. In comparison to the “normal” head model, in the “maxcond” and “mincond” head models we only changed the skull conductivity to 0.2 S/m and 0.0067 S/m respectively, which correspond to the maximal and minimal head conductance estimated in adults. For instance, the conductivity of most soft tissues is around 0.2 S/m (white matter in the adult brain) [Geddes and Baker, 1967], while the lowest value reported for the adult skull conductivity is 0.0067 S/m [Saha and Williams, 1992, Lai et al., 2005] (Table 7.2).

The last two head models, “no fontanelle” and “thick”, were used to test the influence of the anterior fontanelle and skull reconstruction errors on dipole localization. In comparison to the “normal” head model, the “no fontanelle” head model does not

contain the anterior fontanelle and the “thick” head model has voxel-size (0.7 mm) thicker skull with the values between 2.1-2.8 mm (in some cases reaching 3.5 mm in occipital regions). The “no fontanelle” head model was used to explore whether the fontanelles, as thin cartilage structures, create paths of low conductivity for the volume currents in the brain and tend to concentrate dipoles around the current leakage [Bénar and Gotman, 2002]. The “thick” head model was used to examine how the errors in the skull thickness, caused by partial volume effects and MRI segmentation, influence the source estimates. The summary of the five head models is given in Table 7.3. To calculate the dipole shifts (distances) caused by using different head models of the same patient, we used 3D Euclidean distance.

7.4.2 Influence of electrode mislocalization

Since incorrect assumptions of electrode positions on a realistic head model can also introduce source localization errors, we performed the experimental study to investigate how spatial electrode misplacements from the standard 10-20 system influence dipole localization results (using 17 electrodes). To estimate these errors we used five patients, each with five focal seizures and median GOF < 0.20 , and we displaced the electrodes from their initial 10-20 position. This is achieved by angular displacement of the parameters θ and φ (see 7.4), where it is assumed that these displacements were zero-mean Gaussian with the same standard deviation σ for all electrodes [Khosla et al., 1999] (see Fig. 7.9). We did four experiments with different standard deviations: 2° , 5° , 10° and 12° . For each standard deviation and for each patient we generated eight different electrode position sets by adding Gaussian displacements to the original electrode positions using the “normal” head model (see Table 7.3). This resulted in 200 inverse problem calculations for each experiment. To calculate the dipole shifts (distances) caused by electrode mislocalization we used 3D Euclidean distance. The results of this experimental study should help in understanding how important it is to know the exact electrode positions in solving the inverse problems and whether the electrode mislocalization errors are big enough to justify the additional cost of digitizing electrode positions.

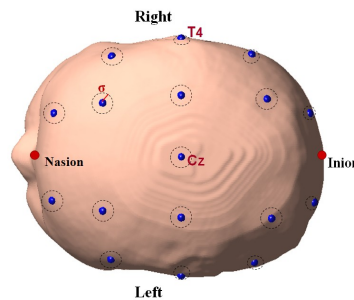


Figure 7.9: Standard 10-20 system electrode placement of the 17 electrodes projected onto the scalp and dashed circles represent the area of the electrode misplacement.

7.5 Results

7.5.1 Relationship of seizure foci to brain lesions detected by MRI

To compare 3D EEG source localization results with well-defined brain lesions seen on MRI, for all 10 patients we used the “normal” head models since they provided the best GOF. A description of brain lesions visible on MRI (clinical diagnosis) and dipole localization results is shown in Table 7.4 for each patient. To better understand the locations of MRI lesions and dipoles within the brain see Fig. 7.1, where the brain on the top illustrates the location of the four brain lobes.

No.	MRI lesions (clinical diagnosis)	Dipoles positions (localization results)
1	Bilateral (right > left) watershed (sub)cortical lesion in occipital lobe	Right occipital lobe
2	Watershed (sub)cortical lesion in right posterior frontal and parietal lobes	Right posterior frontal and parietal lobes
3	Bilateral (sub)cortical injury, mainly in frontal and occipital lobes	Bilateral posterior frontal and parietal lobes
4	Bilateral infarction in temporal and parietal lobes	Bilateral posterior frontal, temporal and parietal lobes
5	Ischemia and hemorrhage left basofrontal and frontal periventricular	4 dipoles (left frontal lobe) and 1 dipole (right posterior frontal)
6	Subdural and subarachnoid hematoma in the left occipital region	Left occipital lobe
7	Bilateral white matter hemorrhages in posterior frontal, parietal and occipital lobes	Bilateral posterior frontal and parietal lobes
8	Infarction, in right parietal, posterior frontal and frontal lobes	Right frontal, posterior frontal and parietal lobes
9	Bilateral (right > left) white matter and (sub)cortical injuries in frontal, occip. and temporal lobes and basal ganglia.	Bilateral (three right and 2 left) posterior frontal and temporal lobe
10	Bilateral white matter injury in frontal lobe	Left posterior frontal lobe

Table 7.4: Description of MRI lesions and localized dipoles’ positions. No.: number of patient. The second column of the table describes the lesions seen on MRI including their location (the side and the lobe of the brain). The third column describes the dipole localization results (the side and the lobe of the brain).

For all patients, the dipole source localization results together with delineated MRI lesions (marked with red color) with axial, coronal and sagittal views are shown in Fig. 7.10, 7.11, 7.12, 7.13 and 7.14. Different EEG events (seizures) are illustrated with different color and a corresponding topological plot, and for each seizure dipole, GOF and the distance from the closest lesion border are displayed.

Since we hypothesized that the location of the seizure would be on the lesion border [Hartings et al., 2003], we classified localized dipoles in three categories: dipoles very close or on the edge of the lesion (≤ 5 mm), dipoles in the vicinity of the lesion (≤ 15 mm) and dipoles far from the lesion (> 15 mm) [Ding et al., 2007]. For each patient, good relationship between the estimated dipoles and MRI lesions was accepted only if the following conditions were simultaneously satisfied: (1) lesions and dipoles are located at the same side and in the same lobe of the brain (co-localization is positive “+”), (2) the majority of dipoles are located ≤ 5 mm from the edge of the lesion, (3) the majority of the remaining dipoles are in the vicinity of the lesion (≤ 15 mm) and (4) median GOF is ≤ 0.20 . If the majority of dipoles are located far from the lesion > 15 mm, good relationship is rejected (see results for patient 5, Fig. 7.12). These relationship results are summarized in Table 7.5, which shows that in 9 of 10 patients we found good relationship between localized dipoles and visible MRI lesions. In all 9 cases, majority of dipoles were located at the edge or very close to the edge of the lesion and no single dipole is located far from the lesion, > 15 mm.

No.	Coloc.	GOF	No. of dipoles with dist. (mm)			Relationship
			≤ 5	≤ 15	> 15	
1	+	0.16	3	1	0	Good
2	+	0.12	4	1	0	Good
3	+	0.12	4	1	0	Good
4	+	0.10	3	2	0	Good
5	+	0.22	0	0	5	Not good
6	+	0.9	4	0	0	Good
7	+	0.9	5	0	0	Good
8	+	0.12	4	1	0	Good
9	+	0.14	5	0	0	Good
10	+	0.09	2	0	0	Good

Table 7.5: Relationship results between localized sources of EEG seizures and MRI lesions. No.: number of patient. The second column of the table shows the colocalization results between dipoles and lesions (described in Table 7.4), where “+” and “-” indicate positive and negative colocalization. Median goodness of fit is shown in the second column, while the qualitative results from the measured dipole-lesion distances are summarized in the third, fourth and fifth column. The dipoles are classified into three groups: very close or at the edge of the lesion (≤ 5 mm), in the vicinity of the lesion (≤ 15 mm) and far from the lesion > 15 mm. The last column shows the final relationship results (good/not good) between MRI lesions and dipole locations. Coloc.: colocalization, dist.: distance of the dipole from the edge of the nearest lesion.

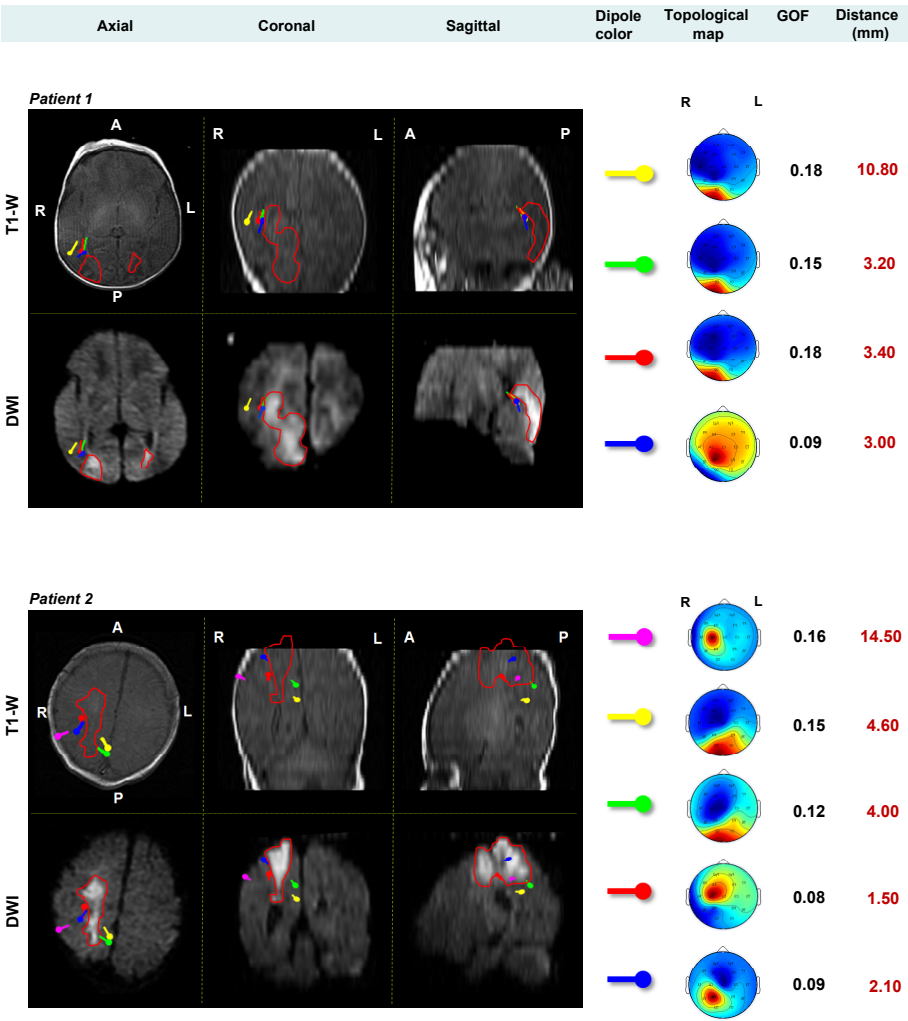


Figure 7.10: Dipole localizations results for Patient 1 (up) and Patient 2 (down). 3-D dipole fit results are plotted onto the patients' T₁-W and DWI MRI using projections on three planes: axial, coronal and sagittal. The color of the dipole represents different EEG events (seizures), which are also illustrated with a corresponding 2D topological plot (derived from PARAFAC analysis that represents the spatial distribution of the seizure discharges over the EEG channels). For each seizure dipole, the goodness of fit (GOF) and the distance from the closest lesion border are given next to the topological plot.

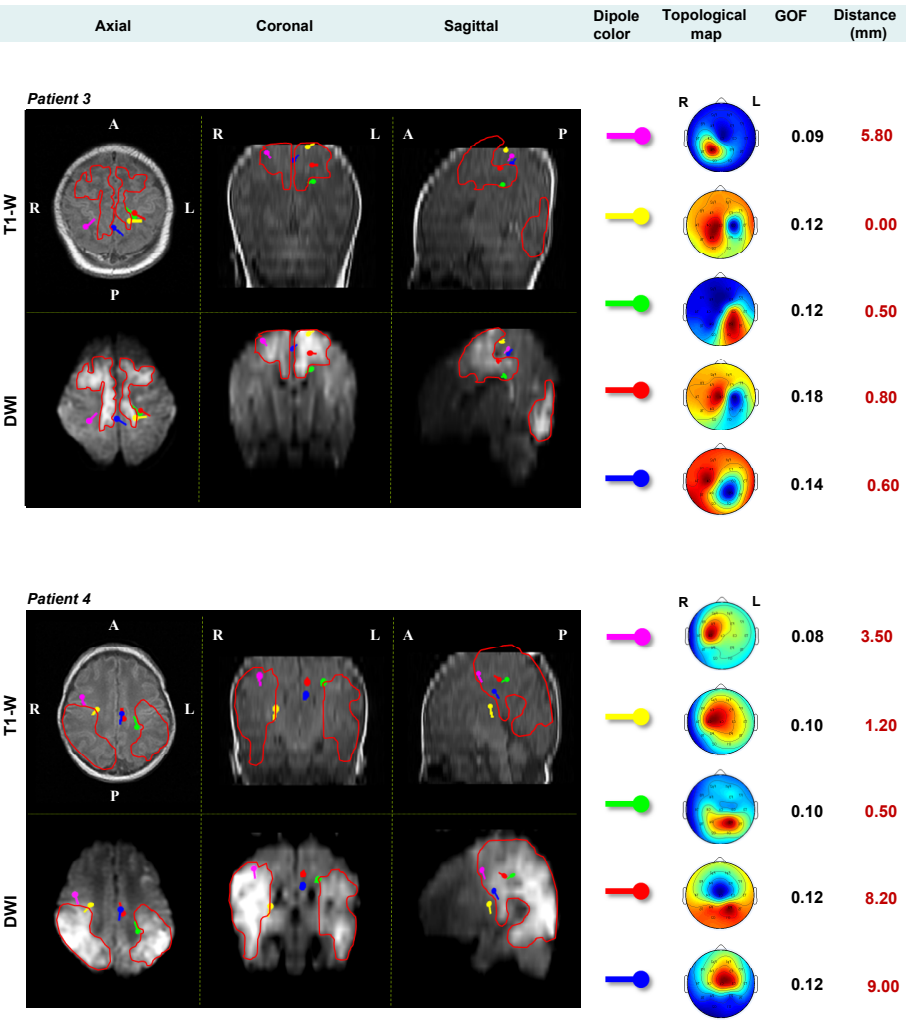


Figure 7.11: Dipole localizations results for Patient 3 (up) and Patient 4 (down). 3-D dipole fit results are plotted onto the patients' T₁-W and DWI MRI using projections on three planes: axial, coronal and sagittal. The color of the dipole represents different EEG events (seizures), which are also illustrated with a corresponding 2D topological plot (derived from PARAFAC analysis that represents the spatial distribution of the seizure discharges over the EEG channels). For each seizure dipole, the goodness of fit (GOF) and the distance from the closest lesion border are given next to the topological plot.

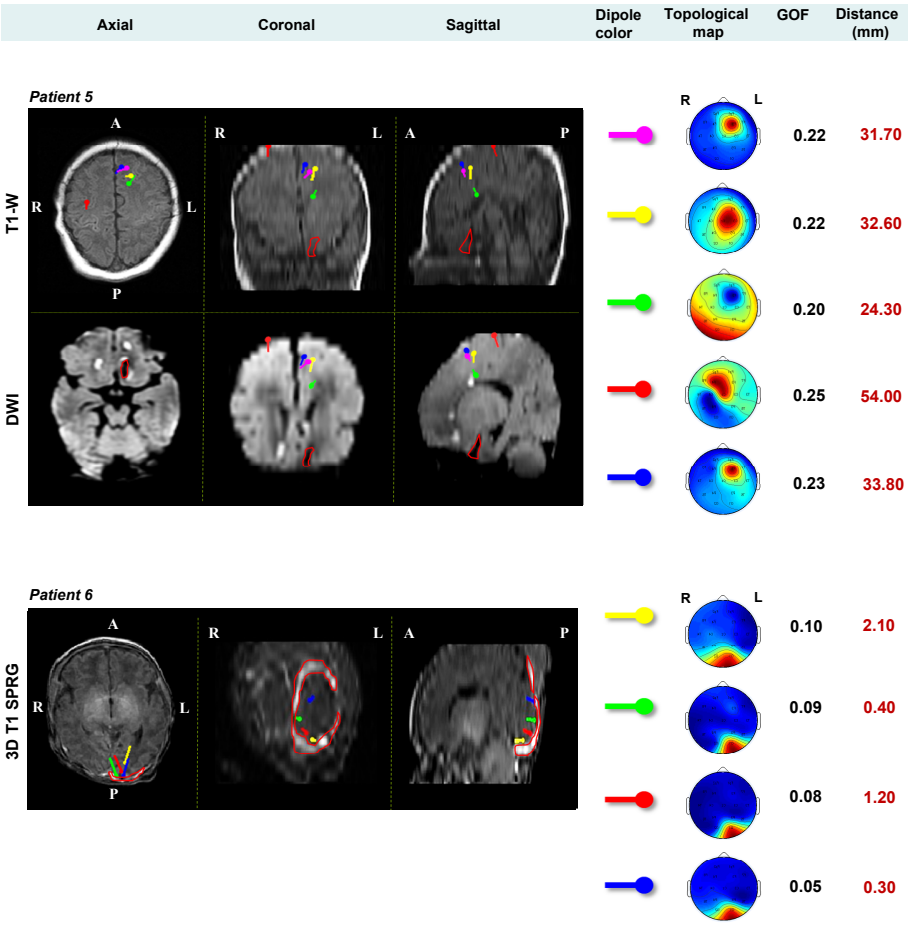


Figure 7.12: Dipole localizations results for Patient 5 (up) and Patient 6 (down). 3-D dipole fit results are plotted onto the patients’ T₁-W and DWI MRI using projections on three planes: axial, coronal and sagittal. The color of the dipole represents different EEG events (seizures), which are also illustrated with a corresponding 2D topological plot (derived from PARAFAC analysis that represents the spatial distribution of the seizure discharges over the EEG channels). For each seizure dipole, the goodness of fit (GOF) and the distance from the closest lesion border are given next to the topological plot.

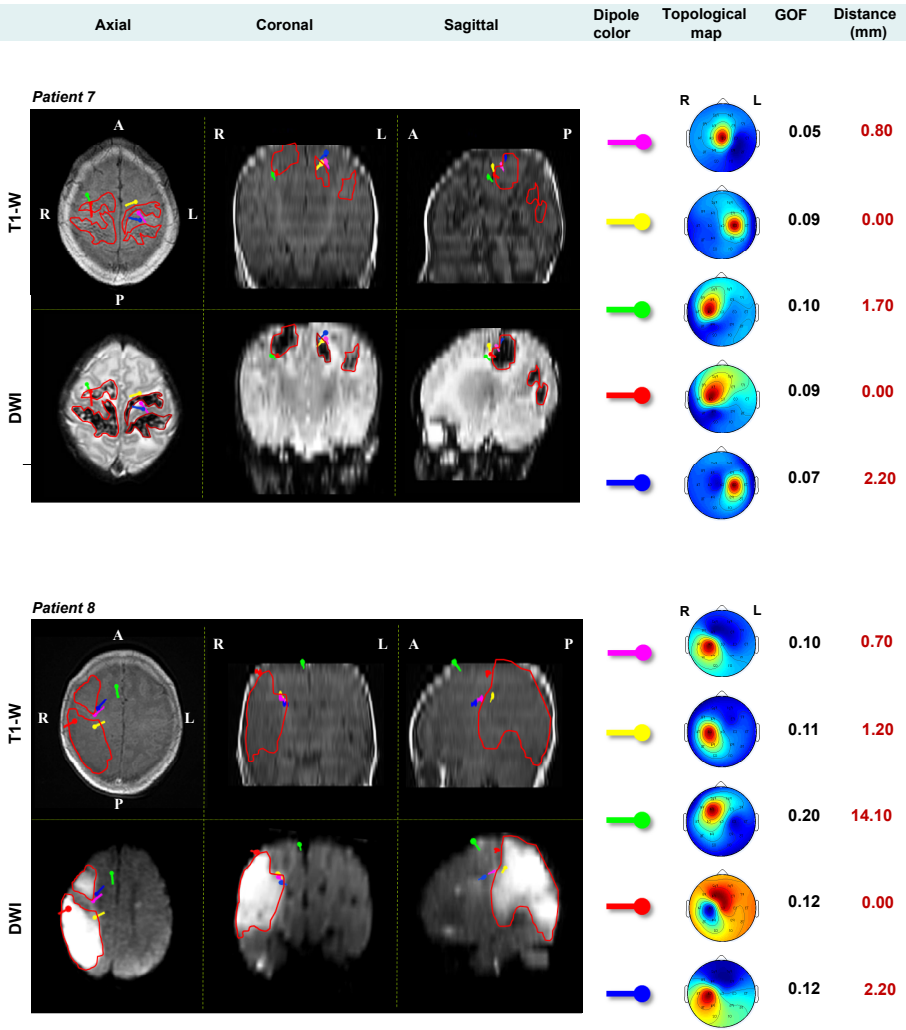


Figure 7.13: Dipole localizations results for Patient 7 (up) and Patient 8 (down). 3-D dipole fit results are plotted onto the patients’ T1-W and DWI MRI using projections on three planes: axial, coronal and sagittal. The color of the dipole represents different EEG events (seizures), which are also illustrated with a corresponding 2D topological plot (derived from PARAFAC analysis that represents the spatial distribution of the seizure discharges over the EEG channels). For each seizure dipole, the goodness of fit (GOF) and the distance from the closest lesion border are given next to the topological plot.

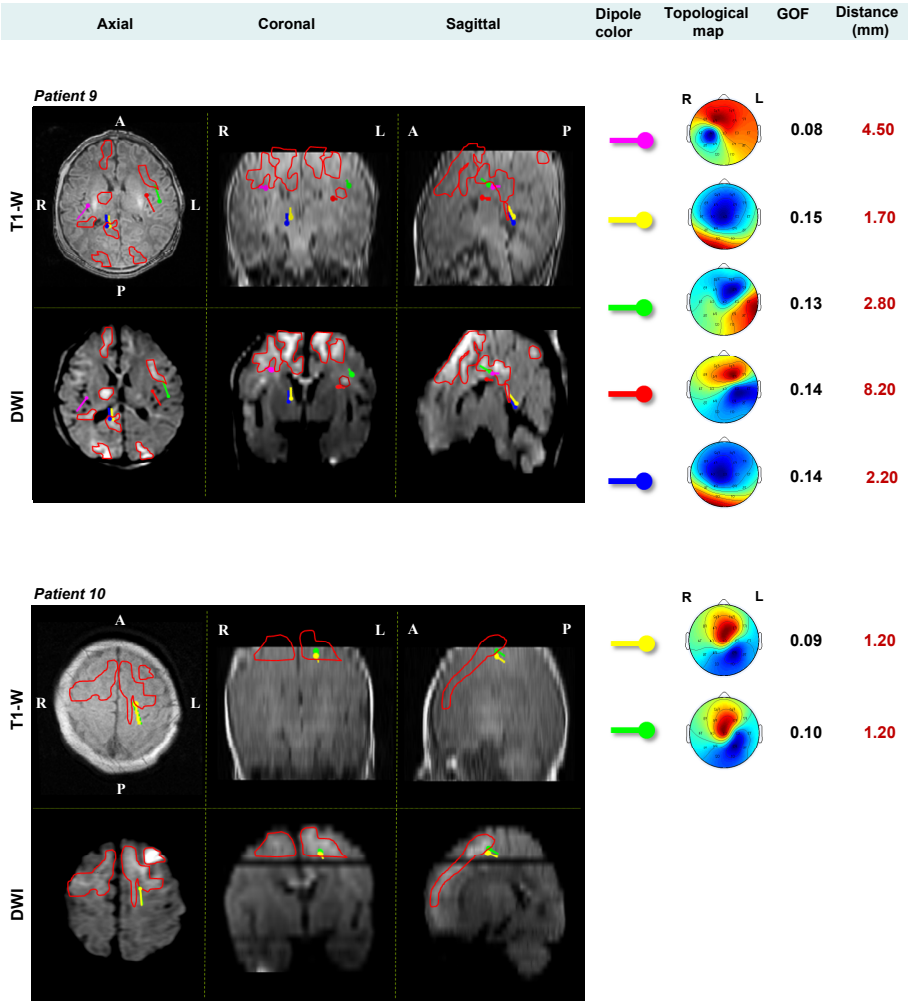


Figure 7.14: Dipole localizations results for Patient 9 (up) and Patient 10 (down). 3-D dipole fit results are plotted onto the patients’ T₁-W and DWI MRI using projections on three planes: axial, coronal and sagittal. The color of the dipole represents different EEG events (seizures), which are also illustrated with a corresponding 2D topological plot (derived from PARAFAC analysis that represents the spatial distribution of the seizure discharges over the EEG channels). For each seizure dipole, the goodness of fit (GOF) and the distance from the closest lesion border are given next to the topological plot.

Patients 7 and 8 are good examples where dipole locations relate very well with the lesions and they are shown in 7.13. These two patients had clinical features of severe HIE. Patient 7 had bilateral white matter hemorrhages (in posterior frontal, parietal and occipital lobes) and dipole locations were bilaterally located at the border of the lesions. Patient 8 had infarcts in the right parietal, posterior and anterior frontal lobes and all dipole locations corresponded to these regions. However, in patient 5 (7.12), who had a small left basofrontal hemorrhage, we found that the dipole locations were situated much higher in the left frontal region. The reason for this is that we have no EEG electrode near the putative seizure focus close to the lesion, located very deep in the brain. It is possible that the seizures in this patient spread vertically [Caviness et al., 1973] leading to secondary sources, resulting in the GOF values for the ictal dipoles of > 0.20 . This patient also illustrates the limitation of volume conductor models of EEG source localization, which do not take into account factors like anisotropies or the presence of various cortico-cortical networks [Plummer et al., 2008], in localizing certain types of seizure foci. Moreover, distinguishing the primary EEG source that initiates ictal activity from secondary sources, which are due to propagation, can often be difficult [Ding et al., 2007], as could have happened in this patient. It is also well-known that some frontal lobe seizures are difficult to localize using non-invasive methods [Quesney, 1991, Salanova et al., 1994]. Our overall results are in agreement with animal experiments, which show that majority of the seizures after perinatal hypoxic ischemic brain injury originate from the periainfarct regions [Hartings et al., 2003, Kadam et al., 2010].

Similar to what has been reported [Bye and Flanagan, 1995, Patrizi et al., 2003], we found that the majority of our seizure foci tend to cluster near the central parasagittal regions. The majority of the brain lesions in our patients also co-localized to these areas. Vulnerability of the perirolandic regions to brain injury may be due to regional metabolic differences [Chugani and Phelps, 1986]. The parasagittal watershed regions are also vulnerable in perinatal HIE [Volpe and Pasternak, 1977].

7.5.2 Dipole position errors due to volume conductor model errors

Sensitivity results due to variations in skull geometry and conductivity are shown in Table 7.6. For each patient, we show the mean dipole shift value of all patient-specific dipoles calculated between two head models indicated in each column. The variability in mean dipole shifts between patients (visible in Table 7.6) is most probably due to differences in the modeled spikes (source topography) and anatomical variability of the lesions. This variation is small and always below 5 mm. In the last row, we show the total mean dipole shift for all 10 patients with the standard error of the mean. The mean dipole shift of dipole locations between “normal” and “thick” head models was 1.42 mm, between “normal” and “no fontanelle” head models was 0.65 mm, between “normal” and “mincond” head models was 1.55 mm and between “normal” and “maxcond” was 2.34 mm. From these results we can say that the influence of the anterior fontanelle to dipole localization is almost negligible (0.7 mm), but increasing the skull thickness for 0.7 mm (from the range of 1.4-2.1 mm to the range of 2.1-2.8

mm) caused mean dipole shift of 1.5 mm. In a previous study [Roche-Labarbe et al., 2008] it was reported that the main source of uncertainty for dipole localization is the skull conductivity. They estimated that the mean dipole shift between head models with skull conductivities of 0.33 S/m and 0.0042 S/m is 11.6 mm. However, selecting 0.033 S/m as a “normal” neonatal skull conductivity, which is six times smaller than 0.2 S/m (“maxcond”) and five times bigger than 0.00067 (“mincond”), we got smaller mean dipole shifts of 2.5 mm and 1.6 mm respectively.

Patient	Dipole shift (mm)			
	Skull geometry		Skull conductivity	
	“normal”- “thick”	“normal”- “no fontanelle”	“normal”- “mincond”	“normal”- “maxcond”
1	3.00	0.40	2.55	2.71
2	1.25	0.56	1.82	4.32
3	3.60	0.81	1.35	1.05
4	0.39	1.61	1.03	1.65
5	1.62	0.62	1.80	1.85
6	1.28	0.10	2.67	2.81
7	0.71	1.23	0.96	4.91
8	0.96	0.92	1.57	1.50
9	0.65	0.40	0.90	1.85
10	0.77	0.86	0.81	0.79
	1.42±1.06	0.65±0.32	1.55±0.67	2.34± 1.36

Table 7.6: Sensitivity results to variations in skull geometry and conductivity. Dipole shift in a table represent mean distance (measured in mm) of all dipoles located in one patient between different head models. The last row in a table shows the mean dipole shift \pm standard deviation between different head models for all patients.

We also calculated the mean dipole shift caused by inaccurate electrode positioning. By increasing the angular mislocalization of the electrode positions by 2°, 5°, 10°, 12°, we obtained mean dipole position shift of 2.80 mm, 6.41 mm, 11.72 mm and 14.79 mm respectively. These shift results are slightly higher comparing with the adult study with a realistic head model (2° electrode mislocalization gives the mean dipole shift of ~ 2 mm, 1:1 ratio) [Wang and Gotman, 2001], where they used 29 electrodes for EEG recording. Since we used only 17 electrodes, we expect that increasing the number of electrodes can cause reduction in the localization error. However, for the purpose of this study we think that this error is acceptable.

7.6 Discussion

7.6.1 Comparisons with previous studies

To our knowledge, there has been only one previously published study about neonatal EEG source localization [Roche-Labarbe et al., 2008] where sensitivity of different parameters on source estimates was evaluated. From a clinical point of view and methodology, our study is different from theirs and is based on a larger number of patients. The main contribution of our study is to show the first clinical results with regard to the feasibility of localizing neonatal ictal EEG activity and its good relationship to acute perinatal brain lesions visible on MRI.

Our method is based on automatic extraction of the seizure topography and more sophisticated MRI segmentation for 3D volumetric modeling of the neonatal head. We localize the pathological seizures (ictal phenomena, that are associated with acute, serious brain injury), while Roche-Labarbe et al. localize transients in neonatal EEG. Our head models consist of 4 compartments: scalp, skull, CSF and brain tissue, while they used a 3-layer Boundary Element Method (BEM) (which uses surfaces tessellations) to model the scalp, skull and brain tissue. A difference of our approach is that together with CSF we model the ventricular system, giving the head model more realistic structure with an additional conductive layer. This is important because the electrode potentials are dependent on the total electrical field generated in the head caused by a current dipole. Also, CSF and the ventricles can be used to constrain the dipole location. Current dipoles cannot be placed in the ventricles or CSF and this can be added in the EEG source localization procedure. In adults, it has been shown in a previous study [Vanrumste et al., 2000] that not incorporating the ventricles in the head model causes a dipole location error of about 7 mm in the vicinity of the ventricles (deep gray matter) and about 3 mm in the brain cortex. However, since neonates have lower volume conduction than adults, we believe that this error could be smaller in babies.

Another difference is that Roche-Labarbe et al. used a patented cap for electrode placement and a magnetic digitizer for 3D digitization of the spatial positions of the electrodes, while we used the standard 10-20 International System to manually place the electrodes on the scalp in a relation to the anatomical markers. However, none of these methods are error-free. Electrode caps can move slightly in position [Atcherson et al., 2007] and may have fixed inter-electrode distances, but less accurate relationship to anatomical landmarks of the skull. In the case of applying individual electrodes, one relies on an experienced EEG technician who should have less margin of error. On the other hand, digitized electrode positions, which were not available for this study, describe the true electrode positions on the scalp more precisely than the standard 10-20 positions. In the study of Khosla et al. [Khosla et al., 1999], it was shown that on average the digitized electrode locations deviated from the standard 10-20 positions by about 4° in adults. This misallocation has not yet been measured in neonates, but it might be very similar if the fine adjustments based on the anatomical markers and

head shape are made during electrode positioning. For studying the relationship of seizures to brain lesion in this pilot study, this mismatch is tolerable. However, if higher precision source localization is desired (e.g. for surgical planning in epilepsy patients), the digitization of electrode positions is recommended.

Finally, this study is the first to evaluate the influence of electrode mislocalizations on source localization in neonates. Our experimental results indicated that the electrode mislocalization is the most critical component for the accurate source localization. Since we used a clinical setup of only 17 electrodes, we believe that using a higher number of electrodes would give more accurate source estimation. This had been already shown in adult studies [Vanrumste et al., 2000]. While highly accurate dipole localization is needed for presurgical evaluation of patients with refractory epilepsy, our primary aim in neonates is to study the relationship of seizures to brain lesions and eventually their pathophysiology. Hence we think that the obtained error is acceptable. The reality in most NICUs doing cEEG is that 8 to 9 scalp electrodes are used for this purpose. Thus the 17 electrodes that we use may be a reasonable compromise between the need to obtain high accuracy (more electrodes) and practical applicability in a NICU setting (less number of electrodes).

7.6.2 Estimation of the skull conductivity

As the skull conductivity has never been measured for human neonates, one of the challenges in this study was to estimate the neonatal skull conductivity using available studies for adults and animals. In adults, the conductivity of the skull was measured both in vitro and in vivo [Geddes and Baker, 1967, Oostendorp et al., 2000, Akhtari et al., 2002, Lai et al., 2005], but still there is little consensus on the absolute skull conductivity value or the brain-to-skull conductivity ratio. Also, the skull conductivity is electrically anisotropic and depends on the skull thickness, skull composition, test frequencies and temperature. The adult skull conductivity reported in the literature ranges from 0.0067-0.015 S/m. It has recently been suggested that the human brain-to-skull conductivity ratio is 15 [Oostendorp et al., 2000] and 25 [Lai et al., 2005] instead of the widely used value of 80 [Rush and Driscoll, 1986]. In the study of Akhtari et al. [Akhtari et al., 2002] the conductivity of the three-layer live human skull was measured (top compact bone, middle spongiform layer and lower compact bone). They reported that the skull conductivity is frequency dependent in the range from 10-90 Hz by as much as 10% in compact bone and 13% in spongiform (percent increase in conductivity). Also, they indicated that there may be a weak relationship between the thickness and conductivity in different skull layers.

In the recent study of Pant et al. [Pant et al., 2011] the first measured conductivity values for neonatal and preterm mammalian skull were reported. They used fresh neonatal piglet skull samples with the average thickness about 1.3 mm and found the average neonatal/preterm piglet skull conductivity in the range 0.025-0.035 S/m (average 0.030 S/m) at 1 kHz. They also found that the skull conductivity increased linearly with the skull thickness. Note that although the piglet brain is a well-accepted preclinical model for neurodevelopmental research in humans (due to its anatomic

and physiologic similarities to humans, like similar patterns in brain growth and development), the similarity between the piglet neonatal/preterm skull and the human neonatal skull is still controversial.

In this study we used three different values for the neonatal skull conductivity (0.2 S/m, 0.033 S/m and 0.0067 S/m) and tested their influence on source mislocalization. In these experiments, we used 0.033 S/m as the “normal”/“true” neonatal skull conductivity value. Taking into account the incomplete development of the neonatal bone, it is reasonable to assume that the neonatal skull has higher conductivity than the adult skull. Also, comparing with the adult studies, the brain-to-skull ratio of 10 seems reasonable. Our results also indicate that the mean dipole mislocalization using conductivities 0.2 S/m or 0.0067 S/m is less than 5 mm. Like in the most EEG source localization studies in adults, we assumed the skull conductivity to be isotropic. It is an open question how this assumption affects the accuracy of EEG dipole source localization in neonates and it should be handled in a separate study.

7.6.3 Strengths and limitations

Strengths of our study include the use of continuous multichannel EEG monitoring for more complete sampling of seizure data, automated seizure localization, as well as the use of a realistic head model. The expertise needed to interpret neonatal EEGs is not available around the clock in the NICU. Also, EEG monitoring is highly labor-intensive as it generates large amounts of data. For these reasons, automated analysis methods are needed in the context of cEEG monitoring in the NICU. We also attempted to place our ictal source localization in the clinical context by relating them to the acute brain lesions seen on MRI.

The limitations of our study are the small number of patients, as well as the deliberate selection of patients with discrete lesions visible on MRI and clear-cut focal seizures recorded on EEG. This may be justified as our aim was to explore the relationship of neonatal seizures to brain injury patterns visible on MRI. These type of studies are useful for hypothesis generation and cannot be generalized to all neonates with HIE and seizures. As compared to interictal spike localization studies, ictal source localization studies are more challenging. By the time the seizure is expressed in the scalp electrodes, a large volume of intracranial tissue is involved by the ictal discharge, and the model may be showing the spread and not the origin [Merlet and Gotman, 2001]. Wide-spread regional propagations of the seizures are expected to be less of a problem in the neonate as compared to older children and adults due to the immature cortico-cortical connections that have been shown by anatomic [Caveness et al., 1973] and metabolic [Kato et al., 1980] studies. We also took care in each patient to select seizure patterns that were reproducible.

7.7 Future directions

The near-term clinical application of dipole localization of neonatal seizures is still limited in the NICU and the studies like ours are needed to close our present gaps in the knowledge about pathophysiology of neonatal seizures. We feel that with further validation, this type of multimodal approaches could improve therapy (for example, by using more targeted neuroprotective therapies for particular type of seizures) as well as outcome predictions in the future. Large, multi-center cEEG studies are needed to study the pathophysiology of neonatal seizures, their relationship to acute brain lesions as well as the effect of their treatment with antiepileptic drugs. Studying large amounts of cEEG data is highly labor-intensive and will be simplified by the use of automated methods like the one we used.

Although evolution of EEG background activity in the first few days after perinatal asphyxia is known to be a robust predictor of clinical outcome [Murray et al., 2009, Watanabe et al., 1980], prediction of outcome in neonates with moderately severe EEG background abnormality is very difficult. In this selected group, multimodal evaluations, such as estimation of MRI lesion location and volume, electrographic seizure burden as well as ictal source localization may help to improve prognostication. A recent study showing that watershed brain injuries are related to impaired language ability [Steinman et al., 2009] in survivors of HIE, is a step in this direction.

Long-term follow-up is needed in our patients to look for neurocognitive deficits and epilepsy. This is further emphasized by the fact that patient nos. 5 and 7 in this study developed epileptic seizures on follow-up. A recent study using an animal model of neonatal hypoxic ischemic brain injury has shown that development of epilepsy in later life is strongly related to the presence of pathological brain lesions [Kadam et al., 2010]. Similar studies in neonates with HIE will help to refine our prognostication in patients with particular combinations of seizures and brain injury patterns on MRI.

7.8 Conclusion

This pilot study evaluated the utility of 3D localization of neonatal seizures using a realistic head model and relationship of seizure foci to brain lesions detected by MRI. Despite many difficulties, we have shown that EEG ictal source localization is feasible in newborns and can lead to important new insights into the properties of cerebral neural networks and 3D comparison with brain lesions.

The results have shown that the majority of calculated 3D sources were at the edge or ≤ 5 mm from the nearest MRI lesions. Also, using approximate head tissue conductivities (which were found in literature) with an accurate geometrical description of the head, yielded reasonable results for both cortical and deep EEG sources. Considering that the 3D sources were computed using only 17 electrodes and the standard 10-20 system of electrode placement, our results are very promising for further research on the relationship between EEG source localization and brain injury visible on MRI.

8

Conclusions

There is no real ending. It's just the place where you stop the story.
– Frank Herbert

The recent development of non-invasive and multimodal brain imaging techniques has opened new horizons in understanding and studying the brain structure and function in a way that has never been done before in living humans. Enormous progress in assessing brain injury has been made using MRI, while EEG has been considered as the gold standard in the diagnosis of neurological dysfunction. By combining both EEG and MRI in multimodal imaging of the brain, important aid in the diagnosis and management of neurological dysfunction of the brain and neonatal seizure phenomena has been achieved. This is just one of the reasons why multimodal brain imaging is one of the fastest growing multidisciplinary activity today.

In this thesis, we focused on developing new techniques for multimodal image analysis of the human brain, including brain MRI segmentation and EEG source localization. In doing so, we merged theory with practice and focused on two medical applications:

1. Automatic 3D MRI segmentation of the adult brain and 3D brain cortex segmentation in the presence of FCD lesions;
2. Multimodal EEG-MRI data analysis of the asphyxiated neonatal brain with perinatal brain injuries.

Throughout the thesis we tried to present numerous original interpretations, pictorial explanations and discussions broadening our viewpoints on this topic.

In Chapter 2, we presented the important background of the human brain anatomy where we explained the developmental phases of the brain from fetus till adulthood. Then, we also explained the basic physical principles of MR imaging, how MR images are formed, what they show, how they differ, how we can analyze them, what are the challenges of the brain MRI analysis and what are the differences between adult and neonatal MRI. Furthermore, we explained the basics of EEG brain data analysis that is necessary for understanding multimodal MRI-EEG brain imaging.

In Chapter 3, we explained the most important concepts of MRI segmentation and reviewed the most popular methods commonly used for brain tissue segmentation in MRI. We summarized the main ideas, similarities and differences between segmentation methods. Also, we discussed the validation problem in brain MRI segmentation.

Despite intensive research, brain MRI segmentation still remains a challenging problem with no unique and general solution and there is a continuous need for developing newer and better segmentation methods. Also, segmentation of noisy images is one of the most challenging problems in medical image analysis and any improvement of segmentation methods can highly influence the performance of many clinical applications. Thus, we presented our original contributions in this field in Chapters 4 and 5. In our original contributions, we paid a great attention to improve and develop new methods for accurate and noise-robust image segmentation. Our methods are adapted to the local image context by modeling spatial interactions between pixels/voxels using contextual constraints. In making our way through this research field, we were inspired by the concepts of MRF models. Our contribution here was modeling new/improved locally adaptive methods which employ such concepts. Our segmentation methods were then successfully used for brain MRI segmentation in both adults and neonates, as well as for a realistic head modeling in neonates. We tried to motivate the proposed algorithms in terms of better segmentation results.

In Chapter 4, we addressed the problem of 3D brain MRI segmentation, where we focused on the multilabel min-cut graph cut segmentation and proposed its modification for more accurate and automatic 3D brain MRI segmentation. Our main contribution in this work was to extend the s - t min-cut/max-flow graph cut method for automatic 3D brain MRI segmentation using three-label graph. We also performed comparison study between this and several state-of-the-art brain MRI segmentation methods. Next, we applied the proposed method to automatic brain cortex segmentation in patients with FCD lesions. The proposed method was validated both qualitatively and quantitatively on simulated and real brain MRI datasets. The experimental results showed that our 3DGC method competes favorably with other state-of-the-art methods and is able to enforce the spatial coherence and correctly label the neighboring voxels in the noisy areas. Also, results suggested that the 3DGC method can improve the FCD lesion detection and can be successfully applied in many other clinical applications.

In Chapter 5, we presented a new FCM-based method for spatially coherent and noise-robust image segmentation. In general, the standard FMC clustering has ability to model uncertainty within data and is easily applicable to multimodal data. However, the standard FCM is highly sensitive to image noise, because it does not consider any information about the spatial image context. The contribution of our method is twofold: (1) the spatial information of local image features is integrated into both the similarity measure and the membership function to compensate for the effect of noise; and (2) an anisotropic neighborhood, based on phase congruency features, is introduced to avoid edge smoothing and retain image details. The performance of the proposed algorithm was tested on synthetic images with different noise levels and on real images. The segmentation results demonstrated that our method efficiently

preserves the homogeneity of the regions, without smoothing the line features and important image details, and is more robust to noise than related FCM-based methods.

Following this, we also presented an extension of the new FCM method to multimodal image segmentation, where we integrated multimodal image information into the spatial contextual information to overcome the noise problem. The performance of the proposed algorithm is tested on simulated and real adult MR brain images with different noise levels, as well as on neonatal MR brain images with the gestational age between 39-41 weeks. Experimental results showed that the proposed multimodal method is effective and robust to noise and can be successfully used for complex and noisy image segmentation of the neonatal brain.

In Chapter 6, we presented a new interactive hybrid segmentation method for realistic head modeling in newborn infants. Our method combines our new multimodal FCM clustering, active contours and mathematical morphology. For the purpose of realistic head modeling, we also developed a method for brain volume segmentation in neonates (brain extraction) using multimodal T_1 -W and T_2 -W MRI. This is because the existing brain volume segmentation techniques are mainly developed for adults and are not applicable to neonates or require additional corrections. The brain extraction algorithm was tested on real neonatal brain MR images with the gestational age between 39-41 weeks. The segmentation results were compared to manual segmentation and results showed that our method is effective and more accurate than existing brain volume segmentation methods originally developed for adults.

Furthermore, in Chapter 7 we proposed an integrated multimodal EEG-MRI method for neonatal EEG source localization using a realistic head model. This pilot study evaluated the utility of 3D localization of neonatal seizures and explored the relationship between neonatal EEG seizures and acute perinatal brain lesions visible on MRI. Despite many difficulties, we showed that EEG ictal source localization is feasible in newborns and can lead to important new insights into the properties of cerebral neural networks and 3D comparison with brain lesions. The results showed that the majority of calculated 3D sources were at the edge or ≤ 5 mm from the nearest MRI lesions. Also, using approximate head tissue conductivities (which were found in the literature) with an accurate geometrical description of the head, yielded reasonable results for both cortical and deep EEG sources. Considering that the 3D sources were computed using only 17 electrodes and the standard 10-20 system of electrode placement, our results are very promising for further research on the relationship between EEG source localization and brain injury visible on MRI.

Overall, the strength of this thesis lies in the practical applications of our methods and clinical validation of the quantitative segmentation results in the field of MR imaging. The limitations of the methods proposed in this work are that they are tested on the small number of patients as well as the deliberate selection of patients with discrete lesions visible on MRI. This is the case with both adult patients with FCD lesion and asphyxiated neonates. Next, the MRI segmentation of the adult brain tissue was tested only on MR images recorded with the same 3T MRI scanner, while the realistic head modeling framework was specifically designed for neonatal brain images acquired with a lower-resolution 1.5T MRI scanner. However, to fully evaluate the clinical sig-

nificance of the neonatal EEG source localization, we need bigger set of asphyxiated babies that can be only acquired over a period of at least a few years. We also need more accurate data acquisition with higher MRI resolution.

8.1 Future work

In future research, there is a lot of space for further developments and new applications of the algorithms presented in this thesis. For instance, the performance of the 3DGC method can be potentially improved by including multimodal image information. In the case of FCD patients, lesion detection can be improved by using intensities from both T_1 -W and FLAIR MRI of the brain. This is because in some cases FCD lesions are hardly visible on T_1 -W images, but they can be detected on FLAIR scans. Another possibility is to include the prior knowledge of the probabilistic brain atlas or the training data of the patients with FCD lesions into the segmentation framework. In the case of the noise-robust FCM clustering, future work can focus on extension of the method to deal with volumetric 3D images by incorporating 3D neighborhood information. For both segmentation methods, an automatic calculation of the optimal segmentation parameters and further improvements in both speed and accuracy should be considered in the future work. Moreover, it would be interesting to integrate the bias field correction of MR images directly into the segmentation energy function and to allow the labeling of image elements to be influenced by the neighboring labels and at the same time compensate for intensity inhomogeneities. Finally, the validation of the methods on more patients should be also considered in the future work.

Considering the multimodal EEG-MRI study for neonatal dipole source localization, the near-term clinical application is still limited in the NICU and the studies like ours are needed to close our present gaps in the knowledge about pathophysiology of neonatal seizures. We feel that with further validation, this type of multimodal approaches could improve therapy as well as outcome predictions in the future. Large, multi-center cEEG studies are needed to study the pathophysiology of neonatal seizures, their relationship to acute brain lesions as well as the effect of their treatment with antiepileptic drugs. Long-term follow-up is needed in our patients to look for neurocognitive deficits and epilepsy. Studying large amounts of cEEG data is highly labor-intensive and will be simplified by the use of automated methods like the one we developed. Also, similar multimodal brain imaging studies in both adult and neonates will help to refine our prognostication in patients with particular combinations of seizures and brain injury patterns on MRI.

8.2 Brief summary of the main contributions

To summarize, the novelties and contributions of this research can be divided in two groups: (1) those related to image segmentation with application to brain MRI and (2) those integrating our MRI segmentation research and EEG monitoring of the neonatal brain, and resulting in the application for neonatal EEG source localization.

In the first group we have contributed the following algorithms and methods:

1. An improved 3D graph cut algorithm for brain tissue segmentation with application to more accurate brain cortex segmentation and epileptic lesion detection in FCD patients, [Despotovic et al., 2011b, Despotovic et al., 2011c].
2. A new fuzzy clustering method for accurate and noise-robust image segmentation, [Despotovic et al., 2010b, Despotovic et al., 2010c, Despotovic et al., 2010a, Despotovic et al., 2010d, Despotovic et al., 2013c].
3. An integrated algorithm for the neonatal brain volume segmentation (brain extraction) using multimodal MRI, [Despotovic et al., 2010e].
4. An algorithm for 3D realistic head modeling in newborn infants, [Despotovic et al., 2009a, Despotovic et al., 2009b, Despotovic et al., 2010f, Despotovic et al., 2013b].

In the second group we have created the following contributions:

1. The first integrated method for ictal EEG dipole source localization in newborn infants based on a realistic head model, [Despotovic et al., 2013a, Despotovic et al., 2011a].
2. The experimental studies for investigating the utility of EEG source imaging in neonates with postasphyxial seizures, [Despotovic et al., 2013a, Despotovic et al., 2012].
3. The first objective study of the relationship between the localization of neonatal seizures and associated MRI patterns of brain injury, [Despotovic et al., 2013a].

This work resulted in 2 journal papers cited in the Science Citation Index. In total, 19 other papers appeared in the proceedings of international and national conferences, of which 15 as the first author.

Bibliography

- [Ahmed et al., 2002] Ahmed, M. N., Yamany, S. M., Mohamed, N., Farag, A. A., and T., M. (2002). A modified fuzzy c-means algorithm for bias field estimation and segmentation of MRI data. *IEEE Trans. Med. Imaging*, 21(3):193–199.
- [Akhtari et al., 2002] Akhtari, M., Bryant, H. C., Mamelak, A. N., Flynn, E. R., Heller, L., Shih, J. J., Mandelkern, M., Matlachov, A., Ranken, D. M., Best, E. D., DiMauro, M. A., Lee, R. R., and Sutherling, W. W. (2002). Conductivities of three-layer live human skull. *Brain Topogr.*, 14(3):151–167.
- [Antel et al., 2002] Antel, S. B., Bernasconi, A., Bernasconi, N., Collins, D. L., Kearney, R. E., Shinghal, R., and Arnold, D. L. (2002). Computational models of MRI characteristics of focal cortical dysplasia improve lesion detection. *Neuroimage*, 17(4):1755–1760.
- [Ashburner and Friston, 1999] Ashburner, J. and Friston, K. J. (1999). Nonlinear spatial normalization using basis functions. *Human Brain Mapping*, 7(4):254–266.
- [Ashburner and Friston, 2005] Ashburner, J. and Friston, K. J. (2005). Unified segmentation. *Neuroimage*, 26(3):839–851.
- [Atcherson et al., 2007] Atcherson, S. R., Gould, H. J., Pousson, M. A., and Prout, T. M. (2007). Variability of electrode positions using electrode caps. *Brain Topogr.*, 20(2):105–111.
- [Barkovich et al., 1998] Barkovich, A. J., Hajnal, B. L., Vigneron, D., Sola, A., Partridge, J. C., Allen, F., and Ferriero, D. M. (1998). Prediction of neuromotor outcome in perinatal asphyxia: evaluation of MR scoring systems. *AJNR Am. J. Neuroradiol.*, 19(1):143–149.
- [Barr, 1999] Barr, L. L. (1999). Neonatal cranial ultrasound. *Radiologic Clinics of North America*, 37(6):1127–1146.
- [Bartsch et al., 2007] Bartsch, A. J., Homola, G., Biller, A., Smith, S. M., Weijers, H. G., Wiesbeck, G. A., Jenkinson, M., De Stefano, N., Solymosi, L., and Bendzsus, M. (2007). Manifestations of early brain recovery associated with abstinence from alcoholism. *Brain*, 130(1):36–47.
- [Battaglini et al., 2008] Battaglini, M., Smith, S. M., Brogi, S., and De Stefano, N. (2008). Enhanced brain extraction improves the accuracy of brain atrophy estimation. *Neuroimage*, 40(2):583–589.

- [Baumann et al., 1997] Baumann, S. B., Wozny, D. R., Kelly, S. K., and Meno, F. M. (1997). The electrical conductivity of human cerebrospinal fluid at body temperature. *IEEE Trans. Biomed. Eng.*, 44(3):220–223.
- [Ben-Ari and Holmes, 2006] Ben-Ari, Y. and Holmes, G. L. (2006). Effects of seizures on developmental processes in the immature brain. *Lancet Neurology*, 5(12):1055–1063.
- [Berger, 1929] Berger, H. (1929). Über das Elektroencephalogramm des Menschen. *Arch. Psychiatr. Nervenkr.*, 87:527–570.
- [Bernasconi et al., 2001] Bernasconi, A., Antel, S. B., Collins, D. L., Bernasconi, N., Olivier, A., Dubeau, F., Pike, G. B., Andermann, F., and Arnold, D. L. (2001). Texture analysis and morphological processing of magnetic resonance imaging assist detection of focal cortical dysplasia in extra-temporal partial epilepsy. *Ann. Neurol.*, 49(6):770–775.
- [Besag, 1986] Besag, J. (1986). On the statistical analysis of dirty pictures. *Journal of the Royal Statistical Society. Series B (Methodological)*, 48(3):259–302.
- [Besson et al., 2008] Besson, P., Andermann, F., Dubeau, F., and Bernasconi, A. (2008). Small focal cortical dysplasia lesions are located at the bottom of a deep sulcus. *Brain*, 131(12):3246–3255.
- [Beutel et al., 2000] Beutel, J., Kundel, H. L., and Van Metter, R. L. (2000). *Handbook of Medical Imaging, Volume 1. Physics and Psychophysics*. SPIE - The international Society for Optical Engineering.
- [Bezdek, 1981] Bezdek, J. C. (1981). *Pattern Recognition with Fuzzy Objective Function Algorithms*. Plenum Press, NY, USA.
- [Biagioni et al., 2001] Biagioni, E., Mercuri, E., Rutherford, M., Cowan, F., Az-zopardi, D., Frisone, M. F., Cioni, G., and Dubowitz, L. (2001). Combined use of electroencephalogram and magnetic resonance imaging in full-term neonates with acute encephalopathy. *Pediatrics*, 107(3):461–468.
- [Black et al., 1998] Black, M. J., Sapiro, G., Marimont, D. H., and Heeger, D. (1998). Robust anisotropic diffusion. *IEEE Trans. Image Process.*, 7(3):421–432.
- [Blakemore, 2012] Blakemore, S. J. (2012). Imaging brain development: the adolescent brain. *NeuroImage*, 61(2):397–406.
- [Blink, 2004] Blink, E. J. (2004). *MRI: physics*.
- [Bloch, 1946] Bloch, F. (1946). Nuclear induction. *Phys. Rev.*, 70(7-8):460–474.
- [Bloch et al., 1946] Bloch, F., Hansen, W. W., and Packard, M. (1946). The nuclear induction experiment. *Phys. Rev.*, 70(7-8):474–485.

- [Bénar and Gotman, 2002] Bénar, C. G. and Gotman, J. (2002). Modeling of post-surgical brain and skull defects in the EEG inverse problem with the boundary element method. *Clin. Neurophysiol.*, 113(1):48–56.
- [Boukerroui et al., 2004] Boukerroui, D., Noble, J. A., and Brady, M. (2004). On the choice of band-pass quadrature filters. *Journal of Mathematical Imaging and Vision*, 21(1-2):53–80.
- [Boykov and Funka-Lea, 2006] Boykov, Y. and Funka-Lea, G. (2006). Graph cuts and efficient N-D image segmentation. *Int. J. Comput. Vision*, 70(2):109–131.
- [Boykov and Kolmogorov, 2004] Boykov, Y. and Kolmogorov, V. (2004). An experimental comparison of min-cut/max-flow algorithms for energy minimization in vision. *IEEE Trans. Pattern Anal. Machine Intell.*, 26(9):1124–1137.
- [Boykov et al., 2001] Boykov, Y., Veksler, O., and Zabih, R. (2001). Fast approximate energy minimization via graph cuts. *IEEE Trans. Pattern Anal. Machine Intell.*, 23(11):1222–1239.
- [BrainVisa, 2012] BrainVisa (2012). Mapping functional spm in individual anatomical context. <http://brainvisa.info>.
- [BrainWeb, 2013] BrainWeb (2013). Simulated Brain Database. <http://brainweb.bic.mni.mcgill.ca/brainweb/>.
- [Bushberg and Seibert, 1994] Bushberg, J. T. and Seibert, J. A. (1994). *The Essential Physics of Medical Imaging*. Baltimore: Williams and Wilkins.
- [Bye and Flanagan, 1995] Bye, A. M. and Flanagan, D. (1995). Spatial and temporal characteristics of neonatal seizures. *Epilepsia*, 36(10):1009–1016.
- [Cai et al., 2007] Cai, W., Chen, S., and Zhang, D. (2007). Fast and robust fuzzy c-means clustering algorithms incorporating local information for image segmentation. *Pattern Recognition*, 40(3):825–838.
- [Canny, 1986] Canny, J. (1986). A computational approach to edge detection. *IEEE Trans. Pattern Anal. Machine Intell.*, 8(6):679–698.
- [Caveness et al., 1973] Caveness, W., Echlin, F., Kemper, T., and Kato, M. (1973). The propagation of focal paroxysmal activity in the Macaca mulatta at birth and at 24 months. *Brain*, 96(4):757–764.
- [Chan and Vese, 2001] Chan, T. F. and Vese, L. A. (2001). Active contours without edges. *IEEE Trans. Image Process.*, 10(2):266–277.
- [Chen and Zhang, 2004] Chen, S. and Zhang, D. (2004). Robust image segmentation using FCM with spatial constraints based on new kernel-induced distance measure. *IEEE Trans. System Man Cybernet., Part B.*, 34(4):1907–1916.

- [Chuang et al., 2006] Chuang, K. S., Tzeng, H. L., Chen, S., Wu, J., and Chen, T. J. (2006). Fuzzy c-means clustering with spatial information for image segmentation. *Comput. Med. Imaging Graph.*, 30(1):9–15.
- [Chugani and Phelps, 1986] Chugani, H. T. and Phelps, M. E. (1986). Maturational changes in cerebral function in infants determined by 18FDG positron emission tomography. *Science*, 231(4740):840–843.
- [Clifford, 1990] Clifford, T. (1990). *Markov Random Fields in Statistics*. Clarendon, Oxford.
- [Cocosco et al., 2003] Cocosco, C. A., Zijdenbos, A. P., and C., E. A. (2003). A fully automatic and robust brain MRI tissue classification method. *Med. Image Anal.*, 7(4):513–527.
- [Cohen and Cohen, 1993] Cohen, L. and Cohen, I. (1993). Finite-element methods for active contour models and balloons for 2-D and 3-D images. *IEEE Trans. Pattern Anal. Machine Intell.*, 15(11):1131–1147.
- [Cohen et al., 2000] Cohen, M. S., DuBois, R. M., and Zeneih, M. M. (2000). Rapid and effective correction of RF inhomogeneity for high field magnetic resonance imaging. *Human Brain Mapping*, 10(4):204–211.
- [Coleman and Andrews, 1979] Coleman, G. B. and Andrews, H. C. (1979). Image segmentation by clustering. *Proceedings of the IEEE*, 67(5):773–785.
- [Collier et al., 2003] Collier, D. C., Burnett, S. S. C., and Amin, M. (2003). Assessment of consistency in contouring of normal-tissue anatomic structures. *Journal of Applied Clinical Medical Physics*, 4(1):17–24.
- [Collins et al., 2005] Collins, C. M., Liu, W., Schreiber, W., Yang, Q. X., and Smith, M. B. (2005). Central brightening due to constructive interference with, without, and despite dielectric resonance. *J. Magn. Reson. Imaging*, 21(2):192–196.
- [Collins et al., 1998] Collins, D. L., Zijdenbos, A. P., Kollokian, V., Sled, J. G., Kabani, N. J., Holmes, C. J., and Evans, A. C. (1998). Design and construction of a realistic digital brain phantom. *IEEE Trans. Med. Imaging*, 17(3):463–468.
- [Colliot et al., 2005] Colliot, O., Mansi, T., Bernasconi, N., Naessens, V., Klironomos, D., and Bernasconi, A. (2005). Segmentation of focal cortical dysplasia lesions using a feature-based level set. *Med. Image Comput. Comput. Assist. Interv.*, 8(1):375–382.
- [Cowan and Denis, 2007] Cowan, F. and Denis, A. (2007). Hypoxic-ischaemic encephalopathy. *Paediatrics and Child Health*, 17(2):47–57.
- [Cowan et al., 2003] Cowan, F., Rutherford, M., Groenendaal, F., Eken, P., Mercuri, E., Bydder, G. M., Meiners, L. C., Dubowitz, L. M., and de Vries, L. S. (2003). Origin and timing of brain lesions in term infants with neonatal encephalopathy. *Lancet*, 361(9359):736–742.

- [Crum et al., 2004] Crum, W. R., Hartkens, T., and Hill, D. L. G. (2004). Non-rigid image registration: theory and practice. *Br. J. Radiol.*, 77:S140–S153.
- [Cuffin, 1996] Cuffin, B. N. (1996). EEG localization accuracy improvements using realistically shaped head models. *IEEE Trans. Biomed. Eng.*, 43(3):299–303.
- [D’Agostino et al., 2002] D’Agostino, E., Maes, F., Vandermeulen, D., and Suetens, P. (2002). A viscous fluid model for multimodal non-rigid image registration using mutual information. In *Proc. Medical Image Computing and Computer Assisted Intervention (MICCAI)*, pages 541–548.
- [D’Agostino et al., 2004] D’Agostino, E., Maes, F., Vandermeulen, D., and Suetens, P. (2004). Non-rigid atlas-to-image registration by minimization of class-conditional image entropy. In *Proc. Medical Image Computing and Computer Assisted Intervention (MICCAI)*, pages 745–753.
- [Damadian, 1971] Damadian, R. (1971). Tumor detection by nuclear magnetic resonance. *Science*, 171(3976):1151–1153.
- [Damadian et al., 1977] Damadian, R., Goldsmith, M., and Minkoff, L. (1977). NMR in cancer: XVI. FONAR image of the live human body. *Physiol. Chem. Phys.*, 9(1):97–100, 108.
- [Davies et al., 2008] Davies, R., Twining, C., and Taylor, C. (2008). *Statistical models of shape optimisation and evaluation*. Springer-Verlag, London, UK.
- [de Munck et al., 1988] de Munck, J. C., van Dijk, B. W., and Spereijse, H. (1988). Mathematical dipoles are adequate to describe realistic generators of human brain activity. *IEEE Trans. Biomed. Eng.*, 35(11):960–966.
- [de Oliveira and Pedrycz, 2007] de Oliveira, J. and Pedrycz, W. (2007). *Advances in Fuzzy Clustering and its Applications*. John Wiley & Sons, Inc., New York, NY, USA.
- [De Vos, 2009] De Vos, M. (2009). *Decomposition Methods with Applications in Neuroscience*. PhD thesis, KU Leuven.
- [De Vos et al., 2011] De Vos, M., Deburchgraeve, W., Cherian, P. J., Matic, V., Swarte, R. M., Govaert, P., Visser, G. H., and Van Huffel, S. (2011). Automated artifact removal as preprocessing refines neonatal seizure detection. *Clin. Neurophysiol.*, 122(12):2345–2354.
- [De Vos et al., 2010] De Vos, M., Riès, S., Vanderperren, K., Vanrumste, B., Alario, F. X., Van Huffel, S., and Burle, B. (2010). Removal of muscle artifacts from EEG recordings of spoken language production. *Neuroinformatics*, 8(2):135–150.
- [De Vos et al., 2007] De Vos, M., Vergult, A., De Lathauwer, L., De Clercq, W., Van Huffel, S., Dupont, P., Palmini, A., and Van Paesschen, W. (2007). Canonical decomposition of ictal scalp EEG reliably detects the seizure onset zone. *Neuroimage*, 37(3):844–854.

- [Deblaere and Achten, 2008] Deblaere, K. and Achten, E. (2008). Structural magnetic resonance imaging in epilepsy. *Eur. Radiol.*, 18(1):119–129.
- [Deburchgraeve et al., 2008] Deburchgraeve, W., Cherian, P. J., De Vos, M., Swarte, R. M., Blok, J. H., Visser, G. H., Govaert, P., and Van Huffel, S. (2008). Automated neonatal seizure detection mimicking a human observer reading EEG. *Clin. Neurophysiol.*, 19(11):2447–2454.
- [Deburchgraeve et al., 2009] Deburchgraeve, W., Cherian, P. J., De Vos, M., Swarte, R. M., Blok, J. H., Visser, G. H., Govaert, P., and Van Huffel, S. (2009). Neonatal seizure localization using PARAFAC decomposition. *Clin. Neurophysiol.*, 120(10):1787–1796.
- [Deburchgraeve et al., 2010] Deburchgraeve, W., Cherian, P. J., De Vos, M., Swarte, R. M., Blok, J. H., Visser, G. H., Govaert, P., and Van Huffel, S. (2010). Time varying neonatal seizure localization. *Methods Inf. Med.*, 49(5):473–478.
- [Dekaban and Sadowsky, 1978] Dekaban, A. S. and Sadowsky, D. (1978). Changes in brain weight during the span of human life: relation of brain weights to body heights and body weights. *Ann. Neurol.*, 4(4):345–356.
- [del Fresno et al., 2009] del Fresno, M., Vénere, M., and Clausse, A. (2009). A combined region growing and deformable model method for extraction of closed surfaces in 3D CT and MRI scans. *Comput. Med. Imaging Graph.*, 33(5):369–376.
- [DeLucci et al., 1962] DeLucci, M. R., Garoutte, B., and Aird, R. B. (1962). The scalp as an electroencephalographic averager. *Electroencephalogr. Clin. Neurophysiol.*, 14(2):191–196.
- [Despotovic et al., 2013a] Despotovic, I., Cherian, P. J., De Vos, M., Hallez, H., Deburchgraeve, W., Govaert, P., Lequin, M., Visser, G. H., Swarte, R. M., Vansteenkiste, E., Van Huffel, S., and Philips, W. (2013a). Relationship of EEG sources of neonatal seizures to acute perinatal brain lesions seen on MRI: A pilot study. *Human Brain Mapping*, 34(10):2402–2417.
- [Despotovic et al., 2012] Despotovic, I., Cherian, P. J., De Vos, M., Hallez, H., Govaert, P., Lequin, M., Visser, G. H., Swarte, R. M., Vansteenkiste, E., Van Huffel, S., and Philips, W. (2012). Influence of volume conductor model errors on dipole source localization in neonates. In *Proc. International Society for Magnetic Resonance in Medicine Chapter (ISMRM)*, page 3647, Melbourne, Australia.
- [Despotovic et al., 2011a] Despotovic, I., De Vos, M., Hallez, H., Vansteenkiste, E., Van Huffel, S., and Philips, W. (2011a). Integrating EEG and MRI data for seizure localization in neonates. In *IEEE EMBS Benelux Chapter*, KU Leuven, Belgium.
- [Despotovic et al., 2009a] Despotovic, I., Deburchgraeve, W., Hallez, H., Vansteenkiste, E., and Philips, W. (2009a). Development of a realistic head model for EEG event-detection and source localization in newborn infants. In *Proc. IEEE Engineering in Medicine and Biology Society Conference (EMBC)*, pages 2296–2299, Minneapolis, Minnesota, USA.

- [Despotovic et al., 2010a] Despotovic, I., Goossens, B., Vansteenkiste, E., and Philips, W. (2010a). An improved fuzzy clustering approach for image segmentation. In *IEEE Int. Conf. on Image Processing (ICIP)*, pages 249–252, Hong Kong, China.
- [Despotovic et al., 2010b] Despotovic, I., Goossens, B., Vansteenkiste, E., and Philips, W. (2010b). MRI brain tissue classification using fuzzy c-means clustering with spatial information. In *Proc. Benelux ISMRM Chapter*, Utrecht, the Netherlands.
- [Despotovic et al., 2010c] Despotovic, I., Goossens, B., Vansteenkiste, E., and Philips, W. (2010c). T1- and T2-weighted spatially constrained fuzzy C-means clustering for brain MRI segmentation. In *Proc. SPIE, Image Processing, Medical imaging*, volume 7623, page 9 pages, San Diego, California, USA.
- [Despotovic et al., 2008] Despotovic, I., Goossens, B., Vansteenkiste, E., Pizurica, A., and Philips, W. (2008). Using phase information in ultrasound RF-signals for tissue characterization. In *Proc. ProRISC*, pages 314–317, Veldhoven, the Netherlands. **Best Flash Presentation Award.**
- [Despotovic et al., 2010d] Despotovic, I., Jelaca, V., Vansteenkiste, E., and Philips, W. (2010d). Noise-robust method for image segmentation. In *Advanced Concepts for Intelligent Vision Systems (ACIVS)*, volume LNCS, pages 153 – 162, Sydney, Australia.
- [Despotovic et al., 2011b] Despotovic, I., Segers, I., Platisa, L., Vansteenkiste, E., Pizurica, A., Deblaere, K., and Philips, W. (2011b). Automatic 3D graph cuts for brain cortex segmentation in patients with focal cortical dysplasia. In *Proc. IEEE Engineering in Medicine and Biology Society Conference (EMBC)*, pages 7981–7984, Boston, Massachusetts, USA.
- [Despotovic et al., 2011c] Despotovic, I., Segers, I., Platisa, L., Vansteenkiste, E., Pizurica, A., Deblaere, K., and Philips, W. (2011c). Brain MRI segmentation for focal cortical dysplasia lesion detection. In *Proc. International Society for Magnetic Resonance in Medicine Chapter (ISMRM)*, page 4277, Montreal, Canada.
- [Despotovic et al., 2011d] Despotovic, I., Segers, I., Platisa, L., Vansteenkiste, E., Pizurica, A., Deblaere, K., and Philips, W. (2011d). Brain MRI segmentation for focal cortical dysplasia lesion detection. In *Proc. Benelux International Society for Magnetic Resonance in Medicine Chapter (ISMRM)*, page 119, Roosendaal, The Netherlands.
- [Despotovic et al., 2009b] Despotovic, I., Vansteenkiste, E., and Philips, W. (2009b). 3D MRI head segmentation in newborn infants. In *Proc. 10th FirW Ph.D. Symposium*, pages 32–33, Ghent University, Belgium.
- [Despotovic et al., 2010e] Despotovic, I., Vansteenkiste, E., and Philips, W. (2010e). Brain volume segmentation in newborn infants using multi-modal MRI with a low inter-slice resolution. In *Proc. IEEE Engineering in Medicine and Biology Society Conference (EMBC)*, pages 5038–5041, Buenos Aires, Argentina.

- [Despotovic et al., 2010f] Despotovic, I., Vansteenkiste, E., and Philips, W. (2010f). Realistic head modeling in neonates using MRI segmentation. In *9th Belgian Day on Biomedical Engineering*, page 82, Brussels, Belgium.
- [Despotovic et al., 2013b] Despotovic, I., Vansteenkiste, E., and Philips, W. (2013b). A realistic volume conductor model of the neonatal head: methods, challenges and applications. In *Proc. IEEE Engineering in Medicine and Biology Society Conference (EMBC)*, pages 3303–3306, Osaka, Japan.
- [Despotovic et al., 2013c] Despotovic, I., Vansteenkiste, E., and Philips, W. (2013c). Spatially coherent fuzzy clustering for accurate and noise-robust image segmentation. *IEEE Signal Process. Letters*, 20(4):295–298.
- [Dice, 1945] Dice, L. R. (1945). Measures of the amount of ecologic association between species. *Ecology*, 26(3):297–302.
- [Ding et al., 2007] Ding, L., Worrell, G. A., Lagerlund, T. D., and He, B. (2007). Ictal source analysis: localization and imaging of causal interactions in humans. *Neuroimage*, 34(2):575–586.
- [D’Souza, 2004] D’Souza, A. A. (2004). Using EM to estimate a probability density with a mixture of gaussians.
- [Duda et al., 1973] Duda, R. O., Hart, P. E., and Stork, D. G. (1973). *Pattern classification and scene analysis*. Wiley, New York.
- [Duda et al., 2001] Duda, R. O., Hart, P. E., and Stork, D. G. (2001). *Pattern Classification*. John Wiley & Sons Inc, 2 edition.
- [Dudink, 2010] Dudink, J. (2010). *Diffusion Weighted Imaging of the neonatal brain*. PhD thesis, Erasmus University Rotterdam.
- [Dunn, 1973] Dunn, J. C. (1973). A fuzzy relative of the ISODATA process and its use in detecting compact well-separated clusters. *Journal of Cybernetics*, 3(3):32–57.
- [Duta and Sonka, 1998] Duta, N. and Sonka, M. (1998). Segmentation and interpretation of MR brain images: an improved active shape model. *IEEE Trans. Med. Imaging*, 17(6):1049–1062.
- [Ecabert et al., 2008] Ecabert, O., Peters, J., Schramm, H., Lorenz, C., von Berg, J., Walker, M. J., Vembar, M., Olszewski, M. E., Subramanyan, K., Lavi, G., and Weese, J. (2008). Automatic model-based segmentation of the heart in CT images. *IEEE Trans. Med. Imaging*, 27(9):1189–1201.
- [Erasmus et al., 2004] Erasmus, L., Hurter, D., Naudé, M., Kritzing, H., and Acho, S. (2004). A short overview of MRI artifacts. *South African Journal of Radiology*, 8(2):13–17.

- [Evans et al., 1993] Evans, A. C., Collins, D. L., Mills, S. R., Brown, E. D., Kelly, R. L., and M., P. T. (1993). 3D statistical neuroanatomical models from 305 MRI volumes. *Nuclear Science Symposium and Medical Imaging Conference*, 3(31):1813–1817.
- [Felsberg and Sommer, 2001] Felsberg, M. and Sommer, G. (2001). The monogenic signal. *IEEE Trans. Signal Process.*, 49(12):3136–3144.
- [Fisch, 1999] Fisch, B. (1999). *Artifacts*. In Fisch and Spelmann's EEG Primer, chapter 6. Elsevier, 3 edition.
- [Fischl et al., 2002] Fischl, B., Salat, D. H., Busa, E., Albert, M., Dieterich, M., Haselgrove, C., van der Kouwe, A., Killiany, R., and et al. (2002). Whole brain segmentation: Automated labeling of neuroanatomical structures in the human brain. *Neuron*, 33(3):341–355.
- [Fitzpatrick et al., 2004] Fitzpatrick, J. M., Hill, D. L. G., and Maurer, C. R. (2004). *Handbook of Medical Imaging: Medical Image Processing and Analysis. Image registration*, volume 2.
- [Ford and Fulkerson, 1962] Ford, L. R. and Fulkerson, D. R. (1962). *Flows in Networks*. Princeton university press.
- [Frank, 1952] Frank, E. (1952). Electric potential produced by two point current sources in a homogeneous conduction sphere. *Journal of Applied Physics*, 23(11):1225–1228.
- [Freeman and Adelson, 1991] Freeman, W. T. and Adelson, E. H. (1991). The design and use of steerable filters. *IEEE Trans. Pattern Anal. Machine Intell.*, 3(9):891–906.
- [Geddes and Baker, 1967] Geddes, L. A. and Baker, L. E. (1967). The specific resistance of biological material - a compendium of data for the biomedical engineer and physiologist. *Med. Biol. Eng.*, 5(3):271–293.
- [Geman and Geman, 1984] Geman, S. and Geman, D. (1984). Stochastic relaxation, Gibbs distribution, and Bayesian restoration of images. *IEEE Trans. Pattern Anal. Machine Intell.*, 6(6):721–741.
- [Gerig et al., 1992] Gerig, G., Kubler, O., Kikinis, R., and Jolesz, F. A. (1992). Non-linear anisotropic filtering of MRI data. *IEEE Trans. Med. Imaging*, 11(2):221–232.
- [Gibson et al., 2000] Gibson, A., Bayford, R. H., and Holder, D. S. (2000). Two-dimensional finite element modelling of the neonatal head. *Physiol. Meas.*, 21(1):45–52.
- [Gloor, 1985] Gloor, P. (1985). Neuronal generators and the problem of localization in electroencephalography: applications of volume conductor theory to electroencephalography. *Clin. Neurophysiol.*, 2(4):327–354.

- [Gonçalves et al., 2003] Gonçalves, S. I., de Munck, J. C., Verbunt, J. P. A., Bijma, F., Heethaar, R. M., and Lopes da Silva, F. (2003). In vivo measurement of the brain and skull resistivities using an EIT-based method and realistic models for the head. *IEEE Trans. Biomed. Eng.*, 50(6):754–767.
- [Gonzalez and Woods, 2008] Gonzalez, R. C. and Woods, R. E. (2008). *Digital Image Processing*. Pearson Education.
- [Gotchev et al., 2000] Gotchev, A., Vesma, J., Saramaki, T., and Egiazarian, K. (2000). Digital image resampling by modified B-spline functions. In *IEEE Nordic Signal Processing Symposium*, pages 259–262.
- [Greenspan et al., 2006] Greenspan, H., Ruf, A., and Goldberger, J. (2006). Constrained Gaussian mixture model framework for automatic segmentation of MR brain images. *IEEE Trans. Med. Imaging*, 25(9):1233–1245.
- [Greig et al., 1989] Greig, D. M., Porteous, B. T., and Seheult, A. H. (1989). Exact maximum a posteriori estimation for binary images. *J. R. Statist. Soc. B*, 51(2):271–279.
- [Gudbjartsson and Patz, 1995] Gudbjartsson, H. and Patz, S. (1995). The rician distribution of noisy MRI data. *Magn. Reson. Med.*, 34(6):910–914.
- [Haake et al., 1999] Haake, E. M., Brown, R. W., and et al. (1999). *Magnetic Resonance Imaging: Practical Principles and Sequence Design*. New York: Wiley-Liss.
- [Hajnal et al., 2001] Hajnal, J. V., Hill, D. L. G., and Hawkes, D. J. (2001). *Medical Image Registration*. CRC Press.
- [Hallez, 2008] Hallez, H. (2008). *Incorporation of anisotropic conductivities in EEG source analysis*. PhD thesis, Ghent University.
- [Hallez et al., 2007] Hallez, H., Vanrumste, B., Grech, R., Muscat, J., De Clercq, W., Vergult, A., D’Asseler, Y., Camilleri, K. P., Fabri, S. G., Van Huffel, S., and Lemahieu, I. (2007). Review on solving the forward problem in EEG source analysis. *J. Neuroeng. Rehabil.*, 4(46).
- [Hallez et al., 2005] Hallez, H., Vanrumste, B., Van Hese, P., D’Asseler, Y., Lemahieu, I., and Van de Walle, R. (2005). A finite difference method with reciprocity used to incorporate anisotropy in electroencephalogram dipole source localization. *Phys. Med. Biol.*, 50(16):3787–3806.
- [Hara et al., 1999] Hara, J., Musha, T., and Shankle, W. R. (1999). Approximating dipoles from human EEG activity: The effect of dipole source configuration on dipolarity using single dipole models. *IEEE Trans. Biomed. Eng.*, 43(2):125–129.
- [Haralick and Shapiro, 1985] Haralick, R. and Shapiro, L. (1985). Image segmentation techniques. *Computer Vision, Graphics, and Image Processing*, 29(1):100–132.

- [Hartings et al., 2003] Hartings, J. A., Williams, A. J., and Tortella, F. C. (2003). Occurrence of nonconvulsive seizures, periodic epileptiform discharges, and intermittent rhythmic delta activity in rat focal ischemia. *Exp. Neurol.*, 179(2):139–149.
- [He et al., 2002] He, B., Yao, D., and Lian, J. (2002). High-resolution eeg: on the cortical equivalent dipole layer imaging. *Clin. Neurophysiol.*, 113(2):227–235.
- [Huttenlocher, 1979] Huttenlocher, P. R. (1979). Synaptic density in human frontal cortex developmental changes and effects of aging. *Brain Research*, 163(2):195–205.
- [IBSR, 2013] IBSR (2013). The Internet Brain Segmentation Repository. <http://www.nitrc.org/projects/ibsr>.
- [Inder and Huppi, 2000] Inder, T. E. and Huppi, P. S. (2000). In vivo studies of brain development by magnetic resonance techniques. *Ment. Retard. Dev. Disabil. Res. Rev.*, 6(1):59–67.
- [ITK-SNAP, 2009] ITK-SNAP (2009). www.itksnap.org.
- [Joyce et al., 2004] Joyce, C. A., Gorodnitsky, I. F., and Kutas, M. (2004). Automatic removal of eye movement and blink artifacts from EEG data using blind component separation. *Psychophysiology*, 41(2):313–325.
- [Jung et al., 2000] Jung, T. P., Makeig, S., Humphries, C., Lee, T. W., McKeown, M. J., Iragui, V., and Sejnowski, T. J. (2000). Removing electroencephalographic artifacts by blind source separation. *Psychophysiology*, 37(2):163–178.
- [Kaas et al., 1988] Kaas, M., Witkin, A., and Terzopolous, D. (1988). Snakes: Active contour models. *Int. J. Comput. Vision*, 1(4):321–331.
- [Kadam et al., 2010] Kadam, S. D., White, A. M., Staley, K. J., and Dudek, F. E. (2010). Continuous electroencephalographic monitoring with radio-telemetry in a rat model of perinatal hypoxia-ischemia reveals progressive post-stroke epilepsy. *J. Neurosci.*, 30(1):404–415.
- [Kaiboriboon et al., 2012] Kaiboriboon, K., Lüders, H., Hamaneh, M., Turnbull, J., and Lhatoo, S. (2012). EEG source imaging in epilepsy - practicalities and pitfalls. *Nature Reviews Neurology*, 8(9):498–507.
- [Kaiser, 1990] Kaiser, J. (1990). On a simple algorithm to calculate the ‘energy’ of a signal. In *Proc. International Conference on Acoustics, Speech, and Signal Processing (ICASSP)*, pages 381–384 vol.1.
- [Kato et al., 1980] Kato, M., Malamut, B. L., Caveness, W. F., Hosokawa, S., Wakisaka, S., and O’Neill, R. R. (1980). Local cerebral glucose utilization in newborn and pubescent monkeys during focal motor seizures. *Ann. Neurol.*, 7(3):204–12, 230–2.

- [Khosla et al., 1999] Khosla, D., Don, M., and Kwong, B. (1999). Spatial mislocalization of EEG electrodes - effects on accuracy of dipole estimation. *Clin. Neurophysiol.*, 110(2):261–271.
- [Kliegman et al., 2008] Kliegman, R. M., Behrman, R. E., Jenson, H. B., and et al. (2008). *Nelson Textbook of Pediatrics*. Saunders Ltd., 18 edition.
- [Koh et al., 1999] Koh, S., Storey, T. W., Santos, T. C., Mian, A. Y., and Cole, A. J. (1999). Early-life seizures in rats increase susceptibility to seizure-induced brain injury in adulthood. *Neurology*, 53:915–921.
- [Kolmogorov and Zabih, 2004] Kolmogorov, V. and Zabih, R. (2004). What energy functions can be minimized via graph cuts? *IEEE Trans. Pattern Anal. Machine Intell.*, 26(2):147–159.
- [Kovesi, 1999] Kovesi, P. (1999). Image feature from phase congruency. *Journal of Computer Vision Research*, 1(3):1–26.
- [Kovesi, 2000] Kovesi, P. (2000). Phase congruency: A low-level image invariant. *Psychological Research*, 64(2):136–148.
- [Kovesi, 2002] Kovesi, P. (2002). Edges are not just steps. In *Proc. Asian Conference on Computer Vision (ACCV)*, pages 822–827, Melbourne.
- [Kumcu et al., 2012] Kumcu, A., Platasa, L., Despotovic, I., Vansteenkiste, E., Pizurica, A., Deblaere, K., and Philips, W. (2012). Multi-modal measurement of cortical thickness in brain MRI for focal cortical dysplasia detection. In *Proc. Benelux International Society for Magnetic Resonance in Medicine Chapter (ISMRM)*, page 70, Leuven, Belgium.
- [Lai et al., 2005] Lai, Y., van Drongelen, W., Ding, L., Hecox, K. E., Towle, V. L., Frim, D. M., and He, B. (2005). Estimation of in vivo human brain-to-skull conductivity ratio from simultaneous extra- and intra-cranial electrical potential recordings. *Clin. Neurophysiol.*, 116(2):456–465.
- [Lauterbur, 1973] Lauterbur, P. (1973). Image formation by induced local interactions - examples employing nuclear magnetic-resonance. *Nature*, 242:190–191.
- [Ledda, 2007] Ledda, A. (2007). *Mathematical Morphology in Image Processing*. PhD thesis, Ghent University.
- [Leijser et al., 2007] Leijser, L. M., Vein, A. A., Liauw, L., Strauss, T., Veen, S., and Wezel-Meijler, G. (2007). Prediction of short-term neurological outcome in full-term neonates with hypoxic-ischaemic encephalopathy based on combined use of electroencephalogram and neuro-imaging. *Neuropediatrics*, 38(5):219–227.
- [Lenroot and Giedd, 2006] Lenroot, R. K. and Giedd, J. N. (2006). Brain development in children and adolescents: Insights from anatomical magnetic resonance imaging. *Neurosci. Biobehav. Rev.*, 30(6):718–729.

- [Levine and Barnes, 1999] Levine, D. and Barnes, P. D. (1999). Cortical maturation in normal and abnormal fetuses as assessed with prenatal MR imaging. *Radiology*, 210(3):751–758.
- [Lewis and Fox, 2004] Lewis, E. B. and Fox, N. C. (2004). Correction of differential intensity inhomogeneity in longitudinal MR images. *Neuroimage*, 23(1):75–83.
- [Li et al., 2011] Li, B. N., Chui, C. K., Chang, S., and Ong, S. H. (2011). Integrating spatial fuzzy clustering with level set methods for automated medical image segmentation. *Comput. Biol. Med.*, 41(1):1–10.
- [Li, 1995] Li, S. Z. (1995). *Markov Random Field Modeling in Computer Vision*. Springer-Verlag.
- [Ljunggren, 1983] Ljunggren, S. (1983). A simple graphical representation of Fourier-based imaging methods. *J. Magn. Reson.*, 54(2):338–343.
- [Lombaert et al., 2005] Lombaert, H., Y., S., Grady, L., and Xu, C. (2005). A multilevel banded graph cuts method for fast image segmentation. In *Proc. IEEE Int. Conf. Computer Vision (ICCV)*, volume 1, pages 259–265.
- [Maalouf et al., 2001] Maalouf, E. F., Duggan, P. J., Counsell, S. J., Rutherford, M. A., Cowan, F., Azzopardi, D., and Edwards, A. D. (2001). Comparison of findings on cranial ultrasound and magnetic resonance imaging in preterm infants. *Pediatrics*, 107(4):719–727.
- [Maillard et al., 2008] Maillard, P., Delcroix, N., Crivello, F., Dufouil, C., Gicquel, S., Joliot, M., Tzourio-Mazoyer, N., Alperovitch, A., Tzourio, C., and Mazoyer, B. (2008). An automated procedure for the assessment of white matter hyperintensities by multispectral (T1, T2, PD) MRI and an evaluation of its between-centre reproducibility based on two large community databases. *Neuroradiology*, 50(1):31–42.
- [Malik et al., 2001] Malik, J., Belongie, S., Leung, T., and Shi, J. (2001). Contour and texture analysis for image segmentation. *Int. J. Comput. Vision*, 43(1):7–27.
- [Mangin, 2000] Mangin, J. (2000). Entropy minimization for automatic correction of intensity nonuniformity. In *Proc. IEEE Workshop on Mathematical Methods in Biomedical Image Analysis (MMBIA)*, pages 162–169.
- [Mansfield, 1977] Mansfield, P. (1977). Multi-planar image formation using NMR spin echoes. *J. Phys. C: Solid State Phys.*, 10:L55–L58.
- [Marr and Hildreth, 1980] Marr, D. and Hildreth, E. (1980). Theory of edge detection. *Proc. R. Soc. London Series B Biol. Sci.*, 207(1167):187–217.
- [Marroquin et al., 2002] Marroquin, J. L., Vemuri, B. C., Botello, S., and Calderon, F. (2002). An accurate and efficient Bayesian method for automatic segmentation of brain MRI. *IEEE Trans. Med. Imaging*, 21(8):934–944.

- [Mattes et al., 2001] Mattes, D., Haynor, D. R., Vesselle, H., Lewellen, T., and Eubank, W. (2001). Nonrigid multimodality image registration. medical imaging. In *Proc. SPIE, Image Processing, Medical imaging*, pages 1609–1620.
- [Mayer and Greenspan, 2009] Mayer, A. and Greenspan, H. (2009). An adaptive mean-shift framework for MRI brain segmentation. *IEEE Trans. Med. Imaging*, 28(8):1238–1250.
- [McBride et al., 2000] McBride, M. C., Laroia, N., and Guillet, R. (2000). Electrographic seizures in neonates correlate with poor neurodevelopmental outcome. *Neurology*, 55(4):506–513.
- [Mellor and Brady, 2005] Mellor, M. and Brady, M. (2005). Phase mutual information as a similarity measure for registration. *Med. Image Anal.*, 9(4):330–343.
- [Merlet and Gotman, 2001] Merlet, I. and Gotman, J. (2001). Dipole modeling of scalp electroencephalogram epileptic discharges: correlation with intracerebral fields. *Clin. Neurophysiol.*, 112(3):414–430.
- [Michel and Murray, 2012] Michel, C. M. and Murray, M. M. (2012). Towards the utilization of EEG as a brain imaging tool. *NeuroImage*, 61(2):371–385.
- [Michel et al., 2004] Michel, C. M., Murray, M. M., Lantz, G., Gonzales, S., Spilelli, L., and Grave de Peralta, R. (2004). EEG source imaging. *Clin. Neurophysiol.*, 115(10):2195–2222.
- [Miller et al., 2002] Miller, S. P., Weiss, J., Barnwell, A., Ferriero, D. M., Latal-Hajnal, B., Ferrer-Rogers, A., and et.al. (2002). Seizure-associated brain injury in term newborns with perinatal asphyxia. *Neurology*, 58(4):542–548.
- [Montagnat et al., 2001] Montagnat, J., Delingette, H., and Ayache, N. (2001). A review of deformable surfaces: topology, geometry and deformation. *Image and Vision Computing*, 19(14):1023–1040.
- [Morrone and Owens, 1987] Morrone, M. C. and Owens, R. A. (1987). Feature detection from local energy. *Pattern Recognition Letters*, 6(5):303–313.
- [Murgasova, 2008] Murgasova, M. (2008). *Segmentation of brain MRI during early childhood*. PhD thesis, Imperial Collage London.
- [Murray et al., 2008] Murray, D. M., Boylan, G. B., Ali, I., Ryan, C. A., Murphy, B. P., and Connolly, S. (2008). Defining the gap between electrographic seizure burden, clinical expression and staff recognition of neonatal seizures. *Arch. Dis. Child. Fetal Neonatal. Ed.*, 93(3):F187–F191.
- [Murray et al., 2009] Murray, D. M., Boylan, G. B., Ryan, C. A., and Connolly, S. (2009). Early EEG findings in hypoxic-ischemic encephalopathy predict outcomes at 2 years. *Pediatrics*, 124(3):e459–e467.

- [Murray, 1981] Murray, P. W. (1981). Field calculations in the head of a newborn infant and their application to the interpretation of transephalic impedance measurements. *Med. Biol. Eng. Comput.*, 19(5):538–546.
- [Nagele et al., 2004] Nagele, R. G., Wegiel, J., Venkataraman, V., Imaki, H., Wang, K. C., and Wegiel, J. (2004). Contribution of glial cells to the development of amyloid plaques in Alzheimer’s disease. *Neurobiology of Aging*, 25(5):663–674.
- [Nelder and Mead, 1965] Nelder, J. A. and Mead, R. (1965). A simplex method for function minimization. *Computer Journal*, 7(4):308–313.
- [Nolte, 2002] Nolte, J. (2002). *The Human Brain: An Introduction to Its Functional Anatomy*. Elsevier Health Sciences, 5 edition.
- [Oostendorp et al., 2000] Oostendorp, T. F., Delbeke, J., and Stegeman, D. F. (2000). The conductivity of the human skull: results of in vivo and in vitro measurements. *IEEE Trans. Biomed. Eng.*, 47(11):1487–1492.
- [Pal and Pal, 1993] Pal, N. R. and Pal, S. K. (1993). A review on image segmentation techniques. *Pattern Recognition*, 26(9):1277–1294.
- [Pant et al., 2011] Pant, S., Te, T., Tucker, A., and Sadleir, R. J. (2011). The conductivity of neonatal piglet skulls. *Physiol. Meas.*, 32(8):1275–1283.
- [Parazzini et al., 2002] Parazzini, C., Baldoli, C., Scotti, G., and Triulzi, F. (2002). Terminal zones of myelination: MR evaluation of children aged 20–40 months. *AJNR Am. J. Neuroradiol.*, 23(10):1669–1673.
- [Passat et al., 2005] Passat, N., Ronse, C., Baruthio, J., Armspach, J. P., Maillot, C., and Jahn, C. (2005). Region-growing segmentation of brain vessels: an atlas-based automatic approach. *J. Magn. Reson. Imaging.*, 21(6):715–725.
- [Patrizi et al., 2003] Patrizi, S., Holmes, G. L., Orzalesi, M., and Allemand, F. (2003). Neonatal seizures: characteristics of EEG ictal activity in preterm and fullterm infants. *Brain. Dev.*, 25(6):427–437.
- [Perona and Malik, 1990] Perona, P. and Malik, J. (1990). Scale-space and edge detection using anisotropic diffusion. *IEEE Trans. Pattern Anal. Machine Intell.*, 12(7):629–639.
- [Perumpillichira, 2010] Perumpillichira, J. C. (2010). *Improvements in Neonatal Brain Monitoring after Perinatal Asphyxia*. PhD thesis, Erasmus University Rotterdam.
- [Perumpillichira et al., 2011] Perumpillichira, J. C., Deburchgraeve, W., Swarte, R., De Vos, M., Govaert, P., Van Huffel, S., and Visser, G. (2011). Validation of a new automated neonatal seizure detection system: a clinician’s perspective. *Clin. Neurophysiol.*, 122(8):1490–1499.

- [Pham et al., 2000] Pham, D. L., Xu, C., and Prince, J. L. (2000). Current methods in medical image segmentation. *Annual Review of Biomedical Engineering*, 2:315–337.
- [Plaisier et al., 2013] Plaisier, A., Govaert, P., Lequin, M. H., and Dudink, J. (2013). Optimal timing of cerebral MRI in preterm infants to predict long-term neurodevelopmental outcome: A systematic review. *AJNR Am. J. Neuroradiol.* [Epub ahead of print].
- [Plaisier et al., 2012] Plaisier, A., Raets, M. M., van der Starre, C., Feijen-Roon, M., Govaert, P., Lequin, M. H., Heemskerk, A. M., and Dudink, J. (2012). Safety of routine early mri in preterm infants. *Pediatr. Radiol.*, 42(10):1205–1211.
- [Platasa et al., 2011] Platasa, L., De Smet, A., Kumcu, A., Vansteenkiste, E., Pizurica, A., Deblaere, K., and Philips, W. (2011). Measuring cortical thickness in brain MRI volumes to detect focal cortical dysplasia (FCD) in epilepsy patients. In *Proc. International Society for Magnetic Resonance in Medicine Chapter (ISMRM)*, page 2438.
- [Platasa et al., 2012] Platasa, L., De Smet, A., Kumcu, A., Vansteenkiste, E., Pizurica, A., Deblaere, K., and Philips, W. (2012). Measuring cortical thickness in brain MRI volumes to detect focal cortical dysplasia (FCD) in epilepsy patients. In *Proc. Benelux International Society for Magnetic Resonance in Medicine Chapter (ISMRM)*, Hoeven, The Netherlands.
- [Pluim et al., 2003] Pluim, J. P. W., Maintz, J. B. A., and Viergever, M. A. (2003). Mutual-information-based registration of medical images: a survey. *IEEE Trans. Med. Imaging*, 22(8):986–1004.
- [Plummer et al., 2008] Plummer, C., Harvey, A. S., and Cook, M. (2008). EEG source localization in focal epilepsy: where are we now? *Epilepsia*, 49(2):201–218.
- [Pohl et al., 2002] Pohl, K., Wells, W., Guimond, A., Kasai, K., Shenton, M., Kikinis, R., Grimson, W., and Warfield, S. (2002). Incorporating non-rigid registration into expectation maximization algorithm to segment MR images. In *Proc. Medical Image Computing and Computer Assisted Intervention (MICCAI)*, pages 564–572.
- [Pohl, 2005] Pohl, K. M. (2005). *Prior Information for Brain Parcellation*. PhD thesis, Massachusetts Institute of Technology.
- [Pohl et al., 2006] Pohl, K. M., Fisher, J., Grimson, W. E. L., Kikinis, R., and Wells, W. M. (2006). A bayesian model for joint segmentation and registration. *NeuroImage*, 31(1):228–239.
- [Prastawa, 2007] Prastawa, M. (2007). *An MRI Segmentation Framework for Brains with Anatomical Deviations*. PhD thesis, University of North Carolina at Chapel Hill.

- [Prastawa et al., 2005] Prastawa, M., Gilmore, J. H., Lin, W., and Gerig, G. (2005). Automatic segmentation of MR images of the developing newborn brain. *Med. Image Anal.*, 9(5):457–466.
- [Purcell et al., 1946] Purcell, E. M., Torrey, H. C., and Pound, R. V. (1946). Resonance absorption by nuclear magnetic moments in a solid. *Phys. Rev.*, 69(1-2):37–38.
- [Qu et al., 2013] Qu, X., Kumcu, A., Platasa, L., Despotovic, I., Deblaere, K., Bai, T., and Philips, W. (2013). Blur estimation at the gray-white matter boundary for focal cortical dysplasia in magnetic resonance imaging. In *Proc. IEEE Engineering in Medicine and Biology Society Conference (EMBC)*, page accepted.
- [Quesney, 1991] Quesney, L. F. (1991). Preoperative electroencephalographic investigation in frontal lobe epilepsy: electroencephalographic and electrocorticographic recordings. *Can. J. Neurol. Sci.*, 18(4 Suppl):559–563.
- [Rabi et al., 1938] Rabi, I. I., Zacharias, J. R., Millman, S., and Kusch, P. (1938). A new method of measuring nuclear magnetic moment. *Phys. Rev.*, 53(4):318–318.
- [Rajan et al., 2009] Rajan, J., Kannan, K., Kesavadas, C., and Thomas, B. (2009). Focal cortical dysplasia (FCD) lesion analysis with complex diffusion approach. *Comput. Med. Imaging Graph.*, 33(7):553–558.
- [Rajapakse et al., 1997] Rajapakse, J. C., Giedd, J. N., and Rapoport, J. L. (1997). Statistical approach to segmentation of single-channel cerebral MR images. *IEEE Trans. Med. Imaging*, 16(2):176–186.
- [Rajapakse and Kruggel, 1998] Rajapakse, J. C. and Kruggel, F. (1998). Segmentation of MR images with intensity inhomogeneities. *Image and Vision Computing*, 16(3):165–180.
- [Reddi et al., 1984] Reddi, S., Rudin, S., and Keshavan, H. (1984). An optimal multiple threshold scheme for image segmentation. *IEEE Trans. System Man Cybernet.*, 14(4):661–665.
- [Restak, 1995] Restak, R. M. (1995). *Brainscapes: An Introduction to What Neuroscience Has Learned About the Structure, Function, and Abilities of the Brain*. New York: Hyperion.
- [Roche-Labarbe et al., 2008] Roche-Labarbe, N., Aarabi, A., Kongolo, G., Gondry-Jouet, C., Dümpelmann, M., Grebe, R., and Wallois, F. (2008). High-resolution electroencephalography and source localization in neonates. *Human Brain Mapping*, 29(2):167–176.
- [Rogowska, 2000] Rogowska, J. (2000). *Overview and fundamentals of medical image segmentation*. In: *Handbook of medical image processing and analysis*. Elsevier, Amsterdam, The Netherlands.

- [Roth et al., 1993] Roth, B., Gobraich, A., and Sato, S. (1993). How well does a three-shell model predict positions of dipoles in a realistically shaped head? *Electroencephalogr. Clin. Neurophysiol.*, 87:175–184.
- [Rueckert et al., 1999] Rueckert, D., Sonoda, L. I., Hayes, C., Hill, D. L. G., Leach, M. O., and Hawkes, D. J. (1999). Nonrigid registration using free-form deformations: Application to breast MR images. *IEEE Trans. Med. Imaging*, 18(8):712–721.
- [Rush and Driscoll, 1986] Rush, S. and Driscoll, D. A. (1986). Current distribution in the brain from surface electrodes. *Anesth. Analg.*, 47(6):717–723.
- [Rutherford, 2001] Rutherford, M. A. (2001). *MRI of the Neonatal Brain*. Saunders Ltd.
- [Rutherford, 2012] Rutherford, M. A. (2012). Mri of the neonatal brain. <http://www.mrineonatalbrain.com/ch04-09.php>.
- [Rutherford et al., 1998] Rutherford, M. A., Pennock, J. M., Counsell, S. J., Mercuri, E., Cowan, F. M., Dubowitz, L. M., and Edwards, A. D. (1998). Abnormal magnetic resonance signal in the internal capsule predicts poor neurodevelopmental outcome in infants with hypoxicischaemic encephalopathy. *Pediatrics*, 102(2 Pt 1):323–328.
- [Saha and Williams, 1992] Saha, S. and Williams, P. A. (1992). Electric and dielectric properties of wet human cortical bone as a function of frequency. *IEEE Trans. Biomed. Eng.*, 39(12):1298–1304.
- [Salanova et al., 1994] Salanova, V., Quesney, L. F., Rasmussen, T., Andermann, F., and Olivier, A. (1994). Reevaluation of surgical failures and the role of reoperation in 39 patients with frontal lobe epilepsy. *Epilepsia*, 35(1):70–80.
- [Schaul, 1998] Schaul, N. (1998). The fundamental neural mechanisms of electroencephalography. *Electroencephalogr. Clin. Neurophysiol.*, 106(2):101–107.
- [Scher et al., 1993] Scher, M. S., Aso, K., Beggarly, M. E., Hamid, M. Y., Steppe, D. A., and Painter, M. J. (1993). Electrographic seizures in preterm and full-term neonates: clinical correlates, associated brain lesions, and risk for neurologic sequelae. *Pediatrics*, 91(1):128–134.
- [Scherg and von Cramon, 1985] Scherg, M. and von Cramon, D. (1985). Two bilateral sources of the late AEP as identified by a spatio-temporal dipole model. *Electroencephalogr. Clin. Neurophysiol.*, 62(1):32–44.
- [Schroeder et al., 2006] Schroeder, W., Martin, K., and Lorensen, B. (2006). *The Visualization Toolkit: An Object-Oriented Approach to 3D Graphics*. Kitware Inc., 4 edition.
- [Segers et al., 2010] Segers, I., Despotovic, I., Deblaere, K., and Philips, W. (2010). Detecteren van focale corticale dysplasie-letsels op basis van MRI cortexsegmentatie. Master's thesis, Ghent University.

- [Sezgin and Sankur, 2004] Sezgin, M. and Sankur, B. (2004). Survey over image thresholding techniques and quantitative performance evaluation. *J. Electron. Imaging*, 13(1):146–165.
- [Shattuck et al., 2001] Shattuck, D., Sandor-Leahy, S., Schaper, K., Rottenberg, D., and Leahy, R. (2001). Magnetic resonance image tissue classification using a partial volume model. *Neuroimage*, 12(5):856–876.
- [Shattuck and Leahy, 2002] Shattuck, D. W. and Leahy, R. M. (2002). BrainSuite: an automated cortical surface identification tool. *Med. Image Anal.*, 6(2):129–142.
- [Shen and Davatzikos, 2002] Shen, D. and Davatzikos, C. (2002). Hammer: Hierarchical attribute matching mechanism for elastic registration. *IEEE Trans. Med. Imaging*, 21(11):1421–1439.
- [Shen et al., 2005] Shen, S., Sandham, W., Granat, M., and Sterr, A. (2005). MRI fuzzy segmentation of brain tissue using neighborhood attraction with neural-network optimization. *IEEE Trans. Inf. Technol. Biomed.*, 9(3):459–467.
- [Shi et al., 2011] Shi, F., Shen, D., Yap, P. T., Fan, Y., Cheng, J. Z., An, H., Wald, L. L., Gerig, G., Gilmore, J. H., and Lin, W. (2011). CENTS: cortical enhanced neonatal tissue segmentation. *Human Brain Mapping*, 32(3):382–396.
- [Silva et al., 1999] Silva, C., Almeida, R., Oostendorp, T., Ducla-Soares, E., Foreid, J. P., and Pimentel, T. (1999). Interictal spike localization using a standard realistic head model: simulations and analysis of clinical data. *Clin. Neurophysiol.*, 110(5):846–855.
- [Sled et al., 1998] Sled, J. G., Zijdenbos, A. P., and Evans, A. C. (1998). A nonparametric method for automatic correction of intensity nonuniformity in MRI data. *IEEE Trans. Med. Imaging*, 17(1):87–97.
- [Smith, 2002] Smith, S. M. (2002). Fast robust automated brain extraction. *Human Brain Mapping*, 17(3):143–155.
- [Song et al., 2006] Song, Z., Tustison, N., Avants, B., and Gee, J. C. (2006). Integrated graph cuts for brain MRI segmentation. *Med. Image Comput. Comput. Assist. Interv.*, 9(Pt 2):831–838.
- [Steinman et al., 2009] Steinman, K. J., Gorno-Tempini, M. L., Glidden, D. V., Kramer, J. H., Miller, S. P., Barkovich, A. J., and Ferriero, D. M. (2009). Neonatal watershed brain injury on magnetic resonance imaging correlates with verbal IQ at 4 years. *Pediatrics*, 123(3):1025–1030.
- [Studholme et al., 1999] Studholme, C., Hills, D. L. G., and Hawkes, D. J. (1999). An overlap invariant entropy measure of 3D medical image alignment. *Pattern Recognition*, 32(1):71–86.
- [Swarte et al., 2009] Swarte, R., Lequin, M., Perumpillichira, J., Zecic, A., van Goudoever, J., and Govaert, P. (2009). Imaging patterns of brain injury in term-birth asphyxia. *Acta Paediatr.*, 98(3):586–592.

- [Tao et al., 2002] Tao, X., Prince, J. L., and Davatzikos, C. (2002). Using a statistical shape model to extract sulcal curves on the outer cortex of the human brain. *IEEE Trans. Med. Imaging*, 21(5):513–524.
- [Terzopolous et al., 1998] Terzopolous, D., Witkin, A., and Kaas, M. (1998). Constraints on deformable models: Recovering 3-D shape and non-rigid motion. *Artificial Intelligence Journal*, 36(1):91–123.
- [Therrien, 1989] Therrien, C. (1989). *Decision, estimation, and classification: an introduction to pattern recognition and related topics*. Wiley, New York.
- [Thevenaz and Unser, 2000] Thevenaz, P. and Unser, M. (2000). Optimization of mutual information for multi resolution image registration. *IEEE Trans. Image Process.*, 9(12):2083–2099.
- [Thurai et al., 1984] Thurai, M., Goodridge, V. D., Sheppard, R. J., and Grant, E. H. (1984). Variation with age of the dielectric properties of mouse brain cerebrum. *Phys. Med. Biol.*, 29(9):1133–1136.
- [Tokarieva et al., 2012] Tokarieva, A., Palmub, K., Lanod, A., Metsäranta, M., and Vanhatalo, S. (2012). Phase synchrony in the early preterm EEG: Development of methods for estimating synchrony in both oscillations and events. *NeuroImage*, 60(2):1562–1573.
- [Traynora et al., 2011] Traynora, C. R., Barkerb, G. J., Crumb, W. R., Williamsb, S. C. R., and Richardsons, M. P. (2011). Segmentation of the thalamus in MRI based on T1 and T2. *NeuroImage*, 56(1):939–950.
- [Twieg, 1983] Twieg, D. B. (1983). The k-trajectory formulation of the NMR imaging process with applications in analysis and synthesis of imaging methods. *Med. Phys.*, 10(5):610–621.
- [Ulijaszek et al., 1998] Ulijaszek, S., Johnston, F., and Preece, M. (1998). *The Cambridge Encyclopedia of Human Growth and Development*. Institute of Child Health, University College London.
- [Unnikrishnan et al., 2007] Unnikrishnan, R., C., P., and Hebert, M. (2007). Toward objective evaluation of image segmentation algorithms. *IEEE Trans. Pattern Anal. Machine Intell.*, 29(6):929–944.
- [Uzwiak, 2013] Uzwiak, A. J. (2013). Online rutgers university courses. <http://www.rci.rutgers.edu/~uzwiak/AnatPhys/APFallLect19.html>.
- [Van Leemput et al., 1999] Van Leemput, K., Maes, F., Vandermeulen, D., and Suetens, P. (1999). Automated model-based bias field correction of MR images of the brain. *IEEE Trans. Med. Imaging*, 18(10):885–896.
- [Vanhatalo et al., 2008] Vanhatalo, S., Metsäranta, M., and Andersson, S. (2008). High-fidelity recording of brain activity in the extremely preterm babies: feasibility study in the incubator. *Clin. Neurophysiol.*, 119(2):439–445.

- [Vanrumste, 2001] Vanrumste, B. (2001). *EEG dipole source analysis in a realistic head model*. PhD thesis, Ghent University.
- [Vanrumste et al., 2000] Vanrumste, B., Van Hoey, G., Van de Walle, R., D'Havé, M., Lemahieu, I., and Boon, P. (2000). Dipole location errors in electroencephalogram source analysis due to volume conductor model errors. *Med. Biol. Eng. Comput.*, 38(5):528–534.
- [Vanrumste et al., 2001] Vanrumste, B., Van Hoey, G., Van de Walle, R., D'Havé, M. R., Lemahieu, I. A., and Boon, P. A. (2001). The validation of the finite difference method and reciprocity for solving the inverse problem in EEG dipole source analysis. *Brain Topogr.*, 14(2):83–92.
- [Vansteenkiste, 2007] Vansteenkiste, E. (2007). *Quantitative Analysis of Ultrasound Images of the Preterm Brain*. PhD thesis, Ghent University.
- [Vatta et al., 2010] Vatta, F., Meneghini, F., Esposito, F., Mininel, S., and Di Salle, F. (2010). Realistic and spherical head modeling for EEG forward problem solution: a comparative cortex-based analysis. *Comput. Intell. Neurosci.*, pages 1–11.
- [Venkatesh and Owens, 1990] Venkatesh, S. and Owens, R. (1990). On the classification of image features. *Pattern Recognition Letters*, 11(5):339–349.
- [Viola and Wells, 1997] Viola, P. and Wells, W. I. I. (1997). Alignment by maximization of mutual information. *Int. J. Comput. Vision*, 24(2):137–154.
- [Volpe, 2008] Volpe, J. (2008). *Neurology of the Newborn*. WB Saunders, Philadelphia, 5 edition.
- [Volpe, 2000] Volpe, J. J. (2000). Overview: normal and abnormal human brain development. *Ment. Retard. Dev. Disabil. Res. Rev.*, 6(1):1–5.
- [Volpe and Pasternak, 1977] Volpe, J. J. and Pasternak, J. F. (1977). Parasagittal cerebral injury in neonatal hypoxic-ischemic encephalopathy: clinical and neuroradiologic features. *J. Pediatr.*, 91(3):472–476.
- [Wang and Gotman, 2001] Wang, Y. and Gotman, J. (2001). The influence of electrode location errors on EEG dipole source localization with a realistic head model. *Clin. Neurophysiol.*, 112(9):1777–1780.
- [Wang et al., 2009] Wang, Z., Soh, Y. C., Song, Q., and Sim, K. (2009). Adaptive spatial information-theoretic clustering for image segmentation. *Pattern Recognition Letters*, 42(9):2029–2044.
- [Warfield et al., 1998] Warfield, S. K., Kaus, M., Jolesz, F. A., and Kikinis, R. (1998). Adaptive template moderated spatially varying statistical classification. In *Proc. Medical Image Computing and Computer Assisted Intervention (MICCAI)*, pages 431–438.

- [Watanabe et al., 1980] Watanabe, K., Miyazaki, S., Hara, K., and Hakamada, S. (1980). Behavioral state cycles, background EEGs and prognosis of newborns with perinatal hypoxia. *Electroencephalogr. Clin. Neurophysiol.*, 49(5-6):618–625.
- [Weglinski and Fabijanska, 2011] Weglinski, T. and Fabijanska, A. (2011). Brain tumor segmentation from MRI data sets using region growing approach. In *Proc. Intern. Conf. on Perspective Technologies and Methods in MEMS Design (MEMSTECH)*.
- [Weisenfeld and Warfield, 2009] Weisenfeld, N. I. and Warfield, S. K. (2009). Automatic segmentation of newborn brain MRI. *Neuroimage*, 47(2):564–572.
- [Wells III et al., 1996a] Wells III, W., Viola, P., Atsumi, H., Nakajima, S., and Kikinis, R. (1996a). Multi-modal volume registration by maximization of mutual information. *Med. Image Anal.*, 1(1):35–51.
- [Wells III et al., 1996b] Wells III, W. M., Grimson, W. E. L., Kikinis, R., and Jolesz, F. A. (1996b). Adaptive segmentation of MRI data. *IEEE Trans. Med. Imaging*, 15(4):429–442.
- [Wilke et al., 2003] Wilke, M., Schmithorst, V. J., and Holland, S. K. (2003). Normative pediatric brain data for spatial normalization and segmentation differs from standard adult data. *Magn. Reson. Med.*, 50(4):749–757.
- [Wolz et al., 2010] Wolz, R., Heckemann, R. A., Aljabar, P., Hajnal, J. V., Hammers, A., Lötjönen, J., and Rueckert, D. (2010). Measurement of hippocampal atrophy using 4D graph-cut segmentation: application to ADNI. *Neuroimage*, 52(1):109–118.
- [Xue et al., 2007] Xue, H., Srinivasan, L., Jiang, S., Rutherford, M., Edwards, A. D., Rueckert, D., and Hajnal, J. (2007). Automatic segmentation and reconstruction of the cortex from neonatal MRI. *Neuroimage*, 38(3):461–477.
- [Xue et al., 2003] Xue, J. H., Pizurica, A., Philips, W., Kerre, E., Van de Walle, R., and Lemahieu, I. (2003). An integrated method of adaptive enhancement for unsupervised segmentation of MRI brain images. *Pattern Recognition Letters*, 24(15):2549–2560.
- [Yakovlev and Lecours, 1967] Yakovlev, P. I. and Lecours, A. R. (1967). *The myelogenetic cycles of regional maturation of the brain*. Blackwell Scientific Publications, Oxford.
- [Yan et al., 2010] Yan, P., Xu, S., Turkbey, B., and Kruecker, J. (2010). Discrete deformable model guided by partial active shape model for trus image segmentation. *IEEE Trans. Biomed. Eng.*, 57(5):1158–1166.
- [Yang and Duncan, 2004] Yang, J. and Duncan, J. S. (2004). 3D image segmentation of deformable objects with joint shape-intensity prior models using level sets. *Med. Image Anal.*, 8(3):285–294.

- [Yushkevich et al., 2006] Yushkevich, P. A., Piven, J., Heather, C. H., Rachel, G. S., Ho, S., Gee, J. C., and Gerig, G. (2006). User-guided 3D active contour segmentation of anatomical structures: Significantly improved efficiency and reliability. *Neuroimage*, 31(3):1116–1128.
- [Yvert et al., 1997] Yvert, B., Bertrand, O., Thevenet, M., Echallier, J. F., and Pernier, J. (1997). A systematic evaluation of the spherical model accuracy in EEG dipole localization. *Electroencephalogr. Clin. Neurophysiol.*, 102(5):452–459.
- [Zadeh, 1965] Zadeh, L. A. (1965). Fuzzy sets. *Information and Control*, 8(3):338–353.
- [Zhang et al., 2001] Zhang, Y., Brady, M., and Smith, S. (2001). Segmentation of brain MR images through a hidden markov random field model and the expectation-maximization algorithm. *IEEE Trans. Med. Imaging*, 20(1):45–57.
- [Zitova and Flusser, 2003] Zitova, B. and Flusser, J. (2003). Image registration methods: a survey. *Image and Vision Computing*, 21(11):977–1000.